# Studies on the Role of Microstructure in the Dynamic Strength of Metals




John C. Z. Jonsson

Wolfson College

University of Oxford

Supervised by

Prof Daniel Eakins, Dr David Chapman

A thesis submitted for the degree of

*Doctor of Philosophy*

Trinity 2021

UK Ministry of Defence ©Crown Owned Copyright 2021/AWE

# Abstract

Shock compression is a powerful tool with which to study the high pressure response of matter. Metals subjected to shock wave loading are well-known to behave elastically up to extraordinarily high stress states within a brief time-window after impact, beyond which the yield point quickly decays towards an equilibrium limit as the shock wave propagates further into the target. Despite six decades of study, the microstructural processes which are at the origin of this phenomenon remain obscure and highly material dependent. In this work, the transient states of the dynamic yield point are investigated through the evolution of the elastic precursor wave with propagation distance, enabling study of the time-dependence of dislocation mechanisms and plastic flow which cannot be captured by other means.

In the first of three experimental campaigns, highly textured extruded magnesium is shock loaded along two impact orientations. The dynamic strength is found to be highly dependent on the grain orientation distribution, caused by relative differences in slip system activity. Application of a novel orientation-based analysis framework shows that the yield point of the polycrystalline material can be predicted reasonably well, predicated upon the use of dynamic critical resolved shear stress (CRSS) values from single crystal data modified by a fitted strengthening factor.

Second, the effects of grain size are investigated in conventionally cast and melt-sheared samples of Mg AZ91, in which the latter displays significant grain refinement. Measurements indicate that grain boundaries are inconsequential during dynamic yielding, a result of the short timescales of shock loading inhibiting interactions between moving dislocations and grain boundaries.

In the final study, pure Al and Al 6082 is cold worked to increasing strains in order to study the effects of the initial dislocation density. It is found that a higher initial dislocation density results in a decrease in the dynamic strength, demonstrating for the first time conclusive empirical proof of a reversal in the role of dislocation density when increasing the applied strain rates past $10^4$ $s^{-1}$. Both analytical and numerical precursor decay models applied to the experimental data show that increased stress relaxation is caused by higher initial mobile dislocation densities. On the whole, these results quantitatively establish the relationship between the yield point during high strain rate loading and the dynamic behaviour of dislocations, as determined by microstructural features such as slip system activity and initial dislocation density.

## Presentations

- *Ultrafast yielding of metals under shockwave impact*, Poster presentation, **Defence and Security Doctoral Symposium**, UK, 13/11/18
- *The role of extreme cold work on elastic precursor decay*, Oral presentation, **Mach Conference**, USA, 4/4/19
- *The role of microstructure in elastic precursor decay*, Oral presentation, **SCCM Conference**, USA, 17/6/19
- *Ultrafast yielding of metals at the onset of plasticity under shockwave impact*, Oral presentation, **CornerStone Prosperity Partnership and Doctoral Training Conference**, 30/6/21, UK

## Papers

- **J. C. Jonsson**, L. Farbaniec, E. M. Escauriza, L. C. Smith, D. J. Chapman, and D. E. Eakins, *Effect of texture on elastic precursor decay in magnesium alloy AZ31B*, **In preparation**
- **J. C. Jonsson**, R. Kositski, D. J. Chapman, E. M. Escauriza, L. C. Smith, D. Mordehai, D. E. Eakins, *Role of dislocation density in the dynamic yield of pure aluminium and aluminium alloy 6082*, **In preparation**
- E. M. Escauriza, M. P. Olbinado, M. E. Rutherford, D. J. Chapman, **J. C. Jonsson**, A. Rack and D. E. Eakins, *Ultra-high-speed indirect X-ray imaging system with versatile spatio-temporal sampling capabilities*, **Applied Optics** 57, 8 (2018). https://doi.org/10.1364/AO.57.005004
- E. M. Escauriza, J. P. Duarte, D. J. Chapman, M. E. Rutherford, L. Farbaniec, **J. C. Jonsson**, L. C. Smith, M. P. Olbinado, J. Skidmore, P. Foster, T. Ringrose, A. Rack and D. E. Eakins, *Collapse dynamics of spherical cavities in a solid under shock loading*, **Scientific Reports** 10, 8455 (2020). https://doi.org/10.1038/s41598-020-64669-y
- D. J. Miller, R. S. Crum, M. A. Homel, D. E. Eakins, D. J. Chapman, **J. C. Jonsson**, M. E. Rutherford, E. M. Escauriza, L. C. Smith, E. B. Herbold, J. Lind, M. C. Akin, *Hugoniot measurements utilizing in situ synchrotron X-ray radiation*, **Journal of Dynamic Behavior of Materials** 5 (2019). https://doi.org/10.1007/s40870-019-00187-x

## Proceedings

- **J. C. Jonsson**, L. Farbaniec, E. M. Escauriza, L. C. Smith, D. J. Chapman, and D. E. Eakins, *Effect of Texture on Elastic Precursor Decay in Magnesium Alloy AZ31B*, SCCM Conference 2019, **AIP Conference Proceedings** 2272, 120009 (2020). https://doi.org/10.1063/12.0000818

# Acknowledgements

I would first and foremost like to thank my supervisors. Prof. Daniel Eakins has been an ever-present source of vision and scientific knowledge throughout my DPhil. Always ready for a discussion, he steadily guided me until I was able through my own efforts to take large leaps in my research, and for this I am deeply grateful. The results presented in this thesis would also have been impossible without the advice of Dr. David Chapman. Displaying endless patience, he transformed me from a helpless gas gun rookie into a practiced shock physicist, making sure my experiments were sensible every step of the way. I am grateful to both for their encouragement and for pushing me towards ever greater achievements.

I would also like to thank all of my research colleagues at Oxford. Special thanks go to Lukasz Farbaniec, Emilio Escauriza, Liam Smith, Thomas Ota, and Michael Rutherford, who have not only been great friends for many years, but have also spent numerous late evenings and early mornings with me helping out with experiments.

Next, I would like to acknowledge the staff at the IEL. I thank Stuart Carter and Jeff Fullerton for their tireless work constructing the weirdly specific equipment I requested of the workshop. Karen Bamford, for always handling the admin and paperwork with both efficiency and elegance, turning an almost certain source of stress into a completely painless experience. Thanks also go to Jennifer Holter and Ian Griffiths at DCCEM, who not only trained me in microscopy but went above and beyond in helping me with my experiments long after I was done with training.

I'd like to thank EPSRC and AWE for the funding which made this research possible. I have also had the pleasure to work on a collaboration with Roman Kositski and Dan Mordehai. I would like to thank them both for all of our engaging discussions, which provided me with new and invaluable perspective on my research.

Finally, my deepest thanks go to those closest to me.

To Cheryl: these past years have been both joyful and at times difficult. You were always there when needed, and for that I will be forever grateful.

To Ulf, Deying, and Calle: you have been my foundation since the very beginning, and I could not be happier with how things have turned out. Thank you.

# Contents

**List of Figures** **vii**

**1 Introduction** **1**
1.1 The time-dependence of dynamic strength . . . . . 1
1.2 Motivation . . . . . 6
1.3 Structure and goals . . . . . 9

**2 Background to elastic precursor decay** **11**
2.1 Mechanics of deformation and shock loading . . . . . 11
2.1.1 Mechanics of deformation . . . . . 11
2.1.2 Shock waves and the elastic precursor . . . . . 15
2.2 Microscopic origins of plasticity . . . . . 20
2.2.1 Dislocation slip . . . . . 20
2.2.2 Twinning . . . . . 23
2.2.3 Origins of elastic precursor decay . . . . . 25
2.3 Literature review . . . . . 31
2.3.1 Early observations of precursor decay . . . . . 31
2.3.2 Role of strain rate and temperature in aluminium . . . . . 36
2.3.3 Role of crystal orientation in magnesium . . . . . 40
2.4 Overview of precursor decay models . . . . . 45
2.4.1 Analytical precursor decay models . . . . . 46
2.4.2 Dislocation-based numerical dynamic strength model . . . . 50
2.5 Summary . . . . . 51

**3 Experimental methods** **53**
3.1 Development of the precursor decay experimental platform . . . . 53
3.1.1 Summary of experimental challenges . . . . . 53
3.1.2 Plate impact experiment overview . . . . . 55
3.1.3 Vacuum system upgrade . . . . . 56
3.1.4 Barrel mount design . . . . . 59
3.1.5 Projectile design . . . . . 60
3.1.6 Target assembly design . . . . . 61
3.1.7 Sample preparation . . . . . 65
3.2 Diagnostic methods . . . . . 67
3.2.1 PDV . . . . . 67
3.2.2 Tilt Analysis . . . . . 70

3.3 Material characterisation . . . . . 71
3.3.1 EBSD specimen preparation . . . . . 71
3.3.2 TEM specimen preparation . . . . . 73
3.3.3 Dislocation density measurement techniques . . . . . 77
3.4 Summary . . . . . 85

**4 Effects of crystal orientation on the dynamic strength of magnesium alloy 86**
4.1 Overview and motivation . . . . . 86
4.2 Material characterisation . . . . . 90
4.3 Plate impact experiments . . . . . 94
4.4 Discussion . . . . . 101
4.4.1 Propagation distance and strain rate dependence . . . . . 101
4.4.2 Calculation of shear and activation stress as function of loading direction . . . . . 106
4.4.3 Orientation-based prediction of dynamic yield points . . . . 122
4.5 Effect of grain size in Mg AZ91 . . . . . 132
4.6 Chapter summary . . . . . 138

**5 Effects of cold work on the dynamic strength of aluminium 141**
5.1 Overview and motivation . . . . . 141
5.2 Material processing and rotary swaging . . . . . 147
5.3 Material characterisation . . . . . 150
5.3.1 EBSD characterisation . . . . . 150
5.3.2 TEM characterisation . . . . . 157
5.3.3 Estimation of GND density . . . . . 163
5.4 Plate impact experiments . . . . . 167
5.5 Discussion . . . . . 171
5.5.1 Propagation distance and strain rate dependence . . . . . 171
5.5.2 Grain size and dislocation density dependence . . . . . 176
5.5.3 Strain rate dependence of the effects of cold work . . . . . 189
5.6 Orientation analysis . . . . . 193
5.7 Application of dynamic strength models . . . . . 198
5.7.1 Overview of modelling . . . . . 198
5.7.2 Analytical modelling of precursor decay . . . . . 200
5.7.3 Dislocation-based numerical model . . . . . 205
5.8 Chapter summary . . . . . 217

**6 Conclusions 220**
6.1 Summary of work and results . . . . . 220
6.2 Synthesis and future work . . . . . 222

**References 228**

# List of Figures


1.1 Flow stress as a function of strain rate in Al 6061-T651. . . . . 2
1.2 Representative graphic of elastic precursor decay. . . . . 4
1.3 Target stress profiles at varying sample thickness in LiF . . . . . 5

2.1 Typical stress-strain behaviour of a ductile material under quasistatic loading. . . . . 13
2.2 Representation of a shock wave. . . . . 15
2.3 Hugoniot and Rayleigh lines with a corresponding shock propagation. 17
2.4 Emergence of a two-wave shock in a material with strength. . . . . 19
2.5 Schematic of crystal structures. . . . . 20
2.6 Edge and screw dislocations. . . . . 21
2.7 Example of a twinned crystal . . . . . 24
2.8 Illustration of the regions of an under-driven shock wave. . . . . 28
2.9 Three regimes of dislocation mobility. . . . . 29
2.10 Lattice energy barriers caused by Peierls stress. . . . . 30
2.11 Free surface velocity traces in shock loaded Armco iron. . . . . 32
2.12 Peak precursor velocity versus thickness in Armco iron. . . . . 33
2.13 Precursor decay in LiF crystals of varying impurity concentration. . 35
2.14 Peak elastic stress versus thickness and strain rate in pure aluminium. 37
2.15 Slip planes in HCP crystals. . . . . 41
2.16 Twinning systems in HCP crystals. . . . . 41

3.1 Schematic of the gas gun and target chamber setup. . . . . 55
3.2 Picture of the gas gun. . . . . 56
3.3 Example of an air ramp. . . . . 57
3.4 Vacuum system performance comparison before and after upgrades. 58
3.5 Design of the new barrel mount . . . . . 59
3.6 Schematic of projectile tilt. . . . . 61
3.7 Design of the extended sabot. . . . . 61
3.8 Schematic of the target assembly. . . . . 62
3.9 Pictures of target being prepared. . . . . 64
3.10 Picture of a target mounted in the target chamber. . . . . 64
3.11 Example of a PDV spectrogram. . . . . 69
3.12 Schematic of tilt measurements in planar impact. . . . . 70
3.13 Examples of sample preparation damage caused by ion milling and electropolishing. . . . . 76

3.14 TEM sample thickness lineouts calculated from EELS measurements 80

4.1 EBSD measurements of the AZ31 samples. . . . . 91
4.2 Schmid factor distributions of AZ31 samples. . . . . 93
4.3 Velocity profiles of Mg AZ31 loaded along the extrusion and transverse directions at varying thickness and impact velocity. . . . . 97
4.4 Peak elastic stress in AZ31 plotted against propagation distance, compared to single crystal magnesium data. . . . . 102
4.5 Peak elastic stress in AZ31 plotted against strain rate. . . . . 103
4.6 Definitions of coordinate systems in magnesium. . . . . 108
4.7 Error of the uniaxial strain assumption and pure longitudinal wave propagation in magnesium. . . . . 110
4.8 Dynamic orientation factor for various deformation modes in magnesium as a function of loading angle. . . . . 114
4.9 Calculated activation stresses for pure Mg at 2 mm propagation distance. . . . . 120
4.10 Predicted yield stresses of individual grains within the orientation distributions of ED and TD samples. . . . . 123
4.11 Predicted proportions of deformation mode activity. . . . . 124
4.12 Predicted peak elastic stress versus propagation distance in pure Mg and Mg AZ31. . . . . 129
4.13 Optical micrographs of conventional and melt conditioned Mg AZ91. 133
4.14 PDV spectrogram from an Mg AZ91 experiment. . . . . 135
4.15 Velocity profiles of melt-sheared and conventionally cast Mg AZ91. 136
4.16 Peak elastic stress in AZ91 and AZ31 plotted against propagation distance. . . . . 137

5.1 Schematic of rotary swaging. . . . . 148
5.2 EBSD IPF maps and pole figures for 5N-Al. . . . . 152
5.3 EBSD IPF maps and pole figures for Al 6082. . . . . 153
5.4 EBSD grain boundary maps and misorientation distributions for 5N-Al. . . . . 154
5.5 EBSD grain boundary map and misorientation distributions for Al 6082. . . . . 155
5.6 TEM micrograph of a high dislocation density grain in 5N-Al. . . . 157
5.7 TEM micrographs of 5N-Al with increasing rotary swaging passes. . 158
5.8 TEM micrographs of Al 6082 showing high dislocation densities and precipitates. . . . . 160
5.9 TEM micrographs of Al 6082 with increasing rotary swaging passes. 161
5.10 GND density calculations in 5N-Al and Al 6082. . . . . 164

5.11 Illustration of the stages of GND and SSD evolution with increasing strain. . . . . 166
5.12 5N-Al velocity profiles at increasing thickness and swaging passes. . 169
5.13 Magnified view of elastic peaks in 5N-Al velocity profiles at increasing thickness and swaging passes. . . . . 169
5.14 Al 6082 velocity profiles at increasing thickness and swaging passes.170
5.15 Magnified view of elastic peaks in Al 6082 velocity profiles at increasing thickness and swaging passes. . . . . 170
5.16 Peak elastic stress in 5N-Al and Al 6082 plotted against propagation distance comparing present results to literature data. . . . . 172
5.17 Peak elastic stress in 5N-Al and Al 6082 plotted against strain rate. 174
5.18 Peak elastic stress versus dislocation density from plate impact experiments on 5N-Al and al 6082-T6. . . . . 183
5.19 Schematic diagram of the relationship between the yield point and the dislocation density. . . . . 190
5.20 Strain rate dependence of flow stress in quasistatic, SHPB and shock loading experiments on pure aluminium. . . . . 192
5.21 Dynamic orientation factor and Schmid factors in Al for two loading axes. . . . . 195
5.22 Linear elastic model of precursor decay in pure aluminium. . . . . 201
5.23 Nonlinear elastic model of precursor decay in pure aluminium. . . 203
5.24 Simulation of free surface velocity histories in pure aluminium of two different swaging levels. . . . . 206
5.25 Simulations of 5N-Al S0 with varying immobile dislocation density. 207
5.26 Effect of varying the initial mobile dislocation density in the dynamic strength model. . . . . 208
5.27 Effect of varying the mobility law in the dynamic strength model. . 210
5.28 Effect of varying the multiplication parameter in the dynamic strength model. . . . . 212
5.29 Effect of varying the nucleation parameter in the dynamic strength model. . . . . 212
5.30 Illustration of precursor wave variations. . . . . 214
5.31 Illustration of the suggested reversal in strengths of an annealed and cold worked metal. . . . . 214

# 1 Introduction

## 1.1 The time-dependence of dynamic strength

Solid materials such as metals exhibit what we call strength, meaning they are able to resist permanent shape change by an outside force by deforming elastically. After the force is removed, the solid returns to its original form. However, given enough stress, even the strongest of metals will eventually yield and begin to deform permanently through plastic flow. Consider what happens when a body with a finite amount of strength is impacted by a heavy mass travelling at speeds of several hundred meters per second. There is no question that most materials would not be able to withstand such an impact for long. On the other hand, just like water needs to move out of the way as a diver hits the surface, so does a metal need time to flow and deform in response to an applied load. There is a reason why most divers jump from tens of meters in altitude and not much higher; the experience of reaching the surface when going faster is usually disappointing.

The analogy between the impact on water and the one on a metal breaks down upon close inspection. The former is a fluid, the latter has strength. But they do both share a fundamental rule: time is required for matter, whether liquid or solid, to move and to deform under load. The fact is that the results which occur when a body is subjected to a rapid change in load can be vastly different from those which occur during slower, quasistatic conditions. Consequently, learning about the time-dependence of how atoms in a crystal lattice adapt and move as a

result of plastic deformation can be very difficult under low loading rates, where these mechanisms occur so fast relative to the deformation rate that they can be considered instantaneous. In order for the time-dependence of plastic flow to actually affect the macroscopic behaviour of a material when it yields, the speed at which deformation is applied to a body needs to rival the speed at which the body can adapt to it. The work described in this thesis is dedicated to this very goal, namely to advance our understanding of the time-dependent aspects of strength by subjecting materials to very high strain rate loading conditions.

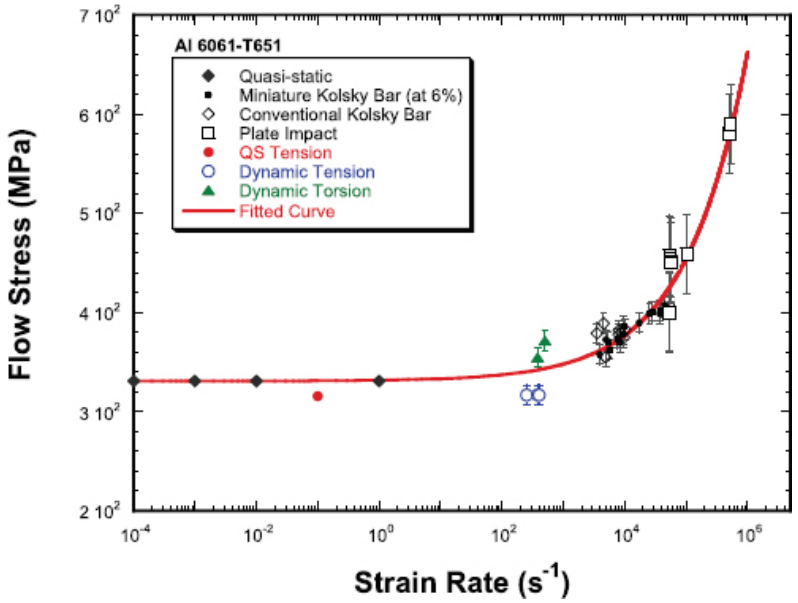



**Figure 1.1:** Flow stress as a function of strain rate in Al 6061-T651 [1]. A sharp increase in flow stress is observed above strain rates of $10^3$ $s^{-1}$, demonstrating the need for separate treatment and study of material behaviour during high strain rate loading.

The difference between high and low strain rate loading can be exemplified by a plot of flow stress as a function of strain rate. For most crystalline solids the flow stress is, under normal circumstances, only lightly dependent upon the rate of deformation. This dependence becomes much stronger once one reaches strain rates of $10^3 - 10^4$ $s^{-1}$, where a sharp increase in the strength of metals is usually observed. Figure 1.1 shows this transition occurring in Al 6061-T651. The challenge lies in understanding the origins of this rapid increase in flow stress, i.e. why materials essentially behave with higher strength as the rate

of deformation is increased. The accepted view attributes the phenomenon to physics at the micro-scale. It is well-known that the rate of plastic flow during high strain rate deformation is correlated to the transient movement and generation of dislocations, which in turn is a complex function of strain rate, temperature, crystal structure, orientation, and more. The transition in strain rate dependence can be explained by a shift from thermal activation to dislocation drag as the limiting factor controlling dislocation mobility [2, 3]. However, as will be explored in this work, quantitative descriptions of this behaviour to this day lack the understanding of microstructural influences necessary to enable their wide-spread use.

Deformation at higher strain rates is generally studied through split-Hopkinson pressure bar (also called Kolsky bar), gas gun, or laser shock experiments, where the latter two are often necessary to reach the regime associated with a dominance of dislocation drag phenomena. The study of dislocation dynamics and the origins of high strain rate yielding has therefore long been carried out through use of plate impact experiments, and more specifically through measurements of the decay of the *elastic precursor wave* as a function of strain rate and propagation distance [4–6]. The concept of elastic precursor decay is best explained through the example shown in Figure 1.2. When a projectile strikes an impact surface, a shock wave is propagated into the material. If the impact stress is chosen carefully such that it is above the yield point of the material, but not overwhelmingly high, then a two-wave structure will emerge in the form of a plastic wave preceded by a faster elastic precursor. The latter constitutes an elastic compression wave with a stress amplitude corresponding to the dynamic yield point of the material. This amplitude will initially assume the impact pressure of the loading event, and will then over the course of around a microsecond quickly decay towards an equilibrium limit at a rate determined by dislocation-mediated plastic flow behind the shock front. In other words, the material will behave elastically up to unusually high stress states within a very short time-window after impact, after which the yield point quickly returns to a steady-state stress range.

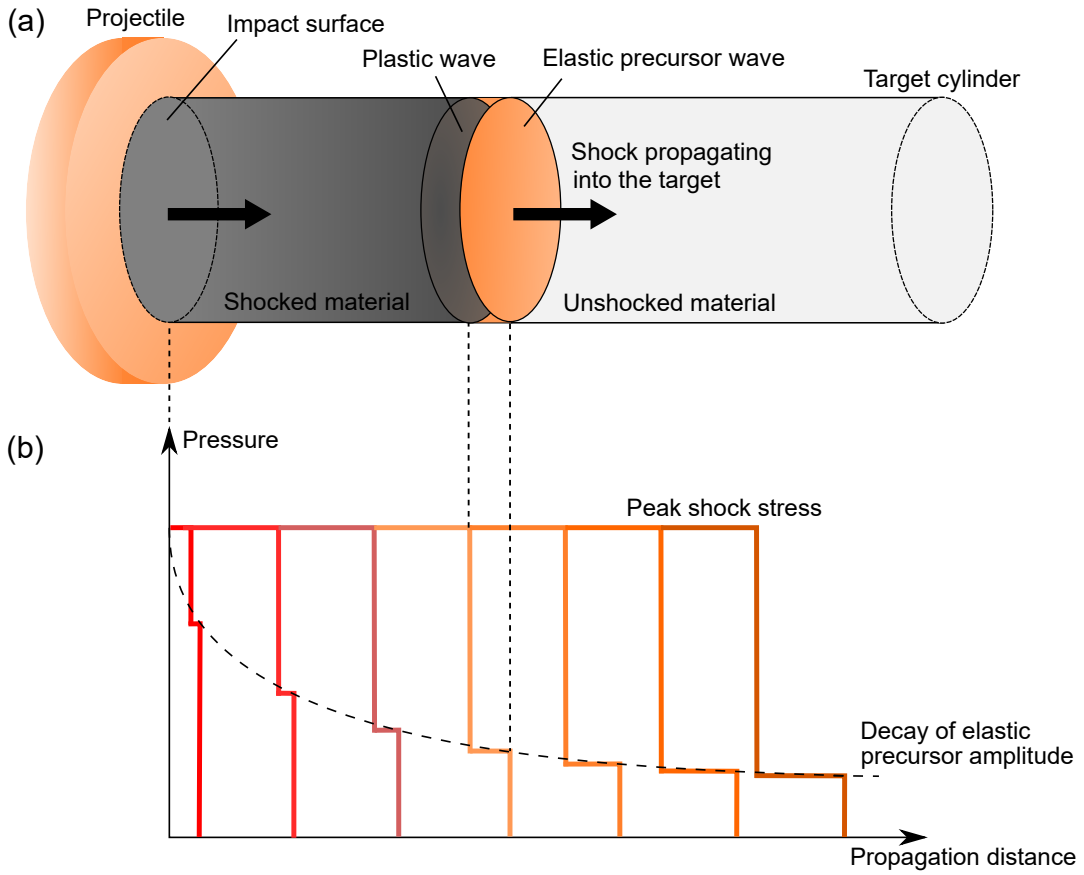



**Figure 1.2:** Illustration of elastic precursor decay. A projectile impacting a cylindrical target causes a shock wave to propagate from the impact surface, a snapshot of which is illustrated in a) in an idealised pure 1D deformation scenario. At relatively low impact velocities, the shock will take the form of a two-step wave, consisting of a plastic wave and a higher-velocity elastic precursor wave. The amplitude of the precursor wave represents the dynamic yield point. As the shock propagates into the target, the elastic precursor amplitude will decay from a non-equilibrium high stress state down towards a steady value. This is shown in b), where the shape of the shock wave profile evolves with increasing time and propagation distance. This phenomenon of attenuation of the dynamic yield point is what is termed elastic precursor decay.

Shown in Figure 1.3 is a classic example of how measurements of elastic precursor decay appear in practice [6], in this case for LiF single crystal. The experimental configuration is similar to that of Figure 1.2, where the propagation of the wave is measured through multiple experiments on increasingly thick targets. In each experiment, the rear free-surface velocity of the LiF target is measured using velocimetry techniques, after which the data can be converted to stress and plotted against time as shown in the figure. Each curve therefore serves as a snapshot of the shock wave as it travels through a LiF crystal. The material close to the impact surface clearly exhibits a temporary increase in the transient yield point, which then quickly attenuates towards an equilibrium value as the loading event progresses. These measurements represent a highly compelling real-world example of the concepts mentioned in the beginning of this chapter: what we observe are unique aspects of material behaviour which appear only when the loading rate rivals the maximum rate at which plastic deformation can occur. This technique of measuring the time-dependence of material strength constitutes the experimental foundation of the work in this thesis.

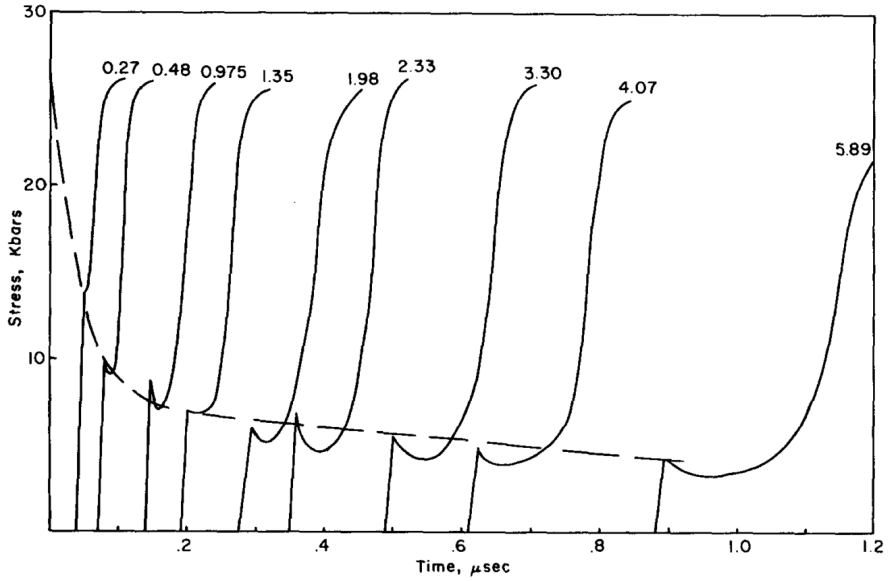



**Figure 1.3:** Target stress profiles in shock loaded LiF single crystals plotted against time at varying sample thickness (mm), shown in the figure [6]. The peak stress of the elastic precursor wave is observed to quickly decay with increasing propagation distance, reaching close to an equilibrium value at around 6 mm. The rate of precursor decay in this study was shown to depend on sample purity, as is discussed in Section 2.3.1.

## 1.2 Motivation

The study of the time-dependence of high strain rate material deformation is of high importance to the areas of shock physics and materials science in general. Measurements across a wide range of strain rates and loading conditions are necessary for the advancement of constitutive models with wide applicability in scientific or industrial settings, including for the development of better materials in automotive, aerospace or defence applications. To this end, measurements of the evolution of the precursor amplitude can provide rich information regarding transient effects of plastic flow which cannot be captured by other means, as they become obscured in the later stages of the macroscopic response when stress-relaxation effects reach an equilibrium with the applied load. It is widely accepted that these time-dependent phenomena originate from the movement and generation of dislocations (and sometimes twins, depending on the material) [7–9]. Dynamic models based on dislocation theory are thus able to utilise the decay of the precursor wave as a validation or calibration tool to examine the microstructural origins of high strain rate material behaviour.

Traditional methods of understanding time-dependent plasticity on a theoretical level rely on fitting phenomenological dislocation models to records of precursor amplitude versus propagation distance [10–13]. However, such models tended to over-predict initial mobile dislocation densities by 1-3 orders of magnitude [11, 14]. In fact even after six decades, the exact mechanisms behind its decay rate still remain an active area of research [5, 7–9, 11]. The dynamic response is far from universal, as remarkable differences can be observed even amongst metals. Body-centred cubic (BCC) systems such as iron or steel for example have very different flow stress behaviours than the face-centred cubic (FCC) aluminium shown in Figure 1.1; the initial flow stress is higher, the initial strain rate dependence is also higher, and the transition to the dislocation drag regime occurs at different strain rates [15]. Not only are these differences apparently linked to crystal structure, but dislocation behaviour as a whole is

known to be dependent on strain rate, temperature, slip system, sample purity and more. The respective influence of each of these factors is still insufficiently understood and highly material dependent. As a result, models have to be individually tailored to the material being studied, or parameters have to be manually adjusted in order to provide a good fit to experimental data [9, 11, 16–19]. The goals are often limited to drawing theoretical conclusions from these fits, whereas this work aims to expand on the quantitative foundations used for predictions of experimental data.

A great deal of studies of precursor decay have been conducted in materials such as aluminium [20–25], iron [10, 26, 27], lithium fluoride [6, 13, 28], copper [29, 30], magnesium [31–34] etc., where the sample materials tend to be in the rather idealised annealed or single-crystal conditions. The large number of physical parameters which can influence the elastic limit means that these studies have been invaluable in providing a baseline understanding of dynamic yield; the uncomplicated initial state simplifies the analysis and allows for investigation of only one parameter such as slip system or temperature. However, it also precludes study of important microstructural features such as defect density, grain size or texture. Where polycrystalline materials are studied, it is often accompanied by only limited characterisation of the initial state, such as the initial defect density or material processing history. Indeed, the initial dislocation density is, theoretically, highly dominant in determining the dynamic yield point [9, 11, 19], and yet direct experimental study of variations in measured initial dislocation densities has been minimal. Similarly, while it is well known that different slip systems can display drastically different behaviour at high strain rates [11, 15], especially in hexagonal close packed (HCP) metals [31, 34], how this affects the behaviour of real-world polycrystalline materials is poorly understood. While more microstructural parameters can be listed, the above two shortcomings in our understanding form the basis for the two primary bodies of work in this thesis on aluminium and magnesium. In the former, the material is cold worked to varying degrees in order to study the effect of variations in initial dislocation density on

the dynamic strength. In the latter, the role of crystal orientation distribution is studied by impacting a highly textured extruded magnesium rod in two different impact orientations. Also included in the study on magnesium is a secondary investigation on the role of grain size.

More detailed motivations can be found in the introductions of Chapters 4 and 5. For now it will be emphasised that while these studies may appear disconnected upon first inspection, they are very much interlinked. Whilst subjecting aluminium to cold work changes the initial dislocation density, it inevitably also produces some amount of grain reorientation. This accentuated the importance of the study on magnesium in Chapter 4, where the initial material states were kept identical apart from the grain orientation distribution. Indeed, the effects of cold work in magnesium itself have in previous studies been dominated by the resulting changes in orientation distribution [35], necessitating its separate study. Further complicating matters, cold work will in addition also lead to grain refinement. This in part motivated yet another study, in this case on Mg AZ91, in which the grain size was varied through a melt-shearing technique. This enabled the examination purely of variations in grain size, without influence from the changes in initial dislocation density or crystal orientation usually associated with cold work.

In summary, the study of polycrystalline metals is associated with a host of microstructural complexity which can be ignored in single crystal conditions (or many annealed metals). This project aims to carefully consider these effects by extending precursor studies to commercially important FCC and HCP metals, through explorations of material specific properties such as defect densities and crystal orientation. This is accomplished by leveraging both robust material characterisation, which is of chief importance in polycrystalline materials, as well as modern diagnostic techniques. The primary aspects of material microstructure which are covered in this thesis include crystal orientation distribution, dislocation density, grain size and alloying. Consequently, the combined results from this research provide a comprehensive review of the influence of key material

properties on the dynamic strength of materials, and is demonstrated to present a valuable resource for the development and validation of models of high strain rate deformation.

## 1.3 Structure and goals

The primary goals of this research project can be summarised as follows:

1. Development of a high precision plate impact experimental platform capable of measuring the low velocity yield points of metals up to time resolutions of around 1 ns.

2. Careful characterisation of the initial microstructure (grain size, boundary misorientation, grain orientation, dislocation density etc) of the materials under investigation, beyond what is customary for shock wave studies.

3. Measurements of elastic precursor decay in a series of FCC and HCP metals with varied processing histories or initial states, the majority of which have yet to be studied under dynamic loading conditions.

4. Novel analysis of the effects on precursor decay of select microstructural parameters, focused primarily on the initial dislocation density, grain size, grain orientation, and secondary phase particles, enabled by combination of steps 2 and 3.

5. Analysis of the new measurements in context with literature reports, in which the effects of parameters such as prior cold work or crystal orientation on the dynamic yield point are obscure or inconsistent.

6. Application of both analytical and numerical models to a selection of the experimental measurements, supported by characterisation data, in order to provide new quantifiable evaluations of model predictions, and to analyse the influence of dislocation density, generation and other model parameters.

Finally, the structure of the thesis is described by the following:

Chapter 2 covers the fundamental aspects of the mechanics of deformation and shock physics required to understand the emergence of the elastic precursor wave. It also presents the basics of dislocation theory and establishes its crucial relationship with material yielding, particularly in the context of high strain rate loading. The importance of this relationship is demonstrated through a review of a selection of literature in which the decay of the elastic precursor has been studied and analysed in a variety of materials. This literature review forms part of the motivation for the present research. A brief introduction is also given to the models applied to the experimental measurements.

Chapter 3 details the development of the high precision plate impact experimental platform used throughout this project. Time is taken to carefully explain the experimental challenges involved in acquiring precursor measurements, including the sample preparation methods and gas gun re-designs which were implemented in order to produce high quality experimental data. Also explained are the separate difficulties inherent to preparing Al and Mg samples for EBSD and TEM characterisation, and the steps applied to overcoming these challenges.

Chapters 4 and 5 constitute the two main bodies of work in this thesis, focused primarily on quantifying the roles of crystal orientation and grain size in magnesium, and initial dislocation density in aluminium, respectively. Finally, the conclusions from these studies are presented in a combined form in Chapter 6.

# 2

# Background to elastic precursor decay

## 2.1 Mechanics of deformation and shock loading

The following sections lay out the fundamentals of material deformation and shock physics relevant to the study of strength during dynamic loading. This provides an overview of the origin of the elastic precursor and its ties to dislocation mechanics, highlighting the need for deeper understanding of the role of the time-dependent response of dislocations under dynamic loading conditions.

### 2.1.1 Mechanics of deformation

First, a mathematical description for deformation and yield during dynamic loading needs to be outlined. Deformation refers to any change of shape or size of an object due to an applied force or temperature change. Measured in units of stress, $\sigma$, it is defined as the ratio of force, $F$, over the area, $A$, it is acting on, according to $\sigma = F/A$. The complete stress state of a given point in a material is described by the Cauchy stress tensor,

$$\boldsymbol{\sigma} = \begin{bmatrix} \sigma_{11} & \sigma_{12} & \sigma_{13} \\ \sigma_{21} & \sigma_{22} & \sigma_{23} \\ \sigma_{31} & \sigma_{32} & \sigma_{33} \end{bmatrix}, \tag{2.1}$$

in which the diagonal terms represent the normal stresses, and the off-diagonals represent shear stresses, often denoted by $\tau$ instead of $\sigma$ (i.e. $\sigma_{12} = \tau_{12}$). In shock physics, normal stresses (and strains) are defined as positive in compression.

Shear stresses are applied transverse to the plane and are able to induce shape change. Due to symmetry, $\sigma_{ij} = \sigma_{ji}$, meaning the complete stress state of a body can be described by 6 independent components. The amount of deformation caused by the applied stress is quantified as strain and can be defined in a number of ways, the most common being engineering strain, $\varepsilon$, given by,

$$\varepsilon = (l - l_0)/l_0, \tag{2.2}$$

where $l$ is the current length of the sample and $l_0$ is its original length. A strain tensor, $\varepsilon_{ij}$, can be defined similarly to the stress tensor. While the orientation of the coordinate system is arbitrary, for any given stress state one can find three orthogonal planes upon which the shear stresses are zero [36]. The normal stresses acting on these planes, $\sigma_1 \geq \sigma_2 \geq \sigma_3$, are called the *principal stresses*, and contain the maximum and minimum magnitudes of the stress for all possible orientations. In high strain rate loading, $\sigma_1$ is typically defined as the longitudinal stress along the loading direction, and $\sigma_{2,3}$ are the transverse stresses. Note that the maximum shear stress within the body can then be determined from,

$$\tau_{max} = \frac{1}{2}(\sigma_1 - \sigma_3). \tag{2.3}$$

In linear theory of elasticity, one can relate stress to the strain in the elastic regime of an isotropic homogeneous solid through Hooke's Law, which in tensor notation can be written as,

$$\sigma_{ij} = C_{ijkl}\varepsilon_{kl}, \tag{2.4}$$

where $C_{ijkl}$ is the stiffness tensor and depends on variables such as temperature and microstructure. In conditions of uniaxial stress, typical for low strain rate (i.e. *quasistatic*) loading, stress is only applied in the longitudinal direction, and transverse stresses are zero, i.e. $\sigma_1 \neq 0$, $\sigma_2 = \sigma_3 = 0$, and $\varepsilon_1 = \varepsilon_2 = \varepsilon_3 \neq 0$. Under these conditions, the longitudinal stress and strain in Hooke's law can be written simply as $\sigma_{11} = E\varepsilon_{11}$, where $E$ is Young's modulus.

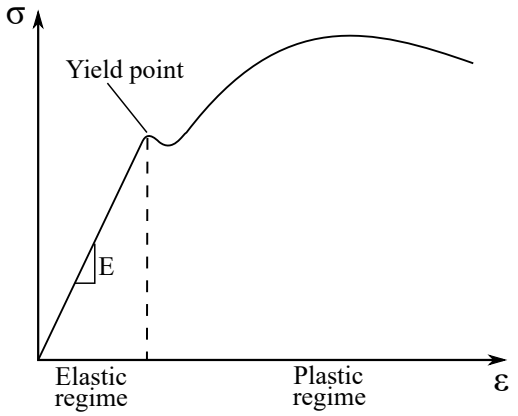



**Figure 2.1:** Typical stress-strain behaviour of a ductile material under quasistatic loading. The linear portion of the curve is the elastic regime, with the slope given by Young's modulus.

This relationship is illustrated in the quasistatic compression curve in Figure 2.1, where the elastic regime extends across the linear part of the curve. A body subjected to stresses within this regime will revert back to its original shape once the stress is relaxed. Permanent shape-change will only occur after the yield point, when the material transitions into the plastic deformation stage. The microscopic origins behind the elastic-plastic transition in crystalline materials will be further discussed in section 2.2.1. A yield criterion is often used to describe the stress states at which the elastic-plastic transition occurs, a simple version being the Tresca yield criterion (based on Equation 2.3),

$$Y = 2\tau_{max} = (\sigma_1 - \sigma_3), \tag{2.5}$$

where $Y$ is the empirically determined yield strength. Under uniaxial stress conditions, $\sigma_3 = 0$, and the maximum shear stress at yield can be found from the yield point, $\tau_{max} = Y/2$. Further analysis of the relationship between yield and the resolved shear stress is of high importance to this thesis; not only is it more complicated under uniaxial strain conditions, but is on a microstructural level also related to dislocations and slip systems orientation (see Section 2.2).

The flow stress, as shown in Figure 1.1, is the instantaneous value of stress needed to continue to plastically deform a material as a function of strain. The

flow stress therefore starts at the yield point, $Y$, and then typically increases due to strain hardening effects. The flow stress in Figure 1.1 is plotted against the strain rate, which is the rate at which material deformation occurs, and is given by,

$$\dot{\varepsilon} = \frac{d\varepsilon}{dt} = \frac{d}{dt}\left(\frac{l - l_0}{l_0}\right). \tag{2.6}$$

Quasistatic stress-strain curves such as Figure 2.1 are characterised by very slow strain rates of $10^{-3}$ $s^{-1}$ or less. During shock loading however one often reaches strain rates of up to $10^9$ $s^{-1}$, producing significant differences in material behaviour. For the purposes of this study, the interest lies mainly in the initial value of the flow stress, i.e. the yield point, as this is readily observable in shock physics experiments (see Section 2.1.2).

The stress at the steady-state (fully decayed) yield point in a shocked material is called the Hugoniot Elastic Limit (HEL). The HEL is higher than the yield strength during quasistatic loading, because shock loading occurs under conditions of uniaxial strain rather than uniaxial stress, i.e. $\sigma_1 = \sigma_2 = \sigma_3 \neq 0$, $\varepsilon_1 \neq 0$, and $\varepsilon_2 = \varepsilon_3 = 0$. The transverse stresses under shock loading can be expressed as,

$$\sigma_2 = \sigma_3 = \frac{\nu\sigma_1}{(1 - \nu)} \tag{2.7}$$

where $\nu$ is Poisson's ratio. Using Equation 2.3, the maximum shear stress under shock loading can then be given by,

$$\tau_{max} = \frac{\sigma_{11}}{2}\frac{1 - 2\nu}{1 - \nu}. \tag{2.8}$$

Finally, relating this to the yield strength using Equation 2.5, $\sigma_{11}$ can equivalently be defined as $\sigma_{HEL}$, and written as,

$$\sigma_{HEL} = Y\frac{1 - \nu}{1 - 2\nu}. \tag{2.9}$$

From Equation 2.9 one may observe that the HEL stress is always higher than the conventional yield stress. The concepts explained above are expanded upon in Chapter 4 where they are used in order to calculate resolved shear stresses

along specific crystallographic planes, ultimately enabling a calculation of the yield point under uniaxial strain conditions.

### 2.1.2 Shock waves and the elastic precursor

To measure the stress-strain behaviour of a shocked material one must first understand the nature of shock waves and how the quantities measured in a dynamic experiment (typically the shock and particle velocities) can be translated into stress in order to quantify the strength.

A shock wave is a propagating discontinuous change in the thermodynamic state of a material, as illustrated in Figure 2.2. The relationship between the states on either side of the shock front can be described by the Rankine-Hugoniot jump conditions, which are a set of conservation relations for mass, energy and momentum [37]:

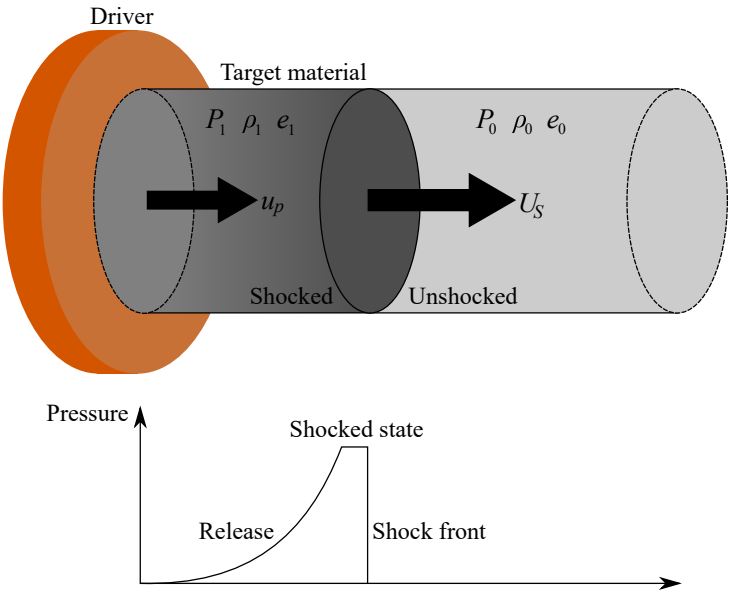



**Figure 2.2:** Representation of a shock wave propagating through a target material. The shock front, travelling at velocity $U_S$, separates the unshocked $(P_0, \rho_0, e_0)$ and shocked $(P_1, \rho_1, e_1)$ states. The graph shows the discontinuous change in pressure caused by the shock front, followed by the fully shocked state with a trailing region of gradual pressure relief caused by release waves.

Conservation of mass,

$$\rho_0 U_s = \rho_1 (U_s - u_p). \tag{2.10}$$

Conservation of momentum,

$$P_1 - P_0 = \rho_1 u_p (U_s - u_p) = \rho_0 U_s u_p. \tag{2.11}$$

Conservation of energy,

$$e_1 - e_0 = \frac{1}{2}(P_1 + P_0)(v_0 - v_1). \tag{2.12}$$

Here $\rho$ is the density, $U_s$ is the shock velocity, $u_p$ is the particle velocity, $P$ is the pressure, $e$ is the specific internal energy, $v$ is the specific volume, and the subscripts $0$ and $1$ refer to the states before and after the shock, respectively. The relations are based on the following assumptions: the shock wave is a steady, discontinuous jump in stress; the material is in a state of uniaxial strain; and the process is adiabatic without phase transitions. Such an idealised shock is illustrated in Figure 2.2.

The conservation equations do not a permit a full description of the relations between the shock parameters. In practice, a fourth experimentally determined relation called the shock Hugoniot is required, usually a linear equation of the form [38],

$$U_s = c_0 + S u_p, \tag{2.13}$$

where $c_0$ is the bulk sound speed and $S$ is an empirical constant determined from the slope of the experimental data. Higher order terms can be included but the linear form is usually sufficient for metals. Combined with the conservation relations, this equation can for example be used to determine the shock Hugoniot in pressure-volume or pressure-particle velocity space. This set of empirical

relations contain all possible thermodynamic states achievable through dynamic loading from a given reference state. In pressure-particle velocity form, the intersection of the Hugoniot curves of a projectile and a target can be used to predict the shock stress and velocity after impact (called impedance matching) [15]. This is a fundamental calculation often employed when planning or analysing shock loading experiments, including the ones conducted in this project (where the impact stress is calculated from the intersection of the sapphire and Al or Mg Hugoniots).

While the Hugoniot determines the state of a material behind the shock front, it does not represent a thermodynamic path, as a shock is in theory discontinuous. The loading path of a shocked material is instead described by a straight line between the initial and final states, called the Rayleigh line. Both curves are illustrated in Figure 2.3 in pressure-volume space, together with the corresponding shock wave. The concave nature of the Hugoniot demonstrates why high pressure ramp compression waves will in general gradually steepen into discontinuous shock waves, because the wave speed, $c$, increases with the pressure slope following $c = -v\sqrt{\frac{\partial P}{\partial v}}$.

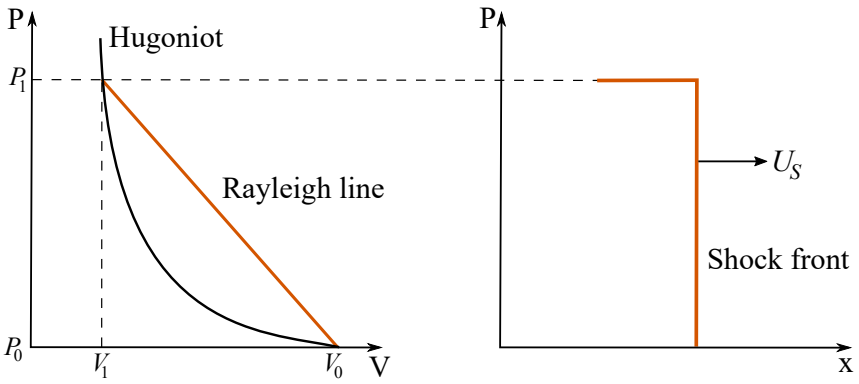



**Figure 2.3:** Left: Hugoniot and Rayleigh lines in pressure-volume space for an idealised shock. Right: The resulting shock propagating left to right with shock velocity $U_S$.

Real materials, and therefore real shock waves, are far more complex than the idealised case in Figure 2.3. This becomes apparent when changes in material

properties are incorporated into the Hugoniot curve. Any shift in material behaviour, such as a phase transition or elastic limit, will result in cusps in the Hugoniot which affect the loading path. Reaching a Hugoniot state directly above such a transition requires a separation of the Rayleigh line into two parts. The physical manifestation of this is a splitting of the shock front into several smaller waves travelling at different velocities. Assuming these multiple waves are also steady, the Rankine-Hugoniot jump conditions are still applicable to each individual wave.

Figure 2.4 illustrates the shock behaviour of a material with a finite amount of strength. Here the cusp in the Hugoniot line is caused by the transition from elastic to plastic deformation at the HEL of the material in question. Reaching any pressure states below or significantly above the HEL only requires a single Rayleigh line, however by loading the material to pressures just above the transition one observes the emergence of a two-wave structure. The first of these waves, called the elastic precursor, is a propagation of the initial pressure pulse up to the HEL. The precursor wave, being an elastic compression wave, travels at the longitudinal elastic wave speed, $c_l$. Trailing the precursor wave is a lower velocity plastic shock, which accounts for the remaining jump up to the final peak stress state. These types of double shock fronts are typical for experiments at pressures above but close to the HEL, and provide a direct method for measuring the yield point of a material under dynamic loading. By using velocimetry techniques to measure particle velocity in the shock wave one can employ Equation 2.11 to convert the particle velocity measured at the peak of the elastic precursor into the stress at the HEL. The two-wave structure is sometimes referred to as an *under-driven* shock, as it requires relatively low shock pressures. Conversely, in an *over-driven* wave, the material is loaded to such a high peak stress that the plastic wave velocity is faster than the elastic precursor. In this case the precursor wave is overtaken and the shock again assumes the form of a single high pressure wave shown in Figure 2.4.

The traditional Hugoniot shock wave concept of two discontinuous pressure steps corresponding to the elastic and plastic waves is only a first approximation. Further examination of the fine structure of the stress-time profile presents important features such as rise times, precursor spikes, and pressure pull-backs. The peak elastic stress depends fundamentally on the behaviour of the crystal lattice, and thus provides a macroscopic means of investigating microstructural phenomena at high strain rates.

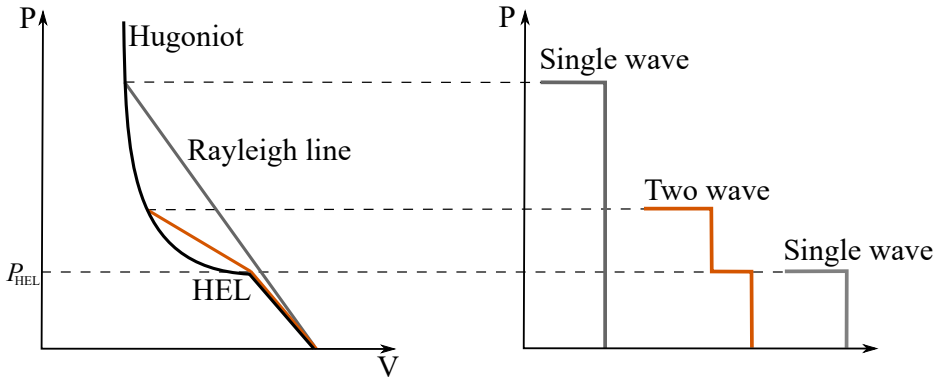



**Figure 2.4:** Figure showing the emergence of a two-wave structure in relatively low pressure shocks in materials with strength. The first wave is called the elastic precursor, with an amplitude equal to the peak elastic stress sustained by the material in question.

A shock physics experiment aimed at investigating the dynamic yield stress usually takes the form of a plate-impact experiment. A planar flyer is accelerated by a gas gun to several hundred meters per second and impacts a target. The impact pressure is chosen such that it launches a two-wave shock into the target as shown in Figure 2.4. The velocity at the peak of the precursor wave can be measured through laser velocimetry and converted to pressure using the jump conditions. Utmost care has to be taken during the experiment that the precursor wave is not obscured by air ramps (necessetating high vacuum) or tilt. A full description of these experiments is given in Chapter 3.

## 2.2 Microscopic origins of plasticity

### 2.2.1 Dislocation slip

Materials such as metals are arranged on the atomic level into ordered crystal lattices. The shape of these lattices is highly significant, as metals will exhibit vastly different material properties depending on whether their crystal structure is e.g. FCC (face-centred cubic), BCC (body-centred cubic) or HCP (hexagonal close-packed), illustrated in Figure 2.5. However, most crystals aren't perfect, instead containing crystallographic defects or irregularities within the otherwise highly ordered crystal structures in the form of point, line or boundary defects. Line defects are called dislocations and are characterised as either edge or screw (see Figure 2.6), although they are in reality usually found as a mixture of both (distinguishing between dislocation types becomes important when modelling dislocation mobility, as in Section 2.4.2). The Burgers vector of a dislocation defines the magnitude and direction of the lattice distortion it causes.

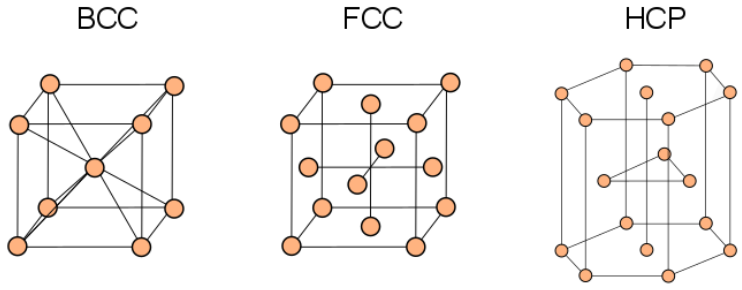



**Figure 2.5:** Schematic showing the atomic configurations of FCC, BCC and HCP crystal structures.

When a crystal is loaded at small stresses, the structural arrangement of the lattice will at first be unaffected, i.e. it remains within the elastic regime. By increasing the shear stress one will eventually reach a point where relative motion between the planes of the crystal results in plastic deformation. In the absence of dislocations, this would entail an entire plane of atoms moving in unison past another plane, requiring shear stresses around $\tau \approx G/30$, where

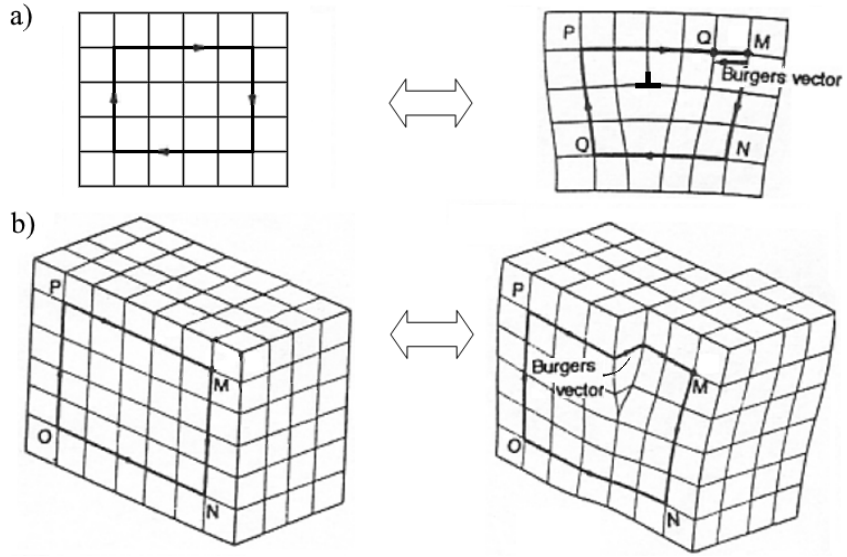



**Figure 2.6:** Illustrations of an a) edge dislocation and, b) screw dislocation [39]. A Burgers circuit and the resulting Burgers vector are shown in the figures.

$G$ is the shear modulus [39]. This is at least an order of magnitude higher than observations, which is a discrepancy that is resolved by accounting for the presence of dislocations. When a shear stress is imposed onto a lattice containing a dislocation, the dislocation itself will be moved along a slip plane until reaching a grain boundary (assuming no other obstacles). At this point, the whole lattice becomes sheared and the imposed stress state is relaxed. The stress needed to move a dislocation through a crystal lattice is called the Peierls-Nabarro stress (commonly just Peierls stress), which varies periodically due to the successive breaking and rebuilding of lattice bonds. It can be estimated however to $\tau \approx G/500$, i.e. much lower than the shear stress needed to displace a perfect lattice.

Crystal plasticity originates from the behaviour of dislocations, more specifically the effects of dislocation movement, multiplication, annihilation, etc., as well as interactions with microstructural features such as boundaries and second phase particles. This is why the Peierls stress plays a major role in determining material deformation behaviour. Covalent crystals with highly localised bonds have very large Peierls stresses, resulting in strong but brittle materials [40]. Materials such

as metals on the other hand are much more ductile as they facilitate dislocation motion through much smaller Peierls stresses. Accounting for the Peierls stress in dynamic deformation and its effects on dislocation motion is therefore an important component of the current research. For example, when contrasting the behaviour of FCC versus BCC metals, it is noted that the former are in general associated with lower Peierls stresses and greater dislocation mobility, which is critical when explaining differences in strain rate dependence (see Sections 2.2.3 and 2.3).

Whether or not the dislocation will move depends not only on the Peirels barrier but also on the component of the shear stress which is resolved onto the slip plane and along the slip direction. A slip plane is simply a close packed plane of atoms within which dislocation motion can easily occur, with the slip direction being the crystallographic direction of movement. Together these form slip systems, which are sets of symmetrically identical slip planes and directions. Which slip systems are available for dislocation movement is dependent on the crystal structure. In FCC metals, slip most commonly occurs on the $\{111\}$ planes along the $\langle 1\bar{1}0\rangle$ directions. The portion of the applied stress which is resolved along a specific slip plane and direction can be calculated using the Schmid factor, $m$, following,

$$\tau_{RSS} = m\sigma, \tag{2.14}$$

where $\tau_{RSS}$ is the resolved shear stress, and $\sigma$ is the externally applied normal stress. The Schmid factor is given by,

$$m = \cos\chi \cos\lambda, \tag{2.15}$$

where $\chi$ is defined as the angle between the loading axis and the slip plane normal, and $\lambda$ is the angle between the loading axis and the slip direction. Using Schmid's law, one can use measurements of the yield strength in order to calculate the critical resolved shear stress (CRSS) which is needed to initiate slip in a given slip system,

$$\tau_{CRSS} = mY \tag{2.16}$$

where $Y$ is the yield stress as before. Note the difference between this relation and the Tresca yield criterion (Equation 2.5). The latter can be viewed as a specific case of Schmid's law, in which it is assumed that the active slip system is at 45° to the loading axis, meaning $m = 0.5$ and the resolved shear stress along the slip system is maximised. The Tresca yield criterion is a suitable approximation for isotropic polycrystals under uniaxial stress. In single crystals however, the active slip system can be oriented along angles other than 45° to the loading axis, meaning Schmid's law gives a better indication of the yield stress. This is particularly important in HCP metals, as will be seen in Chapter 4, where the strength along different loading orientations varies drastically due to large variability in the CRSS. It should be noted that in the case of a multi-axial stress state, such as uniaxial strain conditions, the shear stress resolved onto a slip plane may be opposed by transverse stresses which are not accounted for in Schmid's law. Application of the Schmid factor is generally most suited for single crystal loading under uniaxial stress.

### 2.2.2 Twinning

Mechanical twinning is an alternative mechanism, other than dislocation slip, which can be responsible for plastic deformation. A twinned crystal is one in which there is an interlocking of two or more neighbouring grains such that one is mirrored or rotated with respect to the other, as illustrated in Figure 2.7. While twinning occurs naturally during crystal growth (i.e. an annealing twin), it can also be induced mechanically, in which case it's called a mechanical or deformation twin.

During slip, the the orientation of the lattice on either side of the slip plane is the same. By contrast, when shear is applied along a twin plane, each atomic plane is displaced by an amount proportional to the distance to the twin

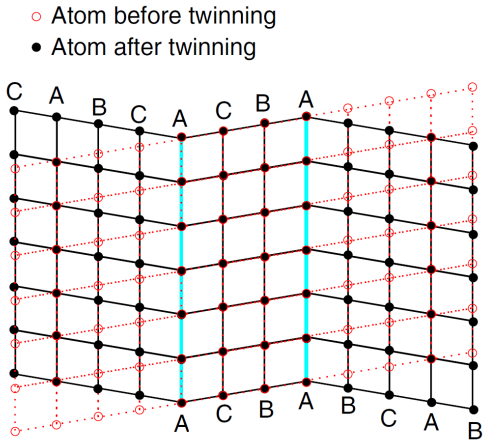



**Figure 2.7:** Example lattice of a twinned crystal [41]. Red and black dots show the lattice configuration before and after twinning, respectively. The lattice sites are symmetrical about the twinning planes, denoted by the blue lines.

plane, such that the lattice is divided into two mirrored halves with different orientations. The result is a permanent shape change which, similar to slip, causes only a small change in volume. The exact change in angles across a twin boundary is a characteristic of the crystal structure, as is the crystallographic planes and directions in which twinning occurs. In magnesium, the two active twinning mechanisms are contraction and extension twinning, formed via either compression or tension along the $c$-axis, respectively. In contraction twinning, which occurs on the $\{10\bar{1}1\}$ plane in the $\langle 10\bar{1}\bar{2}\rangle$ direction, the $c$-axis is reoriented by 56.2°. Extension twinning, on the $\{10\bar{1}2\}$ plane in the $\langle 10\bar{1}1\rangle$ direction, instead results in a reorientation of 86.3° [42, 43].

Whether a material will slip or twin depends on both the loading conditions and the material properties. In general, a transition from dislocation slip-dominated deformation to twinning-dominated deformation is tied to a decrease in dislocation mobility. At low temperatures, the shear stress required to overcome the Peierls barrier for dislocation motion can become higher than the activation stress for twinning. Likewise, at higher strain rates the increased stress requirements for slip signify that twinning may become more favourable, possibly even as a result of exceeding the capacity for slip alone to accommodate the imposed strain rate [44]. Materials with low stacking-fault energies such as many FCC metals, e.g.

copper [45], are likely to twin even under quasistatic loading. Out of the two metals studied in this project, aluminium has a high stacking fault energy and does not typically deform through twinning at all [46]. In magnesium however, there is a lack of easily accessible slip planes which makes twinning favourable in certain loading directions, further discussed in Section 2.3.3.

### 2.2.3 Origins of elastic precursor decay

Constitutive models describing the plastic response of materials are traditionally phenomenological in nature, meaning they are formed by fitting equations to experimental data using only partial underlying theoretical justification (i.e. the Johnson-Cook model [47]). Modelling pursuits using this method require empirical data specific to each material in order to determine model parameters, and dislocation theory is disregarded. A more direct approach lies in modelling dislocation motion explicitly using dislocation dynamics [8, 48]. Here individual dislocation lines are resolved and their motion through the crystal is simulated. However, as typical solids exhibit dislocation densities of up to $10^{14}$ m$^{-2}$, such attempts are extremely computationally challenging even in the quasistatic regime.

Current efforts to model plasticity at high strain rates usually take an Orowan-based approach. The Taylor-Orowan equation is a geometric model relating shear strain, $\gamma$, to the initial density of mobile dislocations, $\rho_m$, given by,

$$\gamma = \rho_m \vec{b} l, \tag{2.17}$$

where $\vec{b}$ is the Burgers vector and $l$ is the average separation between dislocations. Orowan's equation is applicable for problems ranging from creep rate calculations [49] up to dynamic deformation [16]. Taking the time-derivative yields,

$$\dot{\gamma} = \rho_m \vec{b} v + \dot{\rho}_m \vec{b} l, \tag{2.18}$$

which states that the strain rate $\dot{\gamma}$ depends on the density, velocity, $v$, and generation rate, $\dot{\rho}_m$, of dislocations. At lower strain rates, where the density

of mobile dislocations is often far greater than the nucleation rate ($\rho_m >> \dot{\rho}_m$), one can neglect the second part on the RHS of Equation 2.18. However, the dislocation mobility can become a limiting factor at higher strain rates, in which case generation takes an active role in determining deformation behaviour. Indeed, a material recovered after shock loading will in general exhibit dislocation densities several orders of magnitude higher than the initial state [14]. Various models by Smith, Hornbogen, Meyers [15, 50], and others, have been proposed which describe the rapid generation of dislocations during shock loading. These typically take the form of dislocation planes moving with, or sequentially nucleated by, the propagating shock front.

At strain rates of about $10^4$ $s^{-1}$ or more, one reaches a point where the rate of dislocation-based stress relaxation becomes unable to keep pace with the rapid increases in imposed stress. The rise time of the elastic precursor wave (the time from zero to peak stress) is often on the order of only a few nanoseconds, which is comparable to the timescales of dislocation movement (nanoseconds) and generation (tens or hundreds of picoseconds, depending on the generation mechanism) [8]. The dislocation-mediated onset of plastic relaxation can therefore be delayed when faced with this extremely rapid ramp-up in stress, causing materials to behave elastically up to much higher stress states than under normal conditions. The result is that the elastic precursor wave reaches peak amplitudes several times higher than the equilibrium HEL stress. This extremely high stress state quickly decays as the precursor wave propagates into the material (as exemplified in Figure 1.3), due to the stress relaxation mechanisms eventually catching up to and attenuating the peak stress. How quickly the decay of the precursor wave occurs is therefore dependent on the rate of plastic flow behind the precursor front, meaning the evolution of the precursor amplitude with time and propagation distance can be used as a quantitative tool to study time-dependent effects of dislocation behaviour.

This link to the microstructure is illustrated in Figure 2.8. As the shock propagates through a material, relaxation waves are emanated from the generation and movement of dislocations. Because the elastic wave speed within the compressed material is faster than the precursor wave, the relaxation waves are able to catch up to and attenuate the peak precursor stress [9]. At high propagation distances, an equilibrium is eventually reached between the stress increase imposed by the shock wave, and the stress relaxation from the resulting dislocation activity. These mobile dislocations are shown in the illustration moving along a slip plane at an angle, $\theta$, from the loading axis, and with a velocity, $v(\tau)$. It is again emphasised that factors which influence this dislocation velocity, as well as dislocation generation, will have a large influence on the precursor decay rate. Not only does the decay curve vary from material to material, but it is also altered by anything which can influence dislocation behaviour, such as the slip plane, its orientation, the amount of nucleation points, the temperature, the peak shock stress etc.

The dislocation mobility has in studies by Johnston and Gilman in LiF been shown to be related to the resolved shear stress in the slip plane, $\tau_{RSS}$, as follows [51],

$$v = v_\infty e^{(-D/\tau_{RSS})}, \tag{2.19}$$

where $v_\infty$ is the shear wave velocity and $D$ is a drag coefficient. Approximations can be made to reduce this mobility expression to [10],

$$v = v_0(\tau_{RSS}/D)^m, \tag{2.20}$$

where $v_0$ and $m$ are constants. This forms a link, through the Orowan equation (Equation 2.18), between the resolved shear stress and the plastic strain rate, and is the starting point for the analytical models covered in Section 2.4.1.

Johnston and Gilman found a quasi-linear relationship in LiF of $m \approx 1$ between the dislocation velocity and the applied stress. This relationship, called the *mobility*

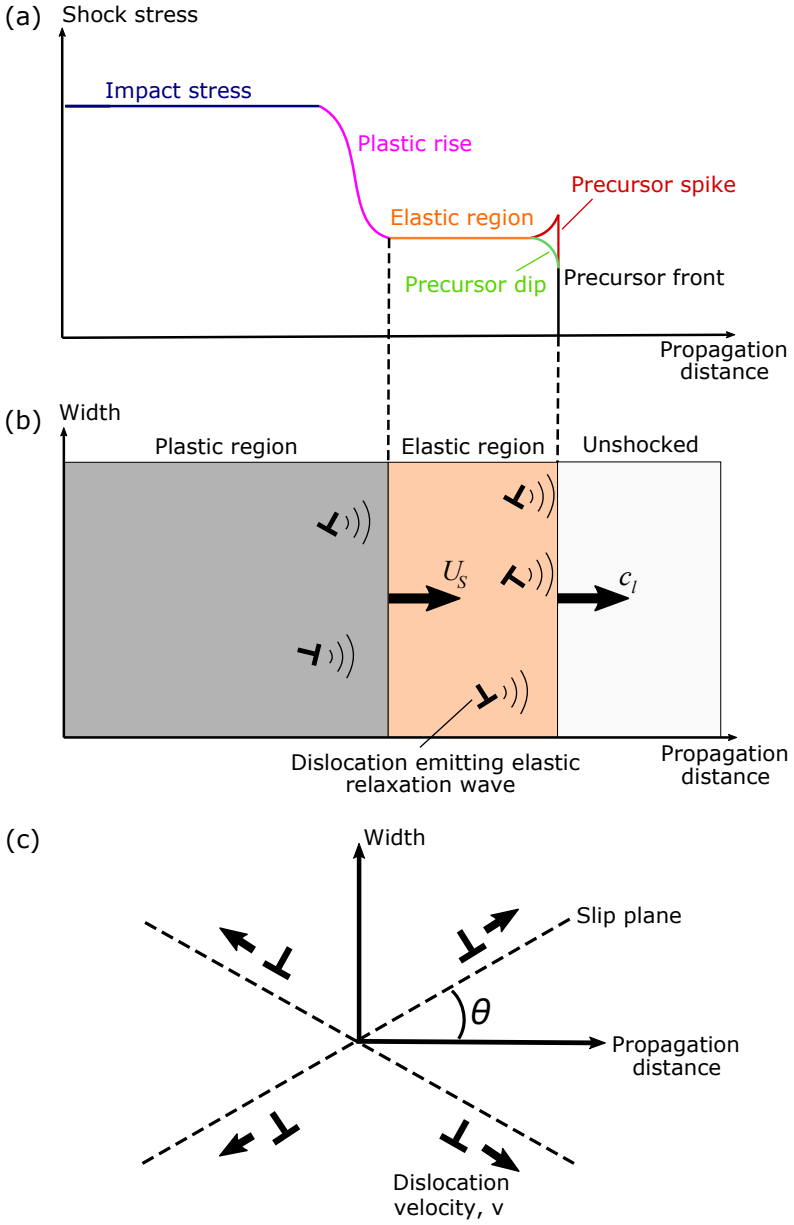



**Figure 2.8:** a) Illustration of a generic under-driven shock wave. The precursor displays either a spike or a dip at the front, depending on the mobility or initial density of mobile dislocations. Shown in b) are the corresponding elastic and plastic regions inside the material. The precursor wave travels at the longitudinal sound speed (in the linear elastic approximation), whilst the shock travels at the shock velocity given by Equation 2.13. Dislocations at the wave front produce relaxation waves which are responsible for attenuating the precursor stress amplitude. In the nonlinear elastic formulation (see Section 2.4.1), the relaxation wave speed is faster than the precursor front, meaning dislocations generated or moving behind the shock front are also able to contribute to stress attenuation. These dislocations are shown in c) moving at velocity, $v(\tau)$, along a slip plane at an angle, $\theta$, from the loading axis. The resolved shear stress acting along these planes of dislocation movement is calculated in Chapter 4.

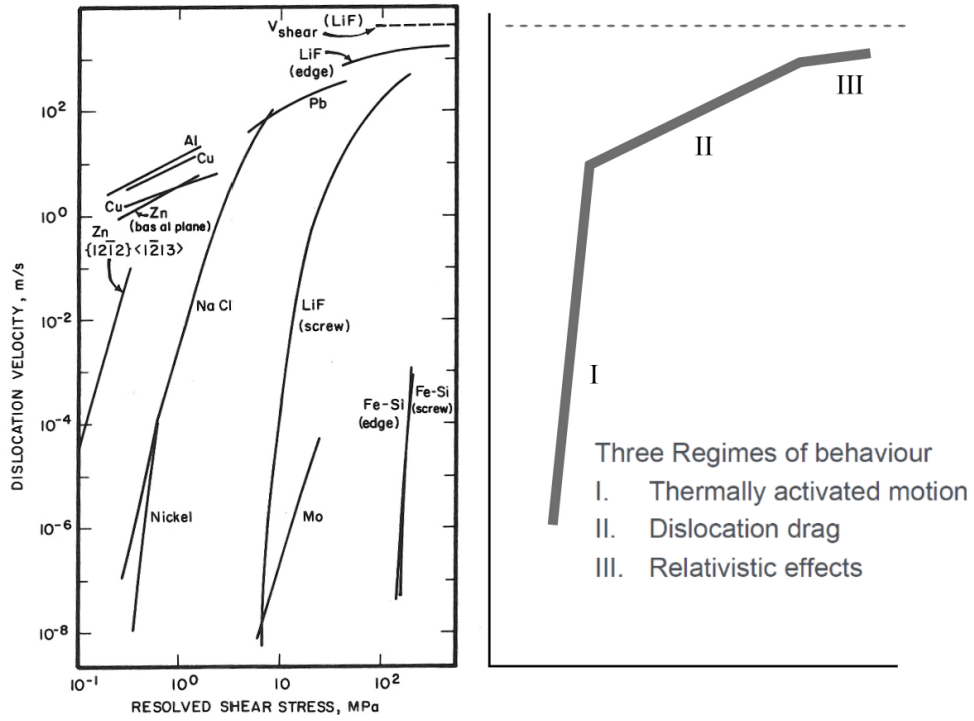



**Figure 2.9:** Experimental data of dislocation mobility as a function of the resolved shear stress in a variety of materials. Dislocation velocity will at first increase rapidly with shear stress, but starts to plateau when approaching the limiting velocity set by the shear wave speed. This behaviour can be classified into three regimes of dislocation mobility [14].

*law*, is essentially dependent on the time taken for dislocations to travel between short-range energy barriers, and the time taken to overcome those barriers. While this power law is entirely phenomenological, it is found that the empirically determined values of $m$ can be split into three categories, called the thermal activation, dislocation drag, and relativistic damping regimes, shown in Figure 2.9 [15]. In most cases of low shear stress, the motion of dislocations is dominated by obstacles like the Peierls barrier or imperfections in the lattice such as impurities, precipitates and grain boundaries. Dislocation mobility in this regime is referred to as thermally activated motion, as velocity is determined by the thermodynamic probability to surpass the peak in the potential barrier, as in Figure 2.10. Here the $m$ in Equation 2.20 is given by $m > 1$, and a relatively small increase in the applied stress leads to significant increases in dislocation velocity. BCC metals such as iron are associated with large Peierls barriers and are usually found within this region [52].

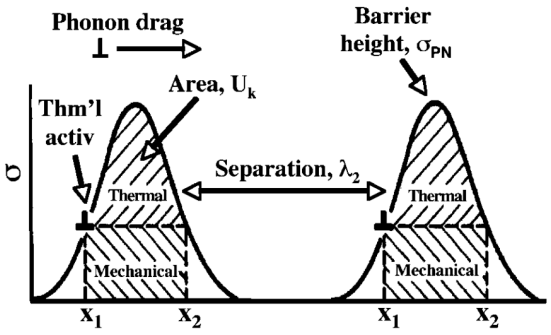



**Figure 2.10:** Schematic showing lattice energy barriers caused by the Peierls stress, $\sigma_{PN}$ [53]. The x-axis is representative of the lattice distance. Thermal fluctuations are required to overcome the barrier height at low stress, and phonon drag only becomes dominant once stress is high enough to easily overcome the Peierls barriers.

The large differences in these barriers is at the heart of the major disparities in strain rate sensitivity between BCC and FCC systems. Dislocations in metals with low Peierls barriers such as aluminium or copper are instead primarily opposed by dislocation forests, meaning the threshold stresses are lower and the material is closer to the dislocation drag regime. In this regime the stress is high enough that dislocations may easily overcome lattice obstacles [54]; glide becomes steady and velocity is limited by drag effects [18, 48]. A great deal of research is focused on the origins of dislocation drag, generally attributing it to phonon scattering, thermo-elastic damping, radiative damping or others. Out of these, phonon scattering is often accepted as the dominant mechanism, caused by the energy loss from phonons inelastically scattered by moving dislocations [55, 56]. Dislocation velocity in this regime scales linearly with shear stress ($m \approx 1$), which is often applicable to shock loading conditions. The final stage of relativistic damping is reached when the dislocation velocity approaches the absolute limiting velocity set by the shear wave speed, characterised by $m < 1$.

The impact of these mobility relations becomes evident from comparisons of precursor decay curves in different metals. In aluminium, the attenuation rate is very quick and the majority of the decay occurs within 1 mm of propagation [23]. In contrast, lower mobility materials such as tantalum or iron alloy display

significant decay up to at least 5 and 50 mm, respectively [5, 19, 57]. It is generally accepted that the higher mobility of aluminium ([58]) permits faster rates of stress relaxation, thus cutting short the time window within which the precursor wave is in its non-equilibrium state. As already discussed however, a material's base mobility curve is only one aspect of the many factors which influence the decay rate. In the literature review in Section 2.3, the roles of temperature, strain rate, loading orientation and more will be explored further.

## 2.3 Literature review

### 2.3.1 Early observations of precursor decay

The shock waves described in the previous sections can be experimentally generated using the detonation of explosives, with plane driver plate impact, or through laser shock loading. By increasing the driving amplitude above the elastic limit, or the HEL, the wave splits into an elastic precursor trailed by a plastic shock. The exact value of the HEL is highly dependent on the material, and can vary from around 100 MPa for metals like aluminium and copper [29, 59], to more than 18 GPa for ceramics such as boron-carbide [60]. These pressure ranges were well within the capabilities of even the earliest shock physics experiments, with the first observations of the precursor wave being attributed to Goranson et al. [61]. Consequently, dynamic loading has long been a well-established technique in the determination of material properties. Early ventures in the 1950s focused on investigating the equations of state of shocked solids [62, 63], with later work moving to examining the predictions of elastic-plastic theory through the dynamic development of stress and strain [4].

The decay of the elastic precursor with distance was first observed in the 1960s by Taylor and Rice in iron [5], and by Jones, Neilson and Benedick [64] in steel. The study by Taylor and Rice consisted of plane impact experiments on Armco (commercially pure) iron at pressures up to 8 GPa. Shock wave profiles were recorded using time-resolved free surface velocity measurements on samples of

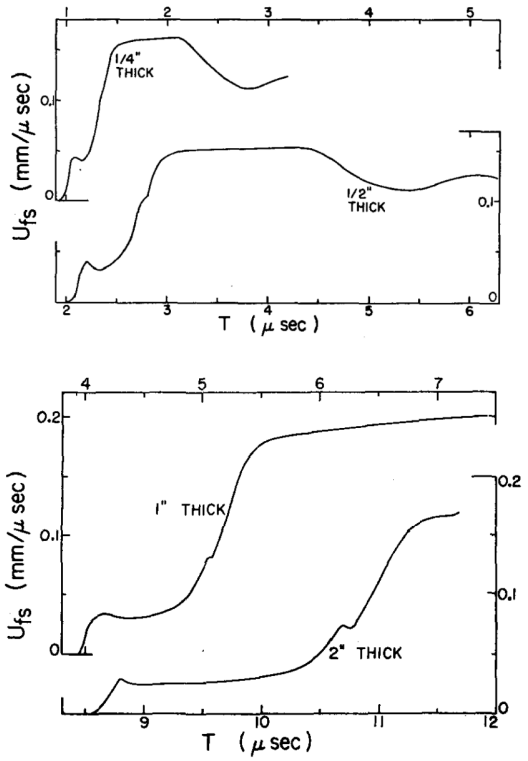



**Figure 2.11:** Free surface velocity traces in shock loaded Armco iron plates of varying thickness [5]. Attenuation of the peak elastic wave amplitude is observed.

thicknesses ranging from 0.2 to 50 mm, examples of which are shown in Figure 2.11. Clear precursor waves are resolved in all velocity traces, with a peak and a subsequent velocity pullback. The plastic wave follows at an increasingly greater delay due to its slower wave speed (see Section 2.1.2).

The full set of precursor amplitudes measured by Taylor and Rice are plotted against propagation distance in Figure 2.12. There is a clear trend of precursor attenuation with distance, which was found to be very weakly dependent on the driving pressures used. Taylor was later among the first to apply the expressions for dislocation velocity as laid out by Johnston and Gilman (see Section 2.2.3) to describe the observed relaxation behaviour [10]. An analytical model was fit to the data based on the mobility relation in Equation 2.19, the jump conditions (Equation 2.11), the Taylor-Orowan expression (Equation 2.18), and the relations for stress and strain as derived from the generalised form of Hooke's law (Equation 2.4). A similar model is described in Section 2.4.1. This produces a reasonable fit

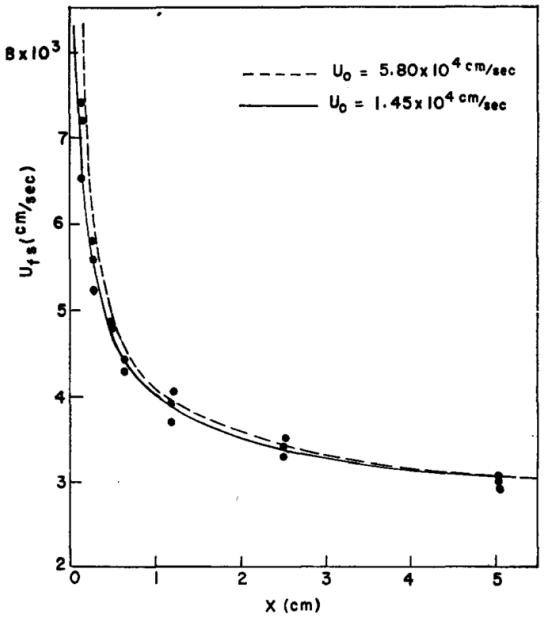



**Figure 2.12:** Decay of the precursor wave, demonstrated through the gradual decrease in the free surface velocity at the precursor peak with propagation distance in annealed Armco iron [10]. The solid and dashed lines are calculated from an Orowan-based model, where $U_0$ is the impact velocity.

to the experimental results, as demonstrated by the two lines in Figure 2.12, giving credence to the predicted exponential relationship between dislocation velocity and shear stress as well as the applicability of the Orowan equation. Several approximations had to be applied however, such as assuming that the mobile dislocation density is constant and active only along slip planes inclined 45° to the shock front.

Investigations soon shifted towards measuring microstructural dependencies, with a series of studies in iron and steel finding that the yield stress is dependent on ageing time but not on grain size [65–67]. Studies by Johnson, Jones and Michaels [11] showed that elastic wave attenuation is highly dependent on the direction of wave propagation with respect to the slip plane, which they proved by confining dislocation glide to specific slip systems in anisotropic single crystals (as opposed to the polycrystalline materials discussed so far). The results showed good agreement with results for copper [68] and sodium chloride [69] single crystals, where in the former the HEL varies between 0.2 and 0.7 GPa depending

on whether the crystal is shocked along the [100] or [110] directions respectively. Similar analysis techniques to the work by Taylor were employed to fit the stress relaxation to various functional forms of the Orowan equation and the dislocation velocity relationship. However, the predicted dislocation densities needed to fit the data were 1-3 orders of magnitude too large.

Building upon these investigations of microstructure, Asay et al. studied the effects of impurity concentration in single crystal lithium fluoride and found a strong link to precursor attenuation [6]. Traditional quasistatic compression loading was first employed to determine yield stress, which was found to increase linearly with impurity concentration. Having thus established the low strain rate behaviour, the effects of impurities in high strain rate deformation could be investigated through measurements of elastic precursor peaks. Figure 1.3 in Section 1.1 shows the velocity traces of the highest impurity samples investigated in the study. Note again that the majority of the stress relaxation in LiF, with its simple cubic crystal structure, takes place within 1-2 mm from the impact surface, as opposed to BCC iron in which this takes place across 50 mm.

Significant differences in the decay rate were observed depending on the impurity concentration. Figure 2.13 shows the elastic precursor peaks measured across a set of samples of varying purity, displaying very different behaviour to the low strain rate experiments. Both the samples of the highest and lowest yield stress exhibit a similar, relatively fast, stress relaxation trend. In samples of intermediate yield stress however (between 0.32 and 0.37 kbar as shown in the figure), there is a significant decrease in the decay rate. The proposed explanation incorporates the effects of both dislocation drag and heterogeneous nucleation on the mobility and generation of dislocations. By increasing the number of impurities present in the crystal lattice one inhibits dislocations glide, essentially moving further into the dislocation drag regime shown in Figure 2.9. This causes the observed decrease in relaxation rate seen in materials I-IIIa. However, point defects and impurities may also serve as sites for facilitated

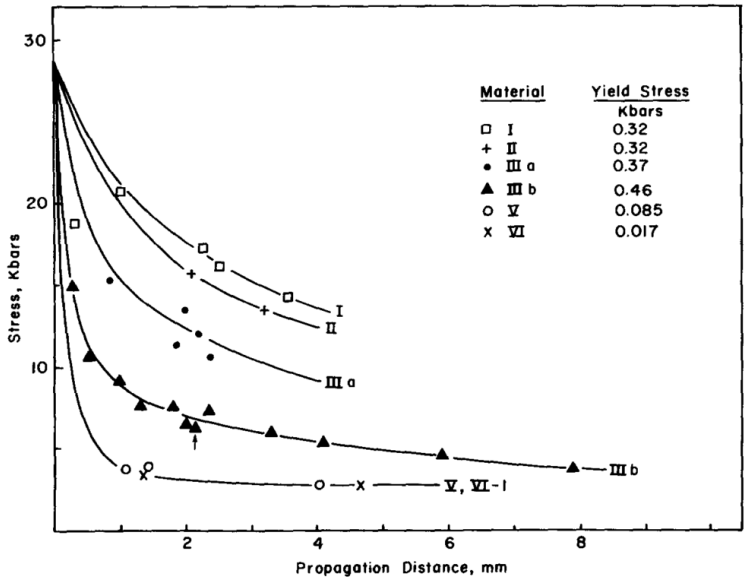



**Figure 2.13:** Precursor decay in LiF crystals of varying yield stress/impurity concentration. The yield stresses shown in the figure correlate linearly with impurity concentration, meaning materials IIIb and VI had the highest and lowest impurities, respectively. The shock wave profiles for material IIIb are shown in Figure 1.3. It is found that the decay rate first decreases with increasing impurity concentration up to material I, and then reverses and increases again to produce the fast decay rate in sample IIIb.

dislocation nucleation. By continuing to increase impurity concentration, a point is reached where heterogeneous nucleation of dislocations offsets the disadvantages of increased drag, causing the attenuation rate to once again match those of the softer crystals. This highlights the complications of experimentally investigating the competition between dislocation mobility and nucleation.

Attempts were once again made to model the experimental data based on the Gilman-Johnston expression (Equation 2.19) and the Orowan equation (Equation 2.18), producing the fitted curves shown in Figure 2.13. As before this revealed that considerable progress in the application of these expressions was needed. The value of $\rho_m$ required to obtain a suitable fit was in the range of $10^{12}$ m$^{-2}$, whilst typical dislocation densities measured in the LiF crystals were on the order of $10^8$ m$^{-2}$. These analytical treatments only consider the effects of pre-existing dislocations moving directly at the shock front, as linear elasticity is invoked for the dislocation stress fields and their corresponding wave speeds. Solving these

discrepancies requires incorporating dislocation generation as well as release waves overtaking the shock front, as is shown in Section 5.7.

### 2.3.2 Role of strain rate and temperature in aluminium

In Section 2.3.1, it is described how early studies of dynamic strength found direct links between precursor decay rate and the material microstructure. There has by now been studies in a large range of materials including copper [29, 64], steel [70], tantalum [17, 71], tin [72], vanadium [73] amongst many others. Out of these, aluminium is probably one of the single most studied elements in the high strain rate regime [20–25, 59, 74–82]. Whilst the dynamic strength of aluminium and aluminium alloy of varying purity and grain size is by now exceedingly well documented, the specific role of the initial dislocation density has yet to be studied. Consequently, it was an excellent choice as the subject material for the investigation into the role of cold work in Chapter 5. This section is dedicated to an overview of our current understanding of high strain rate yield in aluminium, the majority of which is focused on the effects of propagation distance, strain rate and temperature.

Precursor decay was first observed in aluminium by Arvidsson et al. [20], in conjunction with earlier results by Barker et al.[74]. 1060 (commercially pure) Al plates between 1 to 25 mm produced a small amount of elastic wave attenuation; from about 0.1 to 0.05 GPa across the the entire propagation distance. Due to the small absolute change in precursor amplitude past 1 mm, polycrystalline aluminium was until recently modelled purely as a time-independent elastic-plastic solid. Gupta et al. conducted plate impact experiments in the 40 - 180 $\mu$m region on deposited 99.999% pure Al foils with 3-6 $\mu$m grain sizes [21]. This work represented the first observation of large decay in the peak elastic state of aluminium, from $\sim$1 GPa at 40 $\mu$m to $\sim$0.5 GPa at 180 $\mu$m, showing that the time-dependent elastic-plastic response of aluminium is confined to the material very close to the impact surface. Studies into thin bulk aluminium (0.08 - 1 mm) were first conducted by Winey et al. [22], both in 1050 (commercially pure)

and 6061-T6 alloy samples. It was again shown that the majority of elastic wave attenuation occurs in the less-than 1 mm propagation regime. These results could be combined with the higher thickness results of similar purity by Arvidsson to produce a consistent picture of very rapid precursor decay in pure bulk aluminium. The results in alloyed samples however showed no signs of attenuation even in the thinnest samples; elastic wave amplitudes remained constant at ~0.7 GPa throughout. Additional data for very thin pure Al (<8 $\mu$m) was provided by Whitley et al. [24] with ultrafast laser compression experiments, resulting in very high peak elastic wave amplitudes up to 12 GPa. This was complimented by additional laser ramp compression experiments carried out by Smith [23]. Both of these studies were once again consistent with results from previous pure Al experiments, and the logarithmic plot of peak elastic stress against distance taken from Smith, Figure 2.14, displays the overall trend of precursor decay measured across a wide range of thicknesses.

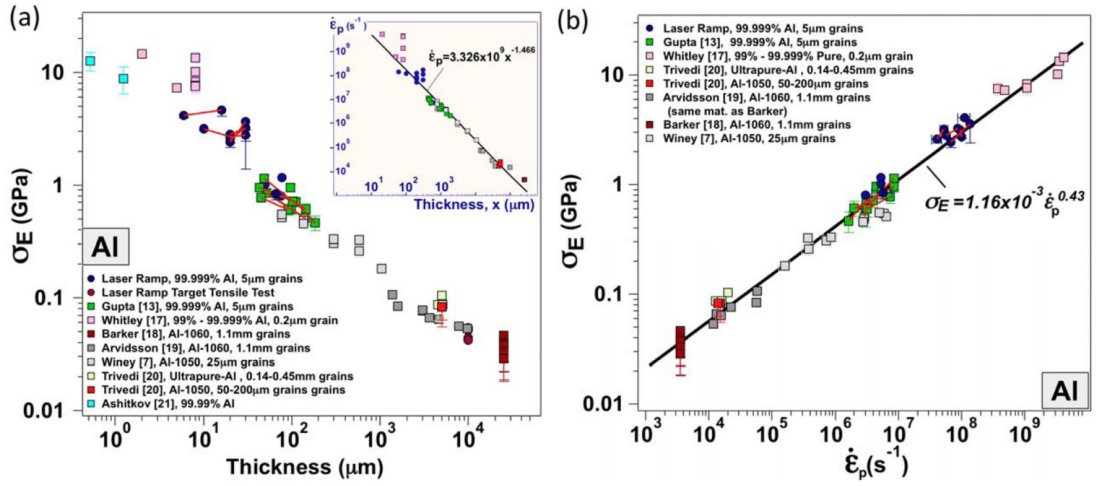



**Figure 2.14:** a) Peak elastic wave amplitudes from ramp (circles) and shock (squares) experiments in pure aluminium as a function propagation distance. b) Peak elastic wave amplitudes as a function of strain rate at the onset of plastic deformation [23].

An important next step is to now reconsider this data on precursor attenuation in terms of strain rate instead of propagation distance. As can be seen from Figure 2.14b, a plot of the strain rate at the onset of plastic deformation, $\dot{\varepsilon}_p$,

shows a strong correlation to the peak elastic stress. Smith defined the strain rate associated with the initial plastic flow at the elastic limit as,

$$\dot{\varepsilon}_p = \frac{d \ln V}{dt} = \frac{du_p/dt}{c_l} \equiv \dot{\varepsilon}_p|_{u_{E,Min}}^{2u_{E,Min}}, \tag{2.21}$$

where $u_p$ is the particle velocity, $c_l$ is the Lagrangian sound speed and $V$ is the volume. In order to represent the strain rate at the onset of plastic deformation, $\dot{\varepsilon_p}$ is defined from the base of the velocity pull back after the elastic peak, $u_{E,min}$, to $2 \times u_{E,min}$.

This analysis shows that the decay of the elastic precursor can be directly related to the more fundamental property of strain rate, instead of simply thickness. It provides a connection to the discussion in Section 1.1 on the effects of strain rate on the flow stress. In Figure 1.1, it is shown that a rapid increase in the flow stress of aluminium occurs at $\sim 10^3$ s$^{-1}$, where the material goes from being essentially strain rate insensitive to abruptly following a relationship of the form $\sigma \propto \dot{\varepsilon}^n$, where $n = 0.43$ as shown in Figure 2.14 by Smith et al. Similar behaviour is observed in other FCC metals such as copper [83]. In contrast, BCC and HCP metals (e.g. iron and titanium) usually show some strain rate dependence even at strain rates below $10^3$ s$^{-1}$ [15, 83], with exponents around $n \approx 0.1$ [82]. Again however a transition point can be found around $10^4$ to $10^6$ s$^{-1}$, where the strain rate sensitivity increases abruptly by a 3-4 fold increase in $n$ [23, 82].

As is discussed in more detail in Chapter 5, these behaviours can be understood as a result of the dominant role played by dislocations in the plastic response. When the strain rate is increased, so are the resolved shear stresses acting on dislocations. This effectively drives the dislocation velocity further up along the dislocation mobility curves shown in Figure 2.9, meaning the material's mobility law will determine how it responds to the increased strain rate. As a material with a very low Peierls barrier, the strain rate sensitivity in aluminium only arises once the effects of dislocation drag become apparent above $10^4$ s$^{-1}$. At

this point, the ability of the material to keep up with the required plastic stress release is negatively affected, and the yield points are rapidly increased with increasing strain rate. Conversely, the large Peierls barriers typical of BCC systems means lower strain rates also have observable effects on the yield point. As with aluminium however, BCC materials will also transition to the phonon drag regime once the applied shear stresses exceed the threshold value set by the Peierls stress. The mobility slope then changes to a linear dependence on shear stress ($m \approx 1$ instead of $m >> 1$, in Equation 2.20), while the strain rate sensitivity exponent, $n$, increases abruptly.

Having thus established a baseline for the strain rate dependence in pure aluminium, it is instructive to examine the effects of variations in material or external parameters. Of primary interest in recent years has been the effects of temperature, which is linked directly to dislocation mobility. In the low strain rate regime, an increase in temperature, $T$, is well-known to reduce the yield point of most metals, caused by the facilitated ability of mobile dislocations to surpass the Peierls barrier through thermal activation. However, in high strain rate loading of aluminium, phonon scattering is the dominant source of resistance to dislocation motion. The magnitude of these drag effects is proportional to temperature ($D \propto T$ in Equation 2.20), which interestingly leads to a reversal of the temperature dependency at higher strain rates. Temperatures between 500 to 900 K have been observed to increase the HEL stress by factors of around 2 up to 7 [25]. Zaretsky and Kanel have conducted a long series of studies into the effects of temperature on a large variety of metals, observing that the dynamic strength increases with temperature for FCC metals like silver [84], aluminium [25], and copper [29], as well as for HCP metals like titanium [85] and cobalt [86]. BCC metals however show a distinct departure from this rule, with tantalum [87], vanadium [87] and iron [27] all exhibiting insensitivity or a decrease in the yield point with $T$. This is theorised to be due to the dominance of thermal activation in these metals. Indeed, recent discrete dislocation dynamics modelling has shown that the temperature insensitivity in iron is in large parts due to its

strong Peierls barrier, in which dislocation generation is likely as important as motion in determining plastic flow [48].

As is shown in Chapter 5, temperature is only one of the avenues through which dislocation behaviour can be influenced in aluminium, with cold work and secondary phase particles being two others. Several studies have been conducted on the effects of prior cold work in a variety of aluminium alloys, however the outcomes have thus far been inconsistent. Cold working has been associated with lower HELs in studies on Al 2024 and Al 1421 [88, 89], but with increased HELs in other alloys such as Al 1070 and Al 5083 [88–92]. Results are similarly varied in other systems, with reduced dynamic strength observed in Ta [57, 71, 93], Ti [88, 94], Mg [35], but increases found in Fe [88] and Cu [88]. While studies agree that the behaviour is explained through alterations to dislocation-mediated stress release, they disagree on how these mechanisms are affected. Where the dynamic strength diminished after cold work, the results were thought an effect of greater grain boundary densities supplying higher dislocation nucleation, as well as the cold work process itself producing an increase in mobile dislocations. Contrary to this, increases in strength after cold work were attributed to higher defect and grain boundary densities obstructing dislocation movement. Investigating and clarifying the influence of cold work and the initial dislocation density is the primary objective of Chapter 5. As a consistent explanation of these previous results necessitates a direct comparison to the experimental measurements in this thesis, further discussion of these studies is deferred to Section 5.5.2.

### 2.3.3 Role of crystal orientation in magnesium

It has long been established that the decay rate in some materials is highly dependent on the loading orientation [11]. This is particularly obvious in HCP systems such as magnesium, due to their highly anisotropic crystal structure. Whilst there has been a variety of high strain rate experiments on Mg focused mainly on either the single crystal or spall behaviours [31–35, 95–102], the relative activity or competition of deformation mechanisms beyond the purely single crystal

loading scenario is not fully understood. As this is the primary motivation for Chapter 4, the present section presents an overview of the deformation modes in magnesium, including our current understanding of their high strain strain rate operation.

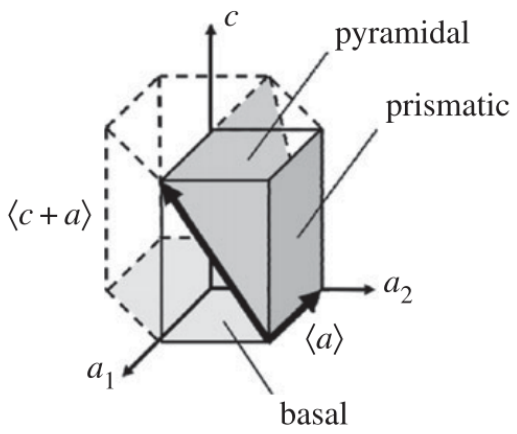



**Figure 2.15:** The three primary slip systems in HCP crystals [103].

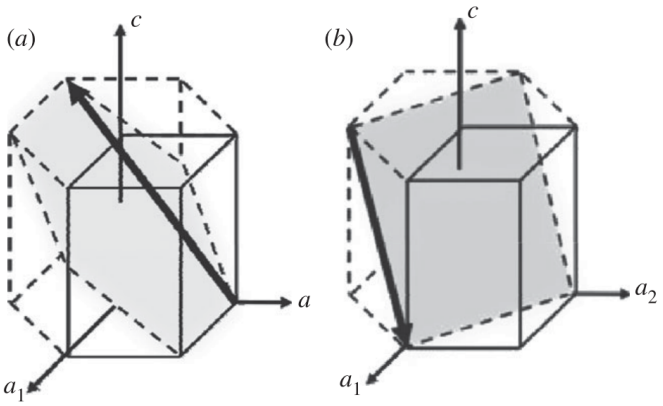



**Figure 2.16:** Twinning systems in HCP crystals [103]. a) $\{10\bar{1}2\}\langle 10\bar{1}1\rangle$ extension twinning, and b) $\{11\bar{2}2\}\langle 11\bar{2}3\rangle$ contraction twinning.

The deformation systems in magnesium under low strain rates are well characterised [104–109]. The Von Mises criterion states that five independent slip systems are required in order to accommodate any arbitrary shape change, however magnesium is only able to provide two of these easily through basal slip,

$\{0001\}\langle 11\bar{2}0\rangle$. The remaining slip systems available to magnesium in the $\langle a\rangle$ directions are prismatic slip, $\{10\bar{1}0\}\langle 11\bar{2}0\rangle$, and first-order pyramidal, $\{10\bar{1}1\}\langle 11\bar{2}0\rangle$. Slip in the $\langle c+a\rangle$ directions include first-order pyramidal, $\{10\bar{1}1\}\langle 11\bar{2}3\rangle$, and second-order pyramidal, $\{10\bar{2}2\}\langle 11\bar{2}3\rangle$. These slip planes are illustrated in Figure 2.15. Furthermore, there exists two twinning modes (shown in Figure 2.16) which are distinguished by the stress direction imposed on the $c$-axis, namely extension twinning, $\{10\bar{1}2\}\langle 10\bar{1}1\rangle$, and contraction twinning $\{11\bar{2}2\}\langle 11\bar{2}\bar{3}\rangle$ (including one variation for each). Out of these, basal, prismatic and second-order pyramidal have the lowest stress requirements for slip [110], which together with extension twinning will most commonly satisfy the Von Mises criterion. The magnitude of the CRSS values in these deformation systems, from lowest to highest, is generally accepted as basal $<$ extension twinning $<$ prismatic $<$ pyramidal [111].

As it has been shown that the critical resolved shear stress (CRSS) for the basal slip system is much lower than non-basal slip at room temperature, plastic deformation in polycrystalline alloys under lower strain rates occurs primarily via basal slip or extension twinning [112–115]. Conversely, whilst pyramidal $\langle c+a\rangle$ slip is a difficult to activate slip mode, its CRSS is still low enough that it may be activated in orientations in which the other slip systems have low Schmid factors (see Equation 2.15) [106]. In fact, in the case of compressive loading perfectly parallel to the $c$-axis, only pyramidal slip or $\{10\bar{1}1\}$ contraction twinning have non-zero Schmid factors and are therefore the only available options.

Similar to quasistatic or low strain rate studies, any analysis of dynamic deformation in magnesium requires detailed knowledge of the crystal orientations in the material. Previous studies have demonstrated that the HEL is heavily dependent on loading direction in shocked single crystal magnesium [31–34]. Shock compression at 45° to the $c$-axis exhibits the lowest HEL stresses at around 70 MPa. A simple calculation using Equation 2.15 yields the maximum Schmid factor of 0.5 for the basal system in this orientation, and lower Schmid factors in all other slip systems. The majority of deformation in this geometry, at least at

the onset of plastic flow, is therefore expected to be satisfied through basal slip. Higher yield stresses were found in the $a$-axis orientation, measured to around 400 MPa at higher propagation distances [31, 33]. Application of the Schmid factor calculation shows that this orientation is likely comprised of prismatic slip and extension twinning. Finally, the highest HELs of around 800 MPa were observed when loading parallel to the $c$-axis, in this case due to the activation of pyramidal slip (with basal and prismatic slip both having Schmid factors of zero) [31, 34]. The relative strengths of these orientations, and their associated slip systems, is in agreement with the low strain rate results, signifying that the CRSS value of a slip system is indicative of its dynamic strength. While these results conclusively prove that the dynamic strength of magnesium is heavily dependent on the crystal orientation, how this determines the deformation of polycrystalline Mg under high strain rates is not well understood, in part motivating the present study.

While there has been a variety of higher strain rate experiments conducted on a range of magnesium alloys [35, 95–102], only a few have studied the orientation dependence. The decay of the elastic precursor with propagation distance has been observed in Ma2-1 and Elektron 675. In the latter, it was shown that aging treatment (strengthening a metal by allowing alloying elements to form into precipitates) causes the decay of the precursor wave to disappear [101]. A comparison of loading both transverse and longitudinally to the extrusion direction (the flow direction during manufacturing) was also performed, however only at a fixed sample thickness. It was observed that the HEL was slightly higher for loading parallel to the extrusion direction, but the difference was within the measurement error. The large thickness (8 mm) at which these experiments were conducted makes it possible that the precursor wave had long reached its steady state, and larger differences could have been observed had thinner samples been used.

An indirect investigation of orientation dependence was conducted in a study by Wang on pure Mg loaded at varying temperatures using a reverse plate

impact configuration at 100 m/s impact velocity [116]. They found that the yield stress decreased with temperature up to 610 °C, after which the trend was reversed and the yield stress increased with temperature from 610 to 630 °C. This seemingly contradicted the accepted understanding of an increased flow stress with temperature at high strain rates, as discussed in Section 2.3.2. It was theorised that this was caused by variations in grain orientation distributions at the different temperatures. In a follow-up paper, each sample was annealed to the impact test temperatures, and the Schmid factors in each sample's grains were calculated using EBSD orientation data and then averaged [117]. Activation stresses were then calculated through Equation 2.16, from which it was concluded that extension twinning was the dominant deformation mode in the room temperature specimens. As sample temperatures were increased, the average Schmid factor for basal slip also increased due to texture softening. Being a lower threshold deformation mode, this theorised increase in basal slip over extension twinning was used to argue that reorientation was the cause for the decreased strength at increased temperatures. It was suggested that at temperatures above 610 °C, the reorientation was concluded and the effects of phonon scattering eventually became more dominant, meaning yield stress started increasing once again.

However, as is discussed further in Section 4.4.2, the use of Schmid factors in shock experiments leads to an overestimation of the resolved shear stress because it does not account for transverse stresses under uniaxial strain conditions. Similarly, CRSS values measured under quasistatic conditions can not be used together with Schmid factors to make a quantitative prediction of the activation stress at high strain rates, as the CRSS value is highly strain rate dependent. While it is reasonable to conclude that an increase in basal slip caused the decrease in flow stress, the Schmid analysis precludes quantitative predictions of slip activity. Indeed it was found that the average Schmid factors remained effectively constant across the entire range of high temperatures, whilst the flow stress continued to evolve.

Aside from these studies, the orientation dependence of HCP metals has been inspected in titanium and zirconium [118, 119]. In 2 mm zirconium samples made from rolled plate, the HEL in the through-thickness direction was higher than the in-plane direction by a factor of 1.9 [119]. This was found to be consistent with the differing elastic moduli in the two orientations, as supported by finite-element modelling of the loading configuration. A study on the anisotropic response of extruded titanium was performed by Millett using lateral stress gauges [118]. Whilst the longitudinal precursor stress was not measured directly, it was shown that the loading direction influenced the degree of hardening behind the shock front at 8 mm propagation. It was again suggested that this behaviour was a manifestation of the differences in the relative activation of slip and twinning caused by the material anisotropy.

To conclude, while the behaviour of single crystal magnesium has by now been thoroughly studied, the question remains to what degree the single crystal response can be used as a guide to understand anisotropic polycrystalline material behaviour. The studies by Gray and Wang into rolled Zr and extruded Mg respectively showed that orientation dependence is likely highly dominant in determining the response of polycrystalline HCP systems. Indeed, as the magnitude of the orientation dependence is similar to or even higher than the temperature or strain rate dependencies, further quantitative investigation of anisotropy is needed before the significance of these other effects can be properly evaluated. This is the primary objective of the study on Mg AZ31 in Chapter 4.

## 2.4 Overview of precursor decay models

Direct experimental observation of the highly transient material states found during plate impact experiments are by nature limited mainly to macroscopic measurements of velocity and stress. Barring a recent rise of real-time synchrotron x-ray diffraction techniques enabling examination of lattice deformation [120–122], direct study of the time-dependent evolution of shocked microstructures

has traditionally been consigned to the realm of modelling. Both analytical and numerical models were applied to the data in this project in order to form quantitative conclusions regarding dynamic dislocation behaviour. The following sections are devoted to summarising the theoretical foundations of these models.

### 2.4.1 Analytical precursor decay models

The traditional area of modelling, which is still seeing advancement, lies in the formulation of purely analytical expressions for the decay of the precursor stress over distance or time. Their advantage is the relative simplicity with which the predicted precursor stress can be directly compared to experimental measurements. Such models were historically troubled by requiring initial dislocation densities 1-3 orders of magnitude too high in order to fit the experimental data (i.e. $10^{12}$ $m^{-2}$ or more when modelling single crystal materials [10, 11, 16]). The discrepancy may be partially attributed to the assumptions that only dislocations either nucleated or accelerated directly at the wave front can contribute to relaxation of the precursor stress. Recent work by Clayton and Lloyd, outlined below, addresses this issue by incorporating nonlinear elastic effects, meaning release waves from dislocations behind the wave front are able catch up and contribute to precursor attenuation.

First, the linear elastic formulation used in Section 5.7.2 will be described. The analysis is adapted from the work by Gillis et al. on modelling the precursor decay in tantalum [16], which was originally based on the approach taken by Taylor [10]. In uniaxial stress, the plastic strain rate is assumed to obey the Orowan equation as follows,

$$\dot{\gamma}_p = \rho_m b v(\tau), \tag{2.22}$$

where $\dot{\gamma}_p$ is the plastic shear strain rate, $\rho_m$ is the mobile dislocation density, $b$ is the Burgers vector (usually equal to around the interatomic distance, ie on the order of $10^{-10}$ m), and $v$ is the dislocation glide velocity, which is a function of the

resolved shear stress, $\tau$, on the slip plane. Since $\rho_m$ can change during the course of deformation, an evolution term is included which transforms the expression to,

$$\dot{\varepsilon}_p = (\rho_0 + \alpha\varepsilon_p)bv(\tau)/\Phi, \tag{2.23}$$

where $\rho_0$ is now the *initial* mobile dislocation density, $\alpha$ is a dislocation multiplication coefficient and $\varepsilon_p$ is the plastic strain. The shear strain has been converted to the normal strain by including an orientation factor $\Phi$. The dislocation velocity is assumed to follow the Johnston-Gilman expression [51],

$$v = v_\infty e^{(-D/\tau)}, \tag{2.24}$$

where $v_\infty$ is the dislocation velocity limit (i.e. the shear wave speed), $\tau$ is the maximum resolved shear stress, and $D$ is a characteristic drag stress of the form $D = D_0 + H\varepsilon_p$, where $H$ is a strain hardening coefficient. The use of Equations 2.22-2.24 was first introduced in Section 2.2.3. In an axially symmetric deformation, such as either uniaxial stress or strain, and under isochoric conditions, the normal plastic strain rate can be related to the maximum plastic shear strain rate following,

$$\dot{\varepsilon}_p = 2\dot{\gamma}_p/3. \tag{2.25}$$

Assuming isotropic conditions and using Hooke's law, the maximum shear stress under uniaxial strain is given by,

$$\tau = G(\varepsilon - 3\varepsilon_p/2), \tag{2.26}$$

where G is the shear modulus and $\varepsilon$ is the total normal strain. The normal stress, $\sigma$, is given by,

$$3\sigma = \frac{E\varepsilon}{3 - E/G} + 4\tau. \tag{2.27}$$

Finally, the expression used by Taylor relating the slope of the decay curve to the plastic strain rate is [10],

$$\frac{d\sigma}{dx} = -2G\dot{\varepsilon}_{p0}/c_l, \tag{2.28}$$

where $x$ is the propagation distance, $c_l$ is the longitudinal sound speed, and $\dot{\varepsilon}_{p0}$ is the *initial* plastic strain rate. The latter is given by Equation 2.23, in which $\varepsilon_p$ is taken as zero to reflect the initial strain rate at the onset of plastic flow. By setting $\varepsilon_p = 0$, Equation 2.26 becomes simply $\varepsilon = \tau/G$, and strain hardening and dislocation multiplication in Equation 2.23 is discarded. Following this, $\varepsilon$ in Equation 2.27 can be substituted to produce,

$$3\sigma = \frac{\tau(12G - 3E)}{3G - E}, \tag{2.29}$$

which rearranges to

$$\tau = \sigma\frac{3G - E}{4G - E}. \tag{2.30}$$

It assumed that this expression is valid during the elastic portion of the wave up to the peak elastic stress. By substituting Equation 2.30 into 2.23, once again using $\varepsilon_p = 0$ , one finds,

$$\dot{\varepsilon}_p = \frac{\rho_0 b v_\infty}{\Phi} \exp\left(\frac{-D}{\sigma}\frac{4G - E}{3G - E}\right), \tag{2.31}$$

which combined with Equation 2.28 produces,

$$\frac{d\sigma}{dx} = -\frac{2G}{\Phi c_l}\rho_0 b v_\infty \exp\left(\frac{-D}{\sigma}\frac{4G - E}{3G - E}\right). \tag{2.32}$$

This equation is integrated numerically in Section 5.7.2, using the parameters listed in Table 5.4, in order to predict the precursor stress as a function of propagation distance.

As is shown however, the main failing of these models is the overestimation of the initial dislocation density. In more recent work by Clayton and Lloyd, it is posited that this can be addressed by incorporating nonlinear elastic effects [9]. In the linear elastic formulation, only dislocations either accelerated or nucleated

directly at the wave front are considered to contribute to precursor attenuation. This is because the wave speed of the material behind the shock front is equal to or less than the speed of the precursor wave itself. Waves emanating through stress fields of dislocations behind the front are unable to reach and interact with the precursor wave. By correcting for the increased sound velocity of the stiffer material behind the wave it is found that the contribution of dislocation nucleation behind the front is highly significant.

The full expression for precursor decay as developed by Clayton and Lloyd can be seen as an extension of the linear formulation, and is given by,

$$\frac{D\sigma}{Dt} = \frac{-\hat{\alpha}G}{t_0[3/2 - (1/2)(c_l^2/U^2)]}\bar{\sigma} \cdot \left[1 + f_t \cdot \left(1 - \frac{U}{c_l}\right) \cdot \frac{M}{\rho_0}\frac{t}{t_0}\bar{\sigma}\right], \tag{2.33}$$

where $U$ is the wave speed of the elastic precursor wave, $M$ is a dislocation generation coefficient, $\hat{\alpha}$ is an orientation constant, $f_t$ is the fraction of transmitted signals at the wave front, and the following quantities have been defined,

$$\overline{\sigma} = (\sigma - \sigma_{HEL})/\sigma_{HEL}, \tag{2.34}$$

$$t_0 = 1/(\rho_0 b v_{D0}), \tag{2.35}$$

where $\sigma_{HEL}$ is the far-field equilibrium HEL stress, $v_{D0}$ is a nominal dislocation velocity, and $\rho_0$ is the initial mobile dislocation density. Note that the precursor wave speed, the longitudinal elastic wave speed, and the shear modulus are all updated following the pressure increase of the wave front. Also note the inclusion of dislocation generation through the adjustable coefficient $M$. A linear elastic formulation is recovered if one sets $U = c_l$ and $G = G_0$, in which case Equation 2.33 is reduced to an expression of the form,

$$\frac{D\sigma}{Dt} = \frac{-\hat{\alpha}G_0}{t_0}\bar{\sigma}, \tag{2.36}$$

where, similar to 2.32, dislocation generation behind the front does not affect the decay rate. The reader is referred to the work by the original authors for

the full derivation of Equation 2.33 [9]. For the purposes of this project, the model is used without modification aside from adjustments to the generation parameter and the material constants.

### 2.4.2 Dislocation-based numerical dynamic strength model

In addition to the analytical expressions outlined in Section 2.4.1, a dislocation-based numerical model was applied to the experimental data in Section 5.7.3, in collaboration with Kositski and Mordehai. This dynamic strength model, first outlined in [19], is a microstructure-based continuum simulation of dislocation-mediated deformation during high strain rate loading. The velocity of dislocations is obtained from molecular dynamics (MD) results, whilst their density is evolved throughout the simulation using a set of rules tracking both mobile and immobile dislocation densities.

Once again, Orowan's equation is used to calculate the plastic strain rate, $\dot{\varepsilon}_p$, given in the form of Equation 2.22 with an additional orientation factor, $\Phi$, which is taken as the Taylor factor,

$$\dot{\varepsilon}_p = \rho_m b v(\tau)/\Phi. \tag{2.37}$$

The mobility curve, $v(\tau)$, is taken from MD simulations of screw dislocations [58]. Screw dislocation velocities are lower but comparable to edge dislocations, meaning a single limiting velocity is chosen for simplicity, rather than accounting for separate populations of dislocation mobility. To calculate the driving shear stress, $\tau$, a Taylor hardening rule is used together with the Taylor factor,

$$\tau = \frac{\sigma_{vm}}{\Phi} - AGb\sqrt{\rho_i}, \tag{2.38}$$

where $A$ is a hardening parameter, $\rho_i$ is the immobile dislocation density, and $\sigma_{vm}$ is the Von-Mises stress. Finally, two separate evolution equations are used

for tracking the mobile and immobile dislocation densities in Equations 2.37-2.38, following,

$$\dot{\rho}_m = \dot{\rho}_{nuc} + \dot{\rho}_{mult} - \dot{\rho}_{trap} - \dot{\rho}^m_{annh}, \tag{2.39}$$

$$\dot{\rho}_i = \dot{\rho}_{trap} - \dot{\rho}^i_{annh}, \tag{2.40}$$

Out of these parameters, the dislocation nucleation, $\dot{\rho}_{nuc}$, is based on the classical nucleation theory where the nucleation rate is given by the Arrhenius equation,

$$\dot{\rho}_{nuc} = \begin{cases} A_{nuc} e^{-\beta(E_0 - V\tau)} & \tau \leq E_0/V \\ A_{nuc} & \tau > E_0/V, \end{cases} \tag{2.41}$$

where $A_{nuc}$ is a rate prefactor, $E_0$ is the stress-free activation energy, $V$ is an effective activation volume, $\tau$ is the shear stress as defined in Equation 2.38, $\beta = 1/k_B T$ with $k_B$ being Boltzmann's constant, and $T$ is the temperature. The other terms in Equations 2.39-2.40 are the multiplication rate, $\dot{\rho}_{mult}$, the trapping rate of mobile turning into immobile dislocations, $\dot{\rho}_{trap}$, and the annihilation rate of both the mobile and immobile dislcations, $\dot{\rho}^m_{annh}$ and $\dot{\rho}^i_{annh}$, respectively. These evolution terms are given by,

$$\dot{\rho}_{mult} = A_{mult}\, \rho_m\, v, \tag{2.42a}$$

$$\dot{\rho}_{trap} = A_{trap}\, b\, v\, \rho_m \sqrt{\rho_i}, \tag{2.42b}$$

$$\dot{\rho}^m_{annh} = A_{annh}\, b\, v\, \rho_m (\sqrt{\rho_i} + \sqrt{\rho_m}), \tag{2.42c}$$

$$\dot{\rho}^i_{annh} = A_{annh}\, b\, v\, \rho_m\, \sqrt{\rho_i}, \tag{2.42d}$$

where $A_{mult}$, $A_{trap}$, and $A_{annh}$ are fitting parameters.

## 2.5 Summary

This chapter was dedicated to the discussion of the theoretical foundations necessary to understand the emergence of the precursor wave in under-driven shocks, and it's decay with propagation distance. First, descriptions are given for the mechanics of deformation, strength, and shock wave loading. Second, the

microscopic origins of yield are discussed, centred on the Orowan equation and the physics of dislocations and dislocation movement. These concepts are then combined in order to explain the phenomenon of elastic precursor decay, as well as the three regimes of mobility which produce distinct differences in the ability of dislocations to generate plastic flow.

The subsequent literature review discusses a selection of previous studies ranging from historical experiments on Fe to more recent studies on Al and Mg. These past investigations demonstrate how precursor decay measurements are uniquely capable of providing knowledge into the time-dependent effects of dislocation movement and generation, as well as how the precursor stress is strongly influenced by factors such as strain rate, temperature, impurity concentration and more. The changes in macroscopic response as a result of these factors can in turn be used to further our understanding of the physics of dislocations and strength. Gaps in current knowledge related to initial dislocation density and polycrystalline behaviour are highlighted. Finally, brief overviews are given of both the analytical and numerical models employed in this thesis, which are used in Chapter 5 to provide quantitative analysis of the physical parameters which affect dynamic strength.

# 3
# Experimental methods

Chapters 1-2 introduce the physics of strength and deformation at high strain rates, and highlight the importance of measurements linking dynamic deformation behaviour to material microstructure. A wide array of experimental challenges had to be surmounted in order to achieve the level of precision required for these measurements, meaning a significant part of the project was dedicated to refining experimental methods. This chapter outlines development of the plate impact experimental platform, as well as the analysis methods and characterisation techniques employed throughout this project.

## 3.1 Development of the precursor decay experimental platform

### 3.1.1 Summary of experimental challenges

The results and analysis described in this report were gathered from a total of 51 experiments (not including a multitude of test shots), out of which 9 were failed shots (making it an 80% success rate). The nature of high precision plate impact experiments is that they are extremely delicate and complex. There are a large amount of systems or factors which have to work correctly in unison, all within a precise time window of $<1$ $\mu s$. These factors include, amongst others: projectile behaviour and impact tilt, target preparation, high pressure systems, vacuum systems, laser alignment, oscilloscopes, etc. The requirements of this

project entailed that heavy emphasis had to be placed on pushing the overall level of precision of the small-bore gas gun to its limits, which demanded upgrades or refinements to many of the components or experimental procedures of the plate impact experiments. These improvements could be categorised as pursuing one or more of the following goals:

- High time-resolution (below 2 ns) and velocity resolution (below 10 m/s)
- Good vacuum (below 50 mtorr)
- Low impact tilt and high surface parallelism (around 1 mrad)
- Good return signal from the target (-20 dB or better), with low background
- Thin target glue layers (1 $\mu$m or thinner), without air pockets

The precursor wave is generally characterised by a low velocity peak and a rise time on the order of a few nanoseconds (depending on propagation distance). The above requirements can therefore be summarised as either maximising the time-resolution or ensuring that experimental artifacts do not interfere with the measurement. Good vacuum levels are needed as the precursor wave may otherwise be obscured by a stress ramp at impact, which can be caused by an air cushion formed in front of the projectile during atmospheric or low vacuum pressures. Thin glue layers are needed for a similar reason, as the shock may otherwise spread into a ramp wave caused by a glue layer "ring-up". That in turn necessitates a good surface finish on the targets for even glue layer spread, which at the same time is needed for a good return signal in the velocimetry probes. The following sections are dedicated to the design of the plate impact experiments and the target preparation procedures which were implemented in order to achieve these goals.

### 3.1.2 Plate impact experiment overview

The primary piece of equipment used throughout these experiments was a 32 mm bore single stage gas gun. Being a relatively small bore gas gun, its advantages lie in its quick turn-around time and relatively low cost per shot. On the other hand, the smaller bore leads to complications mainly in its ability to achieve acceptable impact tilt. It is also precludes loading of multiple samples in one shot, meaning a single target was loaded per experiment, and care was taken to ensure loading conditions were reproducible. Repeat shots were performed in both the aluminium and magnesium experimental campaigns to demonstrate this reproducibility.

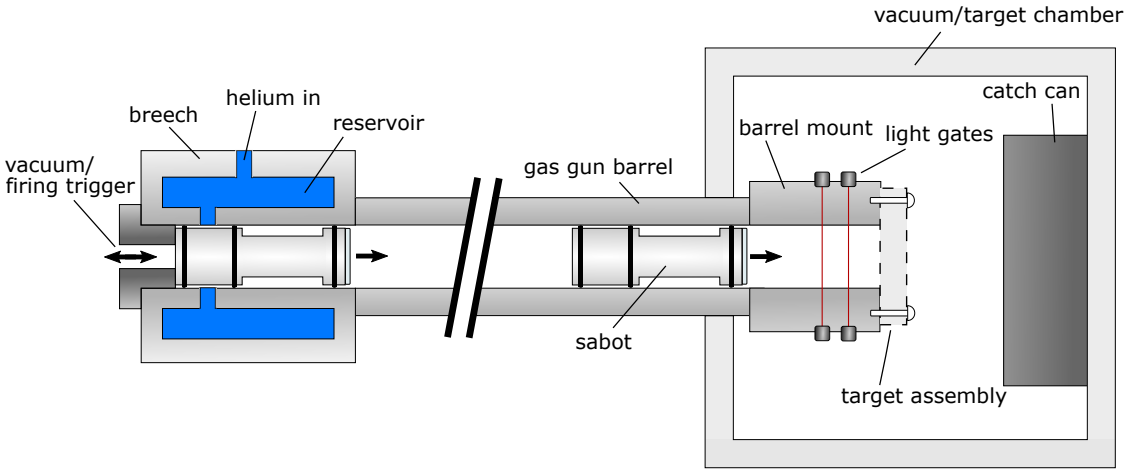



**Figure 3.1:** Schematic of the gas gun and target chamber setup. The sapphire flyer, attached to a polycarbonate sabot, is launched from the breech and travels through the evacuated gas gun barrel propelled by He gas. Upon reaching the barrel mount, it passes through two light gates which act both as a trigger for the oscilloscopes and as a secondary impact velocity diagnostic. It then impacts the target assembly, shown in figure 3.8, and finally is captured by the catch can at the back of the target chamber.

The overall setup of the plate impact experiments is illustrated in Figure 3.1 and pictured in Figure 3.2. The gas gun itself is an iteration of an earlier system used by Eakins and Chapman [123]. The timeline of events during an experiment can be summarised as follows: the target chamber and barrel in front of the loaded projectile is first evacuated down to 50 mtorr or less. The wrap-around breech is then charged with helium and used to launch the projectile through the 3 m long barrel. Two light gates attached to a barrel mount provide triggering for

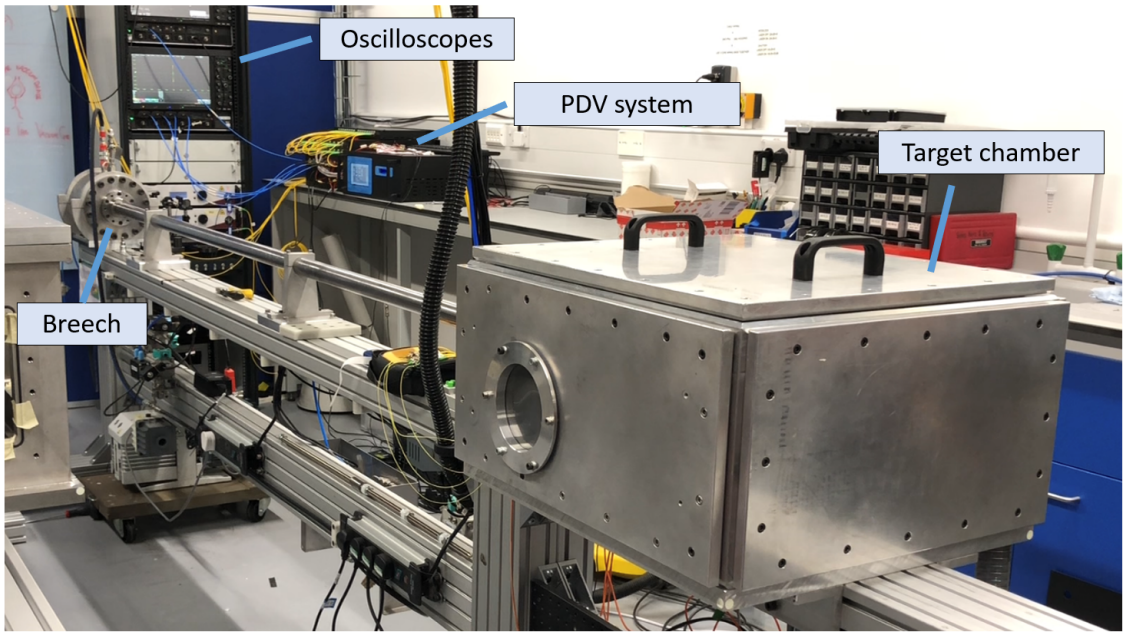



**Figure 3.2:** Picture of the 32 mm bore single stage gas gun setup at the Impact Engineering Laboratory laser enclosure at the University of Oxford.

the oscilloscopes and a secondary impact velocity measurement. The projectile impacts the target assembly (see Section 3.1.6) which is fixed to the face of the barrel mount, and the now triggered oscilloscopes record the evolving beat frequencies of five PDV channels which together measure the target velocity, flyer velocity, and driver breakout. Finally, the projectile is decelerated by the catch can at the rear of the target chamber, concluding the experiment.

### 3.1.3 Vacuum system upgrade

If one conducts a gas gun experiment at ambient pressure or even at a low vacuum, the air within the gun will build up in front of the projectile as it travels down the barrel, forming an air cushion. Upon reaching the end of the barrel, this pocket of air will be further compressed between the projectile and the front surface of the target. This cushions the initial impact, launching a ramp wave into the target before full contact has been achieved.

Measurements of the precursor wave, particularly in low strength materials such as aluminium, necessitates the ability to resolve small velocity changes at the base of the shock wave of around 50 m/s and below. These low velocity features can be obscured by air ramps, which is demonstrated in Figure 3.3. In the successful shot shown in the figure, vacuum levels were at less than 50 mtorr and a precursor wave is clearly resolved at the base of the shock. In the unsuccessful shot, poor vacuum levels of around 1 torr along with what was a possibly an o-ring failure caused a large gradual velocity increase to completely obscure the effects of the elastic-plastic transition.

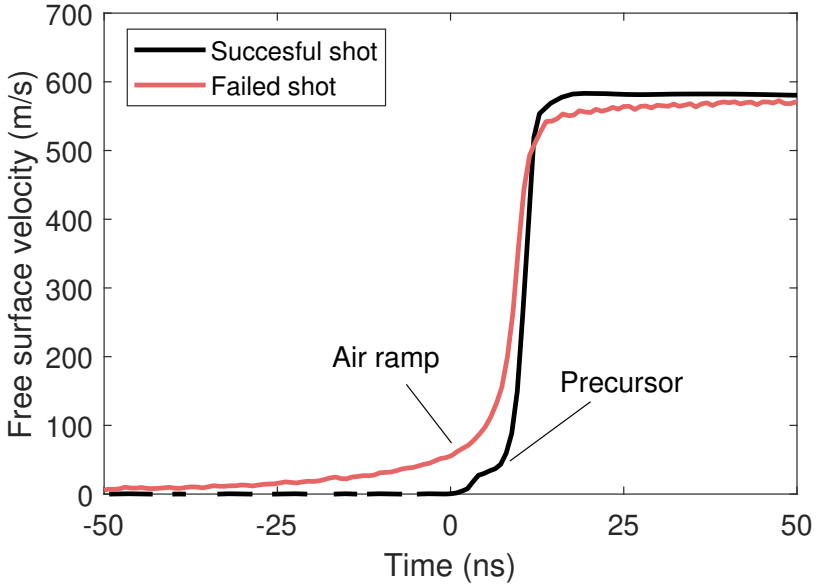



**Figure 3.3:** Example of an air ramp obscuring the precursor wave in a failed experiment on aluminium (before the vacuum system upgrade), likely caused by a combination of poor vacuum levels of 1 torr and a possible o-ring failure. A successful shot at less than 50 mtorr is shown for comparison, in which a clear precursor wave is revealed.

The failed experiment displayed in Figure 3.3 necessitated a major redesign of the gas gun vacuum system. As shown in by the vacuum performance curves in Figure 3.4, the old system was unable to reach pressures of 50 mtorr even after several hours of continuous pumping (the first hour of which is shown in the figure). The vacuum system consists of two pumps, a backing pump for establishing an initial vacuum, and a roots pump for achieving higher vacuum levels. It was identified that major losses in potential performance was due to the

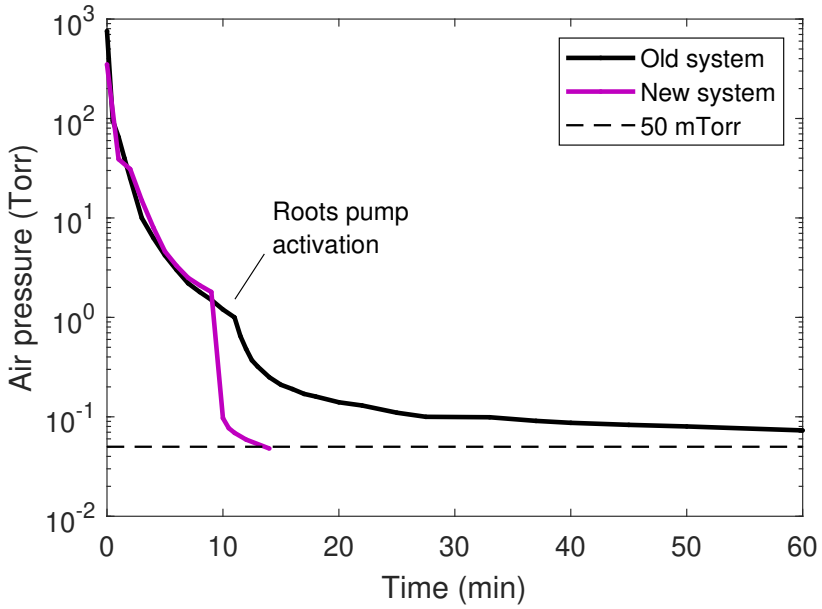



**Figure 3.4:** Comparison of the performance of the old and the newly designed gas gun vacuum systems. Both tests were conducted with completely empty target chambers. The backing pump is activated at t=0 at ambient pressure, and the roots pump is activated at around t=10 min. It is shown that the old system was unable to reach a vacuum of 50 mtorr even after an hour of pumping. By contrast, the redesigned vacuum system was able to reach 50 mtorr only 5 minutes after activation of the roots pump. For the majority of the experiments conducted during this DPhil, the roots pump was active for even longer periods meaning vacuum levels often reached below 30 mtorr.

connecting pipes of the vacuum system being of smaller diameter than the vacuum pump intakes. The system was redesigned from its previous configuration, which consisted of a mix of KF25 and KF40 components, into utilising larger KF40 and ISO100 counterparts. By also shortening the length and widening the diameter of the main line between the pumps and the target, this allowed greater air flow and enabled the full potential of the pumps to be utilised properly. Intermediate components (filters, valves etc) were upgraded to match the new dimensions. This drastically improved performance over the old system, meaning 50 mtorr could be reached in less than 15 min as shown in figure 3.4. Finally, plastic and metal plates were used in the catch can in place of rags, as the latter contain moisture and air which take a long time to extract and significantly worsens performance. The shots presented in this thesis made use of this upgraded vacuum system, and the majority of experiments were conducted under pressures of around 30 mtorr.

### 3.1.4 Barrel mount design

One of the requirements listed in Section 3.1.1 is that of low impact tilt, more specifically low tilt between the projectile and the target at the impact plane. When an impact is non-planar, the shock wave will be gradually transferred onto the target in the form of a line of contact sweeping across the target face from edge to edge. Any system monitoring a finite area on the surface of the target will have a minimum response time determined by the time in which the line of contact can move across the monitored region. For example, for a laser spot size of 0.2 mm and a 400 m/s impact (matching the majority of the experiments in this project), a simple calculation will find that an impact tilted at 3 mrad will take around 1.6 ns to sweep across the laser area. This means the current measurements, which require 1-2 ns time resolution, can easily be degraded. Minimising tilt was therefore a major challenge with this DPhil, as evidenced by the first gas gun shot which had a tilt of 7 mrad, causing a blurring of more than 3 ns.

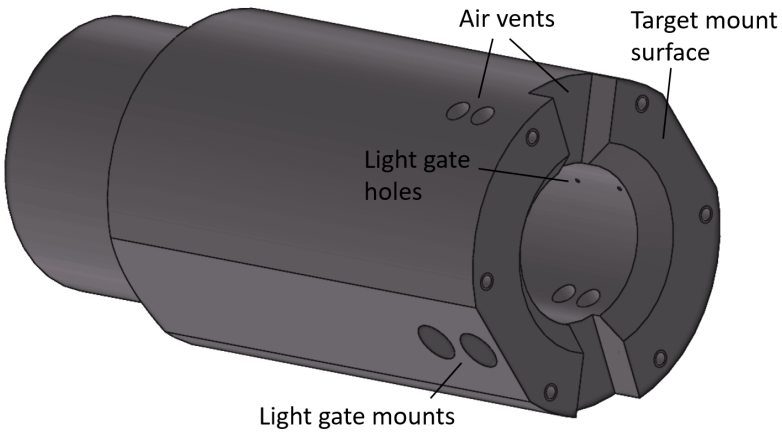



**Figure 3.5:** Diagram showing the final design of the barrel mount. The length of the barrel mount was increased to 140 mm in order to fit the entire length of the sabot (see Section 3.1.5 and to reduce balloting.

One of the primary methods of improving tilt lies in the target mounting method, of which several iterations were attempted. Two main variations are possible: either a free standing target mount in the middle of the target chamber, or a target mount attached directly to the end of the gas gun barrel. In the former

case, the target is aligned with a laser pointed down the central axis of the barrel. Unfortunately it is likely that the barrel is very slightly curved, meaning the exit angle of the projectile as it leaves the barrel is not necessarily completely parallel to barrel laser. In addition, either parts or the whole projectile will experience some time in free flight, depending on projectile length and the distance between the barrel end and the target. This can introduce downwards tilt in the flyer before impact. The alternative option is to attach the target directly onto the end of the barrel using a barrel mount piece. This removes the free flight factor from the experiment. Also, if the barrel mount is constructed such that it fits the entire length of the projectile before impact, it also eliminates the possibly skewed projectile path caused by any curve in the barrel.

It was found that the free standing target mount tended to produce quite high impact tilt, including the 7 mrad experiment mentioned previously. Subsequent tests were conducted using the barrel mount method using several iterations of the mount design. The final design is shown in Figure 3.5, which features holes for light gates as well as air vents. The latter ensures that any air in front of the projectile can escape instead of being trapped in front of the target front surface. By constructing the barrel mount to high precision, the barrel path and the target mounting plane can be made exactly perpendicular, which should produce perpendicular impact if the target is also constructed to high flatness. This also eliminated the need for manual target alignment.

### 3.1.5 Projectile design

Another source of tilt at impact is caused by misalignment in the path of the projectile due to balloting of the sabot inside the barrel. This effect is illustrated in Figure 3.6. Countermeasures for this include making the sabot thicker and longer, essentially decreasing the maximum angle of pitch available to the projectile. The length of the sabot was increased from 30 to 100 mm, and a third o-ring was added for more stability and additional safety against o-ring failure. The o-rings

were upgraded to 3 mm diameter, and the depth of the o-ring groove was adjusted to provide a closer fit to the barrel. The final sabot design is shown in Figure 3.7. Finally, there is also an additional possibility of a slight mismatch between the barrel itself and the mount , which can cause additional tilt as the projectile passes into the barrel mount. The barrel mount featured in 3.1.4 was therefore designed with this sabot in mind, as it allowed the entire projectile length to fit inside the mount, thus avoiding this issue.

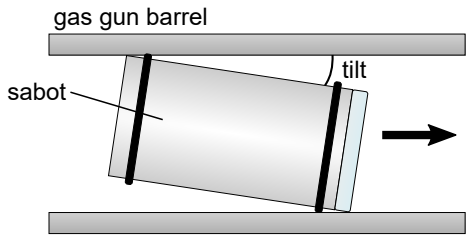



**Figure 3.6:** Schematic showing exaggerated tilt caused by balloting of the projectile inside the barrel.

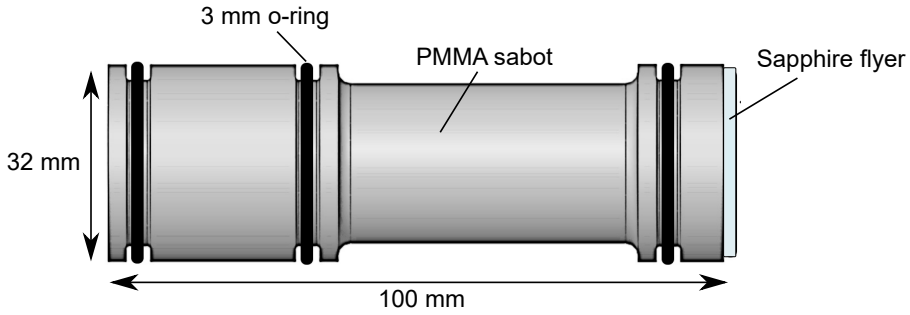



**Figure 3.7:** Diagram showing the final design of the sabot. The length of was increased to 100 mm and the fit of the o-rings was tightened in order to minimise projectile balloting inside the barrel.

### 3.1.6 Target assembly design

The design and preparation of the target is arguably the most important step for a successful measurement of the precursor wave. The intricacies of the preparation of the sample itself are detailed in Section 3.1.7; here the overall construction of the target assembly will be explained. The configuration of the shots was that of a symmetrical sapphire flyer - sapphire driver impact, in which the sample was bonded to the rear free surface of the driver. The sample rear free surface was

measured using PDV, from which a simple approximation of the sample particle velocity can be made by dividing by a factor of 2 [36].

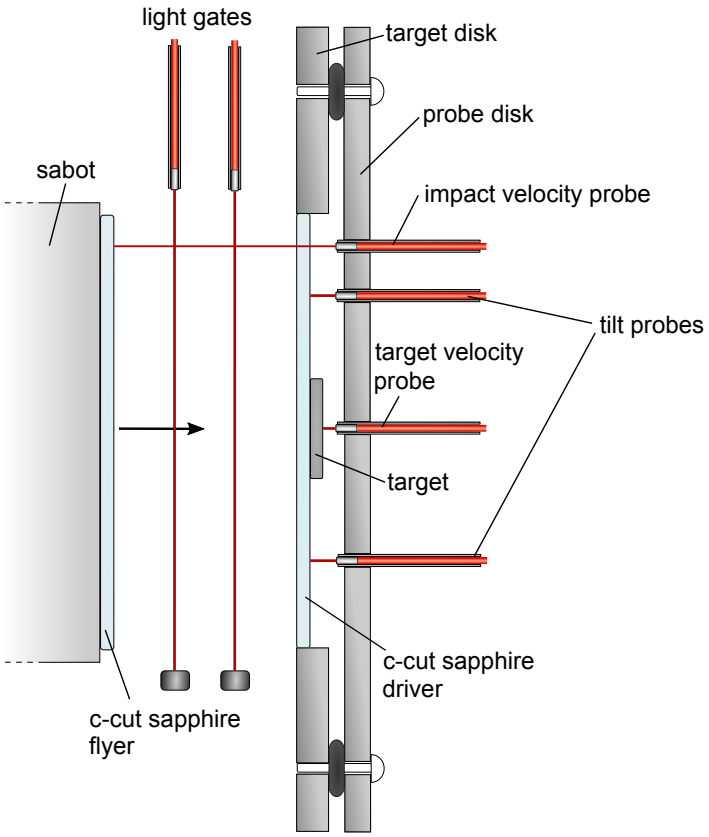



**Figure 3.8:** Schematic showing a cross-section of the target assembly inside the target chamber. The target is bonded to the rear surface of a sapphire driver, which is impacted by a sapphire flyer. The free surface velocity is measured on the target and on three locations on the sapphire driver. Impact velocity is measured on the sapphire flyer through an uncoated window on the driver. The target velocity probe is aligned by adjusting the depth of the screws holding the probe disk.

One of the priorities of the target design was to make it simple, quick to set up, economical and highly repeatable. Note that the entire target assembly, including the PDV probes, is completely destroyed after each shot, meaning that a highly cost-effective design had to be developed in order to accommodate the ambitious number of shots planned for these studies. In the end more than 60 shots (including tests) were conducted, which represents a considerably high number within shock physics studies. The final design is illustrated in Figure 3.8, and features two primary components: the target disk and probe disk, both

constructed from PMMA. The target disk contained the target itself, glued into a central hole, and was bolted onto the end of the barrel mount shown in Figure 3.5. High flatness was ensured by first polishing the impact surface of the disk, and then placing it on a polished flat steel surface in order glue the target (see Figure 3.9a). The driver was comprised of a high flatness $c$-cut sapphire. The barrel mount surface was machined perpendicular to the barrel axis (to 5 micron tolerance), which together with this preparation process ensured that the driver front surface was as perpendicular as possible to the projectile direction.

The five PDV lines used to measure the target, flyer and driver velocities were attached to the probe disk, which was suspended behind the target disk using a set of bolts and o-rings. Conducting more than 60 experiments in which five PDV probes are destroyed per shot can become quite costly, especially since only the target velocity channel actually required high signal-to-noise and temporal accuracy. An exceptionally more cost-efficient alternative was found for the other four channels, consisting of utilising basic optical FC/PC fibre connectors instead of full laser probes. Once the connector housing is removed, these leave a simple fibre end as shown in Figure 3.9c, which can be glued into the probe disk. This was found to give acceptable signals for the purposes of measuring impact velocity (where long STFT windows can be used, see Section 3.2.1) and driver breakout (where only the timing of the initial velocity increase is needed). Note the specific use of PC and not (angled) APC connectors, as the former does not angle the light and also provides a slight return signal which can be used as the reference wavelength for a Gen 1 PDV setup [124].

After bonding the PDV probe and fibres to the probe disk, the target velocity probe is aligned with the sample by adjusting the alignment screws to maximise the back reflection. Reflectance is defined as a ratio of the reflected light compared to the light being transmitted down the fibre, and is measured in dB. For example, -20 dB corresponds to $1\%$ of the transmitted light being reflected back up the fibre line. The reflectance of the probes themselves needs to be low (-55 dB in

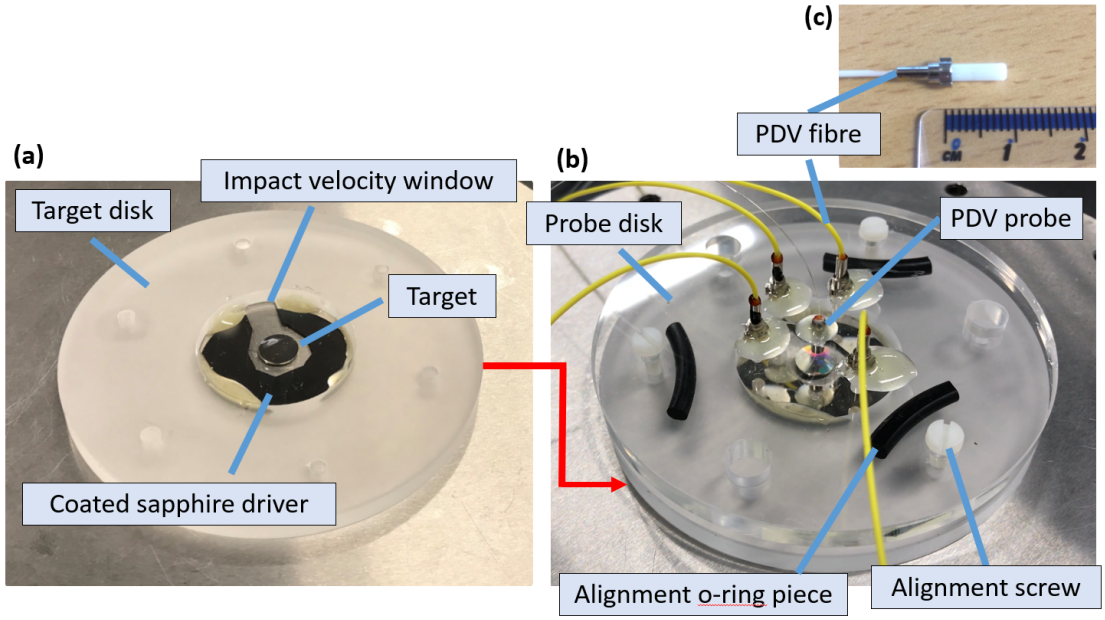



**Figure 3.9:** Pictures of target assembly being prepared. a) A sapphire driver already bonded to a sample (see Section 3.1.7), being glued into the target disk. b) A probe disk suspended on top of the target disk. The alignment screws are tightened such that the central PDV probe is aligned onto the target. The signal from the tilt and impact velocity lines require less precision and do not need separate alignment, and also utilised the fibres (yellow) shown in c), which consist of an FC/PC fibre stripped of the connector housing.

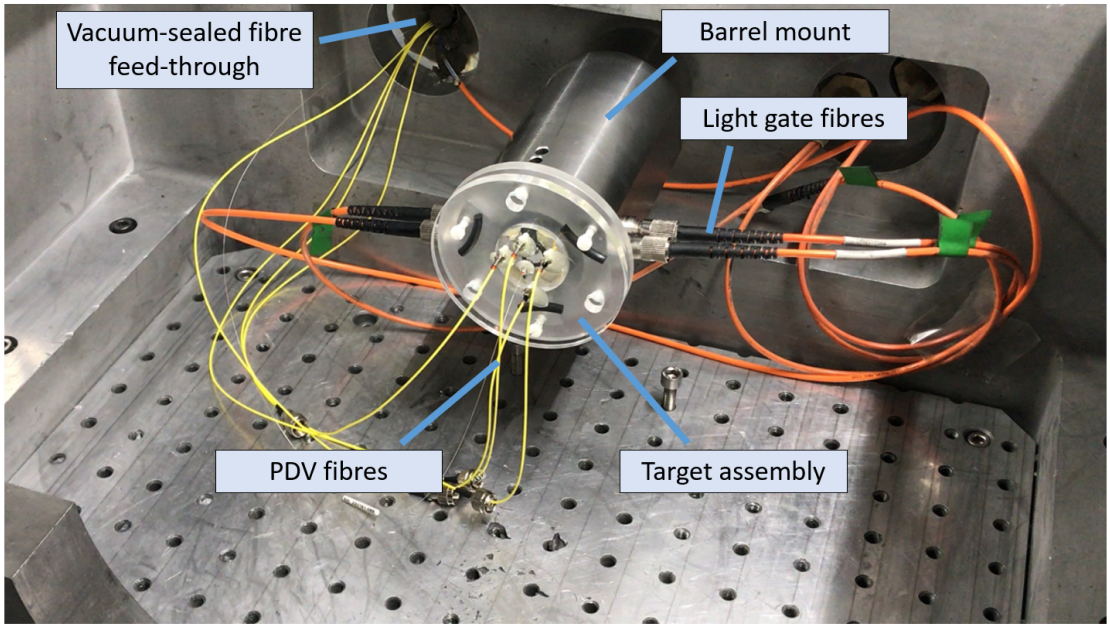



**Figure 3.10:** Picture of the prepared target assembly mounted on the extended barrel mount (Figure 3.5) inside the target chamber (Figure 3.2). Light gate fibres are attached to the sides of the barrel mount, which along with the PDV fibres are fed through vacuum sealed ports to the PDV system and oscilloscopes.

the current experiments), as the resulting PDV beat frequencies will otherwise contain a constant baseline frequency from the light reflected by the probe mixing with the reference light (see Section 3.2.1). In contrast, the reflectance measured from the probe channel once aligned with the target should be high. The sample surface quality in these experiments was close to a mirror finish, which provided back reflections anywhere from -15 up to -5 dB. This guaranteed a high signal-to-noise and a low to non-existent baseline. It was found that the fibre connectors did not need to be aligned separately in order to achieve sufficient signal to resolve shock breakout time.

### 3.1.7 Sample preparation

The three primary steps of the target preparation procedure consisted of cutting the sample from the source material, grinding and polishing the sample, and then bonding it onto the driver. The driver-sample assembly was then glued into the target disk shown in Figure 3.8. Tied to this process were the requirements of minimising both sample tilt and glue layer thickness, as well as achieving a good surface finish, as any of these could otherwise lead to loss of signal or time resolution.

The negative effects of impact tilt were outlined in Section 3.1.4, meaning care had to be taken to ensure the glue layer was of even thickness. In addition, any low impedance layer of finite thickness (such as glue) being loaded by a shock wave will experience several wave reflections between its two interfaces before reaching an equilibrium at the full shock pressure. This is termed a shock "ring-up", and will significantly delay the transfer of the peak shock state from the driver into the target if the glue layer is too thick [15]. Any air bubbles in the glue layer will have a similar effect, essentially leading to a ramp-like wave being transferred into the target. Using the Hugoniot curves for epoxy [125], aluminium [126] and sapphire [127], a ring-up calculation was performed for a 1 $\mu$m glue layer between sapphire and aluminium [15]. It was found that it takes about 0.8 ns at 400 m/s impact for the shock pressure to reach 3.2 GPa (and about 1.6 ns to reach

the peak pressure of 4.6 GPa). However the pressure of the first transmitted wave (at 1.3 GPa) was in fact already higher than the aluminium elastic limit, meaning the subsequent ring-up waves would primarily affect the plastic wavefront. A 1 $\mu$m or thinner glue layer was therefore used as a benchmark for these experiments, which is in line with previous studies [22] and deemed acceptable given the rise times of around 1.5-4 ns in these experiments (see Chapters 4-5).

Actually achieving a thin and even glue layer between the driver and the sample was a major challenge during this project. The source material in both the Mg and Al experiments was in the form of extruded rod, from which samples were cut using electrical discharge machining (EDM). The use of EDM ensures that minimal damage is imparted onto the sample while sectioning. The cut samples were subsequently thinned down to the final thickness and bonded to the driver. Early iterations of these steps consisted of lapping the target surfaces with progressively finer diamond suspensions, down to 5 $\mu$m, followed by hand polishing with micron paper down to 1 $\mu$m. The target was bonded onto the sapphire driver using a low viscocity, 24 hour setting glue (Angstrom Bond), while under a press. Unfortunately, this process gave inconsistent results, as shown by the AZ91 velocity profiles in Section 4.5. Uneven spread of the glue was often visible through the sapphire, including what sometimes could be identified as air pockets, likely caused by an uneven sample surface. Hand polishing also increased the likelihood of degrading the parallelism of the sample surfaces if pressure was applied unevenly (increasing tilt). Finally, the target surface itself also provided a relatively poor return signal of sometimes less than -20 dB.

In the improved preparation method, the samples were instead diamond turned down to the final thickness, which guaranteed a close to mirror finish, as well as high flatness and high parallelism of both surfaces. The bonding process was also changed to instead utilise a spin-coating method, through which an even layer of adhesive was spread onto the sapphire driver before bonding (performed by Scitech Precision Ltd.). This adhesive layer was measured optically to less than

1 $\mu$m using a scratch depth measurement, before performing the actual sample gluing. Note that this pre-thinning step of the glue layer would not be viable if using a conventionally hand polished sample, as the sample would likely have surface roughness larger than 1 $\mu$m, which could lead to unfilled air bubbles. A more conventional gluing process (which would use more adhesive) would be necessary for rougher samples. The diamond turned sample (flat to $<$1 $\mu$m) being pressed into the pre-spread adhesive guaranteed an even glue layer with a final thickness less than 1 $\mu$m (after being pressed).

Finally, an additional advantage of the mirror finish was the excellent return signal strength in the target probe channel, between -15 to -5 dB reflectance once aligned. Note however that a concern with such a highly specular rather than diffuse surface is that any misalignment which occurs during the shot is likely to result in severe signal loss. While this may be a problem if measuring e.g. spall strength, it was found for the purposes of this study that a possible loss of signal in the later stages of the plastic wave was an acceptable trade-off for higher signal strength during the shock rise (and thus in the precursor wave). All in all, this sample preparation method was able to minimise the glue layer thickness, ensured an even glue spread without air bubbles, and maximised sample flatness and parallelism. Together with the target mounting method described in Section 3.1.6, this maximised the potential of the 32 mm bore gas gun to deliver high planarity impact loading.

## 3.2 Diagnostic methods

### 3.2.1 PDV

Photon Doppler Velocimetry (PDV), also known as Het-V, is a laser interferometry technique commonly used during dynamic experiments to measure velocity to a high temporal resolution [124, 128, 129]. Using low cost communications-grade fibre optics, it has in recent years become an often used alternative to the traditional VISAR system. A brand new in-house PDV system was built and fielded

as the main diagnostic for the experiments in this project. Capable of both 1st and 3rd generation (frequency shifted) setups [129], the PDV system featured amplified low-noise detectors and 40 GS/s oscilloscopes.

PDV relies on measuring the Doppler shift of a laser beam reflected from the back of a moving target. The Doppler shifted light is combined with a reference beam within the PDV system in order to produce a beat frequency which is proportional to the velocity of the target, according to,

$$f_{beat} = f_{reflected} - f_{reference} = \frac{2}{\lambda_0} v, \tag{3.1}$$

where $\lambda_0$ is the reference wavelength and $v$ is the velocity of the target [129]. First, the beat signal produced by the PDV system is recorded on the oscilloscope. The beat frequency is then analysed using short-time Fourier transform (STFT) methods to extract the velocity history. This involves taking a time segment, or window, of the full data set and multiplying it with a window function (e.g. a Hamming window). An STFT is performed to generate a power spectrum from the signal segment. A Gaussian function is fitted to the frequency spectrum in a given time step and its peak frequency is extracted, which is assumed to be proportional to the velocity. The free surface velocity is calculated using Equation 3.1, after which the window is moved to the next time segment and the process is repeated. An example of this process is shown in Figure 3.11.

The window length of each segment is usually set to a power of 2, e.g. 64 data points, as this allows for efficient calculation of the STFT. The time resolution of the PDV measurement can then be determined from the window length and the time step per point, where the latter is set by the time resolution of the oscilloscope. At a sampling rate of 40 GS/s, this corresponds to 25 ps per point. A window length of 64 points in this case therefore represents a 1.6 ns segment. The next window segment is usually placed at some level of overlap with the previous window. For example, at a 50% overlap of 32 points in a 64 point window, the

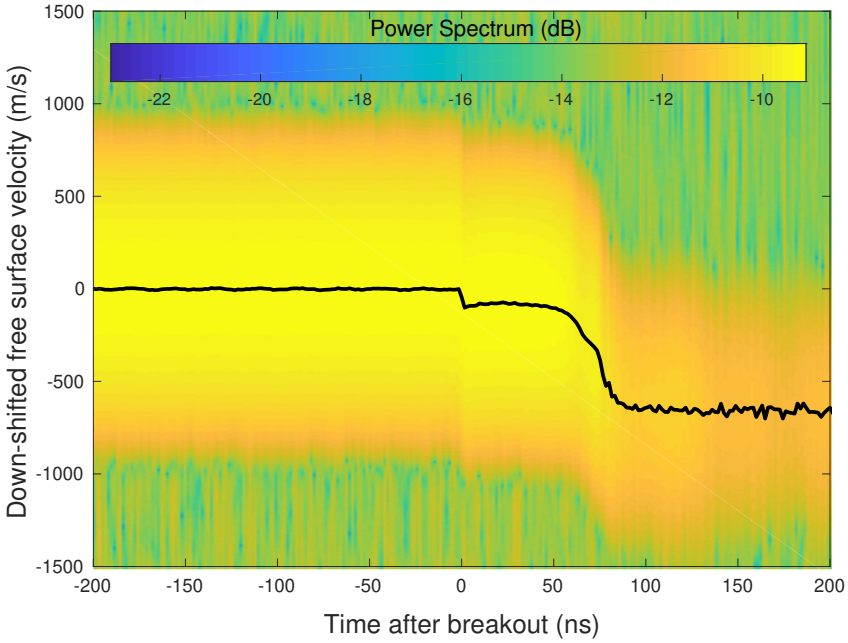



**Figure 3.11:** Example of a representative PDV power spectrogram, showing an impact on 2 mm thick Mg AZ31. The spectrum was obtained using a window length of 64 points corresponding to 1.6 ns time resolution. Frequency has been converted into velocity, and the velocity trace shown in black was fitted to the peak of the power spectrum. The velocity trace is flipped vertically as the laser wavelengths were set up in the down shift configuration.

effective resolution would in this case become 0.8 ns. Note however that using overlapping windows is similar in concept to using a moving average. Using a longer window on the other hand improves the frequency (and therefore velocity) resolution, as more wavelengths are analysed in the STFT. Long windows were used for the impact velocity data where time resolution is of less importance.

In the present experiments, the target velocity channel was frequency shifted to 4 GHz, which effectively makes it more sensitive at low velocities [129]. The laser wavelengths were set up in the down shift configuration (as shown in Figure 3.11), in which the Doppler shift causes a decrease in the beat frequency, because 4 GHz was close to the maximum of the detector bandwidth. The other four PDV channels were set up in the conventional Gen 1 configuration, i.e. without frequency shift [124].

### 3.2.2 Tilt Analysis

Tilt is defined as the angle of the impactor face with respect to the target plane, as shown in Figure 3.12, and can have negative effects as detailed in Section 3.1.4. The tilt was therefore determined in each experiment by measuring the velocity of the rear free surface of the sapphire driver at three positions $A$, $B$ and $C$, as shown in the figure, using PDV fibres (see Section 3.1.6). These points are defined as the positions of the target surface at shock breakout, and can be calculated using the shock breakout time measured by the probes and the impact velocity. It is then possible to calculate two vectors in the plane of the shock front, given by $\vec{x} = B - A$ and $\vec{y} = C - A$. The vector normal to the shock plane, $\vec{n}$, is given by the cross product, $\vec{x} \times \vec{y}$. Finally, the tilt, $\theta$, is simply given by the dot product as follows,

$$\theta = \cos^{-1}\left(\frac{\vec{n}\cdot\vec{m}}{|\vec{n}||\vec{m}|}\right). \tag{3.2}$$

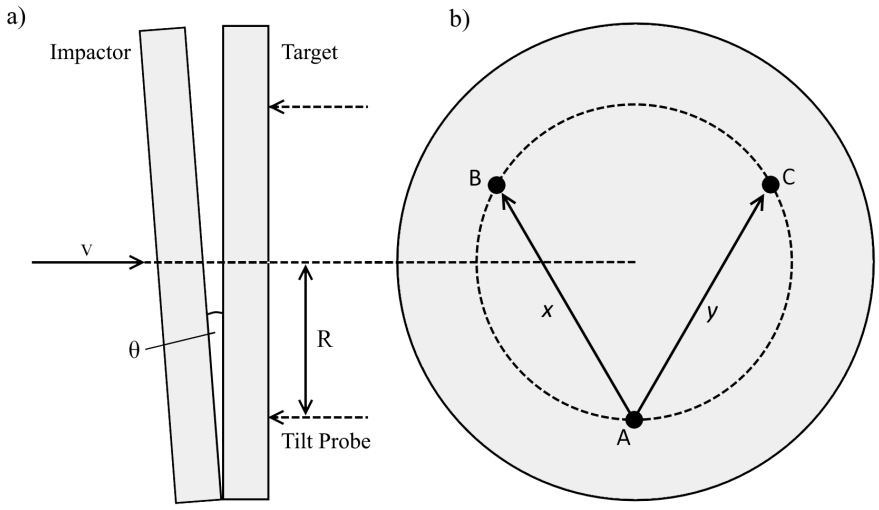



**Figure 3.12:** Schematic of tilt measurements in planar impact. a) Side view of an impact with velocity, $v$, and tilt, $\theta$, with respect to the target. b) On axis view of the back of the target. Three tilt probes are equally spaced in a circle, radius $R$, at positions $A$, $B$ and $C$.

## 3.3 Material characterisation

### 3.3.1 EBSD specimen preparation

Electron backscatter diffraction (EBSD) is a technique used in a scanning electron microscope (SEM) in order to measure a multitude of material properties such as structure, orientation and strain. Electrons are accelerated at a sample, which is held at an angle to the beam (usually around 70°), and backscattered towards a phosphor screen and CCD. The electrons exiting the sample at or close to the Bragg angle diffract to form an image of Kikuchi bands, which can be individually indexed to a specific diffraction plane. From the Kikuchi pattern one can therefore reveal both the material element and its orientation at the scattering origin.

The most important determinant of one's degree of success when employing EBSD lies in sample preparation. As the diffracted electrons originate only from within the first few tens of nanometers from the specimen surface, any deformation, irregularity or even oxidisation can act to stifle the formation of Kikuchi bands. It is therefore paramount to achieve as flat and polished a surface as possible. While this can achieved with relative ease in harder materials such as steel, the aluminium and magnesium studied in this DPhil are very soft in metallurgical terms (especially the pure Al), and are consequently highly susceptible to scratches and other mechanical damage. Some key insights will be shared in this section regarding methods to prepare aluminium and magnesium samples, discovered from many attempts throughout this project at achieving good quality EBSD data.

Samples were cut from the Al and Mg rods in both the longitudinal and transverse sections using electronic discharge machning (EDM). Sample dimensions were 3-12 mm in diameter (depending on the rod diameter) and 2-3 mm thick. The thickness was chosen to allow for a good deal of material removal during the grinding steps. Note that EDM excels in sectioning samples whilst causing very little damage in the material surrounding the cut region, however it is not strictly necessary in the case of EBSD preparation as any damage from a coarser cutting

tool can be ground away. Thinner samples such as the shock experiment targets or TEM samples benefit more from the use of EDM.

The samples were mechanically ground using a Struers Tegramin specimen grinder in a sequence of 500, 800, 1600 and 4000 grade SiC paper for around 3 minutes in each step. These grinding steps were applied for all of the materials studied with EBSD, i.e. Mg AZ31, 5N-Al and Al 6082. Note that it is critical to slowly reduce the grit size for each step and carry out grinding until all deep scratches from the previous stage have been removed. If steps are skipped, it is likely that the smaller grit pads won't be able to completely remove large scratches left from coarse grinding.

In addition, aluminium becomes softer with increasing purity and therefore increasingly prone to scratching and even embedding of abrasives or other particles into the specimen surface. It is therefore necessary to eliminate cross-contamination by keeping each set of grinding pads separated and used exclusively for the specific material being prepared. The SiC pads in particular blunt quickly and need to be refreshed often. After each grinding stage it is likely that large particles or debris which have been removed from the sample are still present on the specimen surface. This can potentially cause large damage in the following finer stages. To help prevent this, at the conclusion of each stage the sample needs to be quickly washed with water, then with ethanol, and finally wiped with ethanol-soaked cotton pads, which should manually remove any of the large left-over particles. Finally, it is critical to inspect the sample after each grinding step using an optical microscope to confirm that all the damage from the previous step has been removed (too much grinding was found to be counter productive). Note that more complex composite grinding pads are sometimes recommended for single-step grinding of Al alloys. While this was attempted, inspection of the resulting surface quality revealed more scratching than what was achieved with the slower progression of SiC pads.

Grinding is followed by polishing using cloth pads with 9 $\mu$m, 3 $\mu$m, 1 $\mu$m diamond suspensions. Once again it is necessary that each cloth pad is used with only one type of abrasive and material (even mixing Al 6082 and pure Al pads may cause complications). Final polish was achieved using a colloidal silica suspension (0.04 $\mu$m grain size). This final step combines mechanical abrasion with chemical material removal to produce a fully deformation-free surface. Inspection by naked eye should present a perfect mirror finish, whilst a dull finish indicates embedded particles or scratches.

Upon completion of the final polishing stage, the samples were washed a final time and then placed in an ultrasonic cleaner for at least 5 minutes. In order to limit any surface degradation due to oxidisation, the samples were then submerged in ethanol after cleaning and kept there until being used. This was done as samples which were exposed to atmosphere showed signs of oxidisation after a few weeks, and possibly earlier. A final 10 minutes of ion polishing was performed using a Gatan PECS II right before insertion into the SEM.

### 3.3.2 TEM specimen preparation

Transmission electron microscopy (TEM) in simple terms consists of transmitting a beam of electrons though a thin (usually $<$200 nm) specimen and onto an imaging surface, such as a fluorescent screen or a CCD. Electrons passing through the sample are absorbed and scattered, depending on the density and orientation of the material, creating contrast in the final image. Any imperfection or defect in the crystal lattice of the sample material is likely to create contrast as the electrons will be scattered to different angles by the contorted lattice surrounding the defect. This is why dislocations can be imaged directly as dark lines in a brightfield TEM image (see Figure 3.13a). Electrons passing through the dislocation line are deviated onto a different course when compared to those in the surrounding regular crystal, creating a dip in the electron density reaching the imaging device.

TEM imaging was utilised in the aluminium project with the main goal of characterising the dislocation densities at increasing levels of cold working. Sample preparation for TEM can, similarly to EBSD, be a very complex issue involving a great deal of trial and error. The most important criterion is to prepare electron-transparent samples which are representative of the bulk material structure. As this requires thicknesses of only a few hundred nanometers for typical TEM imaging, care has to be taken such that specimen preparation artifacts do not affect the measurements. The following section is dedicated to outlining the steps taken to produce suitable samples, including methods which were attempted but proved unsuccessful.

The sample material in the form of 5N-Al and Al 6082 rods was cut in the transverse section using electronic discharge machning (EDM) at thicknesses of 0.5 mm. EDM is recommended as it introduces minimal mechanical damage to the specimen during cutting, and the thickness was chosen such that any damage in the surface layer would be removed during the next thinning steps. The discs were mechanically ground using 800 grit SiC paper to around 200 micron, after which 3 mm diameter TEM samples were punched out using a hole punch. The samples were further thinned by mechanical grinding using SiC papers starting at 800 and finishing at 4000 grit until a thickness of around 70 $\mu$m was achieved. As a general rule, abrasives produce damage to a depth of about 3x the grit size, meaning a 4000 grit SiC paper, which has a particle size of 3 $\mu$m, will produce damage inside the first 9 $\mu$m from the surface. A sizeable undamaged layer of around 50 $\mu$m was therefore left for final thinning. For this last step, a Fischione 1010 was utilised to ion mill the samples until perforation (achieving the required thinness at the perforation edge), using an accelerating voltage of 3 keV and milling angle of 10°. Milling was stopped automatically when a large enough hole was detected by the machine.

Ion milling involves bombarding the centre of the sample with ions (Ar in this case), sputtering material from it until a small hole is formed. The potential

problem with this technique is the extent to which the ion beam can penetrate into the sample, meaning the surface layer of the sample may be damaged or altered chemically [130]. This can result in an amorphised or ion implanted top layers. The low beam energy of only 3 keV used here helps combat this (energies of 4-6 keV are often used), however this comes at the cost of an increased milling duration. In this case it was found that the exchange for longer milling times was worthwhile, and the average milling time of the successfully prepared samples was between 48-76 hours. By contrast, an example of what is very likely ion-damage found in a sample of Al 6082 in this study is shown in Figure 3.13b. The TEM micrographs had evidence of heavy defect density as well as surface roughness, inhomogeneities and likely amorphised material. Consequently, dislocations or other crystalline material microstructures had been effaced and none were visible in any part of the sample. This specific specimen had mistakenly been loaded at a slight angle inside the instrument, causing the top surface of the sample to be milled at a steep angle, whilst the bottom surface was barely milled at all. The result was heavy discolouration on the bottom surface, easily visible by eye, caused by material being continually damaged but not removed due to the very low angle of incidence.

While no evidence of ion damage was found in the successful TEM specimens presented in this study, future experiments would benefit from pre-thinning by dimple grinding to reduce the time needed in the ion mill and possibly further lessen the risk for damage. Dimpling the sample consists of thinning the central area down to thicknesses of around 10 $\mu$m in preparation for the final milling step. This would significantly speed up milling times, and any damage caused by grinding and polishing should in theory be removed by the final thinning process. In the end the method was not tested due to the time commitments required to learn and trial a new technique, as well as the risks associated with introducing another step which could potentially cause mechanical damage to the sample.

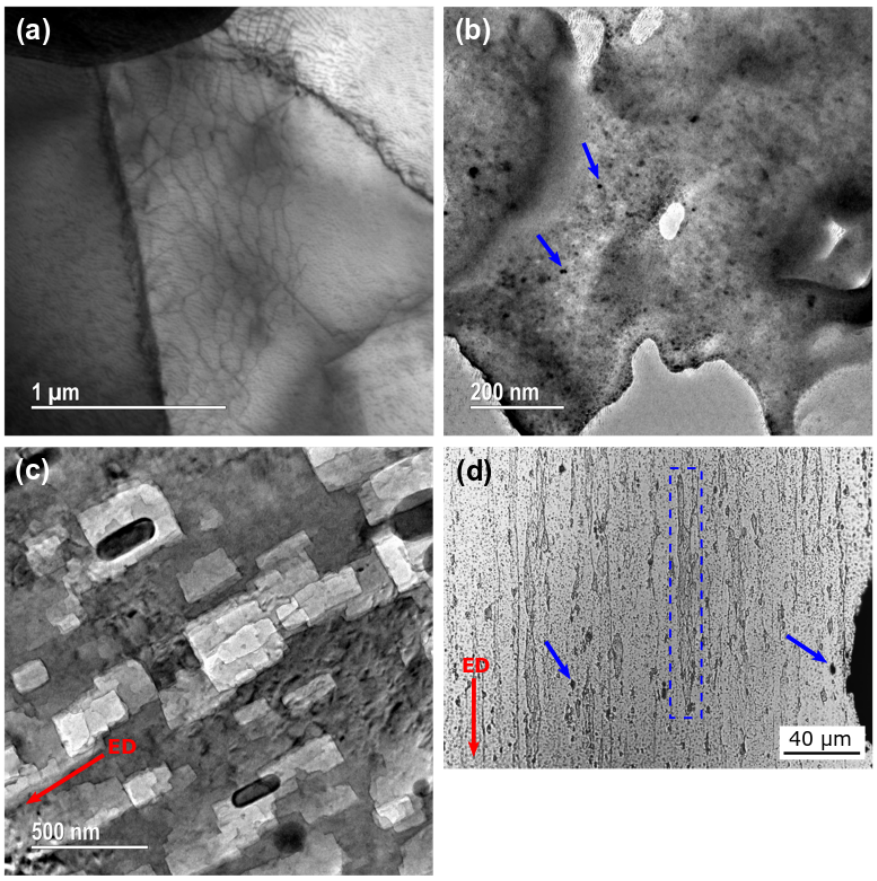



**Figure 3.13:** Examples of sample preparation damage caused by both ion milling and electropolishing. a) Successful TEM micrograph of dislocations inside a grain. b) Failed TEM sample showing evidence of surface roughness, inhomogeneities and defects (small black dots denoted by blue arrows) caused by excessive ion milling in an as-extruded Al 6082 sample. c) TEM micrograph and d) optical micrograph of an electropolished sample, cut in the longitudinal section, from Al 6082 rod after a single pass of rotary swaging. The extrusion direction is indicated by the red arrows. The sample has likely been over etched, and displays anomalous square particles unlike anything found in the literature. It is assumed they were caused by preferential etching of regions with different phase or orientation during the electropolishing phase. The optical micrograph shows evidence of etch pits (blue arrows) as well as the presence of elongated fibrous grains (blue dotted box), similar to those found in EBSD analysis (see Section 5.3, which have been revealed through etching.

Another potential avenue for improvement which was attempted instead was the use of twin-jet electropolishing rather than ion milling for the final thinning step. While the latter is a very commonly used technique, electropolishing is possibly more popular in the case of aluminium [131–134], usually employing solutions of 5-25% acid by volume (often either $HNO_3$ or perchloric acid) with the remainder constituting methanol or ethanol. The main advantage of electropolish-

ing is the speed, as perforation can be achieved in a matter of minutes (instead of hours or days as may be the case for ion milling), depending on the strength of the acid being used. In return, it may require a lot more trial and error in order to perfect.

The process involves applying a voltage between a set of two nozzles and the specimen placed in the middle. A jet of electrolyte is pumped onto both sides of the sample until perforation is achieved (detected using a laser beam). While no mechanical damage is imparted, sample material may be preferentially removed in some regions depending on the microstructure. The applied voltage needs to be chosen such that the anodic dissolution of the material doesn't cause etching or pitting [135]. In a trial attempted for this study, a solution of 5% perchloric acid and 95% ethanol was used to achieve perforation within 2-3 minutes at 18 V. Unfortunately, the aforementioned issues were encountered as shown in Figure 3.13c-d in an Al 6082 sample. The TEM micrograph displayed a dense population of anomalous rectangular-shaped particles, unlike anything found in literature investigations of Al 6082. It is likely these artifacts were created through a difference in the rate of removal in areas of either a different phase (e.g. AlFeSi phase) or orientation. Indeed, investigation of the electropolished samples in an optical microscope revealed tell-tale signs of an over etched sample, in which both the fibrous grain structure and a widespread presence of etch pits is distinguished. Achieving better results with electropolishing would have required further experimentation, and was abandoned in favour of ion milling.

### 3.3.3 Dislocation density measurement techniques

#### Dislocation density measurement using TEM

Dislocation densities were estimated from TEM data using Ham's linear intercept method [136] and are listed in Table 5.2. This technique involves drawing a mesh of randomly spaced lines (6 in this case), and counting the number of

intercepts between the mesh and the dislocations. From this the dislocation density, $\rho_d$, can be estimated using

$$\rho_d = \frac{2N}{Lt} \tag{3.3}$$

where $N$ is the number of intercepts, $L$ is the total length of the mesh, and $t$ is the thickness of the foil. A total of between 30 to 60 images were captured from each sample type. Out of these, the best 10 to 20 images were selected in which dislocations were most clearly distinguished. The line intercept method was applied twice per image and the results averaged, after which an overall area-weighted average, as shown in Table 5.2, was calculated for each sample.

It is important to discuss the uncertainties associated with this method of measuring dislocation density. They originate from four primary sources, namely 1. the loss of dislocations during sample thinning, 2. improper counting of dislocations, including their invisibility in certain orientations, 3. systematic errors associated with the line intercept method, and 4. inaccuracies in determining the specimen thickness. The first of these is discussed further in Section 3.3.2; here it is assumed that any error due to sample preparation damage is smaller than the other error sources.

The second source of uncertainty concerns the more general requirement that all dislocations must be observed, properly identified and counted within an area wide enough to be representative of the bulk state. However, when the scalar product of the diffraction vector and the burgers vector of a given dislocation is zero (also called the invisibility criterion), diffraction contrast will be very small and dislocations become invisible. This criterion is often used to determine the burgers vector of specific dislocations, but can become an issue when attempting to image all the dislocations within a given area. The specimen must therefore be tilted such that most if not all dislocations are observed, or multiple images taken at different orientations if not. In addition, in cases of very high dislocation

density, such as examples shown in Figures 5.6-5.8 in Chapter 5, the contrast caused by the strain fields around tightly packed dislocations are too intense for the dislocation lines to be perceived clearly. This can sometimes be alleviated by using higher magnification, however a full work-around would require the use of STEM in which the background contrast can be heavily reduced [137]. Unfortunately some of the highest dislocation density samples investigated here required evaluation using human judgement and best guesses of the exact count of dislocations in a given area. Finally, as each TEM micrograph represents a local measurement, it is possible that the narrow areas of investigation are not representative of the bulk material. This is can only be directly addressed in the TEM by surveying larger areas. In Section 5.3.3, an alternative macroscopic measurement technique is used to further corroborate the results from the direct dislocation counting method.

The third source of uncertainty listed above was raised by Ham and Sharpe [138] in a follow-up to Ham's original paper detailing the line intercept method [136]. They advise that the method may suffer from a systematic error due to the assumption that all dislocations are completely randomly oriented in the thin film. In fact, as dislocations may preferentially reorient themselves during thinning, this can lead to an underestimation of the bulk dislocation density by up to 20%.

While the dislocation counting method can be associated with ambiguity or systematic error, the fourth and largest source of uncertainty lies in the thickness estimation. Indeed, the difficulty of accurately determining sample thickness means it is very often the dominant source of uncertainty. Thickness measurements in the literature are often either unreported, approximated, or quoted without uncertainty, whilst reported numbers are in some cases simply assumptions or estimations done through comparison to other studies [49, 131, 139–142]. This is partially justified knowing that the uncertainty is ultimately constrained by the thickness range of around 70-200 nm within which foils are transparent and conventional TEM imaging is possible [142]. Once the thickness increases too

much, one starts to see degradation of the spatial resolution caused by the increase in inelastically scattered electrons, as well as an overall loss in the electron density at the CCD due to both scattering and absorption. In other words, the micrographs become both darker and more indistinct, making the identification of dislocations or any other microstructural features impossible. The thickness estimation is indeed the dominant source of uncertainty in the current study.

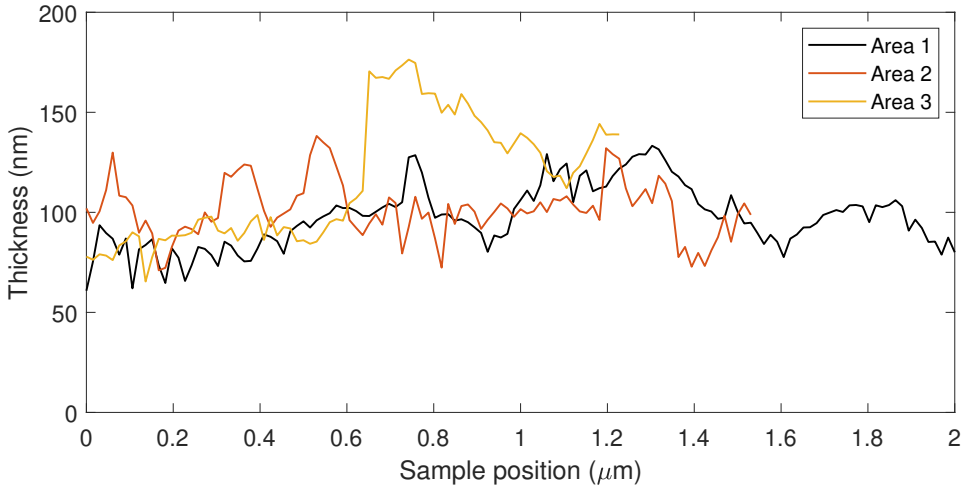



**Figure 3.14:** TEM sample thickness lineouts calculated from EELS measurements on a 5N-Al S1 sample (see Chapter 5). The lineouts were extracted from measurements taken from three different areas on the specimen at increasing distance from the sample edge. The final specimen thickness was estimated as 100 $\pm$ 30 nm.

The estimation of sample thickness can be accomplished using thickness fringe measurements, convergent beam electron diffraction (CBED), or electron energy loss spectroscopy (EELS). EELS, which was the method implemented here, is a technique based on the same effect which makes thick samples difficult to image. Given that the transmission of inelastically scattered electrons, and their energy, is proportional to specimen thickness, one can employ an electron spectrometer to measure the energy of the transmitted electrons and produce an energy loss spectrum. The specimen thickness can then be calculated through knowing the mean free path of the electrons and by extracting the energy loss from the intensity of the spectrum and its zero loss peak [143]. The thickness calculations, shown in Figure 3.14, were here performed using the Kramers Kronig method included in

the Digital Micrograph program by Gatan. The data is displayed in the form of lineouts taken from three separate areas in the sample. The averages of the three lineouts labeled 1-3 were, respectively, 97 $\pm$ 16 nm, 102 $\pm$ 14 nm, and 115 $\pm$ 31 nm, where the uncertainty is the standard deviation of the datapoints.

EELS was chosen as it involved the least amount of time to learn and implement, given the time and resource constraints towards the end of this project. The same reasons meant that only one sample was measured, and as the technique required the use of a separate microscope it was not possible to take measurements at the same time and location of the dislocation images. A resulting concern was that possible thickness variations across the sample surface would be missed. However measurements from different areas shown in Figure 3.14 indicate that thicknesses in different regions of the same sample (in which dislocations were visible) were relatively consistent given the noise. Another potential source of error was that the thickness could vary in different samples. While being a legitimate concern, previously mentioned TEM studies often make use of a single value for the thickness of multiple samples, which is justified by the sample preparation parameters being kept constant and the similarity of the resulting images.

The final specimen thickness was estimated as 100 nm with an uncertainty of 30%. This was deemed reasonable given the fluctuations in the data points, and should cover discrepancies with other samples. On the whole, the dislocation densities presented in 5 are very consistent with pure Al and Al 6082 processed by other severe plastic deformation (SPD) methods [131, 137, 144, 145]. The magnitude of the uncertainty is similar to that reported elsewhere [49, 137], and is acceptable given that the dislocation densities used in models are often estimated simply to orders of magnitude [9, 18, 19]. Assuming specimen thicknesses are relatively constant, the measurements at the very least show clear differences in dislocation densities between samples of varying levels of cold work.

**GND measurement using EBSD**

The determination of dislocation density is a classical material science problem which has resulted in a multitude of measurement techniques each associated with different strengths and weaknesses. TEM is generally the recommended technique as it enables the clear observation of individual dislocations which can then be counted directly, usually with relative ease. At the same time it reveals the substructure and composition of dislocations, cells, grain boundaries and more. TEM however is generally more suited towards determining the dislocation density at the interior of subgrains, whereas EBSD is preferred when characterising the boundary dislocation density [146]. In addition, the magnifications required for TEM means the area surveyed in each measurement is quite small. A large number of such local measurements from different areas are required in order to build towards an average resembling the bulk state. The dislocation densities in aluminium shown in Table 5.2 were calculated from the average of between 10 to 20 TEM micrographs for each sample type, which all together represents an area of around 150 to 300 $\mu$m$^2$ for each sample. In contrast, the EBSD measurements in Al 6082, shown in Figure 5.3, covers an area of around 9,000 $\mu$m$^2$.

As the main concern with TEM is the localised nature of each measurement, it was deemed constructive to perform a small comparative study in which the dislocation density in aluminium is characterised using another technique. Other methods include Vickers hardness tests [147], X-ray diffraction (XRD) profile analysis [148, 149], and the calculation of geometrically necessary dislocation (GND) densities using EBSD [150, 151]. These are indirect methods, as the first relies on mathematical formulations for the relation between hardness and dislocation density, whilst XRD and EBSD methods are based on the measurement of strain fields surrounding dislocations. The advantage however is they they are also macroscopic in nature. The EBSD approach was adopted for this study, making use of the already acquired experimental data.

The calculation of dislocation density with EBSD methods is a highly extensive topic, and the development or implementation of an in-depth model in order to obtain meticulously determined GND densities was outside the scope of this thesis. Instead, the primary goal was simply to confirm the general trends seen in the TEM measurements. Of secondary importance was confirming the dislocation density values to the same order of magnitude. The adopted approach employed methods available in the MTEX package developed for MATLAB [152]. The methods, along with a short introduction to the background theory, are described below.

Dislocations can be categorised as either geometrically necessary dislocations (GNDs) or statistically stored dislocations (SSDs) [153, 154]. SSDs consist of dipoles, multipoles, or tangles; configurations in which the net Burgers vector is close to zero and the overall lattice rotation or strain is very small. Such dislocation structures are formed through mutual random encounters which lead to trapping and storage, often in the form of tangled cell walls called incidental dislocation boundaries (IDBs). In contrast, the presence of strain fields during plastic deformation leads to the storage of GNDs, caused by the geometrical necessities of the lattice rotations. A curved or bent lattice leads to strained crystal planes, in which GNDs are bound in order to compensate for the strain whilst preserving the lattice curvature. While these dislocations may be widely distributed across the lattice, they will often gather into energetically favourable boundary configurations called geometrically necessary boundaries (GNBs), which subdivide grains into subgrains. The misorientation angle across these boundaries are what accounts for the lattice rotation. Given that the crystal orientation is measured at each data point during an EBSD scan, it is possible to calculate the lattice rotation, or strain gradient, amongst neighbouring points and consequently to deduce the GND density. As a simple rule, the GND density, $\rho_{GND}$, can be approximated following,

$$\rho_{GND} \approx \frac{1}{b}\frac{d\gamma}{dx}, \tag{3.4}$$

where $d\gamma/dx$ is the change in shear strain with distance [155]. The method adopted here for calculating the GND density is based on the approach by Pantleon [150]. First, the EBSD data is denoised with a quadratic filter as the GND calculation is very sensitive to excess orientation noise. Next, a curvature tensor is calculated from the derivative of the lattice rotation tensor with respect to the displacement in all three dimensions. Given the two-dimensional nature of EBSD measurements, only six out of the nine curvature components are known, corresponding to the x- and y-directions. At this point, dislocations are defined based on the available slip systems available, which in the case of FCC systems consists of 12 edge and 6 screw dislocations. The relative energy of screw and edge dislocations is set as [151]

$$\frac{E_{edge}}{E_{screw}} = \frac{1}{1-\nu}, \tag{3.5}$$

where $E_{edge}$ and $E_{screw}$ are line energies of edge and screw dislocations, respectively, and $\nu$ is the Poisson ratio, taken as 1/3. A combination of dislocations can be found for each spatial point which gives rise to the six known lattice curvature components. An energy minimisation scheme is run in which sets of possible solutions are found, each representing such a combination of GNDs. Out of the possible solutions, the one which results in the minimum total line energy is chosen. There may be cases where multiple solutions are possible, however in such situations the difference in dislocation density is generally small [151].

## 3.4 Summary

This chapter presented the development of a plate impact experimental platform designed for the high-precision measurement of elastic precursor amplitudes as a function of propagation distance. An overview is given of the overall experimental setup, including the operation of the single-stage gas gun, the equipment augmentations implemented to improve precision, and the design of a highly cost-efficient and quickly repeatable target construction. The challenges inherent to precursor wave measurements are described, along with the experimental reasons for requiring high vacuum, low impact tilt, and thin target glue layers. It is discussed how each of these challenges were solved through the methods and equipment developed in this project.

In addition, explanations are given of the methods used to analyse PDV velocimetry data, including how it can be applied to determine impact tilt. Finally, significant attention is dedicated to the methods used to prepare samples for EBSD and TEM characterisation, which in the case of soft materials such as aluminium and magnesium is often particularly challenging. The techniques used to estimate dislocation density are described, namely the line intercept method using TEM micrographs, and GND density calculation using EBSD data. The uncertainties associated with these methods are also discussed.

# 4

# Effects of crystal orientation on the dynamic strength of magnesium alloy

This chapter presents the work conducted on magnesium alloys, the majority of which was focused on the role of crystal orientation in Mg AZ31. Also included are the details of the investigation of grain size in Mg AZ91, which constituted a comparatively shorter study.

## 4.1 Overview and motivation

The dynamic strengths of many single crystal or pure metals is well documented across a large range of strain rates and temperatures (see Section 2.3) [23–25, 29, 31–34, 48, 84, 86]. The challenge common to these studies is the large number of physical parameters which can influence the elastic limit, including but not limited to strain rate, temperature, defect density, crystal structure, grain size and more. The prevailing approach is therefore to study idealised systems such as annealed or single crystal materials, in which the initial state is simplified and only one or two parameters like impact velocity or initial temperature are varied. In magnesium however, the behaviour is complicated even further due to the high significance of slip anisotropies inherent to the HCP crystal structure. Previous works in which these effects have been documented in single crystals or at lower strain rate are summarised in Section 2.3.3.

Magnesium alloy AZ31, which is the main subject of this chapter, is one of the most commonly employed wrought Mg alloys. It has seen increasing interest in the transportation and defense industries due to its light weight, high specific strength, and good machinability. However, the challenges encountered in its application are its poor ductility and strong directionality. The main deformation systems in AZ31 are basal, extension twinning, prismatic, and second-order pyramidal, with corresponding CRSS values around 20, 35, 55, and 80 MPa, respectively [111]. Due to these large differences in the CRSS of its available deformation modes, wrought magnesium alloy develops a strong texture during the extrusion or rolling process in which the crystallographic $c$-axes become aligned perpendicular to the extrusion direction [156, 157]. As the texture of a polycrystalline material increases, the anisotropy of the single crystal behaviour will manifest more strongly. In rolled magnesium alloy this leads to unwanted directional weaknesses where the material yields at significantly lower stresses during in-plane compression than tension at low strain rates [158]. In split-Hopkinson bar experiments, there is a similar orientation dependence on the yield stress in extruded Mg AZ31 [159].

Such behaviour greatly increases the complexity of the design and practical application of Mg alloys, meaning in-depth experimentation and modelling is necessary for their wide-spread use be enabled. The motivation for the current work is therefore in part to extend such studies of Mg alloys to the realm of shock compression. There has been a variety of high strain rate experiments on magnesium focused mainly on either the single crystal or spall behaviour [31–35, 95–102]. The results, which are reviewed in Section 2.3.3, conclusively demonstrate that the dynamic strength of magnesium is heavily dependent on the crystal orientation. Worth highlighting is a recent study by Wang et al. into the temperature dependence of polycrystalline pure Mg loaded using reverse plate impact at 100 m/s [116]. The yield stress was observed to decrease with temperature initially, and then reverse and start increasing at temperatures above 617 °C. It was noted that significant grain reorientation was being induced due to the high temperatures, thus severely obscuring the effects of the temperature

dependence itself. The reorientation was analysed using a Schmid factor-based treatment in a later paper [117], in which it was found that the initially reduced strength was likely a result of higher proportions of basal slip. However, as is discussed in Section 4.4.2, Schmid factors cannot be applied quantitatively during uniaxial strain conditions, meaning results from this type of analysis are mostly limited to qualitative inferences. Similarly, Yu et al. conducted a study on the effects of equal channel angular pressing (ECAP) on the dynamic strength of rolled AZ31 [35]. It was found that the peak elastic stress decreased after ECAP, which was also attributed to a change in grain orientations.

To summarise, it is well known that the various slip systems in magnesium display exceptionally different behaviours at high strain rates, however the consequences of this diversity are not well understood outside of purely single crystal conditions. This lack of knowledge needs to be addressed, given that anisotropy doubtlessly also has an extensive influence on the dynamic behaviour of polycrystalline materials. In fact, small manifestations of single crystal anisotropy can likely even be found in the polycrystalline shock response of much more isotropic materials such as aluminium [160]. Until these effects are better understood, the influence of factors such as cold work or temperature on HCP systems cannot be properly quantified, as both are over-shadowed by grain reorientations (as was found in the studies by Wang et al. and Yu et al. [35, 116]). Similarly, the behaviour of isotropic polycrystals in models is often simplified by selecting two slip planes at 45° to the shock, corresponding to the planes of maximum resolved shear stress [7, 9]. Extending these models to anisotropic polycrystals however requires knowledge of orientation distributions, slip plane behaviour and preferred directions of plastic shear. To this end, the current work is comprised of a series of plate-impact experiments in which the role of crystal orientation and texture is investigated in an extruded AZ31 alloy loaded at varying orientation, sample thickness and impact velocity.

A secondary study into the role of grain size was also conducted on magnesium alloy AZ91. The results of increasing the grain boundary density is of interest due to the opposing outcomes of either boundary strengthening (the Hall-Petch effect), or increased dislocation nucleation (and thus faster stress relaxation). Which of these is the case is difficult to investigate in HCP metals, due to the already discussed grain reorientations produced when attempting to refine grain sizes through cold work. This issue may be circumvented however by studying cast metals such as AZ91, in which the grain size can be reduced through the application of melt-shearing. This is a technique which increases nucleation points for grain growth during the solidifaction phase of the casting process, resulting in finer and more equiaxed grains. Crucially, this grain refinement method is accomplished without major changes to the grain orientation distribution. It was therefore possible in the study of AZ91 to directly investigate the difference between fine grained and coarse grained magnesium.

Ultimately these studies are designed to inform our knowledge of the relationship between an alloy's microstructure or processing history to its dynamic properties at engineering length-scales. The behaviour of real-world polycrystals is vastly complicated by the presence of grain boundaries, which can act as both sources or barriers to dislocations, and by distributions of glide systems all operating simultaneously. Single-crystal experiments are typically employed to circumvent these complications, and whilst their behaviour has by now been thoroughly studied, it remains to be seen to what degree the single crystal response can be used as a guide to understand anisotropic polycrystalline material behaviour.

The primary goals and novelties of this chapter can be summarised as follows:

1. Measure precursor decay in magnesium alloys AZ31B and AZ91D.
2. Investigate the effects of variations in grain orientation distribution on the dynamic yield point in Mg AZ31.

3. Contextualise the new measurements through comparison with literature investigations of the anisotropy of single crystal magnesium.

4. Evaluate the ability of Schmid factor analysis to explain the experimental results.

5. Investigate if an orientation factor for uniaxial strain conditions can be used to quantitatively evaluate the effects of crystal orientation.

6. Study the effect of grain size on the dynamic yield point in Mg AZ91.

The majority of this chapter is dedicated to the study of Mg AZ31. First, EBSD characterisation data taken from the initial sample material is discussed in Section 4.2, and the results from high strain rate plate impact experiments are described in Section 4.3. In Section 4.4, the complete data set is analysed using a novel orientation-based analysis developed during this project. Finally, Section 4.5 is focused on the results of grain refinement in Mg AZ91.

## 4.2 Material characterisation

The sample material used in the present study was prepared from a commercially-sourced extruded rod of AZ31B (3% Al, 1% Zn by weight). Electrical discharge machining (EDM) was used to cut 12.7 mm diameter specimens in which the specimen surface normals were aligned either parallel or perpendicular to the extrusion direction, hereafter denoted as ED (extrusion direction) and TD (transverse direction) samples, respectively, as shown in Figure 4.1a. The preparation steps for EBSD are discussed in detail in Section 3.3.1. Characterisation was performed with a Zeiss Merlin SEM equipped with a Bruker Quantax EBSD system and eFlash camera, operating at 20 kV. Figures 4.1b-c show results collected from representative regions of unshocked samples of both orientations. The microstructure images are taken from the plane normal to the shock direction for both specimens.

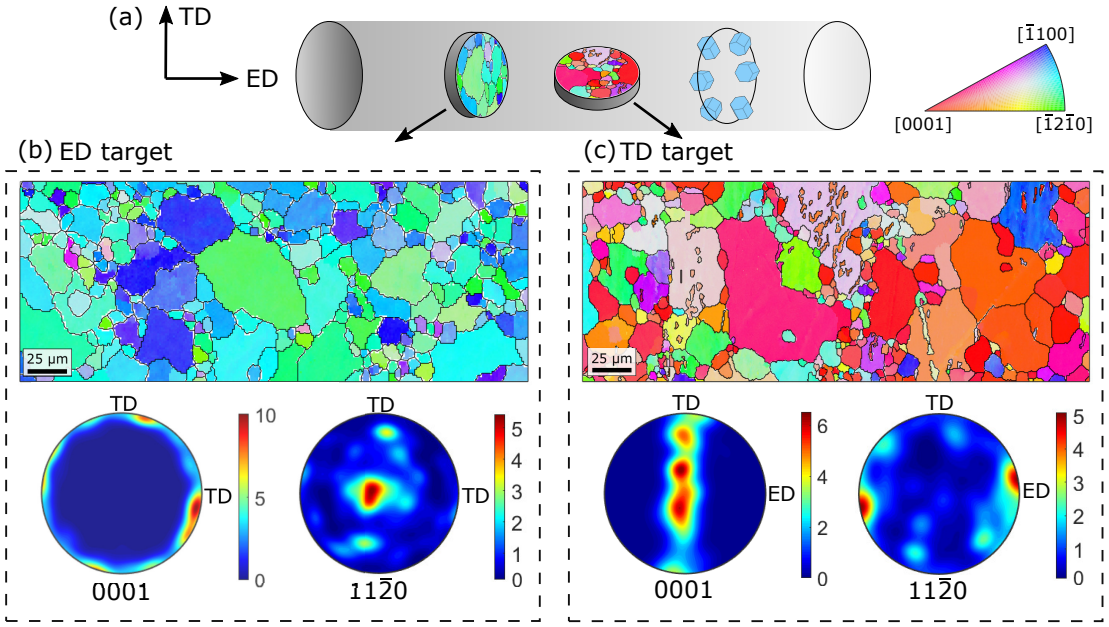



**Figure 4.1:** a) Illustration showing the orientation of the specimens, as well as the dominant orientations of the HCP crystals, with respect the source rod-stock. The sample surface normals are aligned to either the extrusion or the transverse directions, referred to as ED and TD respectively. Also shown are EBSD measurements from the b) ED and c) TD oriented samples. The maps are taken from representative regions of the samples, with an average grain size of 25 $\mu$m in both orientations. The pole figures demonstrate a strong basal texture in which the $c$-axes are closely confined to the plane normal to the ED.

The microstructure is primarily composed of grains between 10 to 50 $\mu$m in diameter, with an average grain size of 25 $\mu$m in both orientations. The extrusion process has generated a ring fibre texture typical of extruded HCP metals [156, 159, 161–163], meaning the $c$-axes are primarily distributed uniformly over the radial directions of the source rod, resulting in basal planes aligned parallel to the extrusion direction. The average angle between the basal plane normals and the extrusion direction measured in the EBSD data was 91.4°, with a standard deviation of $\sigma = 9.1°$.

High angle grain boundaries (HAGBs) and low angle grain boundaries (LAGBs) are defined by misorientations of $>$15°and 2-15°, respectively. The HAGB and LAGB densities listed in Table 4.1 are calculated using $\rho_{GB} = L/A$, where $L$ is the total length of the boundaries and $A$ is the total area of the scan. Also shown are estimated geometrically necessary dislocation (GND) densities

calculated following the method outlined in Section 3.3.3, as well as Vickers micro-hardness measurements. While these parameters are important for the analysis of aluminium in Chapter 5, here the measurement differences between the two sample variants are very minor. This emphasises that the microstructural comparison being carried out in this study on AZ31 is constrained to the changes in orientation distribution.

**Table 4.1:** Material properties of the AZ31 samples used in this study. GND densities and grain boundary densities are calculated from EBSD results. The measured material properties are found to be very consistent across both orientations.

| Sample orientation | GND density ($10^{13}$ m$^{-2}$) | HAGB density ($\mu$m$^{-1}$) | LAGB density ($\mu$m$^{-1}$) | Vickers hardness |
|---|---|---|---|---|
| ED | 1.5 | 0.16 | 0.03 | 61 |
| TD | 1.6 | 0.15 | 0.04 | 58 |

Figure 4.2 shows the distributions of Schmid factors for basal, prismatic, second-order pyramidal slip as well as extension twinning for both ED and TD targets. Given by Equation 2.15, the Schmid factor, $m$, represents the fraction of applied stress which is resolved onto a specific slip plane for a given orientation. With values ranging from 0 to a maximum of 0.5, using it to calculate the resolved shear stress is only strictly accurate under uniaxial stress conditions. Its use here is therefore restricted to simply assessing how favoured each slip system is by the orientations in the samples, which can provide guidance as to which deformation modes are most likely to activate. The distributions were calculated from combined EBSD measurements taken from multiple areas of both sample variants. The averaged Schmid factors, $m_{ave}$, as well as the area fraction of grains with Schmid factors above 0.4, $AF_{0.4-05}$, are displayed in each figure.

The ED specimens exhibit very high Schmid factors for prismatic slip ($AF_{0.4-05} = 95\%$) and twinning ($AF_{0.4-05} = 58\%$), but very low Schmid factors for basal slip ($AF_{0.4-05} = 3\%$). This is a result of the high proportion of grains with $c$-axes aligned close to perpendicular to the loading direction. The expectation is

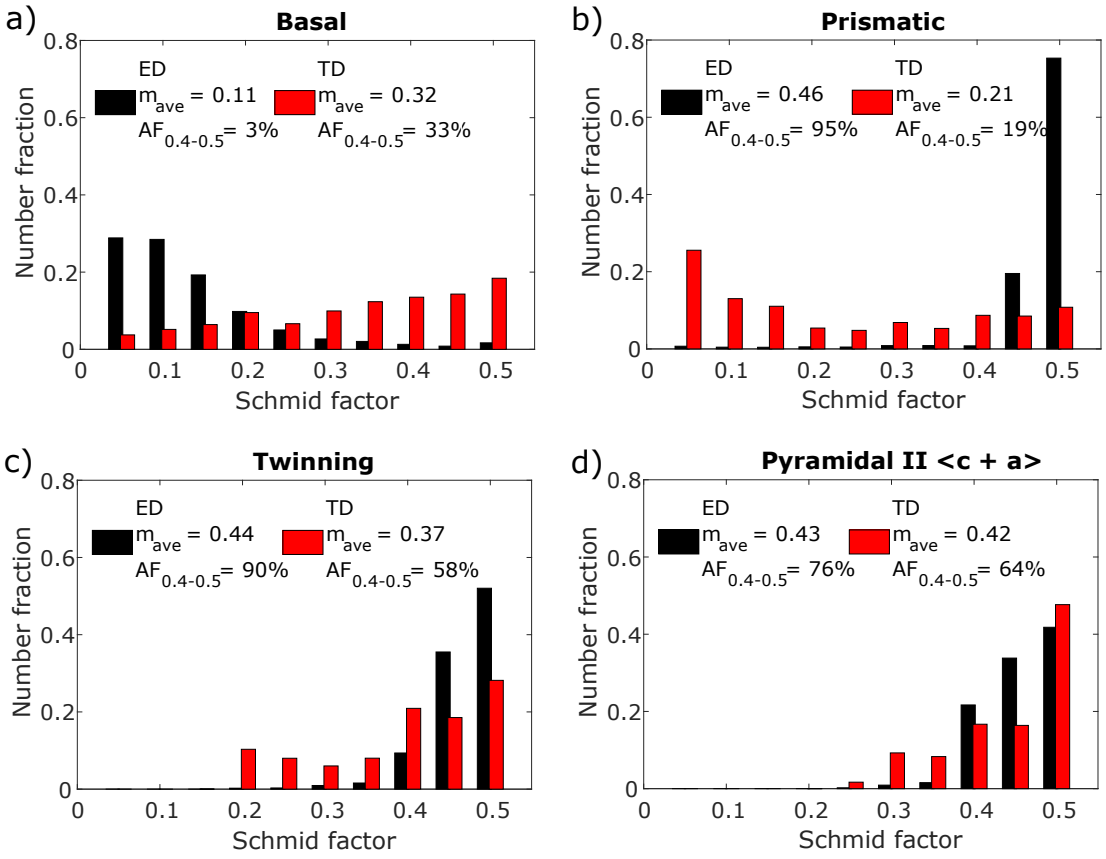



**Figure 4.2:** Schmid factor distributions for a) basal, b) prismatic, c) extension twinning, and d) second-order pyramidal slip for both ED and TD specimens. $m$ is the mean Schmid factor, and $AF_{0.4-0.5}$ is the area fraction of the samples with Schmid factors above 0.4.

therefore that a significant degree of deformation in ED targets will consist of a combination of prismatic slip and twinning. In the TD samples, the Schmid factors for prismatic slip are much lower, while those for basal slip are increased, meaning deformation is instead expected to be supplied through basal slip ($AF_{0.4-0.5} = 33\%$) and twinning ($AF_{0.4-0.5} = 58\%$).

While inspection of the pole figures alone could have yielded similar expectations, it could not have predicted the degree to which the samples are also well oriented for pyramidal slip. In fact here the intricacies of the Schmid analysis start to appear, as one notes that $m_{ave}$ for the pyramidal slip plane is higher than basal slip in the TD samples (this is also the case for first order $\langle a \rangle$ and first order $\langle c + a \rangle$ slip, not shown here). There is a significant fraction of grains in the TD specimen in which the $c$-axes are near parallel to the loading direction,

meaning dislocations with $\langle a \rangle$ Burgers vectors are difficult to activate. This could potentially leave pyramidal slip or contraction twinning as the favoured options in a large number of grains. By extrapolating from single crystal results (in which $c$-axis loading has the highest yield points) one might therefore expect the overall yield point of the TD samples to be of similar magnitude or even higher than the ED samples. However, lower strain rate experiments of extruded rod has shown that the much lower CRSS for basal slip tends to be the dominating factor in these scenarios, producing much higher basal slip activity despite the less optimal orientations of the basal planes in many grains [159, 164]. In fact a high degree of basal slip may also occur in the ED specimens, for the same reason. Whether this is also the case during high strain rates is an open question and cannot be answered purely through Schmid analysis.

## 4.3 Plate impact experiments

A total 12 experiments were carried out at thicknesses between 0.45 mm and 2.3 mm and at elastic impact stresses between 1.4 and 3.3 GPa, and are shown in Table 4.2. The design and implementation of these gas gun shots is described in detail in Chapter 3, and is briefly summarised here.

The usage of plate impact experiments to acquire accurate measurements of precursor states requires low tilt during impact and high flatness and parallelism in the flyer and target plates. This ensures that the very short rise-times of the elastic wave are not smoothed out by ramp-effects caused by poor tilt. To this end, each Mg target was diamond turned on both sides down to its final thickness, shown in Table 4.2, with a final surface planarity of less than 0.1 mrad. The 2 mm thick $c$-cut sapphire drivers and flyers were parallel to less than 0.2 mrad. To achieve thin and even glue layers, a spin-coating method was used to apply adhesive to the sapphire drivers prior to bonding the targets. The glue layers were measured optically to be less than 1 $\mu$m thick, thus ensuring a parallel driver-target interface. A schematic of the final target assembly is shown in Figure 3.8. The

| Expt no | Orientation | Sample thickness (mm) | Impact velocity (m/s) | Elastic impact stress (GPa) | Peak elastic stress (GPa) |
|---|---|---|---|---|---|
| 1 | ED | $0.443 \pm 0.001$ | $396 \pm 1$ | 3.4 | $0.93 \pm 0.07$ |
| 2 | ED | $1.002 \pm 0.001$ | $398 \pm 1$ | 3.4 | $0.69 \pm 0.06$ |
| 3 | ED | $2.002 \pm 0.001$ | $401 \pm 1$ | 3.4 | $0.53 \pm 0.04$ |
| 4* | ED | $2.264 \pm 0.003$ | $463 \pm 3$ | 2.5 | $0.47 \pm 0.04$ |
| 5* | ED | $2.263 \pm 0.002$ | $283 \pm 3$ | 1.4 | $0.42 \pm 0.04$ |
| 6a | TD | $0.449 \pm 0.001$ | $399 \pm 1$ | 3.4 | $0.33 \pm 0.03$ |
| 6b | TD | $0.451 \pm 0.001$ | $399 \pm 1$ | 3.4 | $0.35 \pm 0.03$ |
| 6c | TD | $0.452 \pm 0.001$ | $397 \pm 1$ | 3.4 | $0.38 \pm 0.03$ |
| 7 | TD | $1.071 \pm 0.001$ | $402 \pm 1$ | 3.4 | $0.27 \pm 0.03$ |
| 8 | TD | $1.999 \pm 0.001$ | $396 \pm 1$ | 3.4 | $0.22 \pm 0.02$ |
| 9* | TD | $2.272 \pm 0.001$ | $477 \pm 3$ | 2.5 | $0.20 \pm 0.02$ |
| 10 | TD | $2.253 \pm 0.001$ | $165 \pm 1$ | 1.4 | $0.20 \pm 0.02$ |

**Table 4.2:** Experimental parameters and measured yield points for the Mg AZ31 plate impact experiments. *Experiments were conducted in a symmetric impact configuration using AZ31 flyers.

plate impact experiments were performed using a 32 mm bore single stage gas gun, with which the target assembly was impacted at velocities between 280 and 460 m/s using $c$-cut sapphire flyers.

Free surface velocity histories were obtained using downshifted PDV operating around a base frequency of 4 GHz [165], making use of amplified low-noise detectors and oscilloscopes sampling at 40 GS/s. The front surfaces of the flyers were flash coated with $<$100 nm of Al, from which impact velocities were measured as shown in Table 4.2. The rear surface of the driver was also coated, enabling velocity histories to be measured at three equidistant locations on the driver. This was used to determine adequate impact tilt (around 1.5 mrad or less) and shock arrival times at the driver-target interface. The velocity of the elastic wave was calculated from the transit time between the front and rear sample surfaces. The experiments were conducted under vacuum levels between 10 and 40 mtorr, minimising any effects of air-ramps ahead of the shock. Note that three experiments (numbers 4,5 and 9) with 2.3 mm thick targets were instead performed in a symmetric impact configuration using AZ31 flyers cut in the ED orientation (impact pressures were matched to the sapphire experiments).

The elastic impact stress is here calculated using the intersection of the elastic longitudinal stress-particle velocity Hugoniots for c-cut sapphire and AZ31 [15, 166]. The PDV for each shot was processed with STFT methods as outlined in Section 3.2.1 using a window length of 64 points with 50% overlap, corresponding to a time-step of 0.8 ns. Free-surface velocity profiles, corresponding to break-out of the structured shock-wave at the sample rear surface, are calculated from a Gaussian fit to the power spectrum at each time-step. The specular target surfaces, along with the use of low-reflectance optical probes, resulted in the complete absence of a baseline signal in the majority of the present experiments (as shown by the example in Figure 3.11). This is optimal when attempting to resolve low velocity signals which could otherwise be obscured. Only in experiments 4, 5 and 9 was a small baseline detected. For these experiments the baseline was reduced by subtracting a sinusoid which was fitted by minimising the total power in the signal [165]. To demonstrate the repeatability of the experiments, three shots with the same experimental parameters were performed on the 0.45 mm TD samples, as these featured the most difficult to distinguish elastic stresses (experiments 6a-c).

The combined wave profiles measured in the impact experiments are shown in Figure 4.3, with loading orientation, thickness and elastic impact stress as indicated in the figures. Note that experiments 6b and 6c are not plotted as these were repeats of experiment 6a and exhibited very similar velocity response. The elastic precursors are clearly revealed in all experiments, demonstrating the expected decrease in the peak of the elastic wave with increasing propagation distance. There is also strong evidence of large differences in time-dependent effects in the two target orientations, as evidenced by the different decay rates.

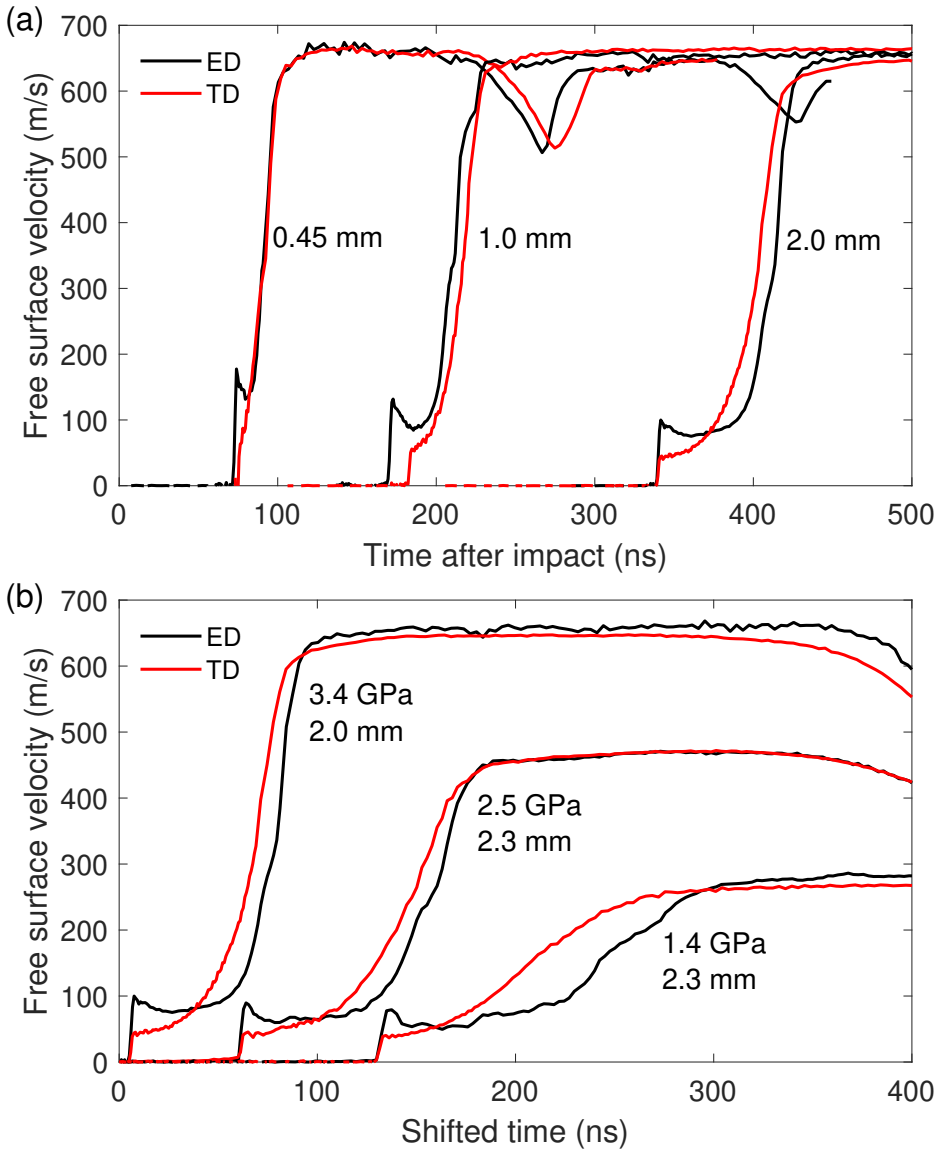



**Figure 4.3:** a) Rear surface velocity histories of the ED (black) and TD (red) Mg AZ31 specimens at 3.4 GPa. Thicknesses are shown next to each pair of velocity traces. Time at t = 0 is at impact of the front surface of the specimens. The velocity traces clearly display decay of the precursor wave with distance, as well as significantly higher elastic stresses in the ED orientation. The TD 1.0 mm profile is displaced slightly when compared to the ED 1.0 mm breakout time due to a slightly larger thickness. b) Comparison of velocity traces at 2.0 - 2.3 mm thickness (experiments 3-5, 8-10), at varying impact velocity. The elastic impact stress and thickness is shown next to each pair of velocity traces, and time has been shifted for clarity. A slight decay in peak elastic velocities is observed for decreasing shock stress.

The peak elastic stresses, shown in Table 4.2, were calculated using the standard expression,

$$\sigma_y = \frac{1}{2}\,\rho_0\,c_l\,u_{fs}, \tag{4.1}$$

where $\rho_0$ = 1.77 $\pm$ 0.01 g/cm$^3$ is the unshocked density [96], $c_l$ = 5.92 $\pm$ 0.05 mm/$\mu$s is the longitudinal sound speed, and $u_{fs}$ is the free surface velocity at the precursor peak (uncertainty taken as 3 m/s). The longitudinal sound speed was taken as the average of the elastic wave speed measurements, which were consistent across all thicknesses and orientations and resulted in good agreement with similar measurements in the literature [33, 96]. The uncertainty in the elastic stress is calculated through error propagation (thin sample peaks are extracted with slope fitting [167]).

At the highest impact stress it is observed that the elastic states in the ED orientation decay to almost half their starting value, from 895 MPa to 505 MPa, over the examined propagation distance. In the TD orientation on the other hand they only decrease by about a third, from 330 MPa to 210 MPa, and are also less than half the magnitude than ED experiments across all thicknesses (the ratio of ED to TD starts out at 2.7 and decreases to around 2.3). The TD configuration thus exhibits not only significantly lower elastic limits, but also a notably faster wave attenuation, already reaching elastic stresses close to the steady state precursor stress even in the thinnest sample. The rise-time of the plastic portion of the wave profiles also increases with increasing propagation distance and with decreasing impact velocity. The rise-times of the precursor waves are all on the order of the time resolution of the experiments.

For loading along ED, a spike consisting of a strong peak followed by an abrupt velocity pull-back is observed in all experiments. The shape of these curves is qualitatively very similar to previous results of shock compression along both the $c$-axis and $a$-axis in magnesium single crystal [31–33]. Such drops in stress have been theorised to be due to a lack of dislocations in the material leading to

intense multiplication of mobile dislocations at the onset of yielding [12]. This is in contrast to compression along TD, where there is no evidence of any velocity relaxation behind the elastic peak. Along with the faster decay rate, this behaviour is more akin to the precursor profiles in 45° single crystal [31, 34]. There were also no observations of spikes in alloys Elektron 675 and Ma2-1 [31, 100, 101], nor in ECAE-processed AZ31 [96, 102].

In the case of Ma2-1, the lack of a precursor spike was theorised to be due to an already high dislocation density in the initial state of the alloy [31]. However, both spike and and non-spike precursors were observed in the same material in the present results. The reason for the spike in the ED targets is probably not due to a difference in dislocation density compared to the TD samples, as the GND density (and most likely also the total dislocation density) was measured as being very similar in both (see Table 4.1). The results of variations in dislocation density is the main topic under investigation in Chapter 5, from which it can be deduced that even if dislocation densities are not equal, there would likely have to be exceedingly large (order of magnitude) differences across the two sample orientations in order to explain such a large discrepancy in the yield points. It will here be assumed that the dislocation densities are close to equal in both orientations.

Consequently, it is probable that the appearance of a spiked precursor wave in ED targets is instead caused by differences in dislocation mobility in the active deformation modes. Compared to the other slip systems, the very low CRSS of basal slip should greatly facilitate the movement of pre-existing dislocations in order to accommodate the imposed stress. Indeed, out of the shocked single crystal experiments in previous studies, the only orientation without a precursor spike was the one aligned for basal slip. Presumably there is a lack of need for intense dislocation multiplication along this loading configuration. Similarly, TD samples were favourably oriented for basal slip, whilst ED specimens were not (as shown in Figure 4.2). It is theorised that samples in which a significant population of grains

are able to deform through basal slip will be able to accommodate the precursor stress through the motion of pre-existing dislocations, without the need to support stress relaxation through intense multiplication initiated at higher shear stresses. This analysis is supported by the numerical modelling detailed in Section 5.7.3, in which a lowered mobility or dislocation nucleation rate causes the appearance of a precursor spike in simulated velocity profiles. While grain orientations were not measured in the Ma2-1 study, it was reported that the material was annealed prior to shock loading, which implies a higher degree of randomisation or lower texture [168]. As a result, it is likely that a significant population of grains were loaded at angles around 45° to the $c$-axis, similar to the TD samples in the present study.

The results in Figure 4.3b also indicate that for similar thicknesses there is a slight decrease in the peak elastic amplitude with decreasing elastic impact stress. This is especially evident when comparing experiments 4 and 5 on the 2.3 mm ED targets at 2.5 GPa and 1.4 GPa. In the TD targets however the change is smaller than the measurement error. The change in elastic state with impact stress observed in the ED orientation is significantly larger than what was observed in extruded AZ61 also impacted in the ED orientation [98], or in ECAE processed AZ31 [96] (although both were measured at higher thickness). Note that it was also reported that a minimal-to-no shift in elastic stress was seen with decreasing impact stress for both $a$-axis magnesium [33] and Elektron 675. In $c$-axis magnesium, the converse was observed, where decreasing impact stress was in fact associated with an increase in the elastic stress [32]. No such unusual increase in the elastic stress is observed for either impact orientations in the present data.

## 4.4 Discussion

### 4.4.1 Propagation distance and strain rate dependence

To further analyse the role of texture and crystal anisotropy, the measured elastic stresses are plotted against propagation distance in Figure 4.4 and compared directly with literature data. The dashed curves represent power law fits to either the current results at 3.4 GPa, or the single crystal (SC) data. It is found that the yield points are located at intermediate pressures between those found in SC experiments. The yield points for ED targets match the slope of the $\{10\bar{1}1\}$ or $a$-axis loaded SC reasonably well, but at a consistently higher pressure. The same is observed for TD targets when compared to SC impacted at 45° to the $c$-axis. Elastic stresses from TD tests are also in reasonable agreement with Yu's study of rolled AZ31 [35], however it should be noted that Yu's experiments were performed by impacting along the rolling direction, similar to ED loading in the present study. Given the texture similarities between the present samples and what was used in Yu's study, this discrepancy is at present difficult to explain. Comparison of the 2.5 and 1.4 GPa impact stress experiments to the 3.4 GPa trendlines demonstrates a significant reduction in elastic state with decreasing impact stress in the ED case, and a slight decrease in the TD samples.

Note that the primary active slip systems in the elastic peaks of the single crystal experiments at 0°, 45° and 90° to the $c$-axis were pyramidal $\langle c+a \rangle$, basal and prismatic respectively [31–34]. According to the EBSD data the loading angle in the majority of grains in the ED samples was around 90° to the $c$-axis. Comparing the alloy and SC yield points and orientations therefore lends credence to the Schmid factor calculations in Figure 4.2 showing that there is a high degree of prismatic slip or twinning in ED loading. The higher yield in the alloy can possibly be explained as strengthening effects caused by grain boundaries and alloying elements. Similarly, one may draw the initial conclusion that the TD samples likely display a higher degree of basal slip.

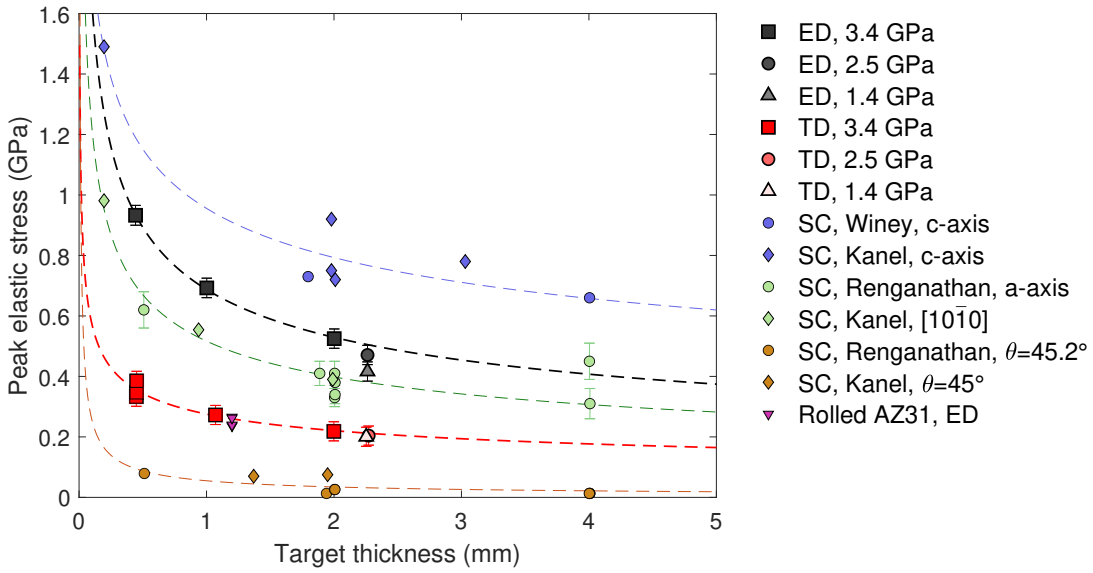



**Figure 4.4:** Peak elastic stress plotted against sample thickness in all of the present data, compared to previous results from single crystal Mg shock experiments along the $c$-axis [31, 32], $a$- or $\{10\bar{1}0\}$-axis [31, 33], and at 45°to the $c$-axis [31, 34]. Also plotted are results from rolled AZ31 impacted in the ED orientation [35]. Any absent error bars are equal to or smaller than the size of the data points. Dashed lines represents power law fits to the available data in either the current or single crystal experiments.

Comparison of the 2.5 and 1.4 GPa impact stress shots (at 2.3 mm) to the 3.2 GPa trendline clearly demonstrates that the lowered elastic stress is caused not only by the slight additional propagation distance (compared to the 2 mm experiment) but also due to the reduced impact stress. In order to form a more complete picture which includes the lower impact stress experiments, the elastic stress is instead plotted versus the strain rate, $\dot{\epsilon}_p$, for the present results in figure 5.17. Specifically, the initial plastic strain rate at the onset of plastic flow is used, as this is considered indicative of the plastic strain rate experienced at the elastic limit. The initial plastic strain rate is here defined as [23],

$$\dot{\epsilon}_p = \frac{du_p/dt}{c_l} \equiv \dot{\epsilon}_p\Big|_{u_{E,min}}^{2u_{E,max}}, \tag{4.2}$$

where $u_p$ is the particle velocity, and $u_{E,min}$ is the particle velocity at the base of the plastic wave. Following Smith's method [23], the values for $u_{E,min}$ are taken from the peak in the TD velocity profiles, and from the bottom of the velocity

pull-back in the ED profiles. The definition of initial plastic strain rate used here encompasses the strain experienced by the target from the transition to the plastic wave at $u_{E,min}$, up to $2 \times u_{E,min}$. This measure of strain rate is indirectly dependent on the target thickness: for larger thicknesses there is more time for elastic-plastic wave separation and dispersion to occur, and thus for the plastic portion of the wave to extend. As the rise-time of the plastic shock becomes increasingly gradual, the initial plastic strain rate is lowered. The same effect is also achieved by lowering the impact velocity: as the peak shock stress and therefore the plastic wave speed is lowered, the wave separation at a given thickness also increases. The end result is that the elastic stress from all of the experiments at both varying thickness and impact velocity is demonstrated to be reasonably fitted to a power law of the form $\sigma_y = \sigma_0 \dot{\epsilon}_p^n$, where $\sigma_0$ and $n$ are the fitting parameters, leading to,

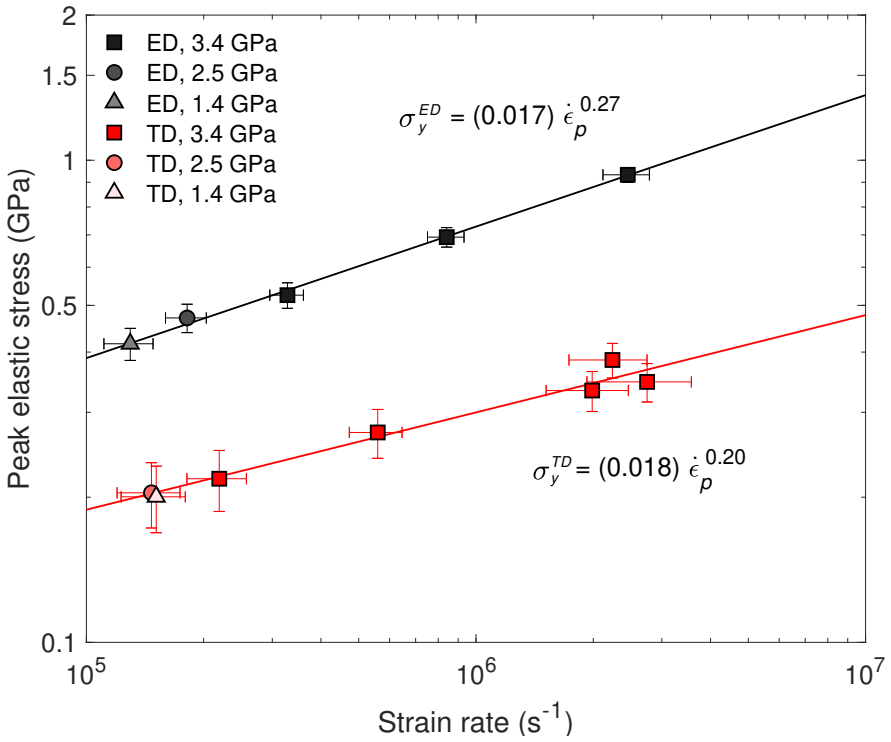



**Figure 4.5:** Peak elastic stress versus initial plastic strain rate, calculated using equation 4.2. The data is fitted to power laws, plotted as the black and red lines. It is observed that the strain rate dependence is more pronounced in the ED than in the TD targets, probably tied to a reduced mobility in the slip planes which are active during ED loading.

$$\sigma_y^{ED} = (0.017)\,\dot{\epsilon}_p^{\,0.27\pm0.02}, \tag{4.3}$$

for the ED orientation, and,

$$\sigma_y^{TD} = (0.018)\,\dot{\epsilon}_p^{\,0.20\pm0.04}, \tag{4.4}$$

for the TD orientation. Note that the velocity histories of the 2.4 and 1.5 GPa experiments in the TD direction effectively overlap in the initial rise of the plastic wave. This explains their close to identical peak elastic stresses, as the strain rate at the onset of plastic deformation was also the same. In quasistatic studies on AZ31 in the plastic strain rate regime of $10^{-3}$ to $10^{-1}$ s$^{-1}$, the dependence of the flow stress on the strain rate, $\sigma \propto \dot{\epsilon}_p^{\alpha}$, has values of $\alpha < 0.01$ at room temperature [169]. There is therefore a significant upturn in the strain rate sensitivity of the flow stress at higher strain rates, which has commonly been observed to occur around $10^3 - 10^4$ s$^{-1}$ in both FCC metals such as copper [170], as well as in AZ31 [171].

It is observed that the strain rate sensitivity is lower in the TD than in the ED orientation. This is again likely due to the higher fraction of basal slip in TD targets, which has been shown to be completely rate insensitive at lower strain rates [43]. Indeed, MD simulations show that dislocation mobility is the highest in basal plane, followed by prismatic, and with pyramidal having by far the lowest mobility [172]. In other words, the shear stress needed to for example reach a dislocation velocity of 1 mm/$\mu$m in the prismatic plane is about twice that of the basal plane [172]. Model analysis of the effects of dislocation mobility on the decay rate can be found in Section 5.7.3, in which it is shown that decreasing the mobility causes slower precursor attenuation. In short, as loading rates reach $10^5$ s$^{-1}$ and more, the time-window for dislocation-based stress relaxation mechanisms decreases, meaning the slip plane's ability to reach towards higher dislocation velocities becomes increasingly important. High dislocation velocity can be attained in the basal plane without much increase in the resolved shear stress, however in e.g. the

pyramidal slip plane, progressively higher shear stresses are needed before release can be initiated. The end result is that the yield stress is highly dependent on the strain rate in samples with a high portion of non-basal slip activity. Equivalently, when plotted against thickness, the ED samples display significant decay of the precursor stress up to high propagation distances. The TD specimen on the other hand decays quickly within the region close to the impact surface, and is almost at equilibrium by 1 mm thickness.

To summarise, the explanation for the contrasting dynamic behaviour in the ED and TD orientations likely lies in the activation of disparate deformation systems. Given that basal slip has by far the lowest CRSS, yielding in magnesium can most easily occur in grains where the basal planes have the highest Schmid factor, i.e. oriented 45° to the loading direction. As was shown in the EBSD measurements in Section 4.2, such grains primarily exist only in the TD orientation. However, the overall distribution of grain orientations and Schmid factors suggests it is unlikely that the TD specimens are able to deform through basal slip alone. Similarly, analysis of the peak elastic stress and Schmid factors in ED specimens showed that they are likely to deform through some combination of prismatic slip, twinning, and perhaps also basal slip. What is currently left unanswered by this analysis however are the exact proportions of activity which can be attributed to each deformation system. It is unknown whether basal slip induces a significant softening of dynamic yield in ED orientations, or if pyramidal slip strengthens the TD specimens. Indeed the effective yield point likely consists of a bulk average which is a function of all active deformation mechanisms, and their respective activation stresses, across the entire population of grains. A quantitative investigation of this hypothesis requires a deeper analysis, one which can account for the entire distribution of grain orientations and predict the deformation mode in individual grains based on its angle. The development of this orientation-based analysis will be the main focus for the remainder of this chapter.

### 4.4.2 Calculation of shear and activation stress as function of loading direction

It is clear that detailed knowledge of the microstructure in each loading orientation may provide further insight into its mechanical response. The present material's grain orientations led to the qualitative conclusion that basal slip should be the dominant slip system for TD samples, while prismatic slip and twinning are dominant in the ED samples. As basal slip has by far the lowest CRSS, this provided a preliminary explanation for why the yield point is lower in the TD than in the ED orientation.

If this assumption is correct, then it is also noteworthy that the yield points of the TD and ED samples are both higher than their single crystal counterparts deforming, respectively, under basal slip or prismatic slip/twinning. It is unknown to what extent the higher yield of the current polycrystalline samples can be attributed to alloy strengthening on the one hand, and orientation distribution effects on the other. In the latter case, the strength contribution could originate from grains oriented far from an ideal loading angle, thus enduring higher applied stresses and potentially activating higher threshold relaxation mechanisms. If the influence of such grains is small, then detailed knowledge of the crystallographic orientation distribution would be unnecessary. The higher yield points of the alloy samples could in that case simply be attributed to the increase in the CRSS of their respective dominant slip systems.

A more rigorous analysis is needed in order to conclusively determine the influence of the initial microstructure, alloy strengthening, and the active deformation modes at the onset of high strain rate plastic flow. To this end, a framework is presented in which a high strain rate orientation factor is calculated for each potential slip plane as a function of the grain orientation. Coupled with a rate-adjusted dynamic CRSS for each slip or twinning system, as well as a series of simplifying assumptions, this permits an analysis of which deformation modes

will activate during the initial transition to plastic deformation at the elastic peak. It also gives insight into the overall degree to which the measured elastic wave amplitudes are governed specifically by crystallographic orientation.

**Derivation of dynamic orientation factor**

To begin with, the resolved shear stress at the elastic wave front has to be calculated in each relevant slip or twinning system for an arbitrary crystal orientation. The following calculations build on the works by Johnson and Pope [173–176], and are here extended to incorporate the full angular dependence of the resolved shear stress in the basal, prismatic, second-order pyramidal and extension twinning planes in magnesium. For consistency, the coordinate systems and definitions chosen here are based on those used by Pope [176]. Compression twinning and other pyramidal systems are here ignored due to the availability of the lower threshold mechanisms.

As this analysis is limited to the elastic regime, it is first assumed that the stress in the precursor wave can be described by the elastic strain according to Hooke's law,

$$\sigma_{ij} = C_{ijkl}\epsilon_{kl}, \tag{4.5}$$

where $\sigma_{ij}$ and $\epsilon_{kl}$ represent the components of the stress and strain tensors respectively, and $C_{ijkl}$ are the components of the elastic stiffness tensor. As Equation 4.5 is valid for any arbitrary coordinate system, it is possible to define three separate coordinate systems from which the stresses in the shock frame can be transformed to the crystal and slip system frames.

First, the crystallographic coordinate system, $x_i$, is chosen as shown in Figure 4.6 such that the $x_1$ axis coincides with the $a$-axis and $x_3$ coincides with the $c$-axis. The shock coordinate system, $x_i'$, is defined with the direction of shock propagation

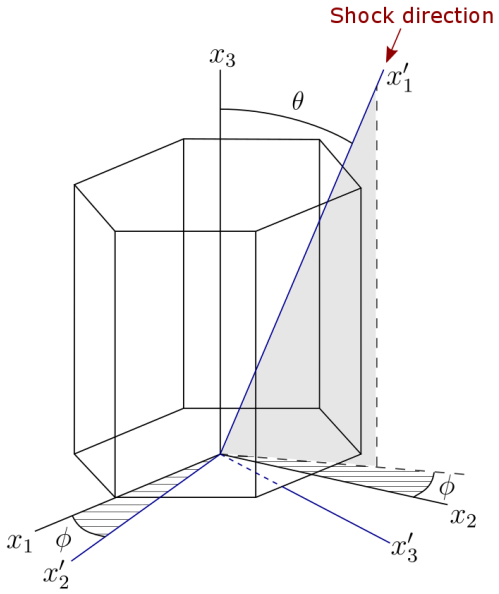



**Figure 4.6:** Definitions of the crystallographic, $x_i$, and shock, $x_i'$, coordinate systems. The $c$-axis is denoted as $x_3$ and the $a$-axis as $x_1$. The direction of shock propagation is given by $x_1'$, which makes an angle $\theta$ with $x_3$. $x_2'$ and $x_3'$ are within the plane parallel to the shock front, with $x_2'$ constrained to the $x_1$, $x_2$ (basal) plane. $\phi$ is given by the angle between $x_2'$ and $x_1$, or equivalently by the angle between $x_2$ (the $10\bar{1}0$ axis) and the projection of $x_1'$ onto the basal plane.

along the $x_1'$ axis, forming an angle $\theta$ to the $x_3$ axis. As the $x_2'$ and $x_3'$ axes can be assigned to any arbitrary orientation within the plane parallel to the shock front, the $x_2'$ axis is chosen to always be constrained to the basal plane. From this one can define an angle within the basal plane, $\phi$, formed between the $x_2'$ axis and the $x_1$ axis. In all cases the axes are chosen to form right-handed coordinate systems, and by always assigning $x_1$ to the $a$-axis closest to $x_2'$, the above constraints result in a set of rules for orienting the $x_i$ coordinate system of any grain. The third set of coordinates, $x_i''$, is chosen such that $x_1''$ is in the slip direction and $x_3''$ is normal to the slip plane of interest. Finally, let $\hat{e}_i$, $\hat{e}_i'$ and $\hat{e}_i''$ be the unit vectors in the $x_i$, $x_i'$ and $x_i''$ directions respectively. Following this, matrices of direction cosines are defined which relate the three coordinate systems,

$$a'_{ij} \equiv \hat{e}'_i \cdot \hat{e}_j, \tag{4.6}$$

$${}^{\alpha}a''_{ij} \equiv {}^{\alpha}\hat{e}''_i \cdot \hat{e}_j, \tag{4.7}$$

$${}^{\alpha}a'''_{ij} \equiv {}^{\alpha}\hat{e}''_i \cdot \hat{e}'_j. \tag{4.8}$$

The presuperscript $\alpha$ is used to differentiate between different slip or twin systems. Conditions of uniaxial strain are applied, in which $\epsilon_{22} = \epsilon_{33} = 0$, and transverse stresses are symmetrical. Using the above definitions, Hooke's law is written in terms of the shock coordinate system as,

$$\sigma'_{mn} = C'_{mn11}\,\epsilon'_{11}, \tag{4.9}$$

where the elastic stiffness tensor in the shock frame is transformed from the crystallographic coordinate system using,

$$C'_{mnpq} \equiv a'_{mi}\,a'_{nj}\,a'_{pk}\,a'_{ql}\,C_{ijkl}. \tag{4.10}$$

The validity of the assumption of uniaxial strain conditions during the elastic portion of the shock wave is addressed later in this section. The shear stress in a specific slip or twinning system, $\tau_\alpha$, can be determined from the stress tensor using,

$$\tau_\alpha = {}^{\alpha}a'''_{1m},\,{}^{\alpha}a'''_{3n},\,\sigma'_{mn}. \tag{4.11}$$

A dynamic orientation factor, $\overline{m}$, analogous to a Schmid factor for uniaxial strain conditions, can now be defined as the ratio between the resolved shear stress in a given deformation system, and the applied longitudinal stress. Using equations 4.6-4.11, this can be written as

$$\overline{m} = \frac{\tau_\alpha}{\sigma'_{11}} = \frac{1}{C'_{1111}}(a'''_{1m}\,a'''_{3n}\,C'_{mn11}). \tag{4.12}$$

By calculating the components of the $a'''_{ij}$ matrices, Equation 4.12 can be used to find the resolved shear stress along every slip or twinning system within a grain of arbitrary orientation relative to the impact direction.

The validity of the assumption of uniaxial strain used in deriving Equation 4.12 should be addressed. Elastic and plastic anisotropies may both independently result in transverse particle motion during plane impact loading. The condition of uniaxial strain during elastic compression is therefore only fully satisfied in cases where purely longitudinal elastic disturbances can be propagated. Impacts

at other angles will result in transverse particle motion due to the propagation of quasi-longitudinal (QL) and quasi-transverse (QT) waves. It is possible however to calculate the ratio between the stresses behind such waves in a linear elastic medium [173] as a function of the loading angle. This in turn can be used as a measure of the error in the stress in Equation 4.12, caused by the departure from single longitudinal wave motion and thus uniaxial strain conditions. This error is plotted in Figure 4.7.

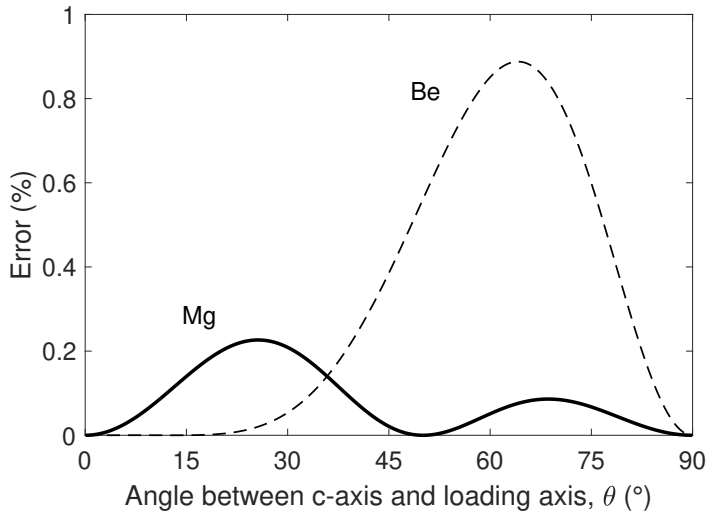



**Figure 4.7:** Error in the elastic wave amplitude caused by the uniaxial strain assumption, calculated following the methods used by Johnson [173]. As a comparison the same calculation is performed for Be, which is the material studied by Pope and Johnson [176].

For magnesium it is found that the only cases of pure uniaxial strain are during plane impact either parallel, perpendicular or at 50.1° to the $c$-axis. However, the maximum error calculated in this fashion is only 0.22% at 25°, and lower at all other angles (going to zero at $\theta$=0°, 50.1° and 90°). Anisotropic elastic effects are therefore negligible in the case of Mg, and like other hexagonal materials such as Be and Ti can be treated as elastically isotropic, meaning the uniaxial strain approximation is reasonable. Note that elastic anisotropy has been shown to be significant in other materials such as quartz [173], so care should be exercised before applying this approximation to other materials. It is likewise not valid in

the plastic regime, in which the QL and QT waves caused by plastic anisotropy in magnesium have been clearly observed before [31, 34]. Magnesium may therefore be approximated as an elastically isotropic, plastically anisotropic solid, which under shock loading in a low symmetry direction will cause the propagation of a single elastic wave. Here the focus is on the elastic wave, and no attempt is made to extend the current analysis beyond the initial yield point.

Given Equation 4.13 and the definition of the coordinate systems as shown in Figure 4.6, the first of the matrices of direction cosines, $a'$, is given by,

$$a' = \begin{bmatrix} \sin\theta\sin\phi & \sin\theta\cos\phi & \cos\theta \\ \cos\phi & -\sin\phi & 0 \\ \cos\theta & \cos\theta\cos\phi & -\sin\theta \end{bmatrix}. \tag{4.13}$$

The second transformation matrix, ${}^{\alpha}a''$, describes the relationship between the crystallographic and slip or twin system coordinates. Due to the rotational symmetry of the HCP lattice, the components of ${}^{\alpha}a''$ depend on the choice of Burgers vector for a given deformation mode. Below, the ${}^{\alpha}a''$ matrices are given for one each of the possible basal, prismatic, pyramidal and twinning directions. In the case of basal slip, by selecting slip in the $[\,1\ 0\ 0\,]$ direction (in $x_i$ coordinates) one finds,

$${}^{bas}a'' = \begin{bmatrix} 1 & 0 & 0 \\ 0 & 1 & 0 \\ 0 & 0 & 1 \end{bmatrix}. \tag{4.14}$$

Similarly, prismatic slip in the $[\,\overline{1}\ 0\ 0\,]$ direction gives,

$${}^{prism}a'' = \begin{bmatrix} -1 & 0 & 0 \\ 0 & 0 & 1 \\ 0 & 1 & 0 \end{bmatrix}. \tag{4.15}$$

Pyramidal slip along $[\,\overline{B}\ \ 0\ \ Br\,]$ gives,

$${}^{pyra}a'' = \begin{bmatrix} -B & 0 & Br \\ 0 & -1 & 0 \\ Br & 0 & B \end{bmatrix}, \tag{4.16}$$

where $r = 1.604$ is the $c/a$ ratio for magnesium, and $B = (1 + r^2)^{-1/2}$. Finally, extension twinning along $[\,0\ \ -\sqrt{3}D\ \ Dr\,]$ gives,

$$ {}^{twin}a'' = \begin{bmatrix} 0 & -\sqrt{3}D & Dr \\ 1 & 0 & 0 \\ 0 & Dr & \sqrt{3}D, \end{bmatrix} \tag{4.17} $$

where $D = (3 + r^2)^{-1/2}$. Using Equations 4.12-4.17, the shear stresses in each of the slip and twinning systems of interest can now be calculated as a function of loading direction, leading to,

$$ {}^{bas}\overline{m} = \left| \frac{\tau_{bas}}{\sigma'_{11}} \right| = \left| \frac{1}{C'_{11}} \left( \frac{1}{2}(C'_{11} - C'_{13}) \sin 2\theta + C'_{15} \cos 2\theta \right) \times \sin(\phi + \beta) \right|, \tag{4.18} $$

$$ {}^{prism}\overline{m} = \left| \frac{\tau_{prism}}{\sigma'_{11}} \right| = \left| \frac{1}{2C'_{11}} \left( C'_{12} - C'_{11} \sin^2\theta - C'_{13} \cos^2\theta - C'_{15} \sin 2\theta \right) \times \sin 2(\phi + \beta) \right|, \tag{4.19} $$

$$ {}^{pyra}\overline{m} = \left| \frac{\tau_{pyra}}{\sigma'_{11}} \right| = \left| \frac{B^2}{C'_{11}} \Big( C'_{13}F_1F_2 - C'_{11}F_3F_4 + C'_{15}(F_2F_3 - F_1F_4) - C'_{12}r\cos^2(\phi + \beta) \Big) \right|, \tag{4.20} $$

$$ {}^{twin}\overline{m} = \frac{\tau_{twin}}{\sigma'_{11}} = \frac{D^2}{C'_{11}} \Big( C'_{11}G_1G_2 + C'_{13}G_3G_4 - C'_{15}(G_1G_3 + G_2G_4) - \sqrt{3}C'_{12}r\sin^2(\phi + \beta) \Big), \tag{4.21} $$

where,

$$ F_1 = r\sin\theta + \cos\theta\sin(\phi + \beta), \tag{4.22} $$

$$ F_2 = \sin\theta - r\cos\theta\sin(\phi + \beta), \tag{4.23} $$

$$ F_3 = -r\cos\theta + \sin\theta\sin(\phi + \beta), \tag{4.24} $$

$$ F_4 = \cos\theta + r\sin\theta\sin(\phi + \beta), \tag{4.25} $$

and,

$$G_1 = \sqrt{3}\cos\theta + r\sin\theta\cos(\phi+\beta), \tag{4.26}$$

$$G_2 = r\cos\theta - \sqrt{3}\sin\theta\cos(\phi+\beta), \tag{4.27}$$

$$G_3 = r\sin\theta + \sqrt{3}\cos\theta\cos(\phi+\beta), \tag{4.28}$$

$$G_4 = \sqrt{3}\sin\theta - r\cos\theta\cos(\phi+\beta). \tag{4.29}$$

Here $\tau_{bas}$, $\tau_{prism}$, $\tau_{pyra}$ and $\tau_{twin}$ are the resolved shear stresses in the basal, prismatic, pyramidal $\langle c+a\rangle$, and extension twinning systems respectively. The angle $\beta$ is set to either $-\pi/3$, $0$, or $\pi/3$, to account for the different available directions in each mode. The second-order elastic constants in the shock coordinate system, $C'_{\mu\nu}$ are identical to those given by Pope [176]. Matrix notation is used such that the index pairs $ij$ = 11, 22, 33, 23, 13, 12 are replaced by $\mu$ = 1, 2, 3, 4, 5, 6 respectively. Values for the elastic constants in the crystallographic frame were taken from [177]. Absolute values are used in all cases except twinning which, being a polar mechanism, allows shear in one direction only.

The orientation factors, $\overline{m}$, calculated using equations 4.18-4.21 are plotted in Figure 4.8 as a function of the angle $\theta$ between the loading direction and the $c$-axis. Each deformation mode is associated with two curves, representing the minimum and maximum orientation factors at a given $\theta$, as determined by the amount of rotation of the HCP lattice about the $c$-axis. This rotation is given by $\phi$, the angle between the $a$-axis and the $x'_2$ axis. Note that $x'_2$ is perpendicular to the shock direction and constrained to the basal plane. For example, at $\theta$=90° and $\phi$=0°, the shock direction is along $\{10\bar{1}0\}$. Due to the rotational symmetry of the HCP unit cell, $\phi$ can vary between $0°$ to $30°$ at the most. As each slip system also has multiple slip directions available, $\beta$ is chosen to maximise $\overline{m}$ in the basal, prismatic and twinning systems. For pyramidal slip there exists a much larger subset of curves, depending on the chosen slip planes and directions. Shown in the figure are two curves with peaks close to $\theta = 0°$.

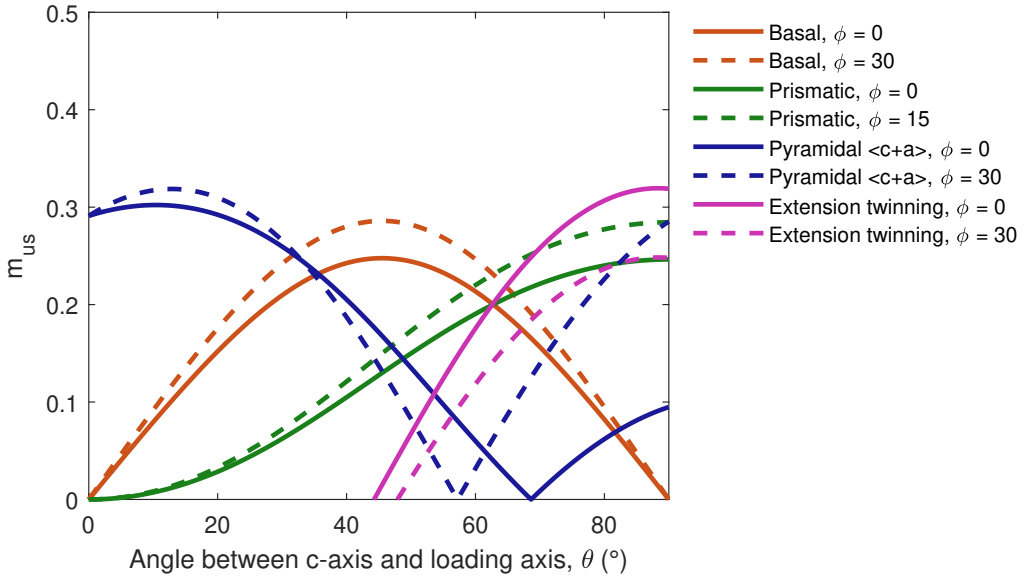



**Figure 4.8:** Calculated values of the dynamic orientation factor, $\overline{m}$, as a function of angle between the $c$-axis and loading axis, $\theta$, for basal, prismatic, second-order pyramidal slip and extension twinning. The maximum and minimum values of $\overline{m}$ are displayed for each deformation mode, as determined by the values of $\phi$ and $\beta$. A wider selection of curves exist for pyramidal slip, shown in the figure are two curves with peaks close to $\theta = 0°$. Loading along $\theta = 0°$, $\theta = 45°$ and $\theta = 90°$ is most favourably oriented for pyramidal, basal, and prismatic slip (and twinning), respectively.

A strong similarity is found when comparing $\overline{m}$ to equivalent plots of Schmid factors, $m$, across loading angle [178] (see also Figure 5.21). In fact the Schmid factor curves are almost identical to $\overline{m}$ if one multiplies the latter by a factor of about 1.7. This similarity is used for aluminium in Section 5.6 in order to compare the expected relative change in strength between different loading angles of the same slip system, which can be accomplished using either orientation factor. In terms of calculating the absolute value of the resolved shear stress however, the Schmid factor is only valid in conditions of uniaxial stress. As shown by Equation 2.15, the Schmid factor is a purely geometrical construct. In other words it is material independent and doesn't account for transverse stresses, meaning it only depends on the direction of the applied stress. In shock compression, the non-zero transverse stresses under uniaxial strain conditions result in lower resolved shear stresses than what would be predicted by Schmid factors. As a result, the maximums of each orientation factor $m$ and $\overline{m}$ are 0.5 and around 0.3, respectively.

Just like with Schmid factors however, the plot of the dynamic orientation factor, $\overline{m}$, can be used to ascertain which deformation mechanisms are likely to activate depending on the loading angle. This is especially useful for strongly textured anisotropic materials, for which Schmid factors have been used in a similar fashion to predict deformation mechanisms associated with samples cut from various orientations of textured specimens [111, 117]. Inspection of Figure 4.8 suggests that for a grain to be most favourably oriented for basal slip, the $c$-axis of the grain should be oriented between around 30° to 60° to the loading direction. Prismatic slip or extension twinning are most favoured when the $c$-axis orientation is close to perpendicular. Finally, pyramidal slip is the only of these deformation modes with non-zero resolved shear stress for loading parallel to the $c$-axis. This picture agrees with the current understanding of the active deformation mechanisms in similarly oriented single crystal magnesium under shock compression [179].

In the present material, loading along ED will compress most grains close to the $a$-axis, causing extension of the $c$-axis. Figure 4.8 confirms that ED loading should be primarily oriented for prismatic slip or extension twinning. Loading in the TD configuration on the other hand is more complicated as the wide distribution of $c$-axis angles means that the prediction of a dominant slip system cannot be achieved using the orientation factors alone.

### Analysis of activation stress versus loading angle

While Figure 4.8 shows the fraction of applied stress which is resolved onto each deformation plane, it contains no information regarding the stress needed to actually activate plastic deformation. In order to make a prediction of the yield stress of a grain at an arbitrary orientation, it is necessary to know the CRSS of every deformation mode. An analysis along these lines was conducted in the recent work by Wang et al., reviewed in Section 2.3.3, in which high strain rate

loading experiments were performed on extruded pure Mg with a very similar texture to the current material, loaded along the extrusion direction [116]. The authors found that the yield point decreased as the ambient temperature was increased. They made use of a combination of CRSS values, measured under quasistatic compression, and Schmid factors in order to predict that extension twinning was the dominant slip system during room temperature impact along ED (due to a low basal Schmid factor) [117]. The decrease in yield at higher temperatures could then be attributed to an increase in the Schmid factors for basal slip caused by grain reorientation during the higher temperatures. Note that a direct comparison between the extruded pure Mg yield points and the current (or single crystal) data is unfortunately difficult due to the reverse impact configuration and low velocity of their experiments. In the study by Yu et al. into shock loaded rolled magnesium sheet, the loading axis was around 90° to the $c$-axis in most grains, resulting in high Schmid factors for extension twinning and prismatic slip [35]. After conducting ECAP, the yield stress was reduced relative to the rolled material, which was again explained as the texture being modified such that the Schmid factor for basal slip was increased.

However, as already shown in Section 4.4.2, the use of Schmid factors is illustrative but not strictly valid during uniaxial strain. Any resolved shear stress calculated through a Schmid factor in these conditions will be an over-prediction, as it neglects the effect of transverse stresses. Equivalently, dividing a CRSS value with the Schmid factor to predict the applied normal stress at the initiation of dislocation movement under uniaxial strain will produce an under-prediction. In addition, the applicability of the CRSS values themselves to high strain rate loading is also limited. In the low strain rate regime, the rate of dislocation unpinning depends explicitly on the size of Peierls barriers, which are overcome through a combination of the energy contributions from the applied stress and thermal fluctuations in the lattice. The traditional definition of CRSS is the resolved shear stress needed to overcome these barriers and initiate slip, i.e. dislocation motion. Shock loading experiments however are characterised by high

yield points which decay towards an equilibrium limit. The magnitude of the acting shear stresses often far exceeds the requirements for thermal activation of slip, meaning dislocation motion is no longer limited by the need to overcome Peierls barriers [15]. The motion of dislocations instead becomes governed by phonon viscous drag [55]. The onset of plasticity in a shock wave is therefore not necessarily limited just by the ability of dislocations to move, but also by the velocity of dislocation motion and the density of available mobile dislocations. As the quasistatic CRSS is a single value which doesn't account for this rate sensitivity, it is of limited use when predicting the yield point at high strain rates, particularly within the region of precursor attenuation.

Altogether, this means for example that the conclusion that extension twinning is dominant during ED loading of extruded magnesium is speculative, as another slip system may be preferred due to a modified CRSS or orientation factor at high strain rates. While an increase in basal slip is a likely explanation for the measured reductions in strength after grain reorientation, the Schmid and CRSS analysis does not grant a quantitative prediction of the amount of basal slip activity. Indeed the peak elastic states in the study by Wang et al. continued to vary with temperature even though the basal Schmid factors remained close to constant.

The issue of the applicability of the Schmid factor to dynamic loading was addressed in Section 4.4.2 by deriving the dynamic orientation factor, $\overline{m}$. Here, an attempt is made to similarly extend the ideas of CRSS and activation stress to the high strain rate regime. First, a straight-forward *dynamic* CRSS is defined, which simply describes the resolved shear stress which is present within a slip or twin system at its activation point during loading. As this is rate-dependent, this value of CRSS matches the higher resolved shear stresses at the initiation of plastic flow in high strain rates. Its value changes as a function of precursor decay or thermal hardening, in which the yield point and thus the resolved shear stresses experienced by the material during yield evolves drastically. Following this interpretation, a rate-dependent *dynamic activation stress* can be defined as

the instantaneous applied stress needed to reach the dynamic CRSS for a given slip system, loading orientation, and strain rate. For single crystal loading, this dynamic activation stress would be exactly equivalent to the peak elastic stress, assuming that only one slip system is responsible for yield at the elastic peak. Similar to the regular CRSS, the dynamic CRSS can therefore be measured in single crystal loading experiments, by first measuring the elastic stress and then calculating the resolved shear stress at the elastic peak in the active deformation system using Equations 4.18-4.21. By knowing the dynamic CRSS in a shock loaded material for a given temperature and strain rate, it is only then possible to make an accurate orientation-adjusted prediction of the activation stress, or yield point, of a crystal loaded at a given angle at those same loading conditions.

In order to enable such a prediction, the dynamic CRSS values are first calculated by extracting them from single crystal data at a given thickness (and room temperature shock conditions) [31–34]. First, $\overline{m}$ in Equations 4.18-4.21 is calculated using the loading orientations of the SC experiments. Following this, it is possible to calculate the resolved shear stress at the yield point according to,

$$^{\alpha}\tau_{crss}(\dot{\epsilon}, T) = \sigma'_{y,sc}(\dot{\epsilon}_p, T)\, \overline{m}_{sc}. \tag{4.30}$$

Here, $\sigma'_{y,sc}$ is the yield point of single crystal magnesium of a given orientation and at a specific strain rate, $\dot{\epsilon}$, and temperature, $T$. It is known that SC loaded along the $c$-axis, 45° to the $c$-axis, and along the $a$-axis results in the activation of pyramidal slip, basal slip, and prismatic slip or twinning, respectively. By inserting the known yield points from these experiments into Equation 4.30, the calculated shear stress, $^{\alpha}\tau_{crss}$, can therefore be taken as the dynamic CRSS for each of these deformation modes, $\alpha$. Using the values of the fitted SC curves in Figure 4.4 at 2 mm thickness (using constant thickness as a proxy for comparable strain rates), this results in $^{bas}\tau_{crss} = 9$ MPa, $^{prism}\tau_{crss} = 98$ MPa, $^{twin}\tau_{crss} = 99$ MPa, and $^{pyra}\tau_{crss} = 231$ MPa. It is again emphasised that these values are highly conditional, in that they represent the resolved shear stress at the onset of plastic deformation specifically at room temperature after 2 mm of shock

wave propagation. Fortunately, the abundance of plate impact data on Mg single crystals means making the same CRSS calculation at other thicknesses is straightforward. Quasistatic CRSS values are typically quoted as around 3 to 20 times lower depending on the slip system [180].

Note that using the propagation distance as a stand-in for the strain rate does not account for the strain rate dependence on impact stress. The curves used to extract yield points for a given propagation distance were fitted to data with varying impact stresses, potentially causing a small error in the fit. However, as the effect of impact stress is comparatively minor both in the current and SC results (especially given the experimental scatter), the additional error from this is assumed small. Moreover, since the $a$-axis experiments result in activation of both prismatic slip and twinning [33], it is unfortunately difficult to separate their individual activation stresses. The assumption is therefore made that both deformation modes activate simultaneously at the $a$-axis yield. It should finally also be noted that for loading constrained to $\theta = 90°$, impacts directly along the $a$-axis are in fact the least favoured for both twinning and prismatic slip, as shown in Figure 4.8. One should instead aim to impact at 15° to the $a$-axis in order to maximise the resolved shear in the prismatic plane, and similarly one should load along the $\{10\bar{1}0\}$ axis for extension twinning.

By employing the values of ${}^{\alpha}\tau_{crss}$ calculated from Equation 4.30, one can now calculate a strain rate and orientation dependent dynamic activation stress for each slip or twin system, according to,

$$ {}^{\alpha}\sigma'_y(\dot{\epsilon}, T) = \frac{{}^{\alpha}\tau_{crss}(\dot{\epsilon}, T)}{\overline{m}} = \frac{\sigma'_{y,sc}(\dot{\epsilon}, T)\,\overline{m}_{sc}}{\overline{m}}, \tag{4.31} $$

where ${}^{\alpha}\sigma'_y$ is the activation stress, or yield stress, of deformation system $\alpha$, and $\overline{m}$ is calculated for the given loading angle and deformation system of interest. Figure 4.9 shows how the activation stresses, calculated using the 2 mm thickness ${}^{\alpha}\tau_{crss}$ values, vary with loading angle and deformation system. Also plotted are

the yield stresses at 2 mm thickness from both present results and single crystal data as a function of the impact direction. For the yield points in the present data, the values of $\theta$ were determined from the ED and TD samples using the EBSD results from Section 4.2. The error bars span 60% of the $\theta$ angles present in the samples. The wide error bar for TD demonstrates its much larger variation in $\theta$.

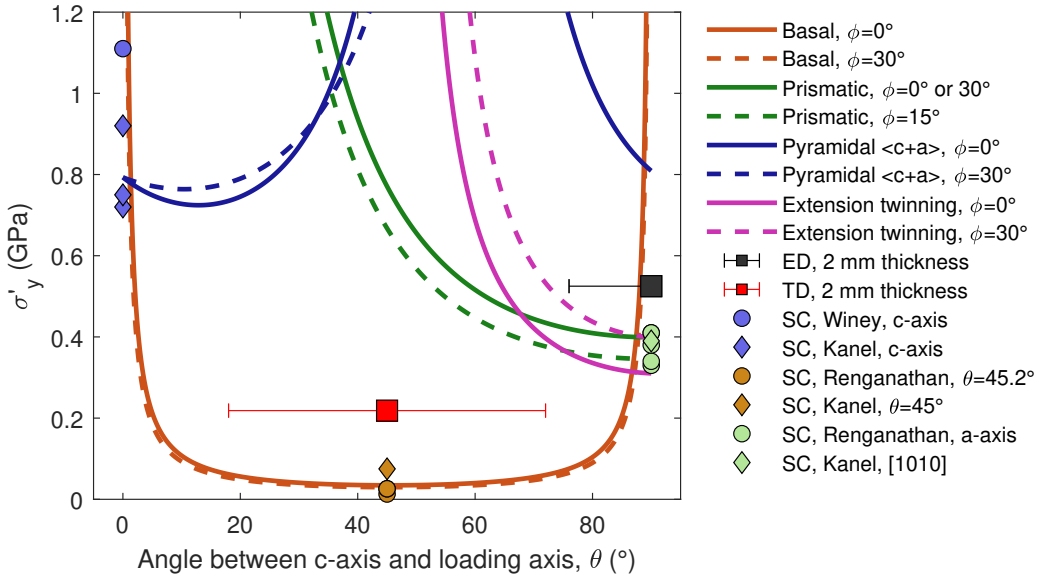



**Figure 4.9:** Calculated activation stresses for pure Mg at 2 mm propagation distance for each deformation mode as a function of loading angle. Also shown are peak elastic stresses at 2 mm propagation distance from both the present experiments and single crystal (SC) results, plotted as a function of $\theta$. As the present material contains a distribution of $\theta$ angles, the error bars in the current data span 60% of the sample grain orientations. Dynamic CRSS values for pyramidal, basal and prismatic slip/twinning are calculated from the shown 2 mm single crystal yield points loaded at $\theta = 0°$, $\theta = 45°$ and $\theta = 90°$, respectively. By computing the activation stresses at these same angles one therefore recovers the SC yield values (as shown by the intersections of the curves and the experimental data). The curves show that the activation stress increases if the loading angle is changed to less favourable orientations.

In Figure 4.9 it now becomes fully apparent which deformation modes are favoured depending on the loading angle. Again this is specific to shocked pure Mg at 2 mm propagation distance, however the general trends persist across a wide range of thicknesses. Focusing first on basal slip at $\theta = 45°$, here the two values of $\overline{m}$ used in Equation 4.31 to calculate ${}^{bas}\sigma'_y$ cancel and one is left with the value of the (fitted) SC yield at $\theta = 45°$. This is consistent with the assumption

that basal slip is the only active deformation mechanism at the precursor peak in SC loaded at this angle. The stress required to activate basal slip increases the further one deviates from the ideal angle of $45°$, as the reduction in $\overline{m}$ means an ever smaller proportion of the applied stress is resolved onto the basal plane. Despite this, the much lower dynamic CRSS of basal slip as compared to other slip systems entails that activation of basal slip is favoured in almost the entire range of loading angles, from around 1.5° to 87° (≈95% of all angles). Only at $\theta > 87°$ does prismatic slip or twinning have lower activation stresses. Similarly, while pyramidal slip has relatively high values of $\overline{m}$ across a wide range of $\theta$, only in grains where the $c$-axis is angled almost exactly parallel to the loading direction is pyramidal the only accessible slip system.

Comparisons can be made to similar activation stress figures under quasistatic loading and uniaxial stress conditions, calculated using Schmid factors. Depending on the CRSS values used, one finds that basal slip in AZ31 requires less activation stress than prismatic slip up to $\theta$ of around 75°-85° [110, 181, 182]. In Figure 4.9, this region is widened further due to the larger disparity in CRSS values in pure magnesium under shock loading.

While the dynamic CRSS values in AZ31 will be different from pure Mg, it is still apparent from Figure 4.9 that basal slip is predicted as the dominant slip system in AZ31 in the TD orientation, while the ED orientation should experience some mixture of twinning, prismatic and basal slip. However, it is also clear that the TD yield point is significantly higher than that of single crystals deforming under basal slip. The same stands true for the ED targets when contrasted to prismatic slip and twinning. Strengthening through lattice defects such as grain boundaries, dislocations or alloying elements can undoubtedly be partially responsible. Likewise, high stress states could be attained in poorly oriented grains which are forced to deform either under a sub-optimal angle, or through a more stress demanding deformation system (such as grains angled at $\theta < 15°$). The original question remains however whether or not the full orientation distribution

of the material can be used to understand this disparity in yield points between single crystal magnesium and polycrystalline AZ31.

### 4.4.3 Orientation-based prediction of dynamic yield points

In Section 4.4.2, a method is developed for calculating the strain rate dependent activation stress of every deformation system within an Mg crystal loaded at a given orientation. It is also possible to extract the distribution of grain orientations in the current samples from the EBSD measurements shown in Figure 4.1. Application of the above methods to the EBSD data therefore enables a prediction the yield point of every grain, assuming that the deformation system with the lowest activation stress initiates yield. By repeating this for all of the measured grains and averaging the yield points, it is possible to establish a simple prediction of the macroscopic yield. Equivalencies can be drawn between this approach and Sachs models employed to predict yield behaviour in quasistatic loading [111, 183].

Figure 4.10 shows the results of implementing this on a subset of grains within the ED and TD targets. Also shown is the area averaged activation stress of all grains, and the yield points from the present AZ31 experiments at 2 mm thickness. Note that since the CRSS values used in Equation 4.31 were calculated from pure Mg data, the resulting distribution of grain activation stresses should in principle mirror that of an extruded pure Mg material with a texture matching that of the current samples, such as the material studied by Wang [117]. Nevertheless, Figure 4.10 forms a useful baseline from which the relative influence of the various deformation modes in the current samples can be considered.

Keeping the above qualifier in mind for the moment, the plot predicts that basal slip is by far the most dominant slip system at the onset of plastic flow in the ED orientation, despite the favourable orientation of the prismatic and twinning planes. It is assumed that the overall yield of the sample can be represented

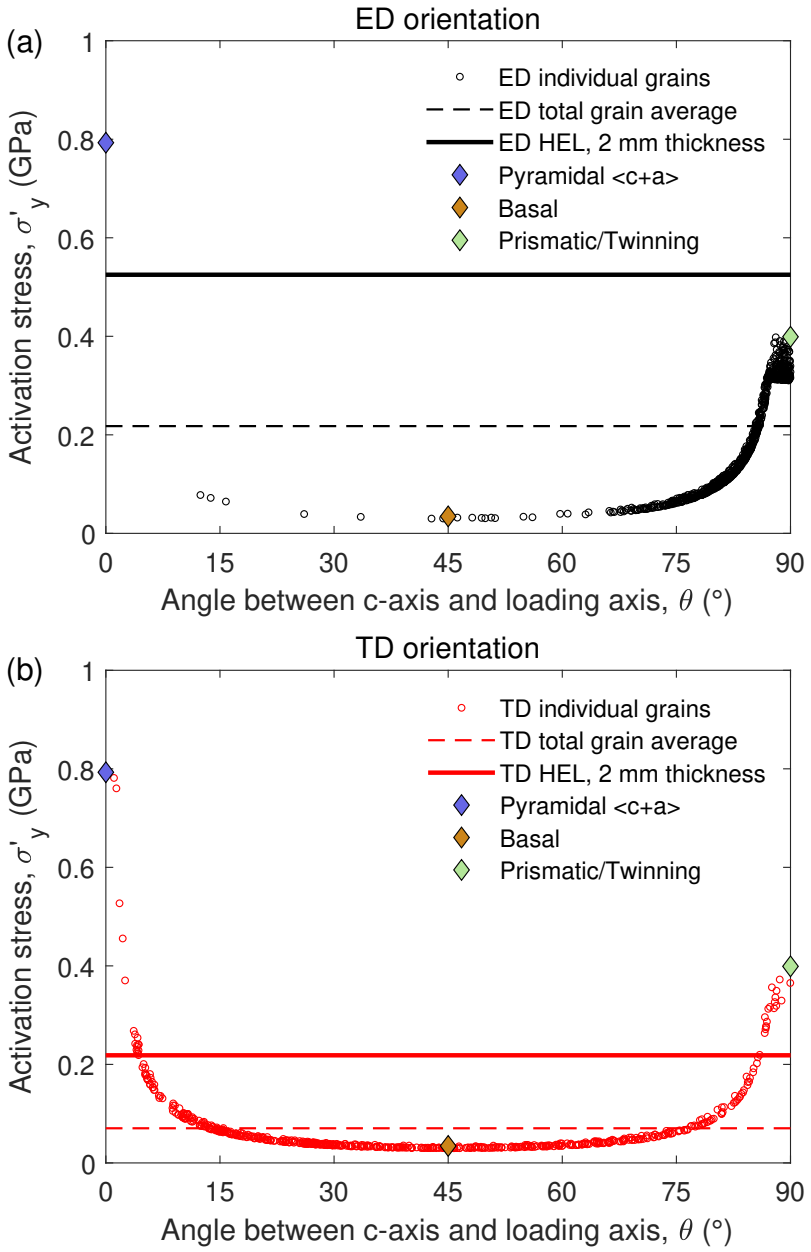



**Figure 4.10:** Predicted yield stresses of individual grains from the current specimens assuming the material consisted of pure magnesium. The distribution of grain orientations is taken from a) ED, and b) TD EBSD data (only a subset is plotted), while the dynamic CRSS of the deformation modes used in equation 4.31 is extracted from single crystal results at 2 mm (hence why the grains are considered to consist of pure Mg, not AZ31). In each grain, the yield stress is taken as the minimum value of the activation stresses in the available deformation modes. The dotted lines represent the area averaged activation stress across all grains. Solid lines are the yield points of the current AZ31 experiments. Diamonds are the yield points of single crystal specimens categorised by their corresponding active deformation systems, as determined from the fitted curves at 2 mm thickness shown in Figure 4.4.

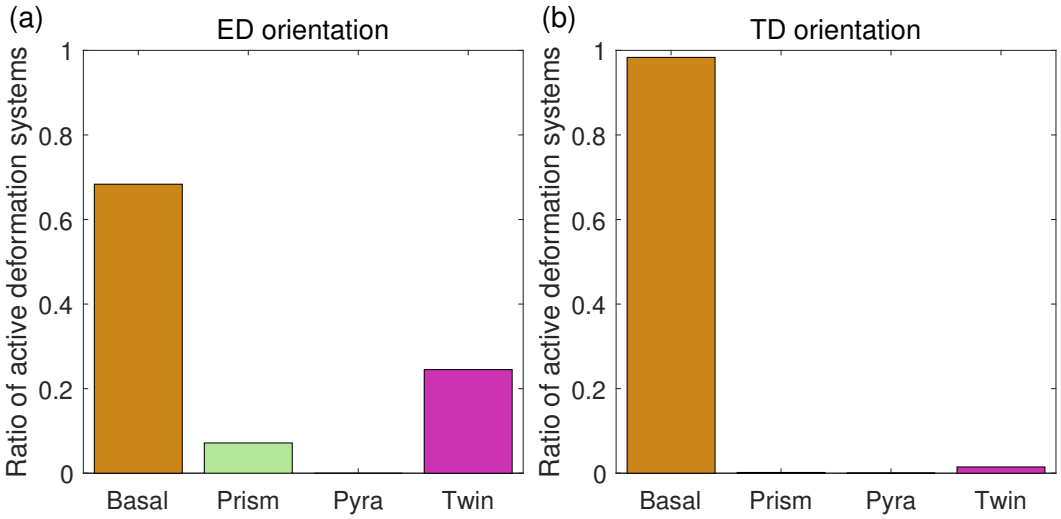



**Figure 4.11:** Predicted proportions of the activity of different deformation modes in the a) ED and b) TD orientations, calculated from the results shown in Figures 4.10a and 4.10b, respectively. It is shown that basal slip is the dominant slip system in both ED and TD specimens. As before, the dynamic CRSS values used for these results were extracted from SC results, meaning the present ratios would best represent an extruded pure Mg material. In AZ31, it is likely that basal slip would be less dominant, due to its higher CRSS relative to the other deformation modes.

by the area-weighted average yield points of all individual grains. Comparing this average to the real yield point in the ED orientation one finds a large stress discrepancy. While there is as predicted a small degree of strengthening due to grains that are poorly oriented for prismatic slip at $\theta < 90°$, it's not enough to bridge the measured gap in strength. Once the grain angle deviates enough from $\theta = 90°$, basal slip becomes favoured instead. The degree of deviation from a perfect ring texture in the ED target therefore causes considerable softening of the material. In this case it is found that basal slip is in fact predicted to be the overall dominant slip system at the elastic peak, accounting for 68% of all active deformation modes. This is counter to previous beliefs, motivated by its high Schmid factor, that extension twinning is the dominant deformation mode at the yield point in extruded pure Mg loaded in the ED orientation (although recovered specimens did display high twinning fraction) [117].

Note that these proportions depend on the relation between the dynamic CRSS values of the different deformation modes at the given propagation distance.

Repeating the same calculation for ED loading at 0.5 mm one finds that basal slip is less favoured but still accounts for 47$\%$ of predicted deformation activity, the remainder being split between twinning and prismatic slip in a 3:1 ratio. Upon twinning, the grain is reoriented by 86°, which is in turn likely to cause subsequent activation of either pyramidal or basal slip in grains where these were originally disfavoured. In fact, inspection of the region $0° < \theta < 4°$ in Figure 4.9 suggests that basal slip would in general still be more favoured than pyramidal slip in the twinned grains, particularly if one considers the presence of more complex post-yield stress states. This may help explain the peak-and-valley type precursor observed particularly in the thinner ED samples. A high degree of twinning at the onset of plastic flow followed by the activation of a softer deformation mode would cause rapid further relaxation of the peak elastic stress. Again, a useful feature of this analysis is that the preferred deformation system can be predicted quantitatively, whereas the preference of either basal or pyramidal slip in twinned grains was a matter of some ambiguity in previous studies [117, 184].

While there is a fraction of grains with $c$-axes close to either parallel or perpendicular to the loading axis in TD targets, again the low activation stress of basal slip prevails and the share of other deformation modes is very low. In fact it is found that the predicted contribution of pyramidal slip is completely negligible in the TD orientation (less than $0.01\%$), whereas basal slip comprises 96-98$\%$ of all active slip system at the elastic limit in the 0.5 - 2 mm thickness range. This is an important result given the earlier, now apparently erroneous, assumption that pyramidal slip in TD samples should be responsible for significant increases in dynamic strength (although grains oriented close to $\theta = 0°$ would still exhibit relatively high yield points due to the poor orientation for basal slip).

It should again be emphasised that these calculations are based on the high strain rate dynamic CRSS values of pure magnesium, and not Mg AZ31. While the analysis should be directly applicable for extruded pure magnesium, which is known to display very similar texture [116], it is likely that both the absolute and

| | Basal (MPa) | Prismatic (MPa) | Extension Twinning (MPa) | Pyramidal $\langle c+a \rangle$ (MPa) |
|---|---|---|---|---|
| Pure Mg | 0.5 | 39 | 12 | 80 |
| Mg AZ31 | 20 | 55 | 35 | 80 |

**Table 4.3:** Representative values of quasistatically measured CRSS for pure Mg and Mg AZ31 [111, 180, 183, 185–190].

relative strengths of the various deformation modes in the alloy are altered. If the basal system is strengthened in relation to the others, then its dominance across the full range of loading angles will be diminished. Consequently, the predicted average yield point in Figure 4.10b should be slightly higher and therefore closer to the real yield point of the TD sample. This explanation is insufficient for the ED target however, as even if a larger fraction of grains were to deform via prismatic slip or twinning, their activation stress would still be lower than the measured yield point. Thus an overall increase in the dynamic CRSS of all deformation systems is also necessary.

It is suggested therefore that the effect of alloying in AZ31 is likely a combination of both overall strengthening of all dynamic CRSS values with respect to pure Mg, as well as an additional increase in the basal CRSS with respect to the other deformation mechanisms. Further substantiation of this is found through comparisons of quasistatic CRSS values between pure Mg and AZ31, shown in Table 4.3. Second-phase particles, increased dislocation densities and more are all sources of higher CRSS values in the alloyed material in low strain rates. Detailed inspection reveals that while the CRSS of prismatic slip and twinning is around 2-3 times higher in AZ31 than in pure Mg under quasistatic conditions, basal slip on the other hand is strengthened by a factor of 10-40 depending on the values used. It is reasonable to assume that this additional strengthening of basal slip will to some degree also manifest in the realm of shock compression. Consequently, basal slip won't be quite as dominant in the current specimens as predicted in Figures 4.10c-d.

Ideally, the calculations used to arrive at Figure 4.10 should have been performed with dynamic CRSS values for AZ31. However, in the absence of such high strain rate CRSS measurements, a substitute can be found by applying a strengthening factor to the pure Mg CRSS. It will be left to future studies to determine the exact magnitude of this strength ratio. For now, the analysis framework is simply tested by checking if a reasonable adjustment to the pure Mg CRSS values can indeed be used to adequately fit the yield points of AZ31. A first order approximation is achieved by applying the same strengthening factor to all deformation systems equally at all thicknesses, and then optimising its value until a good match with the experimental data is produced. It would be tempting to assign separate strengthening factors to each deformation mode (i.e. higher strengthening of basal slip), akin to the ratios found in quasistatic experiments. Unfortunately there is large variability in reported CRSS values, and it is unlikely that the relative strength increase from the pure to the alloyed material would be the same in the shock regime as it is in the quasistatic regime.

First, the analysis carried out to produce Figure 4.10 is repeated across all thicknesses, without modification to the CRSS values. The dynamic CRSS is calculated at each thickness, from which the grain activation stresses for the given propagation distance can be predicted. The area-weighted average of the grain activation stresses is assumed to be an acceptable measure for the macroscopic yield. As the dynamic CRSS values in the single crystals continue to evolve with propagation distance, so does the predicted yield point of the polycrystal. The result is a curve projecting the attenuation of the polycrystalline precursor stress with distance. Shown in Figure 4.12 are two dashed curves which describe the predicted yield of this pure polycrystalline Mg material matching the orientation distributions of the current ED or TD samples. As discussed previously, these peak elastic stresses are significantly below those of the alloyed material, but should be an adequate prediction of plate impact experiments on extruded pure Mg.

Comparison of these curves to the single crystal data enables a quantification of the effects that the orientation distribution has on dynamic strength, mainly caused by the grains in the polycrystalline material which are angled far from optimal loading orientations. It is found that the predicted pure Mg TD curve is higher than single crystals deforming under basal slip (i.e. loaded at 45° to the $c$-axis, data shown in Figure 4.4) by a factor of about 2.0. This higher strength is caused by the high population of grains which are oriented far from the ideal 45° loading angle. Conversely, the ED orientation distribution is predicted to cause a reduction in peak elastic stress by a factor of around 1.7 compared to $a$-axis loaded SC (although there is about a $\pm$0.3 variation depending on the propagation distance). Because of the high prevalence of grains deforming through basal slip in the ED orientation, the yield point is significantly lower than a single crystal deforming purely through prismatic slip or twinning. These results reaffirm the importance of the orientation distributions in polycrystalline magnesium in determining its dynamic response.

A single dimensionless strengthening factor, $A$, is now applied to all dynamic CRSS values equally according to,

$$^{\alpha}\tau_{crss,AZ31} = A\,{}^{\alpha}\tau_{crss,SC}. \tag{4.32}$$

The purpose of this strengthening factor is to account for the additional effects of lattice defects in the alloy, i.e. immobile dislocations, point defects, second-phase particles, grain boundaries, etc., in raising the activation thresholds of all deformation systems. A minimisation routine is run to find the magnitude of $A$ which optimises the fit of both predicted ED and TD curves to the experimentally determined ED and TD yield points simultaneously. It is shown that a reasonable fit is produced for $A$=2.40, as demonstrated by the solid lines in Figure 4.12.

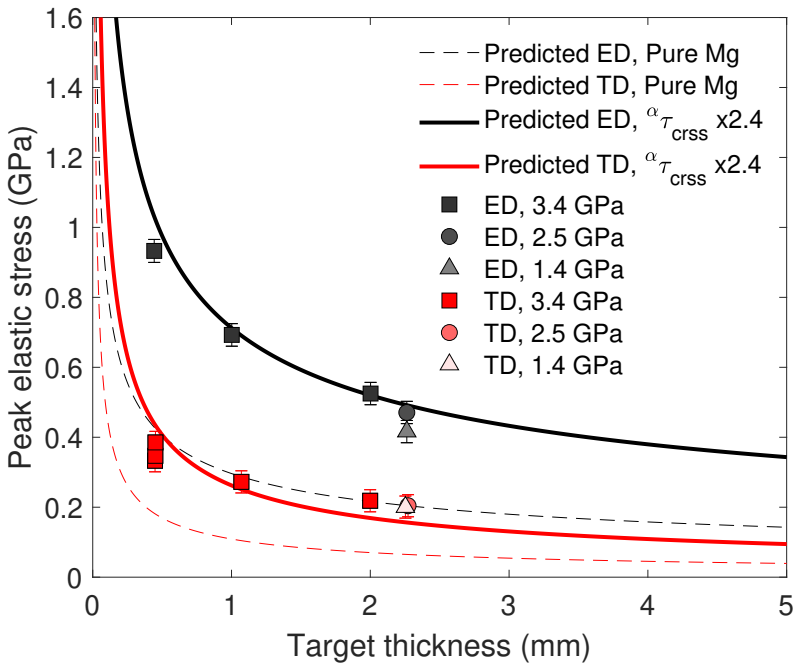



**Figure 4.12:** Predicted evolution of the peak elastic stress with propagation distance for pure Mg (dashed lines) and Mg AZ31 (solid lines) samples with the orientation distribution of the present ED (black) and TD (red) targets. Also plotted are the measured stresses of the ED and TD experiments. A strengthening factor of 2.4 applied to the dynamic CRSS values of pure Mg is found to produce a reasonable fit of both ED and TD simultaneously.

This degree of overall strengthening seems reasonable when compared to the strength ratios of 2-3 between Mg AZ31 and pure Mg for prismatic slip or twinning under quasistatic loading. It also results in a particularly good fit for the ED sample, in which the active deformation systems are prismatic slip, twinning and basal slip. In the case of the TD sample, the fit starts to deviate at larger thicknesses. This is likely due to the disparity between the adjusted and the real dynamic CRSS of basal slip in AZ31. Because of the dominance of basal slip in the TD orientation, the fit would be improved if one were to apply a separate slightly increased strengthening factor to basal slip specifically, as suggested by the quasistatic CRSS data. Too much strengthening of basal relative to non-basal slip systems on the other hand would be counter-productive as it would cause their CRSS values to converge, meaning the two predicted curves would also come together. The results would then fail to capture the large measured difference in the yield of the TD and ED targets which, similar to the difference observed in the

single crystal data, proves that the discrepancy between the activation stresses of basal slip and prismatic slip or twinning needs to be preserved in the alloy. Despite the slight deviations in the predicted curves from the measured values, Figure 4.12 shows that the distribution of grain orientations in AZ31 can indeed be used to adequately model its macroscopic yielding behaviour, given this simple correction to the strength of the active deformation modes.

A number of assumptions have been made in reaching these results. The first is the assumption of conditions of uniaxial strain for all grains. As shown above, the deviation from uniaxial strain in the elastic regime leads to only a negligible error. Secondly, it is assumed that the macroscopic stress is directly imposed on each grain, and interactions between grains are ignored. This is equivalent to assuming that the aggregate response corresponds to the average of a set of independently yielding single crystals. The spot of the PDV laser inherently acts as an averaging measurement, as it gathers the response of thousands of grains across the sample free surface and collects it into a single velocity profile. The assumption is reasonable if one posits that each grain has had very limited capacity to influence its neighbours at the elastic peak. Tied to this is the further assumption that each grain deforms with only a single slip or twinning system. While this is a fairly rudimentary approximation, it should be applicable at the onset of plastic flow, especially given the dominance of basal slip and twinning. All of these assumptions (aside from the uniaxial strain one) are similar to those employed in Schmid factor or Sachs based models. Such analysis is commonly used to predict initial yield behaviour and deformation mode activity, especially in anisotropic materials [111, 183].

A final implied result from the analysis is that each deformation mode's dependence on propagation distance is the same in both alloyed and pure Mg. While the analysis necessitated a linear increase in the CRSS values of the alloy, the time-dependent decay rate of the peak elastic stress did not need adjustment. It is known however that lattice imperfections can contribute not just to an overall

strengthening but may also result in increased attenuation rates. An example of this are the precursor stresses of pure and alloyed aluminium, covered in Chapter 5. Pure Al has a pronounced decay curve, whereas only very minimal precursor attenuation is observed in Al 6061 in the same thickness ranges [23]. The only way to account for this fully in the current framework would be to measure the stress evolution of individual crystals of AZ31. In contrast to Al 6061 however, the present results in AZ31 display significant precursor attenuation, very similar to that of the single crystal measurements. It is therefore inferred from this analysis that the effects of alloying only cause an overall strength increase in AZ31, and that additional nonlinear adjustments to the decay rate are relatively small.

At the minimum, the analysis presented here has permitted a quantitative estimate of the departure in Mg AZ31 from the behaviour of pure Mg, supplied in part through the magnitude of the strengthening factor $A$. It is shown that the crystallographic orientation distribution of a polycrystalline material can be used to predict its peak elastic stress with surprising accuracy, given a set of dynamic CRSS values and simplifying assumptions. Although it should be emphasised that the CRSS values applied to the alloy represented a rough estimate, based on the pure Mg data, it is noteworthy that a reasonable fit was produced simultaneously for both ED and TD orientations without the need for separate corrections to the CRSS for each sample. It is presumed that the same analysis can be applied to magnesium of any texture or loading orientation, or indeed another material entirely, subject to the availability of adequate CRSS data. A full treatment would also require accounting for the exact strengthening of alloying elements, as well as the effect of the dislocation density. In fact the analysis permits further investigation of the effects of temperature and cold work on the dynamic strength, both of which result in grain reorientations which complicated the results in previous studies [35, 116, 117]. By calculating the expected strength based on the orientation distribution, the results of e.g. cold work and changing dislocation density can be quantified with more confidence. Indeed, the effect of cold work on the dynamic strength of aluminium is investigated in detail in Chapter 5, in which

it is shown that large increases in initial dislocation density through cold work can have a significant effect on the precursor amplitude. Although aluminium is much less anisotropic in nature than magnesium, the orientation-based analysis developed in this chapter is used to verify that the changes in grain orientations which developed after cold work did not affect the experimental conclusions.

## 4.5 Effect of grain size in Mg AZ91

**Overview of melt-shear processing**

In the beginning of this thesis, grain size is highlighted as one of the microstructural features with potential influence on the dynamic yield point. Interest is mainly due to the well-known Hall-Petch theory, from which one would expect an increase in the yield strength with increasing grain boundary density. On the other hand, it is also possible that precursor decay might be hastened through increased dislocation nucleation at the grain boundaries. The uncertainty of which response, if any, would manifest during dynamic loading is the main motivation for the study of grain size.

The effects of grain boundary density are discussed in more detail in Chapter 5, in which it is found that aluminium is most likely grain size independent. Being a much more isotropic material than magnesium, aluminium was a better choice for studying changes in dislocation density, as this parameter is difficult to alter without also affecting the crystal orientation distribution. The role of crystal orientation was instead the primary focus of the present chapter, as it is highly dominant in anisotropic materials such as magnesium. It was found however that through the method of melt-shearing, it was possible to also study changes in grain size in magnesium without inducing large changes to its grain orientation distribution. This section is dedicated to a smaller additional study on the dynamic strength of cast Mg AZ91 investigating the effects of variations in grain size through application of melt-shearing.

The melt-shearing method is a new step in the metal casting process developed by BCAST at Brunel university, where a rotor-stator unit induces high shear to the melt before casting [191]. The traditional high pressure die-casting (HPDC) method is both efficient and low-cost, however it frequently leads to substantial porosity, hot tearing, and uneven distributions of grains, inclusions and precipitates in the finished product. melt-shearing greatly reduces porosity and also breaks up inclusions such as oxide layers into finer particulates which are spread out evenly into the melt. This encourages heterogeneous nucleation of grains during the subsequent solidification phase, which produces more uniform, equiaxed, and smaller grains. AZ31 is often preferred over AZ91 because of casting defects associated with the latter, however as was discussed in Section 4.1, AZ31 in turn develops strong texture during forming. melt-shearing of AZ91 is a potential way of producing cast alloys with fewer defects, and also less anisotropy than what is developed in wrought alloys such as AZ31 during the extrusion of rolling processes.

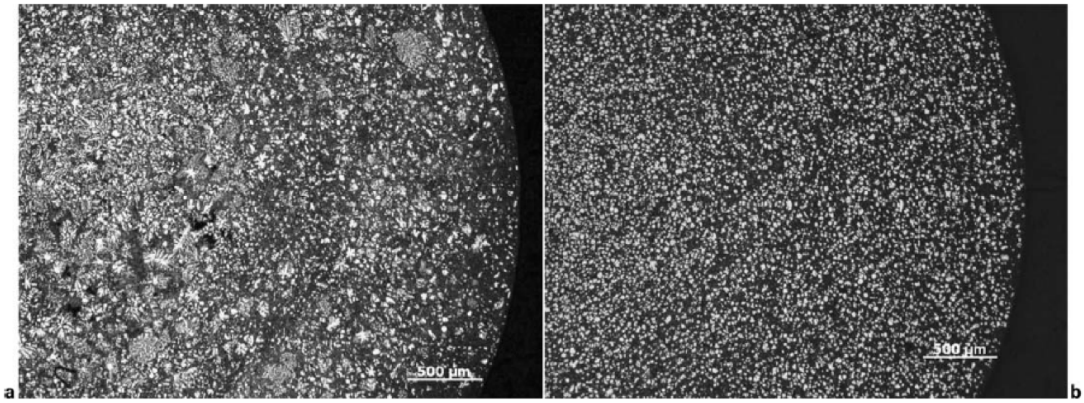



**Figure 4.13:** Optical micrographs of conventionally cast (left) and melt conditioned (right) AZ91D [191]. The grain size of conventionally cast material varies from around 200 to 600 $\mu$m, whilst melt-shearing produces a consistently fine microstructure with an average grain size of around 60 $\mu$m.

Magnesium AZ91 is one of the most frequently used cast alloys, and has so far seen very limited study at high strain rates. Two sample variations of AZ91D were obtained from BCAST, a conventionally cast (CC) material, and a melt-sheared (MS) sample. The microstructure and low strain rate behaviour in both

materials has been studied previously, in addition to that of other melt-sheared cast metals [191–196]. The microstructural differences are demonstrated in Figure 4.13, in which it is shown that the MS method produces smaller grains of more uniform size and equiaxed morphology. In a study by Men et al., modelling of the sample material using a free growth model found that intensive melt-shearing causes MgO particles, originally densely collected into oxide films, to disperse into separate particles spread throughout melt [195]. This causes an increase in the MgO particle density by three orders of magnitude, whilst the density of active nucleating MgO particles is increased by a factor of 20 compared to the conventional material. The grain refinement in MS specimens is attributed to this significant increase in grain nucleation sites during solidification. Indeed, experimentally measured grain sizes in conventionally cast material varies from 200 to 600 $\mu$m, whilst melt-shearing produces a consistently fine microstructure with an average grain size of around 60 $\mu$m [191]. In larger casts the measured grain sizes were reduced from about 2 mm to 1.2 mm [195]. The same comparison in aluminium alloy 5754 found conventionally cast samples have coarse columnar grains near the sample surface with an average grain size of 300 mm. In contrast, the sheared samples exhibited uniform equiaxed grains with an average grain size of 70 mm [191].

**Experimental results on AZ91**

The AZ91 target specimens were prepared using an early and much less developed version of the sample preparation methods described in Section 3.1. The targets were successively lapped down to 5 $\mu$m diamond suspension, followed by manual polishing by micron paper down to 1 $\mu$m. The resulting surface finish was diffuse and mottled, especially as a result of the porosity. A possible solution to the porosity would be to gather samples from closer to the edges of the die-cast bar, rather than from the centre. However, the centre of the bar is also where both optical examinations and mechanical tests reveal the biggest differences between conventional and melt-sheared samples [194], as exhibited in Figure 4.13.

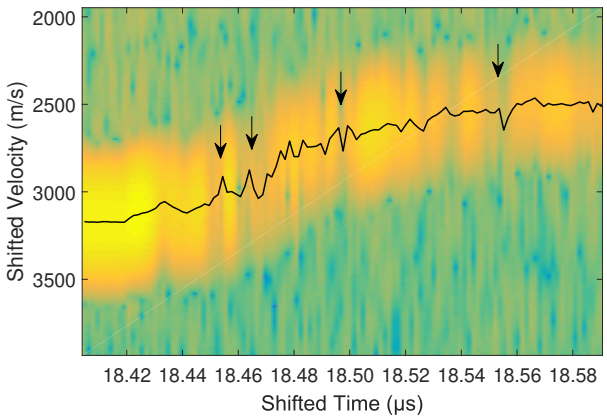



**Figure 4.14:** PDV spectrogram of a 1 mm thick conventional sample of Mg AZ91. While the region around the elastic precursor is observed clearly, the remainder of the shock rise is partly obscured by intermittent loss of signal as indicated by the arrows.

Plate impact experiments were performed on samples between 0.2 and 1.9 mm thickness, using the same setup and experimental parameters as the AZ31 experiments described in Section 4.3. Unfortunately, the signal quality of many of these experiments was quite poor, and parts of the material behaviour is obscured by noise. It is believed that the lower quality of the PDV traces is due to the rougher surface finish on the samples. Examination of the spectrograms reveal multiple areas of signal loss during the rise-time of the shock, as shown in Figure 4.14. This is likely caused by the irregularity of the surface which under motion and compression causes changes in the return signal from of the sample. It is however safe to assume that reliable data can be found in areas in which the signal strength is unchanged relative to the baseline, which is mainly the case in the precursor peaks.

The complete set of velocity profiles from the plate impact experiments on AZ91 are shown in Figure 4.15. The noise caused by signal loss is seen clearly in the plastic rise of some of the velocity traces, especially at 0.9 mm. The 1.9 mm traces on the other hand exhibit very minimal noise during the early rise. It seems clear from the experiments in which noise at the precursor peak is small that there is only a relatively minor difference in the precursor stress between MS and CC samples. This is highlighted in Figure 4.16, in which the yield points are plotted

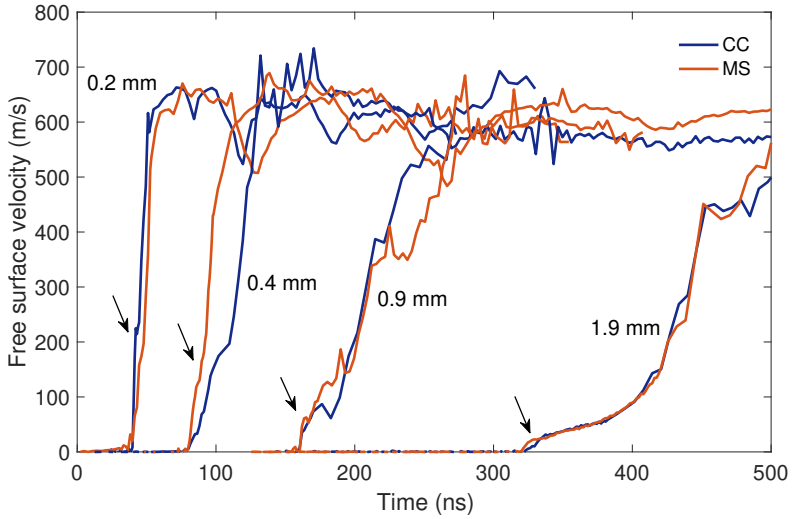



**Figure 4.15:** Free surface velocity histories of the conventionally cast (CC) and melt-sheared (MS) Mg AZ91 specimens, impacted at 400 m/s using the setup described Section 4.3. Thicknesses are shown next to each pair of velocity traces. The breakout time has been shifted for clarity. The decay of the precursor wave is indicated by the black arrows, however signal noise makes pinpointing the exact location of the precursor peak less clear than what was achieved in AZ31, especially in the thin samples. From the high thickness data (0.9 and 1.9 mm) it seems evident that there are only relatively small differences in the peak elastic state between the CC and MS material.

against target thickness together with the results on AZ31 from this chapter. The error bars for 0.2 and 0.4 targets are quite large due to the uncertainty in the elastic peak extraction caused by the noise. The 0.9 and 1.9 mm samples however displayed a stable signal up to and past the initial yield point, meaning their values should be accurate.

It is found that the difference in the yield points between the CC and MS material is smaller than the measurement error for the 0.4 mm targets and above, indicating that AZ91 exhibits a grain size independent dynamic response. This is especially apparent when comparing the AZ91 yield points to the those measured in AZ31. In the latter case, the grain size distributions were identical in both sample variants, as both were cut from the same original rod sample (the equiaxed microstructure ensured that impact direction had no effect on grain boundary density). The opposite held true for the AZ91, as grain sizes were varied whilst the orientation distributions were both randomised, and therefore expected to remain

constant across both CC and MS samples. The difference in the yield of ED and TD versus that of CC and MS targets in Figure 4.16 emphasises the dominance of crystal orientation and not grain boundary density in determining the dynamic response of magnesium alloy. The deeper reasons for why grain boundaries are of less relevance in dynamic loading are examined in detail in Section 5.5.2, where it is concluded that the dynamic strength of aluminium is also independent of grain boundary density. As discussed in the section, it is believed that the short time-scales of shock loading means there is not enough time during which moving dislocations can interact with grain boundaries.

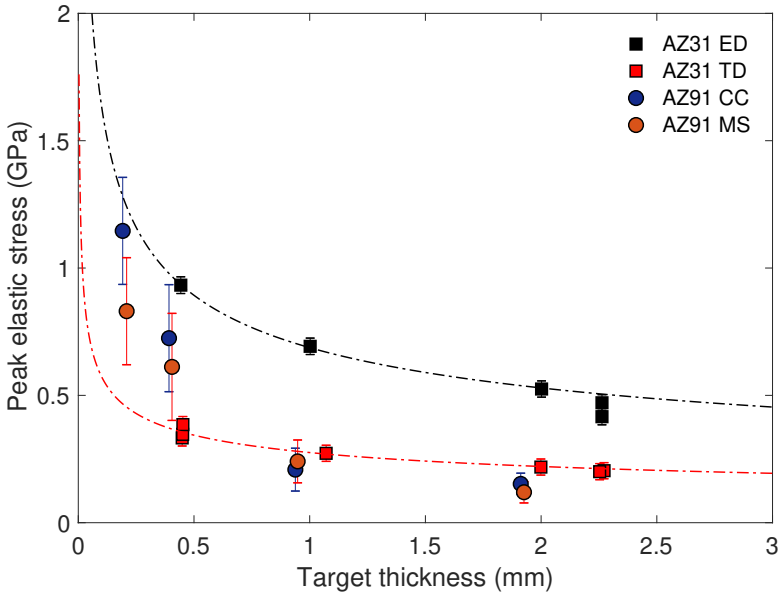



**Figure 4.16:** Peak elastic stress versus propagation distance in conventionally cast (CC) and melt-sheared (MS) AZ91 targets, plotted together with the results on AZ31. Error bars in the AZ91 data points are representative of the noise from the velocity traces. Dashed lines are power law fits to AZ31 data. It is found that the difference in yield between CC and MS material is smaller than the measurement error at 0.4 mm thickness and above. The dynamic strength of AZ91 is slightly below that of AZ31 TD, possibly due to higher rates of basal slip or less alloy strengthening. The plot demonstrates the dominant role played by crystal orientation and not grain boundary density in determining the dynamic strength of magnesium alloy.

Note that it is also found that the strength of AZ91 is slightly lower than that of AZ31 TD. This can be due to higher rates of basal slip (caused by higher randomisation of grain orientations), or because alloy strengthening in AZ91 is

simply higher than in AZ31. Determining which of these possibilities is the case could be accomplished by measuring the grain orientations in the AZ91 samples and comparing their expected strength to the TD specimens, calculated using the orientation analysis developed in this chapter. Finally, as MS samples are essentially more uniform, equiaxed versions of conventional samples, one would expect the behaviour at the elastic-plastic limit to be more random in conventional samples, and more consistent in MS samples. It is concluded from the current data however that the grain size distribution has little effect on the yield point.

## 4.6 Chapter summary

The decay of the elastic precursor wave in extruded magnesium alloy AZ31B has been investigated in plate impact experiments with targets in the 0.45 to 2.3 mm thickness range, and at elastic impact stresses between 1.4 and 3.4 GPa. Surveys of the grain orientations through EBSD measurements revealed that the extruded AZ31 exhibits a strong basal texture, in which the $c$-axes in the majority of grains are arranged along the transverse plane. By impacting targets cut parallel and perpendicular to the extrusion direction (ED and TD, respectively), it is shown that the loading direction causes significant differences in recorded elastic wave amplitudes. Whilst decay of the elastic precursor wave is observed in both sample orientations, it is found that the ED orientation exhibits a precursor peak more than twice the magnitude of the TD orientation.

The measured peak elastic stresses in the current data were found to be at intermediate values between those measured in single crystal (SC) magnesium at varying orientations. The TD samples displayed very similar decay rate to SC impacted at 45° to the $c$-axis, but at consistently higher stresses. Similarly, the ED samples matched the decay curve of $a$-axis SC loading, also at higher stress states. These results were initially made clearer through application of Schmid factors to evaluate the expected slip system activity in the current samples. It

is found that TD loading displayed high Schmid factors for basal slip, while the ED orientation mainly favoured prismatic slip and twinning. These were also the respective primary deformation modes at the elastic peak for SC impacted at 45° to the $c$-axis and along the $a$-axis, likely explaining the similarities between their corresponding precursor decay curves and amplitudes.

More detailed consideration suggested however that the Schmid factor has severe limitations in its ability to quantitatively predict slip system activity. A more thorough analysis was needed in order to predict the exact distributions of slip system activity in each sample, and thus quantify the roles played by the deformation systems in each sample on the one hand, and second-phase particles on the other. A dynamic orientation factor was derived, analogous to a Schmid factor but for uniaxial strain instead of uniaxial stress conditions. As the former is applicable to shock loading, this enabled the prediction of the fraction of the longitudinal stress applied by the shock wave which is resolved onto any slip systems of interest, for any crystal orientation. Next, a dynamic CRSS describing the activation shear stress for slip during shock loading was extracted from the comprehensive single crystal data available in the literature. The dynamic CRSS was combined with orientation factors calculated in each grain of the sample EBSD measurements in order to produce an average activation stress. This was taken as a reasonable prediction of the peak elastic stress at a given temperature and strain rate.

The results indicated that the distribution of grain orientations in the ED samples in fact lead to a weaker response compared to single crystals deforming purely through prismatic slip or twinning, which was due to the high proportions of basal slip activity. Conversely, the TD samples were strengthened by the grains which were poorly oriented for basal slip. By increasing the dynamic CRSS values by a factor of 2.4, it was possible to produce a reasonable fit to the measured precursor stresses of both the ED and TD samples simultaneously. This factor can be taken as a measure of the degree of strengthening caused by alloying elements

in the AZ31, when compared to pure Mg, which was also a reasonable match to the increase in CRSS of AZ31 measured under lower strain rates.

In summary, it is shown that this analysis method enables a prediction of the dynamic yield point of a polycrystalline material based on its orientation distribution. The framework is predicated upon a set of simplifying assumptions, as well as access to constitutive data in the form of dynamic CRSS values of the active deformation modes. It quantitatively predicts the yield point and its dependence on loading conditions. The same methods can be used in other materials (as is done for aluminium in Chapter 5). Notably, the effects of applying increased temperatures or cold work can be divorced from their effects on grain orientations.

Finally, a shorter study was performed on conventionally cast and melt-sheared AZ91D, in which the latter displays a significantly smaller grain size. It is theorised that increasing the grain boundary density may result in higher strength caused by the additional obstacles to dislocation movement. However the higher availability of potential dislocation nucleation sites may alternatively result in higher nucleation rates and lower stress states. The experimental results showed in fact that any differences between samples of contrasting grain size were too small to be detected outside of the measurement error. It is concluded that magnesium likely displays a grain size independent dynamic response, similar to aluminium (as discussed in Chapter 5).

# 5

# Effects of cold work on the dynamic strength of aluminium

## 5.1 Overview and motivation

In Chapter 2 it is described how the attenuation of the elastic precursor wave with propagation distance is commonly studied as a means of probing the time-dependence of yield during high strain rate loading. Its decay rate is primarily ascribed to transient effects caused by dislocation movement and generation. Measurements of the propagation of the elastic-plastic wave in the weak shock regime has therefore become a highly valuable tool for understanding the dynamic strength of materials and the physics of dislocations.

Modern iterations of models of precursor decay have advanced to analytically considering or directly simulating the underlying microstructure, including the evolution of dislocation density [7–9, 17–19, 197]. It is now in many cases theoretically possible to account for the effects of processing history and microstructure during deformation. In continuum analytical theories, the amplitude attenuation of the precursor wave is predicted by modelling dislocations through the Orowan equation, given by, [9–11, 16, 198]

$$\dot{\gamma} = \rho_m b v + \dot{\rho}_m b l, \tag{5.1}$$

where $\dot{\gamma}$ is the plastic shear strain rate, $\rho_m$ is the density of mobile dislocations, $b$ is the Burgers, $v$ is the dislocation velocity, and $l$ is the average separation between dislocations. These approaches are described in more detail in Chapter 2. Other numerical microstructure-focused models make the additional leap to directly simulating interface velocimetry results [17–19, 197], whilst dynamic discrete dislocation plasticity models attempt to explicitly simulate the movement and strain fields of individual dislocations [8, 48, 199]. In general, theoretical results show that reducing the mobility of dislocations leads to a decrease in the decay rate of the elastic precursor amplitude, whereas an increase in the initial mobile dislocation density is shown to increase the decay rate.

The main goal of this thesis is to investigate the role of the initial microstructural state on precursor decay. Many of the above models simply circumvent tackling polycrystalline or textured materials by focusing on single crystals or a single slip plane. In Chapter 4, is is shown how knowledge of the crystal orientation distribution in a polycrystal can be used to predict its dynamic strength, given that the single crystal response is known. However, attempts to extend simulations to polycrystals face the additional problem of a lack of experimental studies which include detailed characterisation of the starting microstructure, including the initial dislocation density in particular. As noted for example by Ding et al. [17], studies are too often compelled to rely on calibrated or estimated values, meaning goals are limited to better understanding experimental observations through fitting, rather than quantitatively predicting them. Even where experimentally informed estimations of dislocation density can be obtained, the parameter sensitivity cannot be properly validated as a range of experimental data points is then needed. Moreover, there is often a large number of calibration parameters, such as the dislocation nucleation, multiplication or trapping rates, which have to be determined through fitting [18, 19]. An example can be found in a recent model by Kositski et al. (described in Sections 2.4 and 5.7.3), where the change in the mobile dislocation density is given by,

$$\dot{\rho}_m = A_{nuc}\dot{\rho}_{nuc} + A_{mult}\dot{\rho}_{mult} + A_{trap}\dot{\rho}_{trap} + A_{annh}\dot{\rho}_{anhh}, \tag{5.2}$$

where subscripts $nuc$, $mult$, $trap$, and $annh$ represent the dislocation density evolution through nucleation, multiplication, trapping and annhilation, respectively. While each term is given by a unique expression, they all require a separate rate prefactor, $A$, which has to be adjusted individually in order to obtain a good fit. Having calibrated the dislocation generation term, it is inserted into Equation 5.1 in order to predict the decay rate. Similar treatments can be found in recent work by Austin et al. [18, 200]. It is clear that if variations in initial dislocation density were to be constrained by multiple experimental measurements, the focus could then shift towards more accurately examining the physics of dislocation movement and generation.

This chapter is motivated by the demand to thoroughly investigate the direct and fundamental connection between the evolution of dislocation density and precursor decay. In the low strain rate regime, the well-known effect of cold work is to increase the number of dislocations which, along with grain boundaries, act as barriers to the movement of other dislocations. In short, dislocation pinning and the formation of tangles, as well as the increased presence of longer range strain fields, causes a decrease in the ability of dislocations to move under applied shear stresses. This is often expressed through the Taylor hardening equation, which states that the flow stress in shear, $\tau$, can be related to the total dislocation density, $\rho_d$, following,

$$\tau = AbG\sqrt{\rho_d}, \tag{5.3}$$

where $G$ is the shear modulus and $A$ is a constant [201]. The resulting increase in both yield strength and ultimate tensile strength has been observed in cold worked aluminium [202, 203], although grain boundary strengthening is also responsible. On the other hand, the Orowan equation (Equation 5.1), which underpins our modern understanding of high strain rate deformation, states that increasing the

density of mobile dislocations leads to an increase in the strain rate. Given that the strain rate is not entirely driven by dislocations generated during the shock, then increasing the initial density of dislocations could therefore lead to faster decay rates and lower yield point values. Despite its importance and relative simplicity, the applicability of this exact assumption still needs to be tested experimentally in quantitative terms, and the relative contributions of initial versus generated dislocations investigated further.

Experimentally, the approach should be to test variations of a single material with different initial dislocation densities, achieved through annealing or cold working, and compare their precursor stress measurements. Such studies have indeed been conducted in a range of FCC, BCC and HCP metals. Unfortunately, results to-date are contradictory in their conclusions, with separate findings showing both increasing and decreasing dynamic strength as a result of cold work. Observations of a decrease in the HEL after cold work have been made in studies on Ta [57, 71, 93], Ti [88, 94], Mg [35], Al 2024 and Al 1421 [88, 89]. Conversely, increases in the dynamic strength after cold work have been found in Fe [88], Cu [88], and in a wide range of other aluminium alloys [88–92]. A consistent explanation for these conflicting behaviours is difficult to extract as the initial microstructural states and dislocation densities are in general not known with enough detail.

In Ta, the decrease in dynamic strength was attributed to an increase in mobile dislocations after cold work [57, 71] (although this was not measured directly), as well as increased dislocation nucleation from the higher number of grain boundaries [93]. In apparent contradiction, in similar studies where the dynamic strength increased it was attributed to grain boundary strengthening and dislocation obstruction caused by higher defect densities [88, 89, 91]. In a review by Garkushin et al. in which both of these opposing trends were noted, the latter explanation was used and the decrease in HEL was left an open question [88]. While it is possible that the behaviour is linked to the crystal system, even within

BCC (Ta and Fe) and FCC (Al) systems of different alloying one finds examples of either trend. Consequently, it is evident that the behaviour is highly dependent on the material and its processing history.

The current confusion regarding the role of cold work illustrates the need for the present investigation, in which the initial microstructure is carefully determined. In concrete terms, this entails measuring the changes in grain boundary density, boundary misorientation, crystal orientation, and initial dislocation density, all within the same study. As an example, analysis of the cold work-induced decrease in HEL observed in Ti [88, 94] is hampered by the changes to the crystal orientations during processing not being clear. As was shown in Chapter 4, this factor is critical for HCP systems. In fact in the study on Mg by Yu et al., the decrease in HEL after ECAP was attributed to a weakening of the texture as compared to the as-received material [35]. This change in orientations likely led to an increase in activity of basal slip, which is a much softer deformation mode. What is unknown however is how much a potential increase in dislocation density may have also affected these results. In fact the initial dislocation density was (to the author's knowledge) measured in only two of the aforementioned studies on cold work, and then only in a subset of the samples under investigation [89, 90].

The present study is in addition driven by the need to extend high strain rate studies to materials with realistic processing histories and real engineering applicability. The relatively low density and high strength of aluminium and it's alloys makes it suitable for a wide variety of applications in the aerospace and automotive industries. Grain refinement is a proven method for improving its strength, which has led to the growing interest in ultrafine-grained (UFG) and nanocrystalline (NC) materials produced using severe plastic deformation (SPD) methods. Rotary swaging was here employed in order to produce a UFG material with high dislocation and grain boundary densities in both high-purity aluminium (5N-Al, 99.999% pure) as well as Al 6082-T6. Pure aluminium was

chosen as a material which, despite investigations on the effects of grain size [81, 204], temperature [25], and single crystal orientation [59], is still lacking a study where direct quantification of the initial dislocation density is combined with measurements of the precursor decay phenomenon. While it displays only a limited decay rate at propagation distances above 1 mm, significant precursor decay has been observed in thinner samples [21–24].

For pure aluminium, the primary metallurgical barriers to dislocation motion are the interactions with other dislocations or boundaries. It can therefore be contrasted to the 6082 alloy, where dislocation mobility is additionally obstructed by the presence of secondary phase particles. Al 6082 is commonly used in automotive and structural applications, but is currently seldom studied in the high strain rate regime. Aside from an investigation by Millett on the lateral stress and hardening behaviour behind the shock front, most dynamic strength measurements of aluminium alloys focus on the similar Al 6061 [22, 23, 75, 76, 79].

To summarise, the main novelties and goals of this chapter are as follows:

1. Measure precursor decay in new materials, namely SPD processed pure aluminium, and SPD and conventional Al 6082.

2. Measure the microstructural changes in pure aluminium and Al 6082 as a result of rotary swaging.

3. Combine both detailed material characterisation, especially initial dislocation densities, and precursor decay measurements in order to investigate the effects of varying initial dislocation densities on the decay rate.

4. Consider the role of grain boundaries during dynamic yielding.

5. Place the new measurements in context with literature reports, in which the effects of prior cold work in shock loading experiments are inconsistent.

6. Compare the initial dislocation densities to analytical model predictions, and evaluate the influence of dislocation generation.

7. Compare experimental measurements to velocity profile simulations, and investigate variations in model fitting parameters.

8. Consider the strain rate dependence of the effects of prior cold work, and the role of mobile versus immobile dislocations.

The remainder of this chapter is structured as follows: the processing history of the two materials under study is explained in Section 5.2; results from material characterisation using TEM and EBSD are discussed in Section 5.3; the high strain rate plate impact experiments are detailed in Section 5.4; and the resulting combined microstructural and dynamic strength data is discussed in Section 5.5. Section 5.6 contains a brief analysis of the orientation data, using methods developed in Chapter 4. Finally, Section 5.7 is dedicated to the application of two different analytical models to the current data, in addition to detailing the preliminary results from a modelling collaboration aimed at simulating the experimental shock wave profiles gathered during this project.

## 5.2 Material processing and rotary swaging

The material used in the present study was obtained from commercially-sourced rods of 5N-Al ("five-nines" i.e. 99.999 % pure Al) in the as-drawn state, and Al 6082-T6 with chemical composition as shown in Table 5.1, in the extruded state.

**Table 5.1:** Chemical composition of the Al 6082-T6 alloy (wt .%).

| Al | Si | Fe | Cu | Mn | Mg | Zn | Ti | Cr |
|---|---|---|---|---|---|---|---|---|
| bal. | 1.01 | 0.22 | 0.02 | 0.54 | 0.60 | 0.02 | 0.01 | 0.01 |

In order to establish a baseline material state and reduce any effects of its processing history, the 5N-Al was annealed for 1h at 673 K [205–207]. This resulted in recrystallised grains with grain sizes around 300 $\mu$m, as shown in Section 5.3.1. The Al 6082-T6 was not annealed given that the tempered states are

common forms in which the alloy is used. Annealing the alloy would significantly alter its material properties, and then require careful consideration of the ageing treatment in order to produce a conventional material state. Indeed the T6 designation indicates that the material has been specifically processed by solution treatment and artificial aging, which enhances the yield strength by allowing alloying elements to form precipitates. The main result is an even distribution of $Mg_2Si$ second-phase precipitates which act as obstacles to dislocation movement.

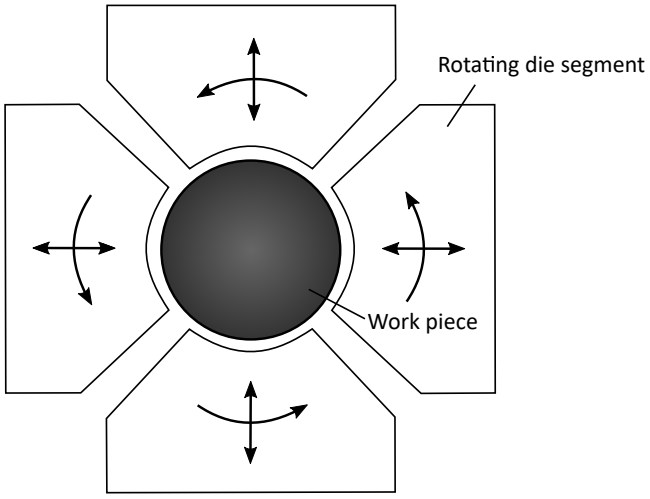



**Figure 5.1:** Schematic of rotary swaging. A cylindrical work-piece is fed through a set of dies which incrementally reduce the cross-section through repeated radial compressions. After each radial compression the dies are rotated and then re-applied.

As the goal of this study was to investigate dynamic strength at varying initial dislocation density, a method to introduce large changes in defect density had to be applied. This is typically achieved with severe plastic deformation (SPD), which describes a family of metalworking techniques which involve imposing very high strains through high stress or shear, increasing strength through grain refinement. Typical industrial metals will have grain sizes on the orders of 10 to 100 $\mu$m, a good example being the as-received Al 6082 used here. With SPD however one can produce microstructures consisting of very high defect densities and grain sizes in the sub-micron range, typically categorised as either ultrafine grains (UFG, grain size $< 1$ $\mu$m) or nanocrystalline structure (NC, grain size $< 100$ nm).

There exists a wide range of SPD techniques which can be utilised to produce a high dislocation density and a UFG structure, including equal channel angular pressing (ECAP) [35, 96, 208, 209], accumulative roll-bonding (ARB) [131, 137], high-pressure torsion (HPT) [207], and rotary swaging (RS) [202, 203, 210, 211]. Swaging was chosen for this study and is illustrated in Figure 5.1. It is a technique in which the cross-section of a cylindrical work-piece is incrementally reduced by radial compressions from a set of dies, usually under cold-working conditions. The dies are continually rotated as material is fed through the machine at speeds usually around a millimeter per revolution, resulting in forming speeds of 100 mm per minute or more [211]. The high output rate of swaging distinguishes it from other SPD methods which are often limited by smaller sample sizes and higher costs. As an example, the entire length of 5N-Al rod procured in this study, at a length of 350 mm, could be swaged within a few minutes at low cost. The effects of swaging on the material properties of aluminium have been studied in alloys of varying impurity content and alloying, including Al 6082 [202, 212–215].

The annealed 5N-Al and as-received Al 6082 rods were subjected to up to three passes of rotary swaging at ambient temperature. Samples were subsequently created from material with 0, 1 and 3 swaging passes, hereafter designated as S0, S1 and S3 respectively. The true strains, listed in Table 5.2, are here defined as,

$$\epsilon = \ln \frac{A_0}{A}, \tag{5.4}$$

where $A_0$ and $A$ are the cross-sectional areas before and after swaging respectively. Vickers hardness tests, also listed in the table, showed a moderate increase in hardness with increasing swaging passes. Note that the Al 6082 was subjected to twice the strain per swaging pass than the 5N-Al, which was a consequence of the material dimensions and the corresponding dies available to Elmill Ltd (the supplier) at the time of swaging. As is further discussed in Section 5.3.1, it would in retrospect have been interesting to investigate the 5N-Al at the same peak strain of 2.8 that was reached in the Al 6082. However, for the purposes of this study, the differences in strain between the two materials have little impact

on research outcomes as direct comparisons between the two is not the current focus. Instead, each material is investigated primarily within the context of its own microstructure and dislocation density. The large differences in the behaviour of the two materials during swaging mean that comparisons of dynamic properties at the exact same strain would have been of limited usefulness.

**Table 5.2:** Material properties of the 5N-Al and Al 6082 used in this study. Sample types are designated as S0, S1, and S3 for 0, 1 and 3 swaging passes respectively. Dislocation densities are estimated from TEM measurements (see Section 5.3.2), and grain boundary densities are estimated from EBSD results (see Section 5.3.1).

| Material | Swaging passes | True areal strain | Dislocation density ($10^{13}$ m$^{-2}$) | HAGB density ($\mu$m$^{-1}$) | LAGB density ($\mu$m$^{-1}$) | Vickers hardness |
|---|---|---|---|---|---|---|
| 5N-Al S0 | 0 | 0 | $0.4 \pm 0.1$ | 0.007 | 0.013 | 20 |
| 5N-Al S1 | 1 | 0.5 | $5.3 \pm 1.6$ | 0.012 | 0.058 | 21 |
| 5N-Al S3 | 3 | 1.4 | $11.2 \pm 3.4$ | 0.042 | 0.126 | 24 |
| Al 6082 S0 | 0 | 0 | $12.9 \pm 3.9$ | 0.241 | 0.229 | 106 |
| Al 6082 S1 | 1 | 1 | $38.7 \pm 11.7$ | 0.626 | 1.023 | 113 |
| Al 6082 S3 | 3 | 2.8 | $29.2 \pm 8.8$ | 4.119 | 2.575 | 122 |

## 5.3 Material characterisation

### 5.3.1 EBSD characterisation

Samples for EBSD were cut in both the longitudinal and transverse sections of the Al 6082 and 5N-Al rods and prepared using methods explained in detail in Section 3.3.1. The EBSD characterisation was performed with a Zeiss Merlin SEM equipped with a Bruker Quantax EBSD system and eFlash camera, operating at 20 kV. The step size of the EBSD scan was varied from 110 nm to 5 $\mu$m depending on the grain size of the specimens. Figures 5.2-5.5 show results collected from representative regions of the samples, analysed using the MTEX package available for MATLAB [152]. High angle grain boundaries (HAGBs) are defined by misorientations of $>$15°, and low angle grain boundaries (LAGBs) by 2-15°, shown as black and red lines respectively in the grain boundary plots.

The microstructural morphology is observed to consist primarily of coarse grains elongated along the extrusion direction, interspersed by finer equiaxed grains of sizes $<10$ $\mu$m for the 5N-Al and $<1$ $\mu$m for the Al 6082. In the 5N-Al, the initial thickness of the elongated grains is approximately 300 $\mu$m. After 1 and 3 swaging passes, the size of the coarse grains remains similar, however the material becomes heavily populated with small equiaxed grains with an average size of 11 $\mu$m for S1 and 5 $\mu$m for S3. In the Al 6082 alloy, the starting material exhibits a very strong fibrous structure along the swaging direction. The initial thickness of the elongated grains is approximately 9 $\mu$m, which is reduced to 4 $\mu$m and 3 $\mu$m for S1 and S3 respectively. The S1 and S3 states also have significant populations of ultrafine grains with an average size of around 600 nm in both cases.

It is known that the quality of an EBSD scan is highly dependent not only on crystal orientation but also on the presence of lattice defects such as dislocations or grain boundaries. Regions in the sample which contain dislocation clusters or low angle grain boundaries are therefore expected to produce low pattern quality. Assuming the sample surface finish is not damaged, regions where the pattern quality is reduced to the point that indexing is impossible represent evidence of very high dislocation densities [49]. Since the sets of samples shown in Figures 5.2b-d and 5.3b-d were prepared identically, the increasing fraction of unindexed (black) regions with number of swaging passes found in the EBSD scans therefore suggest an increased accumulation of low angle grain boundaries and very high dislocation densities. The same conclusion can be drawn from the overall reduction in the pattern quality of the indexed regions (not shown in the figure).

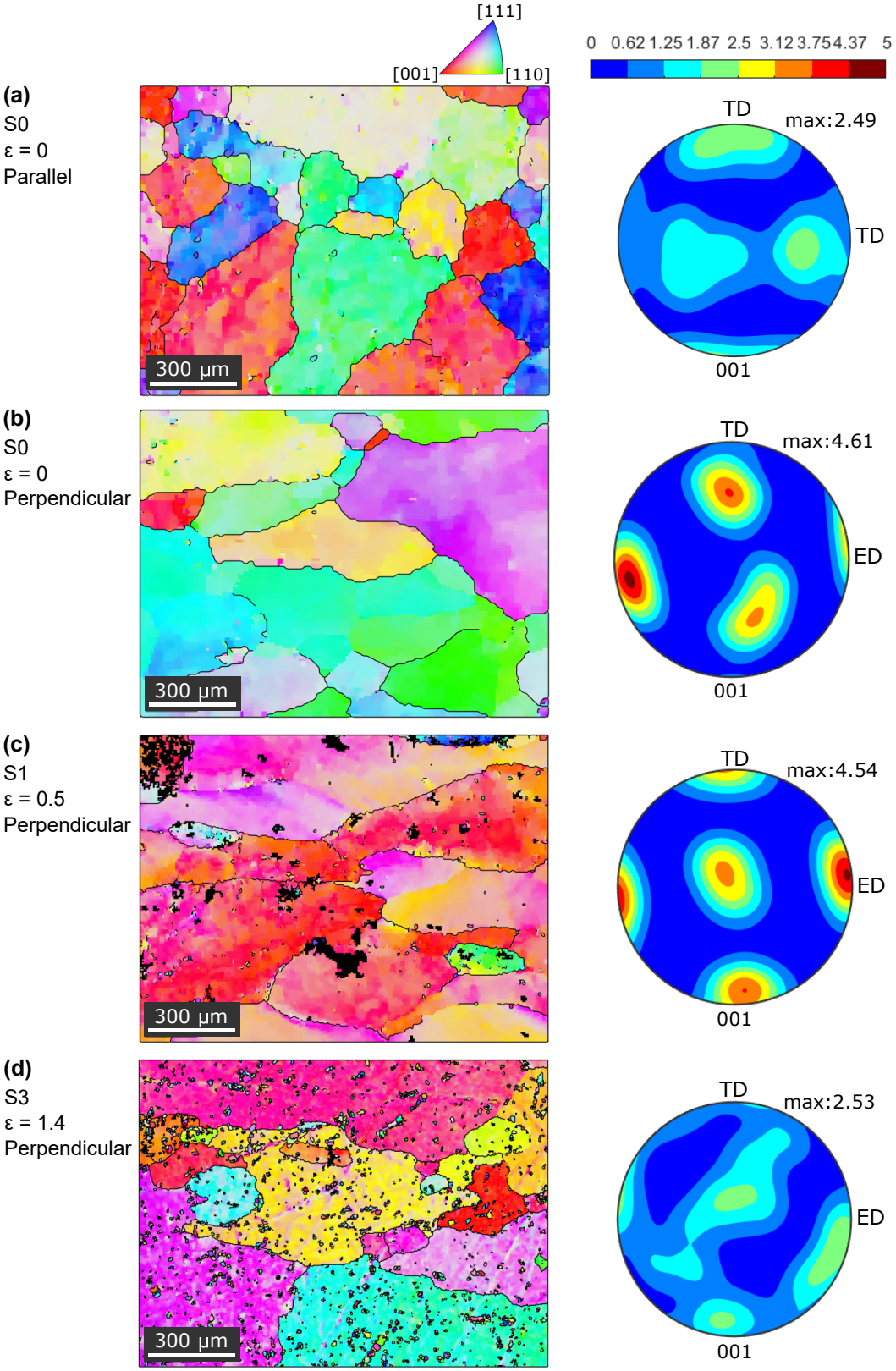



**Figure 5.2:** EBSD IPF maps and pole figures for swaged 5N-Al with a) 0 passes scanned parallel to ED, b) 0 passes perpendicular to ED, c) 1 pass perpendicular to ED, and d) 3 passes perpendicular to ED (maximum times random as shown). Note that ED is also the impact direction.

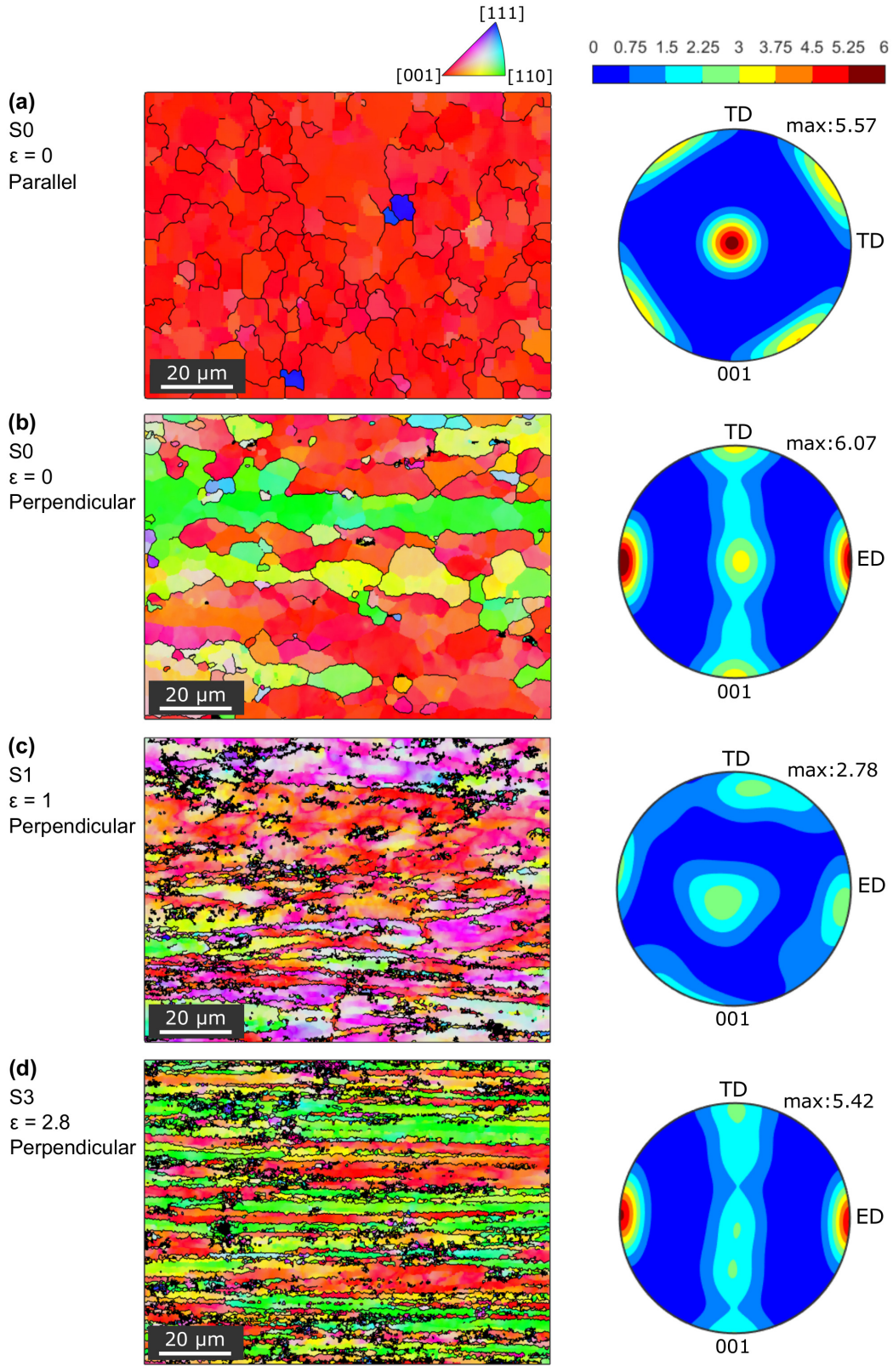



**Figure 5.3:** EBSD IPF maps and pole figures for swaged Al 6082 with a) 0 passes scanned parallel to ED, b) 0 passes perpendicular to ED, c) 1 pass perpendicular to ED, and d) 3 passes perpendicular to ED (maximum times random as shown). Note that ED is also the impact direction.

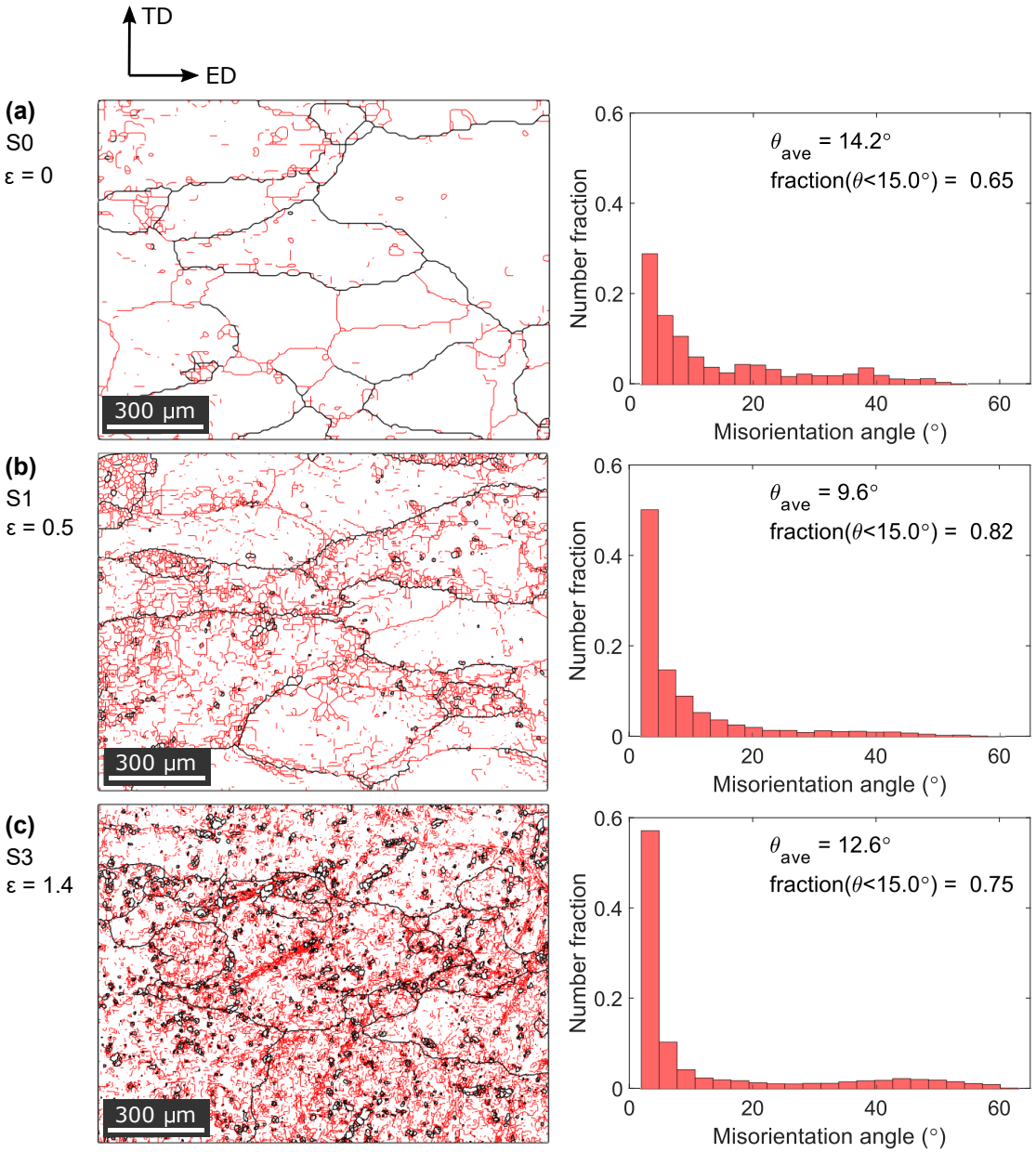



**Figure 5.4:** EBSD grain boundary maps and misorientation distributions for 5N-Al samples with increasing swaging passes scanned perpendicular to the extrusion direction.

Listed in Table 5.2 are the resulting boundary densities, calculated as $\rho_{GB} = L/A$, where $L$ is the total length of boundaries and $A$ is the total area of the scan. The boundary density increases rapidly with increasing swaging, as is also evident from the boundary plots in Figures 5.2-5.3. The corresponding misorientation distribution histograms show that at strains between 0.5 and 1.4 (which encompasses samples 5N-Al S1, 5N-Al S3 and Al 6082 S1), the fraction of LAGBs reaches a peak of 0.82 and 0.61 for the pure and alloyed materials,

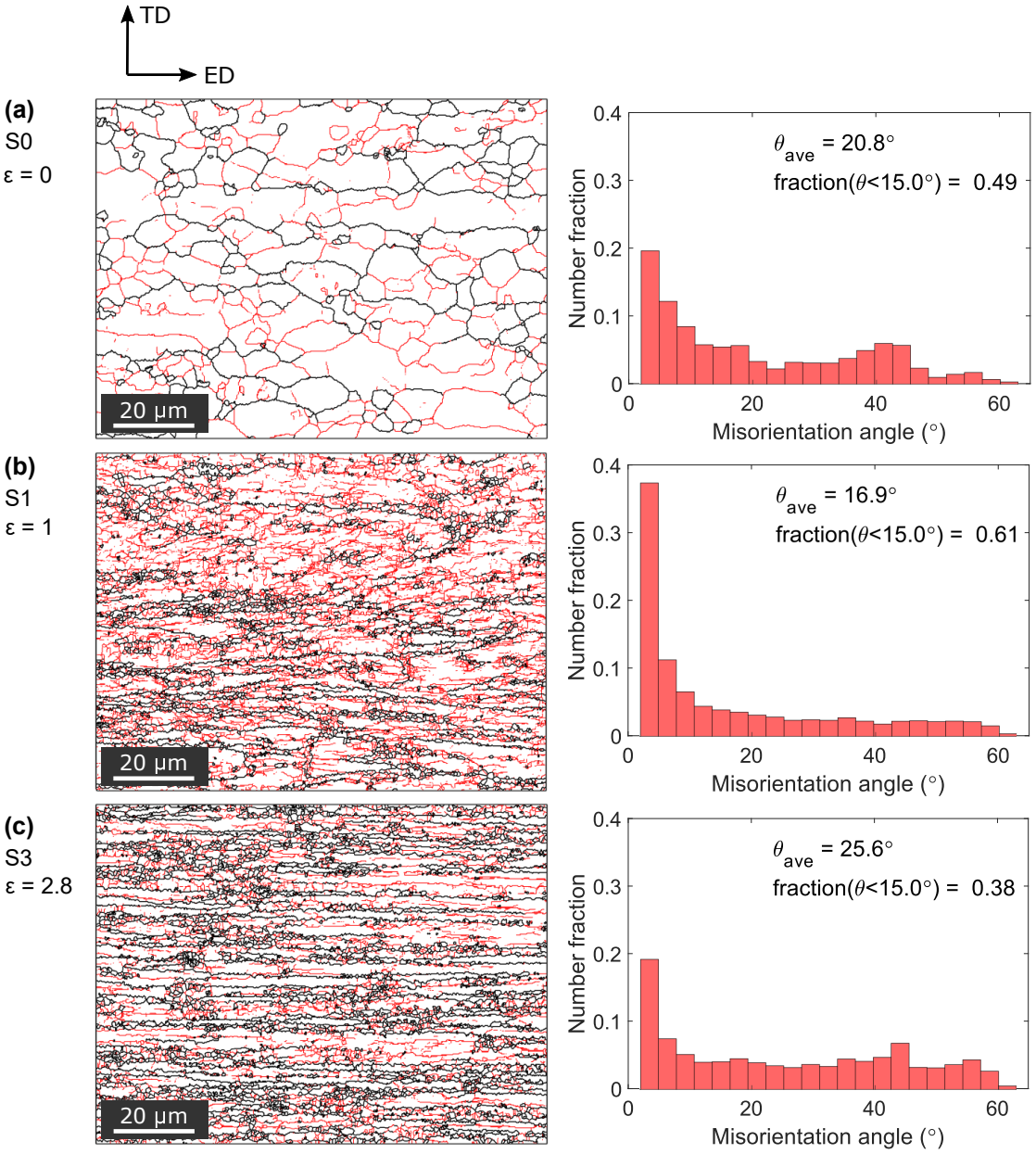



**Figure 5.5:** EBSD grain boundary map and misorientation distributions for Al 6082 samples with increasing swaging passes scanned perpendicular to the extrusion direction.

respectively. The increased misorientation within the grains and the formation of subgrains is evidence of the large increase in dislocation density, as dislocation tangling promotes the formation of LAGBs [207]. However, at the highest studied strain of 2.8 in Al 6082 S3, it is observed that the fraction of LAGB is decreased to below that of the as-received material. It is likely that the dislocation density has started reaching a saturation level in which continued straining causes annihilation of dislocations at the LAGBs, which simultaneously causes an increase in the grain

misorientation angles [207, 216]. The production of ultrafine grains through SPD can therefore be understood as dislocation sub-boundaries with low stability, initially created at low strains, gradually being transformed into ultrafine grains consisting of higher stability high angle boundaries [217]. Small secondary peaks in the misorientation angles are observed between 40-50°, similar to swaged commercially pure Al [202], which is the peak for a randomly oriented polycrystal.

The sequence of grain rotations is also evident from analysis of the pole figures. It is initially observed in the rods before swaging that the 001 poles are preferentially oriented along the extrusion direction in both the pure and alloyed material. After swaging to strains of 1 and 1.4 in the Al 6082 S1 and 5N-Al S3 respectively, significant grain rotation has occurred and the crystallographic orientations are more randomised. Note however that in the 5N-Al, the large grain size as a consequence of annealing meant that it is possible too few grains were measured to gain a complete picture of the texture (as can be observed from the difference in pole figures between the two S0 measurements in 5.2a-b). Finally, at a strain of 2.8 in the Al 6082 S3, the 001 axes have once again become preferentially oriented along the swaging direction, similar to the S0 state. These changes in texture are further evidence of the formation first of LAGBs followed by consolidation into HAGBs. At lower strains, the creation of more randomly oriented subgrains inside the initially strongly aligned material causes the increased spread of grain orientations as shown in the 5N-Al S3 and Al 6082 S1 pole figures. At the highest strain in Al 6082 S3, this is no longer the case as the majority of LAGBs have been absorbed into HAGBs. During this process the consolidated grains which remain have been reoriented back towards their preferred direction, and the random spread of orientations caused by subgrains has been reduced.

### 5.3.2 TEM characterisation

The steps used to prepare samples for TEM, cut in the transverse section of the rod, are covered in detail in Section 3.3.2. TEM imaging was carried out with a JEOL JEM-2100 operating at 200 kV. Dislocation densities were estimated using Ham's linear intercept method [136] and are listed in Table 5.2. A full description of the dislocation counting technique and the associated errors is given in Section 3.3.3. On the whole, the results are in excellent agreement with pure Al and Al 6082 processed by other SPD methods [131, 137, 144, 145], with uncertainties similar to those reported elsewhere [49, 137]. The uncertainty is acceptable given that the dislocation densities used in models are often estimated simply to orders of magnitude [9, 18, 19]. Representative TEM bright-field images from the 5N-Al are shown in figure 5.7. The S0 sample displays a dislocation density on the order of $10^{12}$ m$^{-2}$, indicative of an annealed material with a prior history of extrusion which has partially recovered but not fully recrystallised [132, 137]. Very few grain boundaries are observed, reflecting the large grain size and low boundary density also found in the EBSD analysis.

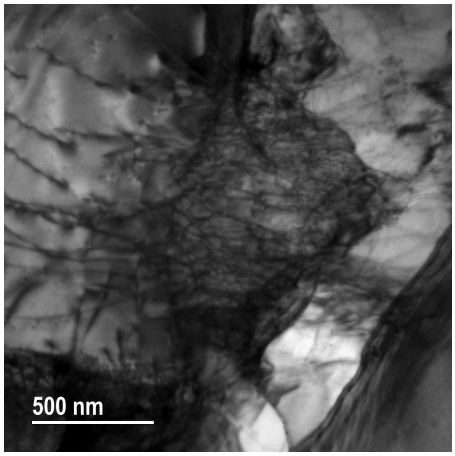



**Figure 5.6:** TEM micrograph of 5N-Al S3 showing the substructure in a high dislocation density grain. This example displays the main difference between the S1 and S3 materials. In S1 most dislocations are concentrated into ordered arrays and cell boundaries. In S3 however, a large fraction of grains display intense dislocation tangling between boundary walls such as the one imaged here. Line intercept analysis of a further magnified version of this image produced a dislocation density of $4 \times 10^{14}$ m$^{-2}$ .

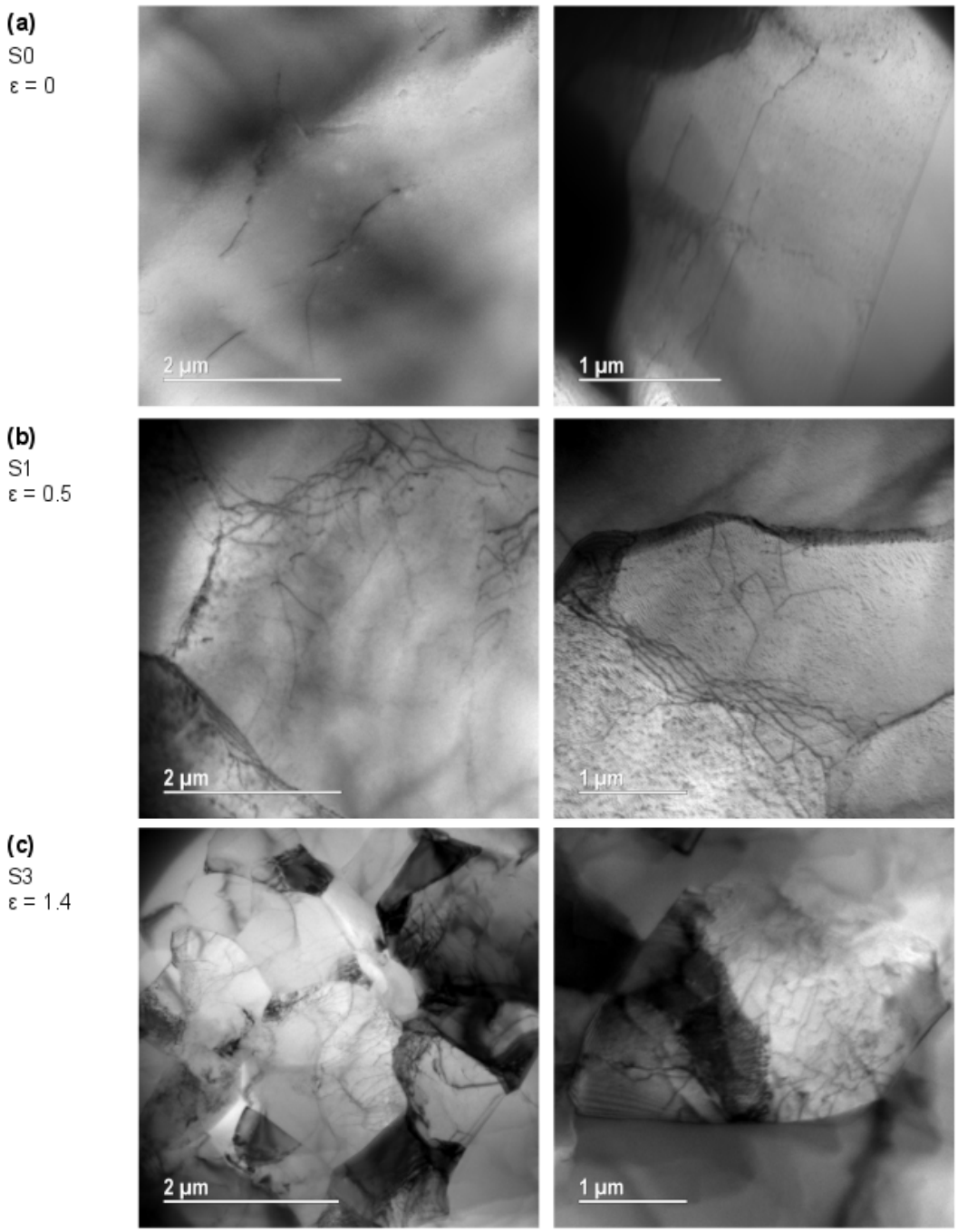



**Figure 5.7:** TEM micrographs of 5N-Al at various magnifications of the a) annealed (S0), b) 1 pass swaged (S1), and c) 3 pass swaged (S3) samples. The S0 sample displays a low density of dislocations and grain boundaries, as expected for an annealed material. S1 shows evidence of the formation of dislocation cells and subgrain boundaries. Cell interiors are mostly free of dislocations. In S3, the grain size has decreased substantially, with high numbers of ultrafine grains which display high inner dislocation densities.

After the first swaging pass, the material displays a significant increase in dislocation density. A typical cellular substructure is observed including dislocation pile ups showing evidence of subgrain boundary formation, with low dislocation densities at the cell interiors [14]. Dislocation walls are formed as accumulated or stored dislocations are arranged into energetically favourable configurations [154]. Similar substructure in swaged Al 1070 has been found by Yang [203] and in pure Al by El-Madhoun [218]. The mutual trapping of mobile dislocations and the formation of cellular structures is generally accepted to be the primary work-hardening mechanism in pure aluminium at this stage of rapid hardening [218]. After 3 passes, grain development has progressed substantially. The loose cell walls comprised of entangled dislocations produced at lower strains in S1 have condensed, and many of the dislocation arrays or sub-boundaries have formed ultrafine grains with high angle boundaries. Misorientations across boundary walls are clearly visible as large changes in the diffraction contrast. Dislocation densities have reached above $10^{14}$ m$^{-2}$, similar to ARB processed pure Al [137], with frequent dislocation tangles observed inside grain interiors such as the one shown in Figure 5.6. This example displays the large difference in substructure between the S1 and S3 materials. In S1, all dislocations are easily distinguished at the higher magnifications shown in Figure 5.7, with most dislocations concentrated in boundary walls. In S3 however, further magnification was required for the large fraction of UFGs in which inner dislocation densities reached values of up to $4 \times 10^{14}$ m$^{-2}$.

In the Al 6082, shown in figure 5.9, the starting as-received material displays an already high dislocation density, as anticipated from an extruded precipitation-hardened alloy, with a much more randomised structure as opposed to the orderly formation of cells seen in the pure aluminium. This trend persists in S1, in which individual dislocations are no longer easily distinguishable at the magnifications shown in the Figure 5.9, and frequent observations are found of heavy dislocation tangling similar to other SPD processed Al 6082 [219–221]. A magnified view of the high dislocation density region in the RHS image of Figure 5.9b is shown

in Figure 5.8, showing a highly tangled structure with an estimated dislocation density of around $7 \times 10^{14}$ m$^{-2}$.

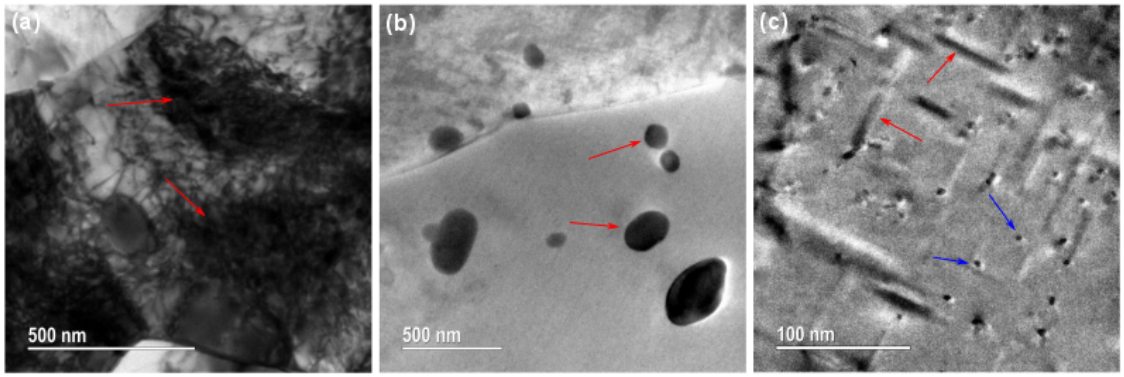



**Figure 5.8:** TEM micrographs of Al 6082 showing a) a magnified view of the substructure in the high dislocation density grain from Figure 5.9b with a dislocation density of $7 \times 10^{14}$ m$^{-2}$ (red arrows indicate dislocation tangles), as well as what can likely be identified as b) $\beta$-$Mg_2Si$ precipitates (red arrows), and c) $\beta'$-$Mg_2Si$ phase aligned along the <100> direction of the matrix (red arrows), along with Mn-containing dispersoids (blue arrows).

Further grain refinement is evident after 3 passes, showing a high fraction of sub-micron sized and even nanostructured grains with very high densities of internal dislocations. However, compared to S1, the overall dislocation density has actually decreased (as shown in Table 5.2). The change can be seen qualitatively in the micrographs, where the density of the dislocation tangles has decreased to the point that individual dislocations are once again distinguishable. As discussed in Section 5.3.1, this is likely a consequence of reaching a saturation stage where hardening is balanced by recovery mechanisms. It has indeed been reported that continued heavy plastic deformation leads to a saturation stage in grain refinement where further straining can instead cause grain coarsening and dislocation annihilation [222]. At the submicron or nanoscale, grain boundary migration can become dominant to the point that grain coarsening occurs at room temperature [223]. The evolution of misorientation distributions and formation of UFGs observed in the EBSD measurements suggests a high degree of dislocation absorption into HAGBs. The low melting temperature and high stacking-fault energy of aluminium also makes dislocation annihilation through dynamic recovery likely [137, 216]. In this high strain regime, dislocation multiplication due to continued straining is

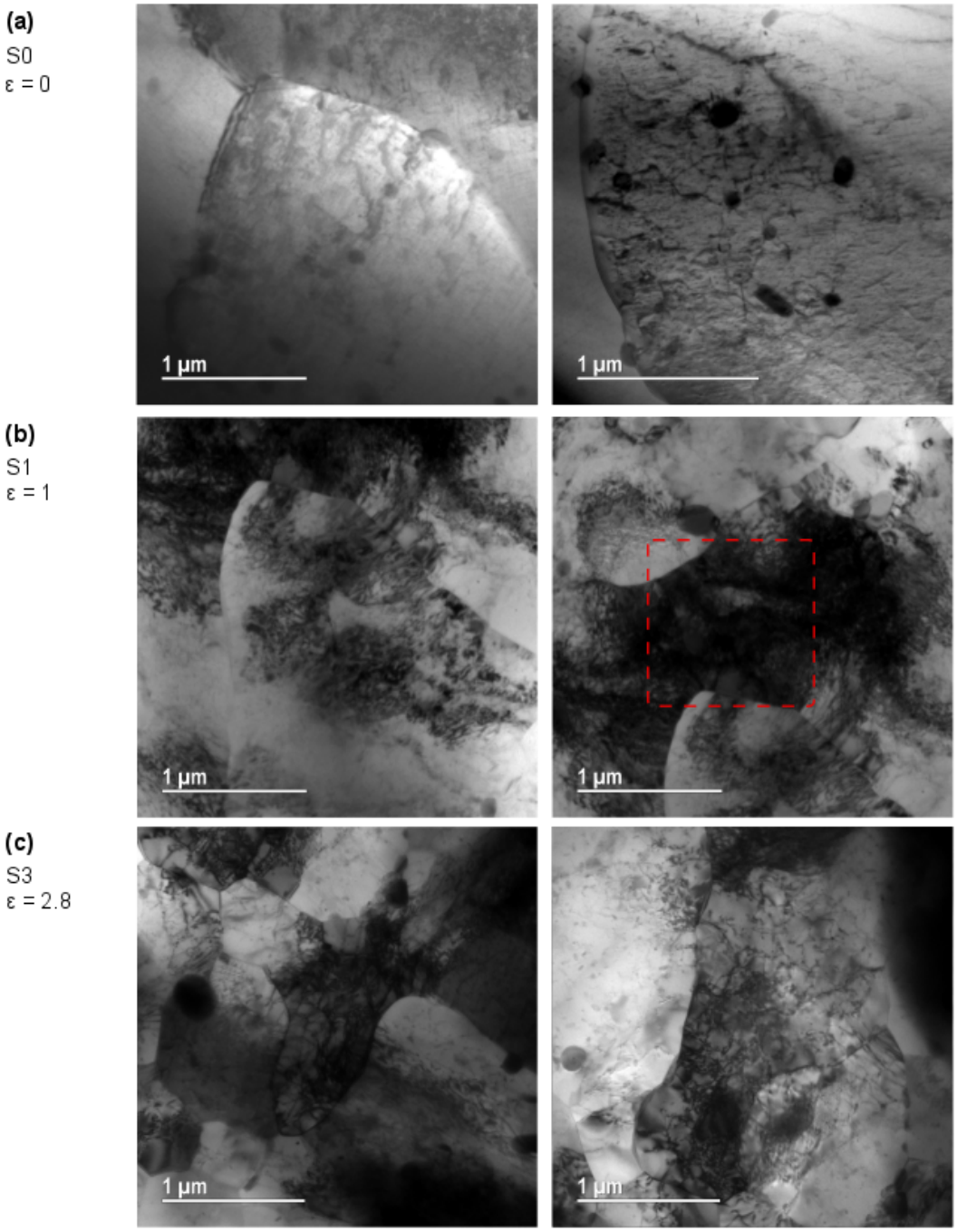



**Figure 5.9:** TEM micrographs of Al 6082 in the a) as-received (S0), b) 1 pass swaged (S1), and c) 3 pass swaged (S3) states. A relatively high dislocation density is found even in the S0 samples. In S1, the dislocations have started to form dense clusters and are no longer clearly distinguished at the magnifications shown here. A magnified view of the high dislocation density region delineated by the red box in the RHS image in b) is shown in Figure 5.8. In S3, grain refinement has progressed substantially, exhibiting frequent sub-micron sized grains, however the dislocation density inside these grains is seen to have decreased when compared to S1.

therefore overshadowed by annihilation and grain boundary migration. Indeed a decrease in dislocation density after reaching the saturation stage has been observed in ARB processed aluminium [224] (dislocation density decreased by an order of magnitude when comparing 2 and 7 cycles), and in ECAP processed copper [139] (dislocation density after 4 and 8 passes decreased from 3.2 to 2.1 $\times 10^{14}$ m$^{-2}$ respectively). The GND density analysis performed on the present specimens, as discussed in Section 5.3.3, also confirms a decrease in the dislocation density. It is therefore unlikely that further straining in the Al 6082 beyond 3 passes would result in any increase in dislocation density; in fact for most metals the dislocation density ceiling is around $10^{15}$ m$^{-2}$ [222].

It is worth noting that, in contrast to the pure Al, grain interiors in the Al 6082 even in the unswaged state are densely populated with dislocations, which can be explained by the addition of alloying elements. The Al 6082 contains a substantial presence of second-phase $Mg_2Si$ particles in various stages of its precipitation sequence ($\beta''$, $\beta'$ and $\beta$), as well as Mn-containing dispersoids [133, 225], both of which are shown in Figure 5.8. As the effect of precipitates is to act as pinning points and prevent absorption at grain boundaries, the alloy exhibits a smaller relative proportion of mobile dislocations and a higher density between boundary walls. This is of course the original purpose of introducing precipitates to the matrix, as they strengthen the material by inhibiting dislocation movement and by enabling greater dislocation densities (see Sections 5.5.1- 5.5.2).

In fact, it has been shown that Mg and Si, the two primary alloying elements in Al 6082, are the most efficient out of the options available in aluminium alloys for decreasing the stacking fault energy [226]. In the pure Al, the higher stacking fault energy causes a narrow separation of partial dislocations, facilitating dislocation motion due to the ease of cross slip and climb during deformation [227]. This promotes the formation of the observed cellular structure in which the cell walls are formed out of tangles of dislocations, with the material being much less likely to store dislocations between these boundaries. In fact, the low

presence of dislocations between boundaries in the pure Al is itself evidence of dynamic recovery [203, 208, 216]. An example of this process would be opposite-signed dislocations annihilating, after which the remaining excess of like-signed dislocations rearrange into the ordered arrays seen here. The result is the formation of low angle grain boundaries which accommodate the lattice curvature, as further discussed in Section 5.3.3. Compared to this, the substructure in the alloy after deformation is much more disorganised and random, as it is unable to form the cellular structures seen in the pure material [228]. So whilst pure aluminium dynamically recovers during the SPD deformation, the alloy is more likely to store dislocations through development of the UFG structure.

### 5.3.3 Estimation of GND density

A concern with TEM data, raised in Section 3.3.3, is that of the localised nature of each measurement. It is possible that the area imaged using TEM is too small to build an accurate average of the bulk state. It was therefore decided that a small comparative study should be performed in which the dislocation density is characterised using another, more macroscopic measurement tool. The results are detailed in this section, in which EBSD data was used to calculate GND densities in the current samples.

The GND densities, $\rho_{GND}$, calculated using the methods described in Section 3.3.3 are shown in Figure 5.10. Apart from 5.10d, the EBSD data used for these calculations is identical to what is used for the IPF maps in Section 5.3.1. The density is calculated for each spatial point and averaged to produce the overall average GND density (in $m^{-2}$) shown below each map. Starting with the 5N-Al results, the expected increase in dislocation density with increasing swaging passes is observed. Remarkably good agreement is found for the 0 pass and 1 pass samples when comparing the densities calculated here with those extracted from the TEM measurements, shown in Table 5.2, although it should be kept in mind that only GNDs and few statistically stored dislocations (SSDs, also covered in

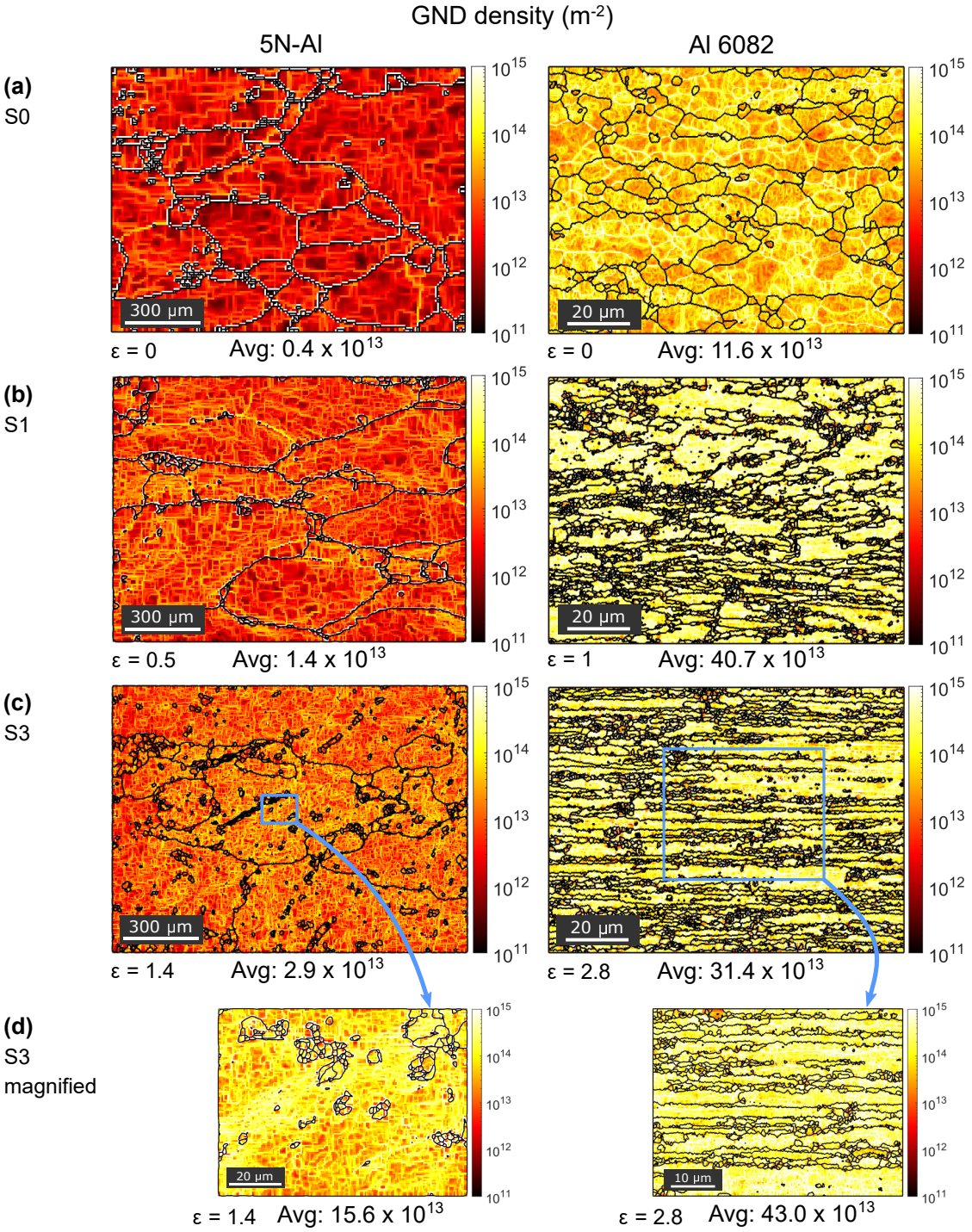



**Figure 5.10:** Estimated GND densities in 5N-Al (left column) and Al 6082 (right column) with a) 0 passes, b) 1 pass, and c) 3 passes of rotary swaging. In d) the calculations are repeated on a separate higher resolution scan taken within a smaller area of the scans in c). The average GND density is shown below each EBSD map. In the 5N-Al an increase in GND density is observed with increasing swaging passes, whilst in the Al 6082 the GND density increases for S1 and subsequently decreases for S3. Both of these trends are consistent with TEM measurements.

Section 3.3.3) will be accounted for in the current calculations. Only a moderate increase in the $\rho_{GND}$ is observed after the third pass, still on the order of $10^{13}$ m$^{-2}$. As is further discussed below, it is possible that the increase in dislocation density observed in TEM between S1 and S3 is caused primarily by SSDs found between boundary walls. It is also found that when scanning a smaller area within the same region but at a higher resolution (or smaller step size), the estimated $\rho_{GND}$ is instead on the order of $10^{14}$ m$^{-2}$.

Inspection of the Al 6082 results again shows very good agreement with TEM estimates, in this case for all sample variants. Notably, the decrease in GND density from S1 to S3 is consistent with the TEM measurements. When scanning a smaller area in S3 at a higher resolution, the GND density is also once again higher than the lower resolution map. This exhibits a significant characteristic where decreasing the step size can lead to an increase in the measured $\rho_{GND}$. This occurs when SSDs, consisting for example of dipoles or multipoles with opposite sign, are split into two different measurement points. While their individual lattice strains would ordinarily cancel each other out if both were contained within a single step, when measured separately they individually contribute to the lattice strain [229]. Other concerns include the level of denoising applied to the EBSD maps before calculating the curvature tensor. Since numerical differentiation usually produces noise, it is possible GND calculations represent over-estimations especially in the higher resolution scans where noise is exacerbated [151].

It should again be emphasised that while some SSDs may contribute to the measurement, the dislocation density estimations using EBSD data are comprised primarily of GNDs and are therefore not directly comparable to the TEM measurements. Zhu et al. performed calculations measuring both types of dislocation densities in quasistatically compressed polycrystalline nickel, in which $\rho_{GND}$ is calculated with EBSD methods and $\rho_{SSD}$ is estimated by subtracting $\rho_{GND}$ from a total dislocation density estimated using a Taylor hardening model [230]. An illustration of the proposed evolution of GND and SSD densities is shown in Figure

5.11. At a low starting strain of 0.05, they estimate the material has a higher $\rho_{GND}$ ($\approx 2 \times 10^{14}$ m$^{-2}$) than $\rho_{SSD}$ ($\approx 9 \times 10^{13}$ m$^{-2}$). GNDs are concentrated at hot spots such as grain boundaries and triple junctions, illustrated in Stage I in Figure 5.11. Further deformation to Stage II involves an increase in the GND density and the formation new sub-boundaries. Meanwhile however $\rho_{SSD}$ increases at a faster rate, forming tangles and cellular substructure, and eventually overtakes $\rho_{GND}$ at strains around a 0.1 (Stages II-III). At the highest investigated strain of 0.5, rapid non-linear multiplication of SSDs has led to a higher $\rho_{SSD}$ ($\approx 9 \times 10^{14}$ m$^{-2}$) than $\rho_{GND}$ ($\approx 4 \times 10^{14}$ m$^{-2}$). While it is shown that the two densities are within the same order of magnitude to plastic strains up to 0.5, it is known that beyond these strains the SSD density may reach an order of magnitude higher than the GND density [230, 231]. Indeed, a similar investigation by Muransky into a nickel alloy found $\rho_{GND}$ on the order of $10^{13}$ m$^{-2}$ and $\rho_{SSD}$ around $10^{14}$ m$^{-2}$ at strains as low as 0.1 [154].

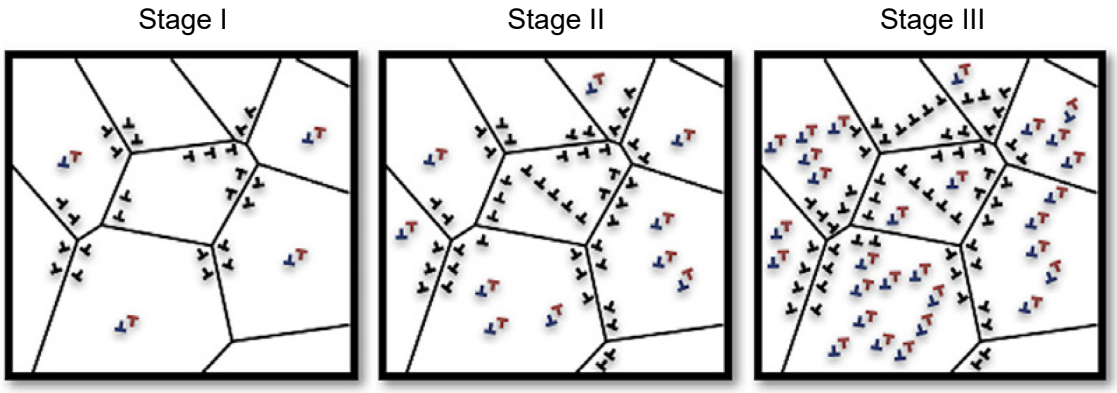



**Figure 5.11:** Illustration of three stages of GND and SSD evolution with increasing strain [230]. Black dislocations represent GNDs, while blue and red dislocations represent SSD pairs. The grain morphology is kept unchanged for illustration purposes.

The above analysis provides further context for the evolution of dislocation structures as discussed in Section 5.3.2. Given the strains of 0.5 and 1.4 in the S1 and S3 5N-Al respectively, it is suggested that the higher dislocation density observed in the TEM micrographs for S3 is made up primarily of SSDs. Conversely, it is likely that a significant portion of dislocations in the lower strain material

are GNDs. This can be tied to the frequent observation of dislocations gathered into ordered walls and subgrain boundaries in the 1 pass 5N-Al sample, indicative of the early straining producing an accumulation of GNDs. The 3 pass samples exhibit dense distributions of dislocation tangles within boundary walls, as is more typical of SSDs. On the whole this suggests that the low strain GND measurements in the 5N-Al should match the TEM data more closely, while GND calculations at higher strains should represent under-estimations. The lower GND density in Al 6082 S3 when compared to S1 reflects the decrease in the LAGB/HAGB ratio discussed in Section 5.3.1. It has been shown at large strains that dislocations being absorbed into GNBs can eventually develop into high angle boundaries equivalent to ordinary grain boundaries [155]. As HAGBs aren't included as part of the strain fields in the GND calculations (only misorientations $<5^\circ$ within grains are counted), the GND density decreases along with the overall dislocation density.

## 5.4 Plate impact experiments

The design and implementation of the plate impact experiments carried out in this study is described in detail in Chapter 3, and will be briefly summarised here. The remainder of this section is dedicated to the resulting free surface velocity measurements gathered during the shots. The 5N-Al and Al 6082 targets were sectioned transverse to the extrusion direction using EDM from rods with 0, 1 and 3 swaging passes (once again designated S0, S1 and S3 respectively). A 32 mm bore single stage gas gun was employed to dynamically load the target at impact velocities of 400 m/s and vacuum levels below 50 mtorr. Downshifted PDV operating at base frequency of 4 GHz [165] was used to measure the velocity histories of the target, driver and flyer. The 22 experiments conducted for this study are listed in table 5.3. The target thicknesses of the samples was varied from 0.2 mm to 1 mm for all three swaging levels of both the 5N-Al and Al 6082. The impact velocity of 400 m/s corresponds to a peak shock stress of about 4.6 GPa in the aluminium. PDV spectrograms were processed using the STFT

**Table 5.3:** Experimental parameters of the plate impact experiments on 5N-Al and Al 6082.

| Expt no | Material | Swaging passes | Sample thickness ($\mu m$) | Impact velocity (m/s) | Peak elastic stress (GPa) |
|---|---|---|---|---|---|
| 1 | 5N-Al S0 | 0 | $200 \pm 5$ | $399 \pm 1$ | $0.435 \pm 0.027$ |
| 2 | 5N-Al S0 | 0 | $202 \pm 1$ | $400 \pm 1$ | $0.440 \pm 0.027$ |
| 3 | 5N-Al S0 | 0 | $403 \pm 1$ | $397 \pm 1$ | $0.237 \pm 0.026$ |
| 4 | 5N-Al S0 | 0 | $539 \pm 1$ | $399 \pm 1$ | $0.235 \pm 0.026$ |
| 5 | 5N-Al S0 | 0 | $609 \pm 1$ | $393 \pm 1$ | $0.180 \pm 0.026$ |
| 6 | 5N-Al S0 | 0 | $1031 \pm 5$ | $426 \pm 1$ | $0.164 \pm 0.026$ |
| 7 | 5N-Al S1 | 1 | $200 \pm 5$ | $400 \pm 1$ | $0.405 \pm 0.027$ |
| 8 | 5N-Al S1 | 1 | $405 \pm 1$ | $398 \pm 1$ | $0.241 \pm 0.026$ |
| 9 | 5N-Al S1 | 1 | $586 \pm 1$ | $396 \pm 1$ | $0.173 \pm 0.026$ |
| 10 | 5N-Al S1 | 1 | $1015 \pm 1$ | $396 \pm 1$ | $0.153 \pm 0.026$ |
| 11 | 5N-Al S3 | 3 | $200 \pm 1$ | $404 \pm 1$ | $0.383 \pm 0.027$ |
| 12 | 5N-Al S3 | 3 | $408 \pm 1$ | $393 \pm 1$ | $0.178 \pm 0.026$ |
| 13 | 5N-Al S3 | 3 | $1002 \pm 1$ | $406 \pm 1$ | $0.108 \pm 0.026$ |
| 14 | Al 6082 S0 | 0 | $203 \pm 5$ | $414 \pm 1$ | $0.932 \pm 0.030$ |
| 15 | Al 6082 S0 | 0 | $404 \pm 5$ | $402 \pm 1$ | $0.835 \pm 0.029$ |
| 16 | Al 6082 S0 | 0 | $968 \pm 5$ | $409 \pm 1$ | $0.722 \pm 0.029$ |
| 17 | Al 6082 S1 | 1 | $195 \pm 5$ | $398 \pm 1$ | $0.731 \pm 0.029$ |
| 18 | Al 6082 S1 | 1 | $402 \pm 5$ | $405 \pm 1$ | $0.731 \pm 0.029$ |
| 19 | Al 6082 S1 | 1 | $968 \pm 5$ | $407 \pm 1$ | $0.568 \pm 0.028$ |
| 20 | Al 6082 S3 | 3 | $183 \pm 5$ | $402 \pm 1$ | $0.829 \pm 0.029$ |
| 21 | Al 6082 S3 | 3 | $401 \pm 5$ | $403 \pm 1$ | $0.857 \pm 0.029$ |
| 22 | Al 6082 S3 | 3 | $888 \pm 5$ | $396 \pm 1$ | $0.720 \pm 0.029$ |

methods detailed in Section 3.2.1, using a window length of 64 points and 50% overlap, corresponding to 0.8 ns time-steps. Velocity histories were computed from Gaussian fits to the power spectrum for each time-step.

The combined wave profiles for the impact experiments are shown in Figures 5.12-5.14, with thicknesses indicated in the figures. The breakout times of the shock waves have been shifted for clarity. The velocity profiles reveal clear precursor waves without peaks, followed by the principal plastic wave at an increasing separation with higher propagation distance. Note that experiment 2 was a repeat of experiment 1 and are both plotted in the 0.2 mm profiles in Figure 5.13, displaying a near identical velocity response. Significant decay of the elastic precursor with propagation distance is exhibited in the 5N-Al, whereas only

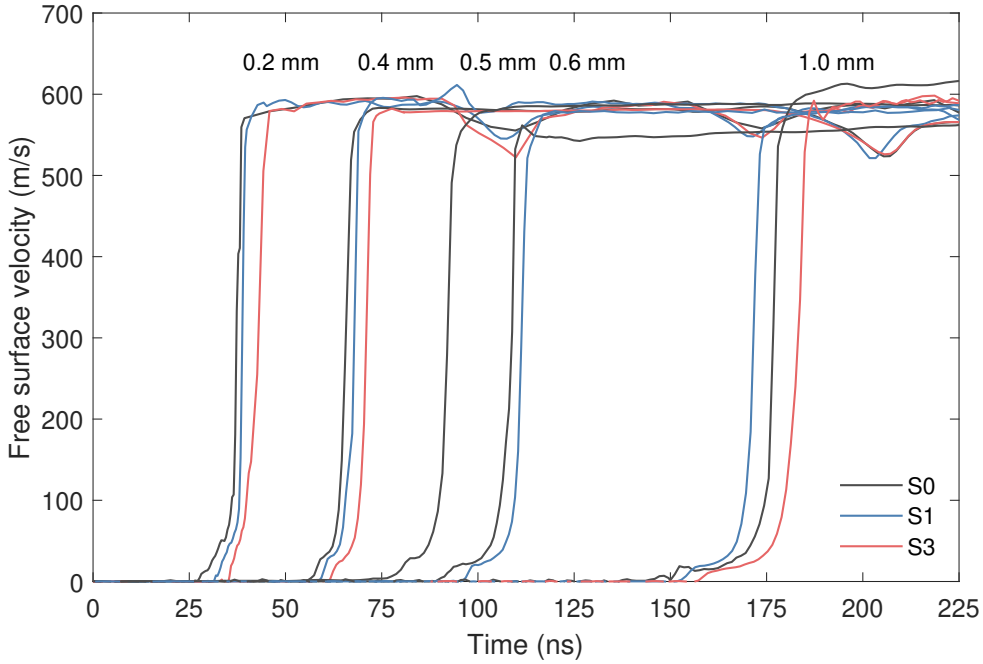



**Figure 5.12:** 5N-Al velocity profiles at increasing thickness and swaging passes. The breakout times have been shifted for clarity.

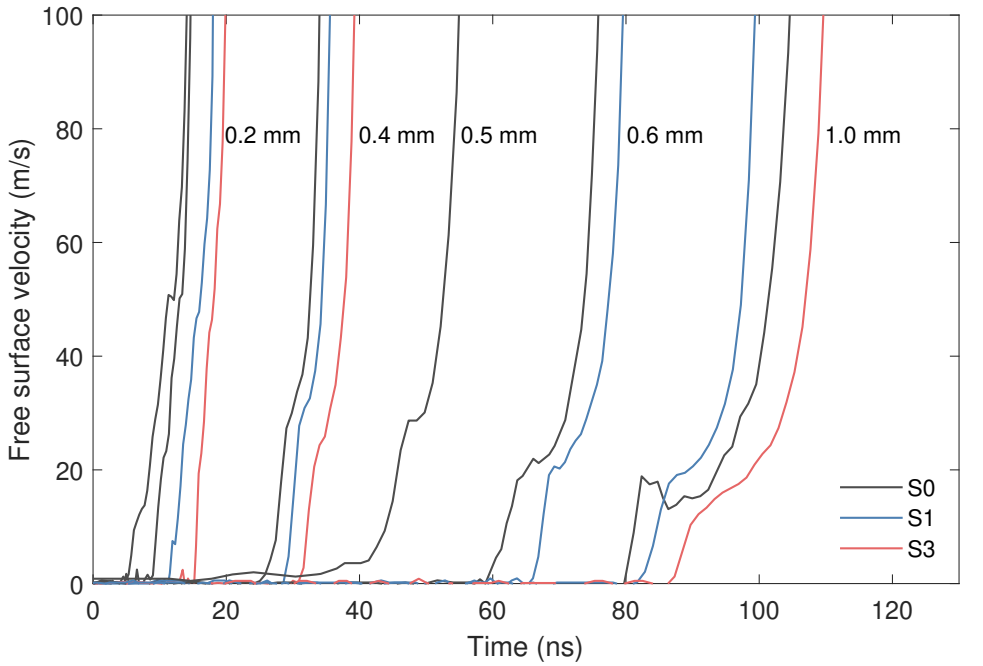



**Figure 5.13:** Magnified view of elastic peaks in 5N-Al velocity profiles at increasing thickness and swaging passes. The breakout times have been shifted for clarity. A decrease in the peak elastic stress with increasing swaging passes is observed across all thicknesses.

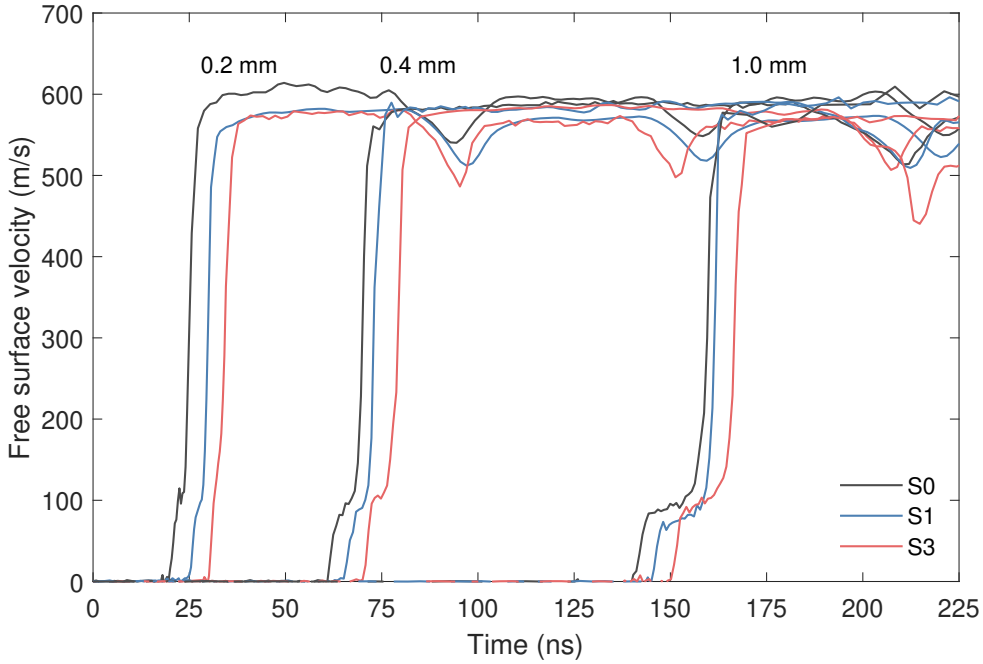



**Figure 5.14:** Al 6082 velocity profiles at increasing thickness and swaging passes. The breakout times have been shifted for clarity.

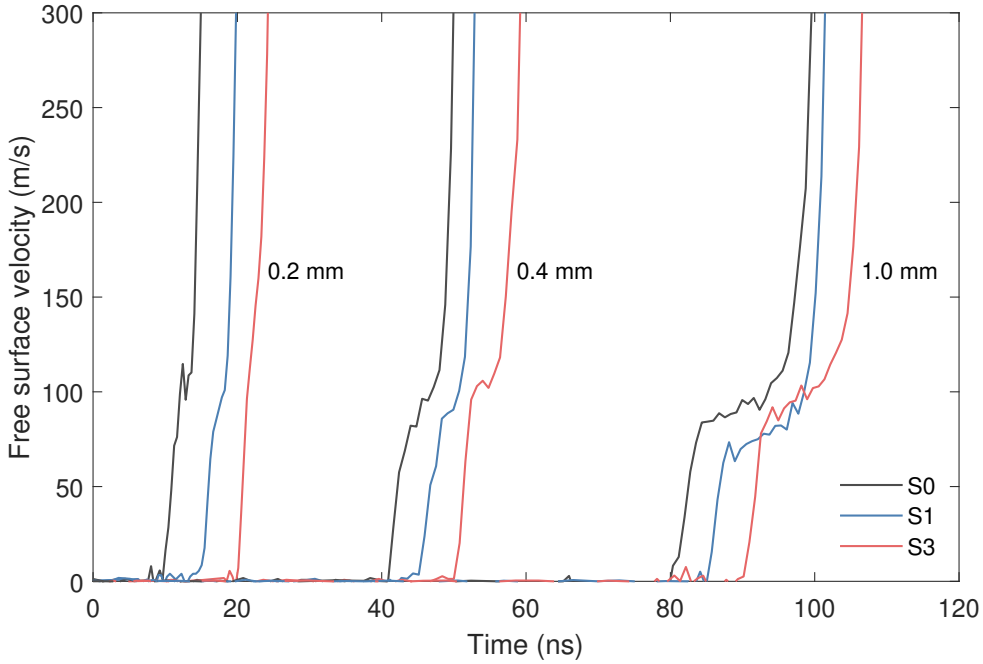



**Figure 5.15:** Magnified view of elastic peaks in Al 6082 velocity profiles at increasing thickness and swaging passes. The breakout times have been shifted for clarity. A decrease in the peak elastic stress is observed after the first swaging pass. It then returns back to the pressures of the as-received yield points after the third swaging pass.

very slight precursor attenuation is observed in the Al 6082. This is in agreement with the numerous previous studies on both pure Al and the very similar Al 6061 alloy. To make direct comparisons, the peak elastic stresses listed in Table 5.3 were calculated from the standard expression,

$$\sigma_y = \frac{1}{2}\,\rho_0\,c_l\,u_{fs}, \tag{5.5}$$

where $\rho_0$ is the unshocked mass density, $c_l$ is the longitudinal sound speed, and $u_{fs}$ is the free surface velocity at the precursor peak (determined using linear fits to the rise and plateau following [167]). The density was 2.70 $\pm$ 0.01 g/cm$^3$ and the longitudinal sound speed was taken as 6.4 $\pm$ 0.1 mm/$\mu$s for both materials [25, 228].

## 5.5 Discussion

### 5.5.1 Propagation distance and strain rate dependence

In Figure 5.16, the computed yield stresses are plotted against propagation distance alongside literature data from a mixture of gas gun and laser shock experiments on both pure Al and Al 6061 in a wide range of thicknesses. The black line represents a power law fit to the available pure Al data. The literature data shows that there is significant precursor decay in pure aluminium from around 10 GPa at 1 $\mu$m down to around 0.05 GPa at 10 mm thickness [20–24]. The two alloys however display only a very slight decay in the measured thickness range, and intersect the pure aluminium at around 100 $\mu$m. Good agreement is found between the yield points of the annealed 5N-Al and the pure aluminium from previous studies, whereas the as-received Al 6082 has slightly higher peak elastic stress than the Al 6061 in the studied thickness range. There is increasing scatter in the experimental data at propagation distances less than 100 $\mu$m, where the time dependence of the yield point is very strong and the time resolutions needed to resolve it start reaching the limit of what is possible with current velocimetry techniques.

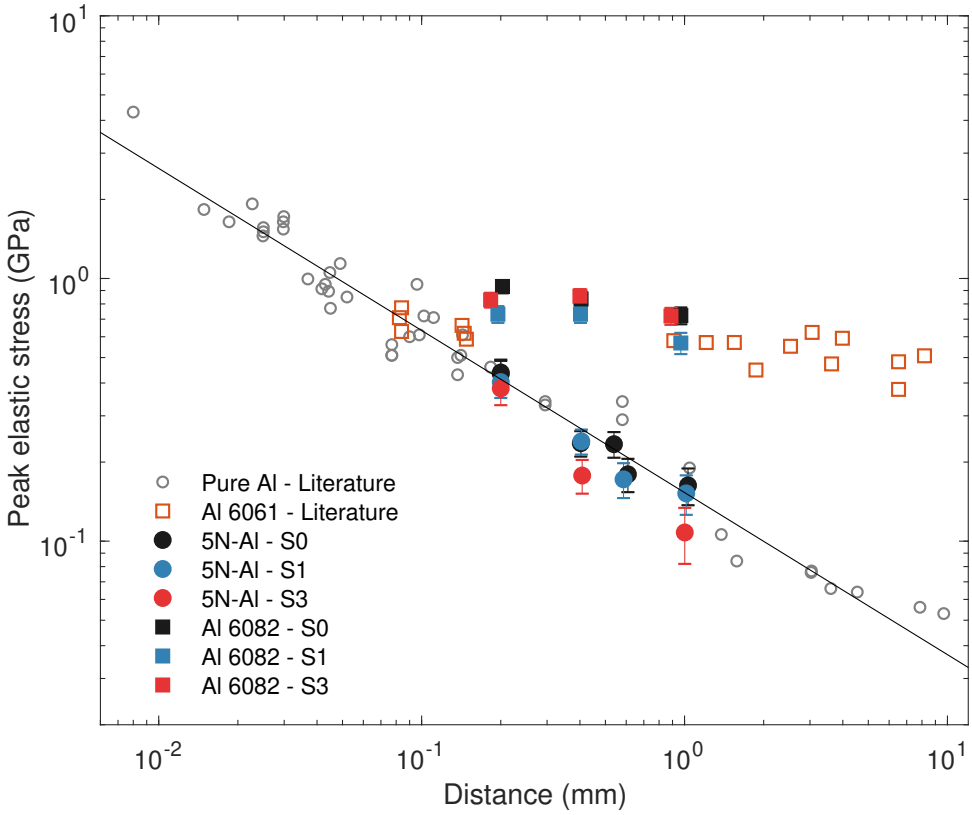



**Figure 5.16:** Peak elastic stress in 5N-Al and Al 6082 plotted against propagation distance comparing present results to literature data [20–24, 75, 76, 79]. Excellent agreement is found between the present 5N-Al S0 and previous results on pure aluminium, whilst the swaged materials are found to be at or lower than the trendline. Whilst the present data represents the only dynamic strength measurements on Al 6082, comparison to the similar Al 6061 alloy reveals an increase in strength in the 6082 variant, as well as a more significant decay slope.

.

Most notable are the significant differences in the yield points of the S0, S1 and S3 samples at constant thickness in both of the present materials. A monotonic decrease in peak elastic stress with increasing swaging passes (up to a true strain of 1.4) is observed in the 5N-Al at all thicknesses. Interestingly, in the case of the Al 6082, the first swaging pass is associated with a decrease in the peak elastic stress, whereas after the third swaging pass there is a reversal in which the dynamic strength reverts back towards that of the unswaged material. It should again be noted that the 6082 was taken to a higher strain than the pure aluminium.

As with the results on magnesium in Chapter 4, the initial longitudinal plastic strain rate is calculated using,

$$\dot{\epsilon}_p = \frac{du_p/dt}{c_l} \equiv \dot{\epsilon}_p|_{u_{E,Min}}^{2u_{E,Min}}, \tag{5.6}$$

where $u_p$ is the particle velocity and $u_{E,Min}$ is the particle velocity at the peak of the elastic wave. The strain is calculated from the onset of plasticity at $u_{E,Min}$, up to $2 \times u_{E,Min}$, which is taken as indicative of the plastic strain rate experienced at the elastic limit. Again a strong correlation is found between the strain rate and the dynamic yield stress, shown in Figure 5.17, in which the results can be reasonably fitted to a power law of the form $\sigma_y = \sigma_0 \dot{\epsilon}_p^n$, where $\sigma_0$ and $n$ are the fitting parameters, leading to,

$$\sigma_y^{pure} = (0.001)\, \dot{\epsilon}_p^{\,0.40\pm0.08}, \tag{5.7}$$

for the 5N-Al, and,

$$\sigma_y^{6082} = (0.12)\, \dot{\epsilon}_p^{\,0.12\pm0.09}, \tag{5.8}$$

for the Al 6082. The fit for the 5N-Al compares favourably to the equivalent fit of $(0.001)\dot{\epsilon}_p^{0.43}$ found by Smith et al. [23]. Sharp up turns in the flow stress have been found above $10^{-3}s^{-1}$ for pure Al [232], associated with a transition into the currently shown region of strong strain rate dependency. This represents the regime in which phonon drag effects are dominant over thermal activation. The applied shear stresses cause dislocations to easily overcome the Peierls barrier, and mobility is instead limited by the drag force caused by resistance of the lattice to motion [14]. As discussed in Chapter 2, dislocation drag is a manifestation primarily of phonon scattering and radiation by dislocations, which are effects known to be proportional to temperature. Indeed, experiments by Zaretsky and Kanel on pure Al at 900K showed an increase of the HEL by 4-5 times compared to room temperature, at thickness ranges of 0.1 to 2 mm [25].

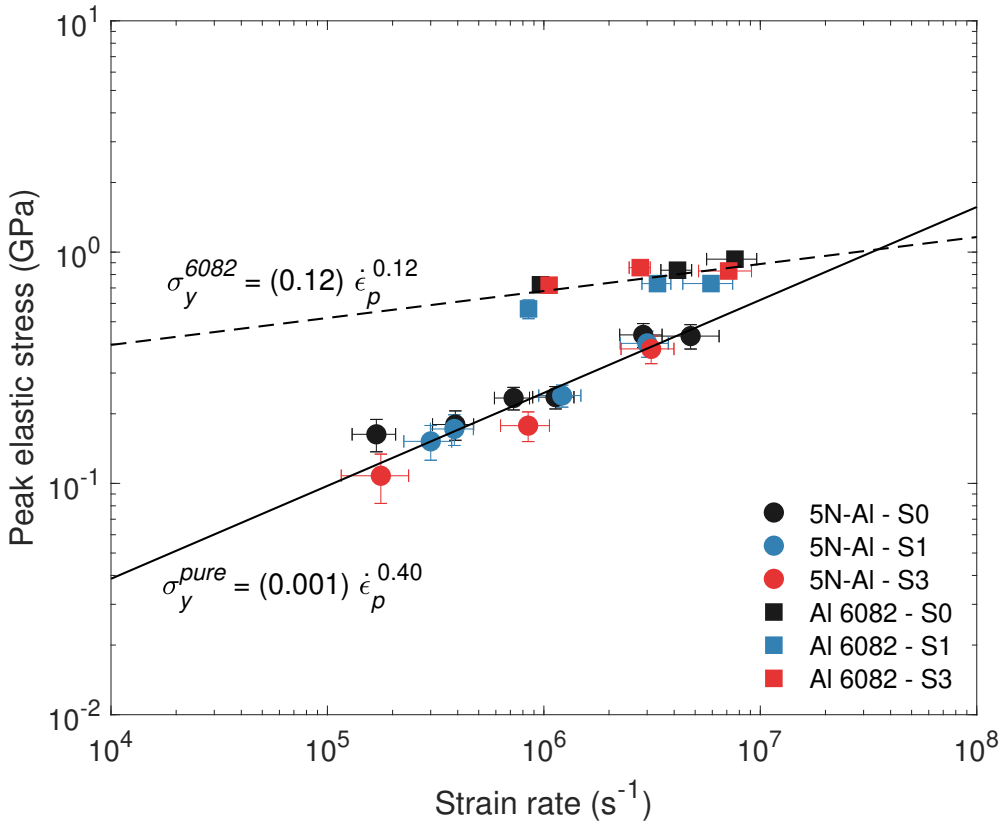



**Figure 5.17:** Peak elastic stress in 5N-Al and Al 6082 plotted against strain rate. The data points are fitted to power laws as displayed in the figure. It is found that the pure aluminium displays a significantly higher strain rate sensitivity than the alloy. The addition of secondary phase particles shifts the aluminium from the phonon drag to the thermal activation regime at these strain rates.

The stress versus strain rate or thickness plots of the Al 6082 shows a much lower strain rate sensitivity, similar to what would be observed for pure aluminium below $10^{-3}s^{-1}$. Here the secondary phase presents additional obstacles to dislocation movement, which increases the shear stress needed to induce plastic flow and therefore the magnitude of the peak elastic stress. It is also shown to decrease the strain rate dependence likely by shifting the material into the thermal activation regime. It is believed that if the strain rate was increased above $10^{7}s^{-1}$, or equivalently the thickness decreased below 200 $\mu$m, only then would phonon drag effects cause the peak elastic stress to increase significantly. Zaretsky et al. investigated this threshold more closely in a series of impact experiments on Al 6061 alloys with increasing levels of aging, i.e. precipitation hardening [82].

Specimens were solid solution-treated and then aged between 0 to 960 minutes. The super-saturated solid solution specimen (which had not been aged) exhibited pronounced precursor decay and therefore a highly strain rate dependent response at thicknesses from 0.2 up to 10 mm, similar to that of pure aluminium. While the difference in shear moduli caused an increase in the absolute values of the dynamic yield points, the similarity of the decay rates was likely due to the absence of strong precipitation in the aluminium matrix. As aging time was increased, the absolute values of the peak elastic stresses increased as expected. In contrast to the solid solution specimen, all of the aged alloys exhibited a flat response at large thicknesses (above 1 mm), but then transitioned to highly strain rate dependent regions in thinner and thinner samples depending on the amount of aging. The sharp upturn in the yield stress was observed below 1 mm for a 7.5 min aged sample, and below 0.4 mm for the 960 min aged sample. In other words, the strain rate needed to reach the transition to the phonon drag regime was found to increase in increasingly aged alloys.

This behaviour can be tied to the precipitation sequence of the alloy during aging, in which Mg and Si form clusters, then small precipitates of unknown structure (also called Guinier-Preston zones, or GP-I), and then $\beta''$ precipitates (GP-II). Further aging beyond this leads to formation of rod like $\beta'$ particles and more as discussed in Section 5.3.2. Each stage of the precipitation sequence is accompanied by an increase in the shear stress needed for dislocations to break free from the second-phase obstacles, from an estimated 67 MPa for the Mg-Si clusters, up to 124 MPa for GP-II zones [82]. Accordingly, the range of applied shear stresses in which dislocations continue to rely on thermal fluctuations to overcome these barriers increases with aging, and the transition to phonon viscous drag occurs at increasingly higher strain rates.

The low strain rate dependence observed in the present results in Al 6082 also fits into this picture, given that the T6 state of the alloy indicates that it has been fully precipitation hardened, as also evidenced by the observation of $\beta'$- and

$\beta$-particles in the TEM micrographs from Section 5.3.2. The present material was aged even further than the longest aged specimens in the study by Zaretksy, and as such an upturn in the flow stress in Al 6082-T6 would likely be observed only for thicknesses below 200 $\mu$m, or equivalently strain rates above $10^7$ $s^{-1}$. Contrast this to a study by Asay into annealed Ta with two different impurity concentrations, in which no difference in yield point was found between the impurity levels [71]. Here it was theorised that any remaining dislocations after annealing the material are pinned to interstitial sites, and that only by loading up to a critical stress (which was relatively unaffected by impurity concentration) were dislocations freed and able to multiply. This behaviour is similar to metals with a high Peierls stress. Consequently, it seems that the precipitation state of the alloying elements has a stronger effect than their concentration. The annealing or precipitation hardening state is also very important in determining the results of any subsequent cold work, as discussed in Section 5.5.2.

### 5.5.2 Grain size and dislocation density dependence

#### Microstructure evolution and relevance of grain boundaries

It is worth noting that the literature data shown in Figure 5.16 was gathered from samples with a wide range of initial grain sizes, including grains around 1 mm in the high thickness experiments by Arvidsson et al. [20], down to 25 $\mu$m [22] and 5 $\mu$m grains at around 100 $\mu$m thickness in experiments by Winey et al. and Smith et al. respectively. A natural question is therefore if these results would be subject to the well known Hall-Petch effect, in which a decrease in grain size produces an increase in strength due to grain boundaries acting as obstacles to dislocation movement. Variations in grain boundary density have been studied as far back as 1968, when Jones and Holland found that the peak elastic stress was insensitive to the grain size of SAE 2018 steel [66]. It was concluded that dislocations under shock loading do not move sufficient distances for their interactions with grain boundaries to take effect. In more recent experiments by Asay et al., pure

aluminium was cold rolled and then annealed at varying temperatures in order to produce a range of grain sizes from 49 to 453 $\mu$m [81, 233]. It was again found that the dynamic strength was insensitive to the initial conditions. A similar study by Huang et al. on variety of initial grain sizes in pure Al (180 to 300 $\mu$m) and Al 6061 (5 to 50 $\mu$m) also showed no indication of a grain size dependent response [204]. The agreement between the wide range grain size results shown in Figure 5.16 reinforces this picture of grain size independence. Finally, while being a very different material, the investigation of AZ91 in Section 4.5 also found very minor differences between different grain size specimens.

Comparisons can be made to the current experiments, where in fact the lower strength samples also had lower grain sizes (but also higher dislocation densities). In the case of the Al 6082, the grain size variation of coarse grains as discussed in Section 5.3.1 is between 3 $\mu$m to 9 $\mu$m, much smaller than the range studied by Huang et al. In the 5N-Al, the size of the coarse grains remains almost unchanged at around 300 $\mu$m. While both materials therefore seem to be within the range of grain size independent behaviour, it is complicated by the increasing presence of micron sized and sub-micron sized grains (and subgrains) in the 5N-Al and Al 6082 respectively at higher swaging levels. Here distinctions become a bit more complicated, as many of these boundaries are not high angle boundaries but instead made up of loosely arranged dislocation arrays, most obvious in the 5N-Al S1 TEM data.

In light of this, it is worth discussing the evolution of dislocations and boundaries during high strain rate loading, and specifically how such dislocation substructure might behave. Unfortunately, due to the timescales and nature of shock experiments, a real time investigation of the defect evolution during the shock is very difficult. Studies are for the most part limited to pre- and post-experiment characterisation techniques (although *in-situ* synchrotron x-ray diffraction is an emerging option [120–122]). While not performed as part of this study, investigations of deformation structures in shock recovered specimens have

been performed exhaustively stretching back to the 1960s [234, 235]. It is well understood that the generation of dislocations is of paramount importance during shock compression given that their velocity becomes a limiting factor. Residual dislocation densities in shock compressed Ni were measured to between $10^{14}$ to $10^{15}$ m$^{-2}$ depending on the shock pressures [14, 236]. TEM characterisation of the substructure in Cu and Ni loaded at 5 and 10 GPa respectively both found that dislocations had arranged into loosely tangled dislocation cells upon release [14]. As shock pressure is increased further, the final dislocation density, $\rho_{Df}$, increases with shock pressure, $P$, following the relationship $\rho_{Df} \propto P^{1/2}$ [236]. As a consequence the dislocation cell size decreases.

In a study on Al 5052 comparing quasistatic loading to dynamic magnetic pulse loading, post-experiment TEM micrographs showed a much higher and more uniform dislocation density after dynamic loading [237], as well as evidence of increased cross-slip. Moreover, dynamic loading of a 20$\%$ quasistatically pre-strained sample lead to a (qualitatively) smaller final dislocation density than the dynamically loaded sample without prestrain. The authors concluded that the deviatoric stresses at the wave front were more easily relaxed by the increased population of initial dislocations in the pre-strained sample. Taking dislocation generation and motion as competing mechanisms, in the sample without pre-strain the imposed stress was instead accommodated by greater dislocation nucleation, culminating in a higher final dislocation density.

Recent experiments by Liu et al. [238] investigated the difference in residual deformation structures in AISI 1045 steel. As strain rate is increased from $10^5$ to $10^6$ s$^{-1}$, a higher fraction of dislocations and LAGBs was observed after loading, and consequently a smaller fraction of HAGBs. This is consistent with the fact that the creation of dislocations (which can take $<$400 ps [239]) is faster than the movement of dislocations or LAGBs to create HAGBs. Given the theoretical maximum mobility set by the transverse wave speed of 3.2 mm/$\mu$s [59] (ignoring the possibility for supersonic dislocations), a line defect traversing the length

of a 10 $\mu$m grain will take at the minimum around 3 ns, and likely more. In other words, there is less time in higher strain rate experiments for dislocations or LAGBs to rearrange or be absorbed, resulting in a higher dislocation and LAGB density and a lower HAGB density.

It is in fact generally accepted that the boundary mobility is higher for high angle than low angle boundaries [240]. The motion of an array of dislocations comprising a low angle tilt boundary can be quite restrictive, with only specific configurations able to glide or climb. On the other hand, shock impact studies have found that dislocations are more easily able to transmit through low angle or $\Sigma 3$ twin boundaries than high angle boundaries [241, 242]. Given that high angle boundaries block dislocation movement, dislocations will tend to form pile-ups and build stress concentrations at the boundary. These eventually induce failure and damage nucleation which can be observed at the boundaries in shock recovery experiments. Low angle or twin boundaries are conversely able to support the transmission of dislocations or activation of slip on the other side of boundary, resulting in less stress build-up and ultimately in lower damage nucleation.

Combined, these facts enable us to build two contrasting summaries for the evolution of dislocations, LAGBs and HAGBs under low versus high strain rate loading. Starting with the response under low strain rates, the microstructural behaviour can be deduced from the EBSD and TEM results in Section 5.3. During plastic deformation, a portion of the deformation energy not dissipated as heat is stored in the form of dislocations. Continued straining under SPD produces a very high dislocation density, in which the ones not annihilated are moved into cell boundary tangles or arrays which form LAGBs [240], as evidenced by the increasing LAGB density in 5N-Al S1 and S3, and Al 6082 S1. As discussed in Section 5.3.3, many of these dislocations are GNDs and form GNBs, which help accommodate lattice curvature. Further deformation produces LAGB motion as well as absorption of dislocations into LAGBs, which increases their misorientation eventually turning them into HAGBs. Under the relatively low strain rates during

rotary swaging, it's found that a large fraction of HAGBs are created as deformation degree progresses to high strains, exhibited by the high misorientation angles observed in Al 6082 S3. Dynamic recovery at this point reaches a balance with and eventually overshadows dislocation nucleation, causing the observation of a decrease in the dislocation density between boundary walls.

In high strain rate experiments on the other hand, only shorter time scale processes are given the opportunity to complete before release waves from the rear free surface (or sides) of the sample arrest further deformation. In this scenario, the large magnitude of the imposed strain rate (rather than just the high total strain as with SPD) leads to high dislocation generation caused by the sudden large increase in deviatoric stress. As before, nucleation is accompanied by dislocation motion and arrangement into LAGBs, however, the window of opportunity for dislocation or boundary movement is in this case very small. Further evolution of the deformation structure through the creation of HAGBs is time consuming and therefore limited. The final state of the dislocations generated in shock compressed Cu and Ni was that of loose dislocation cells and cell blocks [14, 236], rather than the distinct and highly misoriented boundaries observed in aluminium swaged to three passes. Indeed when the shock pulse duration was increased, the dislocation cell boundaries becomes more distinct.

The problem with looking to shock recovery experiments in the current context is that a significant portion of the deformation structures described above are likely created during the plastic part of the shock wave, not to mention the possibility of release waves or even spallation causing a whole other set tensile deformation or failure mechanisms. The rise time of the elastic precursor on the other hand is only a few nanoseconds, and it is known that only the material (and dislocations) at or very close to the wave front is able to affect the elastic limit. Given the relatively short timescales of dislocation generation (on the order of picoseconds) and movement (on the order of nanoseconds) [8], the earliest point at which plastic relaxation can be initiated is likely governed almost entirely by the initial

density of dislocations, their generation, and their mobility. Grain boundaries are less able to affect the yield point directly, and the evolution of the grain boundary structure during the plastic portion of the impact event instead serves more as a window into the mobility of dislocations, LAGBs and HAGBs.

Current theories therefore postulate that the elastic relaxation waves emanated from dislocations generated or moving at or close to the wave front are responsible for the decay of the precursor stress [7–9]. Modelling of shocked aluminium by Gurrutxaga-Lerma found that the relaxation waves created by dislocations homogeneously nucleated at the shock front could account for all of the decay of the precursor wave during very high strain rates of around $10^{10}$ $s^{-1}$, measured within the first 10 $\mu$m from the impact surface [8]. More time consuming mechanics such as the behaviour of boundaries were irrelevant at these strain rates. In fact even heterogeneous dislocation generation mechanisms such as Frank-Read sources, with activation times of around 40 ps, were too slow to have an effect on the decay rate. Homogeneous nucleation requires very high shear stresses as the process essentially involves displacing atoms in a near perfect lattice in order to create a dislocation. When the precursor stress reaches the lower stress amplitudes of the current experiments this is less likely to occur, instead replaced by the slower processes of multiplication or heterogeneous nucleation [19]. Heterogeneous nucleation of dislocations requires less shear stress as it is facilitated by lattice defects such as point defects, secondary phase particles, or grain boundaries [240]. Multiplication mechanisms such as Frank-Read sources are a result of pinned dislocations bowing out until a new dislocation is formed [243], and at these strain rates take between 0.5 up to around 2 ns to complete in aluminium [48].

Both experimental studies and theory therefore indicate that the effect of obstructing dislocation movement by increasing the grain boundary density is likely insignificant in determining the dynamic response. In fact it may possibly instead contribute to a decrease in strength by enabling greater dislocation

nucleation. Indeed, in the recent modelling work by Kositski and Mordehai on shock loaded V and Ta, a good fit to the experimental data was provided by considering nucleation of dislocations primarily occurring on grain boundaries. While not implemented yet, it is possible that the grain boundary densities listed in Table 5.2 could be used in the modelling collaboration, detailed in Section 5.7.3, to provide a physically based motivation for the nucleation rate. The question on the behaviour of grain boundaries should now also be extended to the dislocations themselves. A higher dislocation density undoubtedly causes increased resistance to dislocation glide, however it may also result in greater numbers of dislocations which can be activated to initiate plastic relaxation once the shear stress reaches the right threshold.

**Effects of dislocations on precursor attenuation**

The main hypothesis of this study was that the decay of the dynamic yield point is determined by the density of mobile dislocations in the sample, whether they are present in the material before loading or if they are nucleated during deformation. In Figure 5.18, the peak elastic stresses from the plate impact experiments are plotted against the dislocation densities measured with TEM. Thicknesses are labeled in the figure, with experiments at equal thickness connected by lines. In the 5N-Al, a decrease is observed in the elastic peak with increasing dislocation density and swaging passes at all thicknesses. In the Al 6082, since the dislocation density of the S3 sample is lower than S1, again the result is a trend of decreasing elastic stress with increasing dislocation density for all thicknesses. If, as discussed above, the effect of grain boundaries can be taken as insignificant, then this proves a counter-intuitive inverse relationship between strength and dislocation density at high strain rates. In particular, it shows that increasing the dislocation density is tantamount to growing the population of mobile dislocations, which at high strain rates dominates over the effects of strengthening by immobile dislocations.

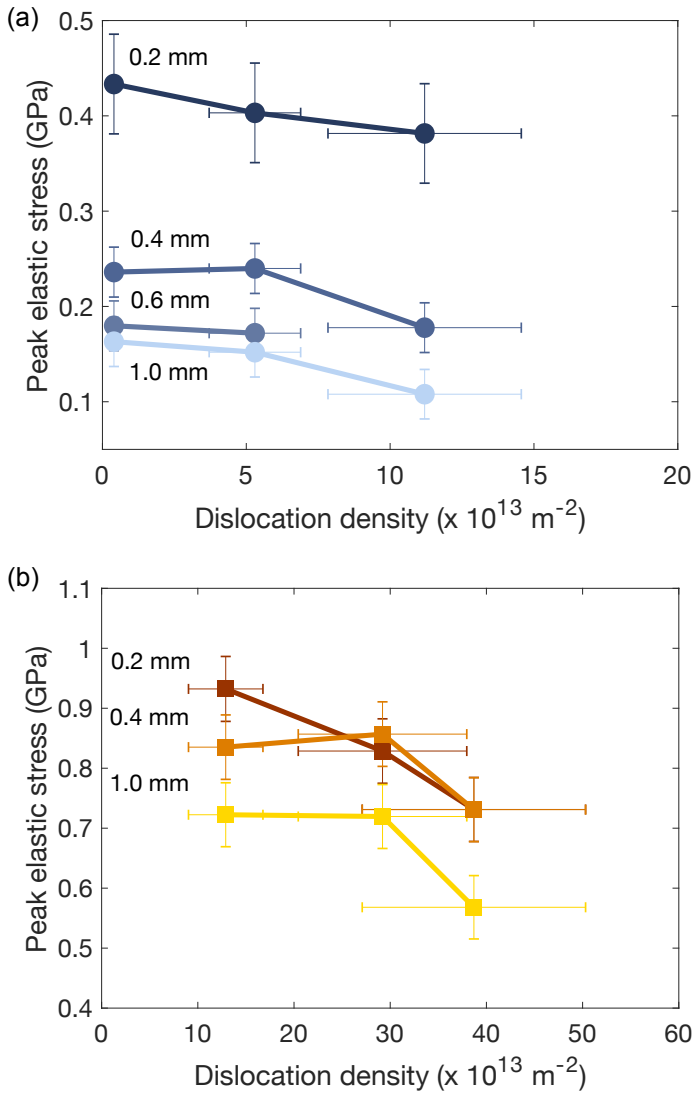



**Figure 5.18:** Peak elastic stress from the a) 5N-Al and b) Al 6082 plate impact experiments, plotted against dislocation densities measured with TEM. Thicknesses are shown in the figure, with experiments at the same thickness connected by lines. A decrease in the yield point is observed with increasing dislocation density for all samples.

Similar observations of a decrease in yield point after cold working have been made in studies on tantalum [57, 71, 93]. Razorenov et al. compared the dynamic strength of UFG tantalum and coarse grained tantalum, finding it to be lower in the UFG Ta [93]. They theorised that the increase in grain boundary density in the UFG material led to a higher rate of stress-relaxation caused by increased dislocation nucleation at the grain boundaries. In the study by Millett, the difference was quite pronounced as the material displayed a peak-and-valley

profile in the as-received state, which turned into the more diffuse shoulder-type yield point after cold working [57]. The material was only cold rolled up to a strain of 0.5 and can therefore not be considered SPD processed. Consequently, the difference in total dislocation density, as indicated by their TEM data, was not as large as the current study (although they did not measure it directly). Despite this, the cold rolled samples had lower yield points than the as-received material even up to the very high propagation distance of 9 mm. It was theorised that the cold-rolling process resulted in a displacement of dislocations away from surrounding interstitial solute atoms which ordinarily would have acted as pinning points. Consequently, even if the total dislocation density change was comparatively small, there was a significant increase in the ratio of mobile versus immobile dislocation densities, thus causing a faster decay rate. The peak-and-valley was replaced by a single gradual yield point, because plasticity no longer hinged upon waiting to reach a threshold shear stress to free dislocations from the interstitials (which would then trigger rapid relaxation and a velocity pull-back). Rather, yielding was achieved by degrees through populations of dislocations being induced to move at a distribution of critical applied stresses. A decrease in yield strength in cold worked tantalum was also found in work by Asay et al. [71], who drew similar conclusions. Zaretsky and Kanel found that annealed Ta had a higher yield point than the as-rolled material [87], prompting them to suggest that defects which ordinarily strengthen the material instead act as sources of mobile dislocations at high strain rates.

The following picture based on the above observations can now be envisioned for the evolution of dislocations during the rise of the precursor wave. First to be considered is the case of an annealed material in which any remaining dislocations are likely to be immobile. As the stress increases beyond the critical stress for dislocation movement, the few pre-existing dislocations which aren't pinned by greater obstacles begin to move and release a small amount of relaxation waves. Under the short time scales of shock compression, these are unable to completely relax the deviatoric stresses, which continue to build until the peak of

the precursor wave is reached. At this point, the shear stresses enable additional mobile dislocations to be generated rapidly [17, 244]. The underlying cause can be nucleation, multiplication, or freeing dislocations from pinning points. In all cases, a sudden increase in mobile dislocations at or close to the wave front releases a large influx of relaxation waves. Again, these relaxation waves are able to catch up to the precursor wave front due to the greater wave speed within the already compressed material [9]. The result in the stress profile is a precursor peak, followed by a relaxation dip [245]. In the aluminium studied here, a more gradual transition is observed without a peak, consistent with other FCC metals in which generation occurs more easily or mobility is less limited [25, 29, 84]. The same theory explains why stress spikes are observed in shock loaded aluminium (with prior annealing) at high temperature but not at room temperature [25]. The initial microstructural state can be assumed close to identical at all temperatures due to the prior annealing, meaning the reason for the spike in this case must lie with the increased drag caused by the higher temperatures. This inhibits the ability for dislocation movement alone to initiate sufficient plastic relaxation.

In cases such as the swaged material where, whether through unpinning or generation during cold work, an already significant number of mobile dislocations are present (densities comparable to the residual densities measured after shock loading), the behaviour during the elastic rise is altered. The greater density of pre-existing mobile dislocations means that a more substantial amount of plastic relaxation can occur early on in the rise of the precursor wave, once dislocation movement is enabled. The increased resistance to dislocation movement caused by the higher dislocation density is possibly less dominant given the already high shear stresses. The overall result is a quicker initiation and more continuous transition to the plastic region of the wave, as the greater amount of relaxation waves from the initially active dislocations are more able to accommodate the early strain build-up. Supplementation through generation mechanisms is less crucial and also more gradual. The final result is a lower precursor amplitude, as seen in the present data. In other materials which display a precursor spike, this may be

decreased or removed entirely. It should be noted that the "elastic" precursor wave is therefore not truly elastic in the classical sense during its attenuation phase. Stress relaxation caused by plasticity, manifested as release waves originating from dislocations within the "elastic region" of the wave, is what causes the decay of the peak precursor stress.

**Inconsistencies within literature results**

Previous studies have recorded a decrease in the yield point after cold work in tantalum [57, 71, 93] up to 9 mm propagation distance, and in Al 2024 and Al 1421 [88, 89] at 2 and 2.7 mm, respectively. However, conflicting results have been found in other aluminium alloys. In a study on Al 5083, high pressure torsion (HPT) was applied to produce a UFG structure with accumulated strains up to 9.3 [89]. Shock wave experiments performed on coarse grained (CG) samples in the initial annealed state resulted in a yield point of 0.4 GPa, whereas the UFG state had much higher yield around 0.8 GPa, both at 1 mm thickness (i.e. opposite trend to the current 1 mm data). Note that the yield point of the initial material was quite low compared to the alloys shown in Figure 5.16.

Similarly, a study comparing CG to ECAP processed Al 6063 led to peak elastic stresses of 0.2 and 0.4 GPa for the CG and UFG materials, respectively, at 2 mm propagation distance [88]. Again however the reported yield point of only 0.2 GPa for the CG material is very low for an aluminium 6000-series alloy. In the current as well as previous alloy data discussed in Section 5.5.1, the yield would instead be expected to be around 0.6 GPa. Supplementary data from the ECAP processed Al 6063 study, discussed by Razorenov [89], displayed very significant attenuation of the precursor stress at thicknesses all the way up to 8 mm. This is again highly inconsistent with the data of very similar alloys, in which the precursor amplitude is almost fully decayed by 0.2 mm. This is likely related to the processing history, which was reported as an annealing step followed by aging [246].

Similar results showing cold work strengthening at high strain rates were found in dynamic channel angular pressing (DCAP) processed aluminium alloys A7, 7075, 3003, 5083 [90, 247], ARB processed Al 1070 [91], and ECAE then cold rolled Al 5083 [92, 248]. In the ARB study, the initial cycles caused an increase in the yield point, which then peaked and eventually decreased. In the ECAE study, no large difference was observed after the initial pass, and only after subsequent cold rolling did the yield point start to increase. Microstructural examination showed that large inclusions were observed in the initial material, which grew and aligned along the rolling direction after cold rolling. The exact effects of this realignment are unclear. In all of the above mentioned studies, the initial reference alloy was annealed to varying degrees prior to applying the cold working method.

A likely explanation of the apparent inconsistency between these studies and the current data can be determined from their material processing histories. Studies by Zaretsky et al. showed that annealing Al 6061-T6 produces an up to three-fold reduction in the peak elastic stress [25, 82]. As reviewed in Section 5.5.1, each consecutive stage of the precipitation sequence following annealing is then accompanied by an increase in the shear stress required for dislocation unpinning. However, Zaretsky and Kanel found that their samples would still display a reduced strength compared to the original condition. At 1 mm thickness, the annealed then partially aged 6061 had a peak elastic stress of only 0.3 GPa, compared to 0.6 GPa of fully age hardened 6061 in the T6 state. At higher propagation distances, the yield points of the annealed samples continue to attenuate down to 0.15 GPa at 6 mm thickness. In contrast, the peak stress of the fully aged 6061-T6 material is still at around 0.5 GPa at 6 mm.

It is therefore clear that the effect of alloying elements and their exact precipitation state in the material has immense repercussions on the yield point, as is also emphasised by the large strength difference between pure aluminium and its alloys. The results of any changes that can be made to the microstructure of pure

aluminium (such as grain boundaries, dislocation densities or grain orientations) are dwarfed by the strengthening caused by the addition and precipitation of secondary phase particles. It is likely that this pattern of strengthening was at play in the previous studies on cold worked aluminium alloys discussed above, where annealing was followed by a combination of cold working and aging (of which the latter occurs even at room temperature in both e.g. the 2000 and 7000 series alloys [249]). First, by annealing to the solid solution state, the dynamic yield point is reduced by a factor of 2 to 3 compared to the same material in the fully precipitation hardened state. Next, while subsequent cold work causes an increase in the dislocation density, the character of these new dislocations is likely heavily weighted towards immobile rather than mobile dislocations (in particular when compared to cold working a pure material). This, combined with a potential increase in the unpinning stress caused by aging, overshadowed any softening effect caused by mobile dislocations.

This distinction in the type of dislocations created through cold working pure versus alloyed material was observed in the TEM data shown in Section 5.3.2. After swaging to the S1 state, the pure aluminium has developed a cellular substructure with low dislocation densities at the cell interiors. Such microstructure is indicative of highly mobile dislocations and a high SFE [227, 250]. In the Al 6082 on the other hand the grain interiors are densely populated with randomly spread immobile dislocations, which is due to the substantial presence of second-phase $Mg_2Si$ particles preventing dislocation movement and absorption at grain boundaries during deformation. These conclusions are supported by the study on Al 2024, which was the only one in which the initial fully age hardened material was compared to the annealed and the UFG states [88], with resulting peak elastic states of 0.73, 0.19 and 0.32 GPa, respectively. Again it was shown that annealing results in a large decrease in strength, and whilst the UFG state did exhibit a higher yield point than the annealed sample, it was low when compared to the fully age hardened material. This general trend seems to be consistent with the above findings, however quantitative knowledge of the microstructures is needed. As is

discussed further in the simulations in Section 5.7.3, from a modelling standpoint, raising the total immobile dislocation density increases the overall strength of the material across all propagation distances. Indeed, this is a possible way in the model of accounting for the existence of precipitates without directly simulating them. The mobile dislocation density on the other hand affects only the decay rate and the time taken to reach the equilibrium stress. It is possible that the increase in dynamic strength observed in these studies may have been less pronounced had measurements been made at lower propagation distances (e.g. 0.2 mm), where mobile dislocations likely play a more dominant role.

### 5.5.3 Strain rate dependence of the effects of cold work

The observations from Section 5.5.2 are summarised in the schematic diagram in Figure 5.19, showing the effects of dislocation density or equivalently cold work in the high and low strain rate regimes. At low strain rates, cold work is well-known to result in higher strength, as described by the Taylor hardening equation (Equation 5.3). Increasing the dislocation density results in an overall increase in the resistance to dislocation glide which, given that the dislocation is the primary carrier for plastic deformation, also increases the yield point. This behaviour is echoed at more intermediate strain rates of around $10^3$ $s^{-1}$, where split-Hopkinson pressure bar (SHPB) experiments on pure aluminium also demonstrate a clear increase in flow stress with increasing cold work [251].

In the high strain rate regime (above around $10^5$ $s^{-1}$), the opposite behaviour has been exhibited. At these strain rates, the availability of mobile dislocations is highly dominant in determining the rate of stress relaxation. Increasing the initial dislocation density addresses the lack of mobile dislocations in the attenuation stage right after impact, resulting in a higher strain rate and lower yield points, as described by the Orowan equation (Equation 5.1). The experimental evidence suggests this is the case both for pure materials and age hardened alloys.

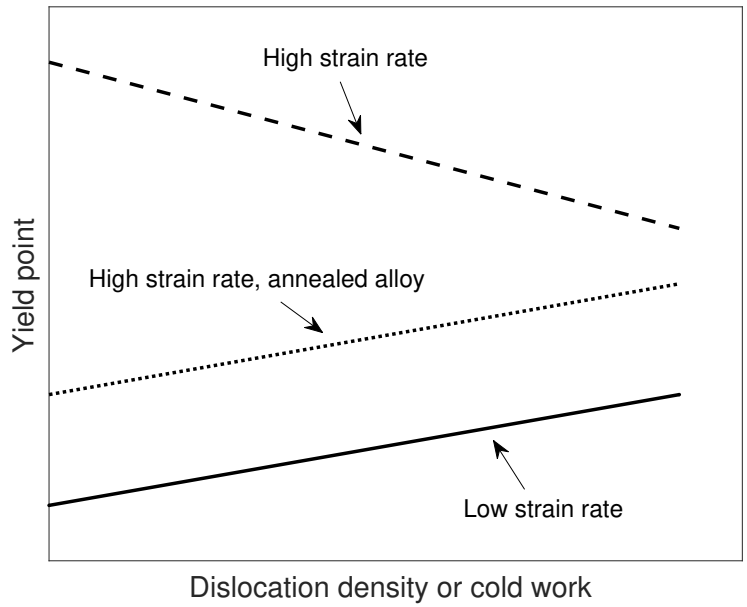



**Figure 5.19:** Schematic diagram showing the relationship between the yield point and dislocation density, or equivalently the amount of cold work, in different strain rate regimes. In the low strain rate (quasi-static) regime, increasing the dislocation density through cold work produces higher strength. In the high strain rate (shock compression) regime, increasing the dislocation density leads to higher availability of initial mobile dislocations which can more quickly accommodate plastic deformation. If the material in question is an alloy such as Al 6061, then annealing will reduce the initial yield stress (before cold work). Subsequent cold work causes increasing dislocation densities, dislocation pinning and hardening, which strengthens it back towards the yield point of the fully age hardened states. The exact transition point between low and high strain rate regimes is material dependent and its determination would require more shock loading experiments in the far field propagation distances, or at high impact velocity with SHPB.

Finally, in the special case when an an alloy such as Al 6061 is annealed, the behaviour is altered in the high strain rate regime because of the exceedingly dominant role played by the alloying elements. Having initially been annealed, the dynamic strength in the "reference" state of these alloys was at its low point. Subsequent cold work likely led to several order of magnitude increases in pinned and immobile dislocations, as well as increases in the unpinning stress caused by aging. Consequently, the overall yield stress increases despite any additional mobile dislocations. A natural next step is questioning exactly at what strain rate the material transitions from the low to the high strain rate behaviours depicted in Figure 5.19. Clearly, this transition must be material dependent, and in pure

aluminium should occur somewhere in-between the strain rates of $10^3$ $s^{-1}$ and $10^5$ $s^{-1}$, possibly in the $10^4$ $s^{-1}$ range. This is shown in Figure 5.20, in which the current experimental results on 5N-Al are plotted together with quasistatic (QS) and SHPB data on 4N-Al from Karnes and Ripperger [251]. Below $10^4$ $s^{-1}$, annealed aluminium very clearly has lower strength, however at around $10^3$ $s^{-1}$ one begins to observe an increase (higher slope) in its strain rate dependence. At $10^5$ $s^{-1}$, this effect is fully realised, and the annealed material has higher yield points than the swaged versions. Note that since the QS and SHPB data represents the flow stress specifically at $2\%$ strain (i.e. not necessarily at the elastic limit), its magnitude and those measured in shock loading are not directly comparable.

Finding the exact transition point between the two regions would mean conducting gas gun experiments at very high propagation distance where strain rates are lower (probably around 10 mm or more based on extrapolation), or SHPB tests at very high impact velocity (150 m/s or more). In the gas gun experiments the precursor amplitudes should converge, after which the annealed yield point would decrease below that of the cold worked specimen at higher propagation. This is discussed further in Section 5.7.3 (and depicted in Figure 5.31), in which transitioning from the low to high strain rate behaviour is caused by rate effects becoming significant enough that the yield point becomes dependent on the mobile dislocation density, and not just on strengthening by the immobile one. Whether or not this transition can actually be measured in gas gun experiments is unclear. The concerns are elaborated on in the section, in short however it seems that the experimental evidence so far may contradict the theory. Current experimental data on Al 6082 and Ta in the far-field propagation distances (close to the equilibrium stress at 1 mm and 9 mm respectively) both still display lower peak elastic stress in the cold worked material.

To conclude, it is found that the dynamic yield stress is primarily a function of the state of alloying elements (if present), followed by the initial dislocation density, with a possible tertiary dependency on nucleation of dislocations at grain

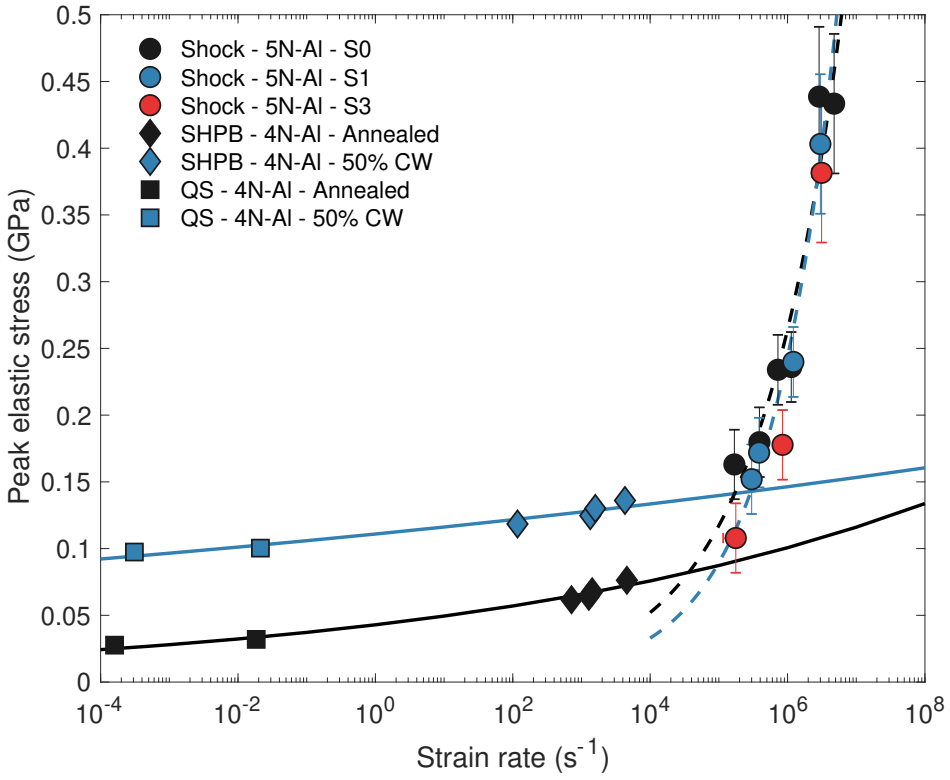



**Figure 5.20:** Strain rate dependence of flow stress in quasistatic (QS), split-Hopkinson pressure bar (SHPB), and shock loading experiments on pure aluminium [251]. The 4N-Al was either annealed or cold worked (CW) up to an engineering strain of 50%, making it very comparable to the 5N-Al S0 and S1 samples, respectively. It is found that a transition between the low and high strain rate behaviours, as shown in Figure 5.19, may possibly occur around $10^4$ to $10^5$ $s^{-1}$. Power law curves have been fitted to the low and high strain rate regions, following Equation 5.6. Note that the QS and SHPB data points represent the flow stress at 2% strain, meaning the magnitude can not necessarily be directly compared to yield during shock loading.

boundaries. Unfortunately, the degree to which the exact interplay between these parameters can be examined quantitatively using experimental techniques has its limits. It is hard to produce materials with high dislocation density without at the same time inducing substantial grain refinement. Similarly, it seems impossible to produce an alloy in the solid solution annealed state without also reducing the dislocation density. Exactly to what extent these disparate factors influence the dynamic behaviour in quantitative terms therefore requires the use of models, in which each factor can be parametrised through careful experimental characterisation data. This is highlighted in the final section of this chapter (Section 5.7), in which two analytical models are applied to the

current experimental data set. Also discussed are some preliminary results from a collaboration in which the experimental wave profiles are simulated directly.

## 5.6 Orientation analysis

In Chapter 4, it was found that the yield points of the textured Mg AZ31 were highly dependent on loading direction. The results were investigated using an orientation-based analysis, in which the expected behaviour of the initial grain orientation was predicted using a uniaxial strain-based orientation factor together with single crystal results. As some changes in the orientation distributions of the aluminium were also observed in Section 5.3.1, the possibility of this having affected the dynamic strength data needs to be addressed. The two samples under question specifically are 5N-Al S3 and Al 6082 S1, which had both lower peak elastic states and more randomised orientation distributions than their counterparts.

Previous studies by Owen [59] and Huang [167] showed that the dynamic strength of single crystal aluminium was highest in the $[111]$ direction, below which the $[100]$ and $[110]$ directions were close to equal, lastly followed by a polycrystalline aluminium sample which had the lowest yield point. The effects of varying the orientation however were much smaller than in magnesium. Due to basal slip being associated with a much lower CRSS than pyramidal slip, the peak stress along the $c$-axis in magnesium is around 0.8 GPa at 2 mm, whilst at 45° to the $c$-axis it's only around 0.03 GPa, representing a decrease of 96.2%. In contrast, in aluminium the majority of slip occurs along the $\{111\}\langle 1\bar{1}0\rangle$ slip system, as there is no orientation in which it cannot be activated. Consequently the orientation dependence in the yield stress is less a function of differences in CRSS values. In Owen's study, the peak stresses of the polycrystalline samples were about 18% lower than that of the $[100]$ and $[110]$ single crystals, and around 30% lower than the $[111]$ single crystal.

Keeping in mind that the above single crystal measurements represent extreme cases in orientation variation, this indicates that the effect of varying the loading direction in polycrystalline aluminium should be relatively small compared to that of an HCP system. Indeed, Whelchel et al. studied cold rolled 5083 loaded along the rolling direction and along the two transverse directions [92, 248]. While the two transverse directions displayed near identical response, the elastic stress in the rolling direction was only around 10% lower when compared to transverse loading.

The observed ordering of the single crystal and polycrystal peak stress states was explained by Owen in an orientation-based calculation similar to the one derived in Chapter 4, but for the specific single crystal directions only. The ratio between the maximum resolved shear stress in the $\{111\}\langle 1\bar{1}0\rangle$ slip systems and the applied longitudinal stress was calculated for the $[111]$, $[110]$ and $[100]$ loading directions. It is reasonable to assume that the orientation in which this ratio is higher will have a lower yield point, as slip becomes facilitated by the larger portion of shear stress applied along the Burgers vector of the slip system. This resulted in the prediction of yield in the $[111]$ direction being higher by a factor 1.3 over $[100]$ loading, which was in good agreement with the experimental results.

In order to extend this analysis further, the orientation factor $\overline{m}$ was derived in aluminium for a subset of specific loading configurations (elastic constants in the shock coordinate system were calculated from the base elastic constants [59] using the transformation relations [176]). The full derivation is lengthy and will not be detailed here as it is a repeat of the approach outlined in Chapter 4. Calculated orientation factors for two sets of loading angles applied to a specific slip plane are shown in Figure 5.21. Taking the example of loading axis 1, the orientation factor starts at a value around 0.18, and as $\theta$ is increased it peaks and then steadily decreases until it reaches 0 at $\theta = 90^{\circ}$, where the loading direction and this specific slip direction are perpendicular. At this point another one of the

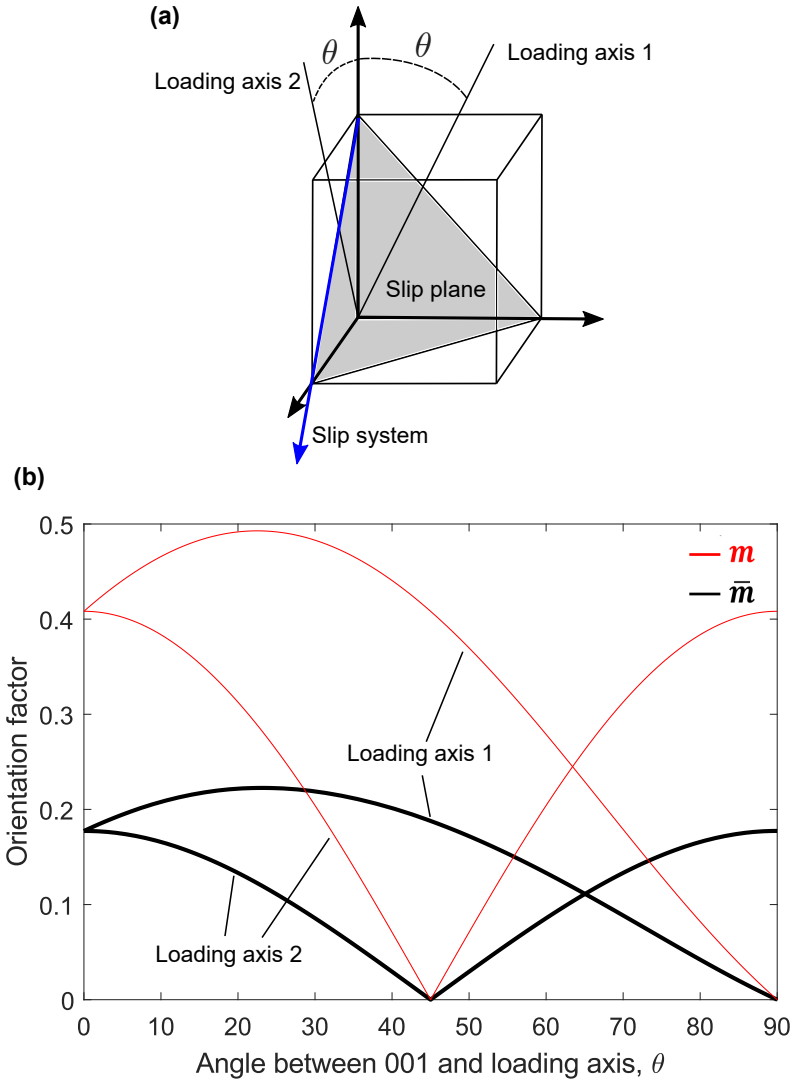



**Figure 5.21:** Dynamic orientation factor, $\overline{m}$, and Schmid factor, $m$, in Al for two sets of loading axes. The two loading configurations are shown in a), along with the $\{111\}\langle 10\bar{1}\rangle$ slip system used for the calculations. The resulting orientation factors for the two loading configurations are shown in b) versus the angle to the 001 axis. The Schmid factor is consistently higher than the uniaxial strain orientation factor by a factor of about 2.3.

available slip systems would have an orientation factor of 0.18

A full analysis similar to what was performed for magnesium would require repeating this derivation for all slip systems and possible orientations in the crystal system. Due to the apparently minor effects of orientation in aluminium, a full treatment was deemed unnecessary. Instead, an alternative method was applied using the Schmid factor, which as discussed in Chapter 4 is closely related to the orientation factor. Plotted in Figure 5.21 are the Schmid factors, $m$, for the

same loading configurations, as given by,

$$m = cos(\phi)cos(\lambda), \tag{5.9}$$

where $\phi$ and $\lambda$ are the angles between the loading axis and the slip plane normal and slip direction, respectively. It is shown that the Schmid factor follows the same curve as the uniaxial strain-based orientation factor but multiplied by a factor of around 2.3 (with negligible variation). This was confirmed for other loading configurations, not shown here. The higher magnitude is a result of the Schmid factor being based on uniaxial stress conditions, meaning the applied stress which is resolved along the shear plane is not opposed by any lateral stresses. As a result, using the Schmid factor to predict the absolute value of the yield point depending on the orientation (similar to how $\overline{m}$ was used in Chapter 4) would produce an underestimation. However, comparing the *relative* strength of different loading orientations can be done using either orientation factor. For example, in the case of loading axis 1 in Figure 5.21, both $m$ and $\overline{m}$ show that the strengths when loading along around $\theta = 10^{\circ}$ and $35^{\circ}$ are close to equal, whilst loading axis 2 goes to 0 at $\theta = 45^{\circ}$ in both. The application of Schmid factors was also successfully used by Owen to explain the ordering of the single crystal dynamic strength data.

Note that this reduced application of Schmid factors would not be appropriate in Mg. In HCP crystals, a change in orientation can initiate the activation of an entirely new slip system with a separate CRSS value, causing a change in magnitude of the strength which would not be captured by a simple comparison of Schmid factors. However, only one slip system needs to be considered for aluminium, meaning the magnitude of the CRSS value can be ignored when analysing the *relative* strength of one orientation with respect to another (as both involve the same deformation mode). It is therefore here assumed that the Schmid factor can be used to gauge the expected relative change in the yield point after a change in orientation distribution in aluminium.

The area-weighted average Schmid factors were calculated for all samples from the EBSD results shown in Figures 5.2 and 5.3 (this can be done very quickly using the MTEX [152] package in MATLAB). For 5N-Al S0, S1 and S3 this led to $m = 0.48$, 0.47, and 0.45 respectively. For Al 6082 S0, S1, and S3 the results were $m = 0.44$, 0.44, 0.43 respectively. The indication from these results is that the overall average effect due to the grain rotations in the less textured samples is very small, as there is an equal distribution of grains rotating to both more and less favourable orientations. For reference, the maximum possible Schmid factor of 0.5 is found at an intermediate angle between the $[100]$ and $[110]$ axes (around 35° from $[100]$). The Schmid factors for loading along $[100]$ and $[110]$ are both 0.41, and for loading along $[111]$ is 0.27. Note again that while the dynamic orientation factors, $\overline{m}$, would be different in magnitude compared to these Schmid factors, the relative difference in $\overline{m}$ between each sample would be almost identical.

Based on the above calculations, the difference between the Schmid factors for single crystal loading is 0.14. Given that even this relatively large disparity in $m$ led to a difference of only about 15% in the yield points, it can again be assumed that a change in $m$ of $<$0.03 in the current data (0.01 in the case of Al 6082) should have a very small effect. While the polycrystalline aluminium from Owen's study was associated with a significant decrease in yield point, the EBSD data showed that most grains were concentrated around orientations in between either the $[100]$ or $[110]$ directions, with few grains close to the $[111]$ orientation. The result would have been a high average Schmid factor and thus lower strength.

Review of the loading directions in the current samples shows that there is a significant spread of loading angles around the $[100]$ axis in the S0 state, which is highly favourable for maximising the resolved shear stress in the $\{111\}\langle 1\bar{1}0\rangle$ slip planes, even more so than that of a pure $[100]$ impact. In contrast, while the 5N-Al S3 and Al 6082 S1 samples also display grains in similarly favourable orientations, a very significant population of grains have been reoriented with the $[111]$ axis towards the impact direction. As this is the lowest Schmid factor orientation, the

overall effect to the average is a slight decrease. As noted above, a reduction in Schmid factor should produce a higher yield given that a smaller portion of the applied stress is resolved along the slip system. Consequently, the decreasing texture in both 5N-Al S3 and Al 6082 S1 results in them both being on average less favourably oriented for slip, which should cause an increased yield point assuming all other things are equal. Contradictory to this, the experimentally measured yield points are in fact lower when compared to the higher texture samples. The conclusion that increasing the dislocation density causes a lower strength is therefore still valid, and the effect may in fact even be slightly underestimated. One should note that this assumes that averaging the orientation factors for the grains is a good predictor of their effects on yield, as was done in Chapter 4.

In conclusion, the concern originally raised at the start of this section was that the measured decreases in dynamic strength could potentially be attributed to the changes to the orientation distributions of the aluminium samples (rather than the changing dislocation densities). It is found however that the effects are in fact most likely negligible, and would at the most produce a slight increase (rather than decrease) in the yield stress.

## 5.7 Application of dynamic strength models

### 5.7.1 Overview of modelling

The data set on aluminium presented in this chapter combines high resolution velocimetry measurements of precursor decay with detailed quantitative microstructural characterisation of the starting material. It provides strong experimental evidence for the role of dislocations at high rate loading, and at the same time addresses a lack of such data sets for the purposes of validating and refining dynamic strength models. Modelling is of high importance to this field, as the difficulty and short timescales of high strain rate experiments limits range of possible experimental measurements.

A more detailed description of dynamic strength models is found in Section 2.4. In one such model from 2010 by Ding et al., wave profiles in tantalum were successfully simulated using an Orowan-based approach accounting for the evolution of mobile and immobile dislocations due to multiplication and annihilation [17]. The authors noted however that, due to a lack of microstructural experimental data, their simulated profiles essentially represented an optimised data set that was best able to describe the experimental measurements. While qualitative conclusions can be drawn, the accuracy of quantitative parameters defined in such models are uncertain. For example, the relative contributions of dislocation density and dislocation velocity to the high rate dependence of tantalum in Ding's model was speculative. The authors emphasise that future development can progress once more data such as measured dislocation densities becomes available.

Indeed, a collaboration with modellers R. Kositski and D. Mordehai was initiated during the aluminium experimental campaign, the purpose of which was to apply their dislocation-based dynamic strength model to simulate velocity profiles using the dislocation density measurements in this study. According to the model, which is described in Section 5.7.3, the initial dislocation density is highly dominant in determining both the precursor amplitude and decay rate. In previous works however, Kositski, like other such researchers, was reliant on estimations and literature values for the dislocation density, meaning validation of the model was hampered. By constraining the initial dislocation density parameter in the model, it is now possible to more thoroughly investigate the physics of dislocation movement and generation.

In the following section, a simple analytical linear elastic expression, as described in Section 2.4, is first applied to the present experimental data on aluminium. The role of dislocation generation and elastic nonlinearity is then

demonstrated by contrasting this with the more advanced treatment as developed by Clayton and Lloyd [9]. Finally, preliminary results from the numerical simulation collaboration are shown in Section 5.7.3

### 5.7.2 Analytical modelling of precursor decay

First, the results from the experiments on 5N-Al are modelled using the classical linear elastic analytical model as described in Section 2.4, which represents a direct application of the Orowan equation to an expression for the decay rate of the precursor stress. The focus here will be on modelling the 5N-Al and not the Al 6082, as the latter is almost fully decayed by 0.2 mm propagation distance, meaning the model's decay rate prediction can not be compared to measurements.

**Table 5.4:** Parameters used for analytical modelling of precursor decay in aluminium [9, 16, 19, 20, 59, 252, 253]

| | | | |
|---|---|---|---|
| $\rho_0$ (g cm$^{-3}$) | 2.7 | $C_{11}$ (GPa) | 106.7 |
| $b$ (m) | 2.86×10$^{-10}$ | $C_{12}$ (GPa) | 60.4 |
| $E_0$ (GPa) | 70 | $C_{66}$ (GPa) | 28.3 |
| $G_0$ (GPa) | 26.3 | $C_{111}$ (GPa) | -1076 |
| $B_0$ (GPa) | 75.8 | $C_{112}$ (GPa) | -315 |
| $D$ (GPa) | 0.5 | $S$ | 1.34 |
| $c_l$ (ms$^{-1}$) | 6400 | $\theta$ (deg) | 35.25 |
| $c_s$ (ms$^{-1}$) | 3200 | $v_{D0}/c_{s0}$ | 0.105 |
| $c_0$ (ms$^{-1}$) | 5200 | $\Phi$ | 3 |
| $\sigma_{HEL}$ (GPa) | 0.1 | $\Gamma$ | 2.3 |

Shown in Figure 5.22 are the results from three calculations in which the initial dislocation density, $\rho_{D0}$, was matched to the experimental measurements. Parameters used for the model are listed in Table 5.4. It is found that dislocation densities on the order of $10^{13}$ m$^{-2}$ are needed in order match the experimental values at propagation distances above 0.4 mm, which is at least one order of magnitude higher than what is found in annealed aluminium. At the same time, the decay rate at thicknesses below 0.4 mm is heavily over-estimated, which is the region in which most of the precursor attenuation takes place. The reverse

is true when $\rho_{D0}$ is on the order of $10^{12}$ m$^{-2}$, in which case the early decay rate is more closely matched, however the yield values overall are consistently too high.

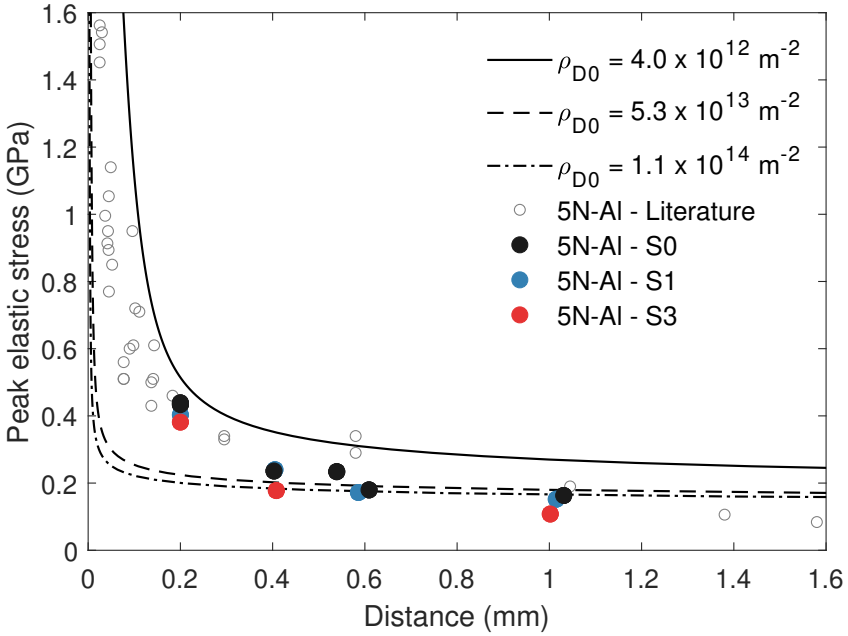



**Figure 5.22:** Linear elastic model of precursor decay in pure aluminium calculated using experimental values of initial dislocation density, $\rho_{D0}$ (see Table 5.2). Also shown are experimental yield points from the current and literature studies [20–24]. It is found that $\rho_{D0}$ on the order of $10^{13}$ m$^{-2}$ or more is needed to fit the experimental data, which is at least an order of magnitude higher than the measurements in annealed aluminium. This leads to an over-estimation of the decay rate in the low propagation distance region, in which the majority of precursor attenuation takes place. This discrepancy is attributable to dislocation generation not being included in the model. Error bars in the experimental data are equal to or smaller than the size of the points.

In his work on tantalum using the same model, Gillis found that using the experimentally measured initial mobile dislocation density of $10^{10}$ m$^{-2}$ also resulted in a predicted decay rate which was far too low to match the experimental data [16]. An increase of two orders of magnitude up to $10^{12}$ m$^{-2}$ was required in order to fit the observed yield stresses. Similar observations in which $\rho_{D0}$ was over-estimated by between 1-3 orders of magnitude were reported by Johnson et al.[11]. The discrepancies are ascribed to the model's assumption that the dislocation density is constant during the rise of the precursor, which effectively means ignoring additional attenuation caused by defects nucleated by the shock

wave. Given that dislocation densities are expected to reach values between $10^{13}$ to $10^{14}$ m$^{-2}$ during loading (see Sections 5.5 and 5.7.3), it stands to reason that when the initial dislocation density is already set to these values, the precursor states in the high thickness region are matched more closely. The side-effect is an over-estimation of the decay rate in thin samples, in which dislocation generation is still underway and densities may not yet have reached the final equilibrium values. Similarly, the fit for $\rho_{D0} = 4\times10^{12}$ m$^{-2}$ is incorrect because there is a lack of generation which would increase the decay rate towards the experimentally measured precursor stresses at higher propagation distances.

The importance of correctly accounting for dislocation generation is highlighted by contrasting the linear model to a 2018 model developed by Clayton and Lloyd (see Section 2.4) [9]. The latter incorporates two major improvements over the previous model iteration. First, the dislocation density is evolved using a breeding expression to account for the effects dislocation generation. The generation rate is dependent on a generation coefficient, $M$, which is set as adjustable. Second, elastic nonlinearity (i.e. dependence of elastic moduli on compression etc) is incorporated directly into the calculations. This addresses a short-coming in previous works which only account for dislocations located directly at the precursor front; a result of the assumption of linear elasticity for the dislocation stress fields and corresponding wave speeds. In the linear elastic approximation, the longitudinal elastic wave speed is equal to or lower than the precursor wave velocity, meaning any defect activity behind the front is not able to influence the precursor wave. In Clayton and Lloyd's nonlinear model, the elastic coefficients and wave velocities are adjusted to account for stiffening caused by the passage of the shock wave. Additional stress attenuation can then be ascribed to rarefaction waves generated behind the shock front catching up to the precursor front. As before however, there was a lack of experimental data to properly validate these studies, meaning Clayton and Lloyd relied on estimated rather than measured dislocation densities when producing the model curves.

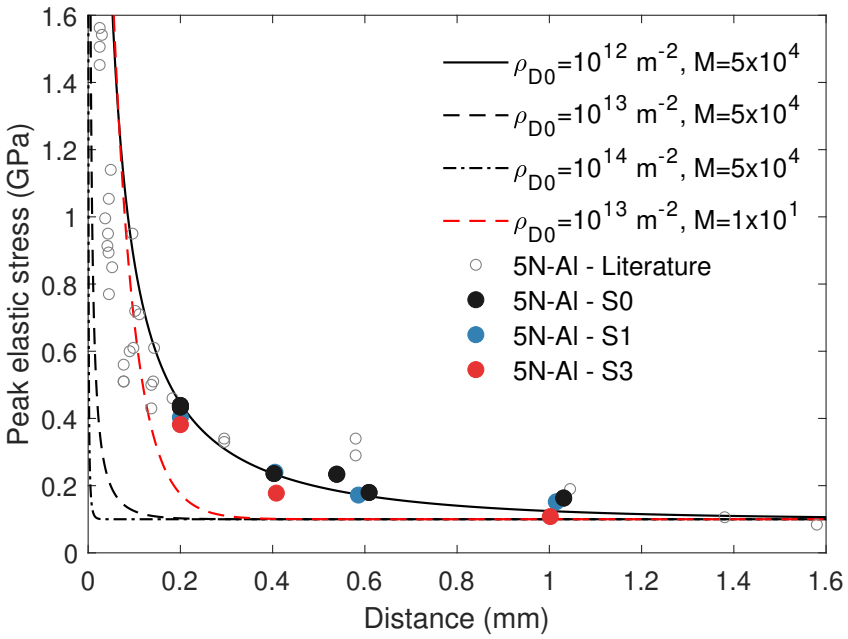



**Figure 5.23:** Nonlinear elastic model of precursor decay in pure aluminium for different initial dislocation densities, $\rho_{D0}$ (m$^{-2}$), and generation coefficients, $M$. Also shown are experimental peak stress states from the current and literature studies [20–24]. A good fit to the 5N-Al S0 is produced when setting $\rho_{D0} = 10^{12}$ m$^{-2}$ (reasonably close to measurement) and $M = 5{\times}10^4$. Increasing the dislocation density to the levels found in 5N-Al S1 and S3 produces a large over-estimation of the decay rate, even when decreasing $M$. This is due to the expression for dislocation generation in the model scaling linearly with the initial dislocation density.

The results from applying the nonlinear elastic model to the present data are presented in Figure 5.23. Note that the model is formulated assuming impact along the $[100]$ direction, and not for polycrystalline loading. Unfortunately, as stated by Clayton, extension of the model to textured polycrystals is not straight forward and was outside the scope of this project. The error however is assumed small given the close orientation to the $[100]$ axis in the present material, as well as the small difference in average Schmid factor as discussed in Section 5.6. It is shown that the best fit to the S0 data points is achieved when setting the initial dislocation density to $1 \times 10^{12}$ m$^{-2}$, which is reasonably close to the experimentally measured value of $4 \times 10^{12}$ m$^{-2}$. Unfortunately, increasing the dislocation density by one and two orders of magnitude, following S1 and S3 respectively, again results in an over-estimation of the decay rate. In fact the model predicts near instant decay after impact once the initial dislocation density is set to $10^{14}$ m$^{-2}$.

As the discrepancies between swaging levels are evidently not as large in the experimental data set, it seems clear that the role of dislocation generation needs to be further refined in future efforts. In particular, thought needs to be given to how the initial state of the material can result in lessened need for nucleation or multiplication during the early stages of rapid precursor attenuation.

Attempts were made to correct the fit in the swaged samples by reducing the dislocation generation coefficient, $M$, an example of which is shown by the red curve in the figure. While this did lessen the decay rate, it was not sufficient to reproduce the measurements. The expression for dislocation generation used in the model is a relatively simple relation in which the rate of change in dislocation density scales linearly with $M$, the stress, and the initial dislocation density (see Equation 2.33). This was reasonable for the single crystal data used in the study, however when $\rho_{D0}$ is unusually high, as is the case in the swaged samples, the resulting final dislocation densities in the model can reach $10^{15}$ or $10^{16}$ m$^{-2}$. This is likely well beyond what is required for plastic relaxation during the shock.

While the generation rate can be manually decreased by reducing $M$, more physically based descriptions require consideration of additional effects such as dislocation interactions, saturation, recovery, mobile vs immobile populations etc. A more advanced treatment is discussed is Section 5.7.3, in which the dislocation evolution is split into separate expressions governing multiplication, nucleation, annihilation and trapping. The annihilation rate for example is defined as dependent on the instantaneous dislocation density within the material, meaning scenarios in which $\rho_{D0}$ is already high at the beginning of the impact event consequently results in greater dislocation annihilation and more reasonable final dislocation densities. It is worth noting again that this analysis on how to adjust this imbalance in dislocation generation hinges on experimental data in which a range of initial dislocation densities are measured and tested, further emphasising the significance of the current study.

### 5.7.3 Dislocation-based numerical model

This section is dedicated to ongoing work which is being carried out through a collaboration with researchers Roman Kositski and Dan Mordehai from Technion Isreal Institue of Technology. Described are the results from using a dislocation-based dynamic strength model together with the present microstructural characterisation results to directly simulate the plate impact velocity profiles in aluminium. It should be noted that the original formulation and construction of the model was carried out in previous works by Kositski and Mordehai [19, 254]. The manner in which it was implemented and adapted to the current project was the result of a joint effort between Kositski and the present author. The model is briefly outlined in Section 2.4.2, and the results from fitting the model to the experimental velocity profiles are presented here. The fitted simulations are also employed in order to discuss the effects of varying specific model parameters describing dislocation physics, including the initial density, mobility, multiplication and nucleation. As this is an ongoing project at the time of writing, the data and conclusions presented in this section are preliminary. Again, the focus will be on the development of the model for pure aluminium.

The model distinguishes between two types of dislocations, that of mobile dislocations, $\rho_m$, which are responsible for plastic relaxation, and immobile dislocations, $\rho_i$, which contribute to strengthening the material (see Section 2.4.2). The change in mobile dislocation density is determined by,

$$\dot{\rho}_m = A_{nuc}\dot{\rho}_{nuc} + A_{mult}\dot{\rho}_{mult} + A_{trap}\dot{\rho}_{trap} + A_{annh}\dot{\rho}_{anhh}, \tag{5.10}$$

where subscripts $nuc$, $mult$, $trap$, and $annh$ represent the dislocation density evolution through nucleation, multiplication, trapping and annhilation, respectively, and each $A$ is a rate prefactor which is adjusted separately in order to obtain a good fit. Figure 5.25 shows the simulated velocity histories compared to experimental measurements from 5N-Al S0 and 5N-Al S3. In the S0 simulation, the best fit was provided by the initial mobile dislocation density set to $\rho_{m0} = 1 \times 10^{12}$ m$^{-2}$, and

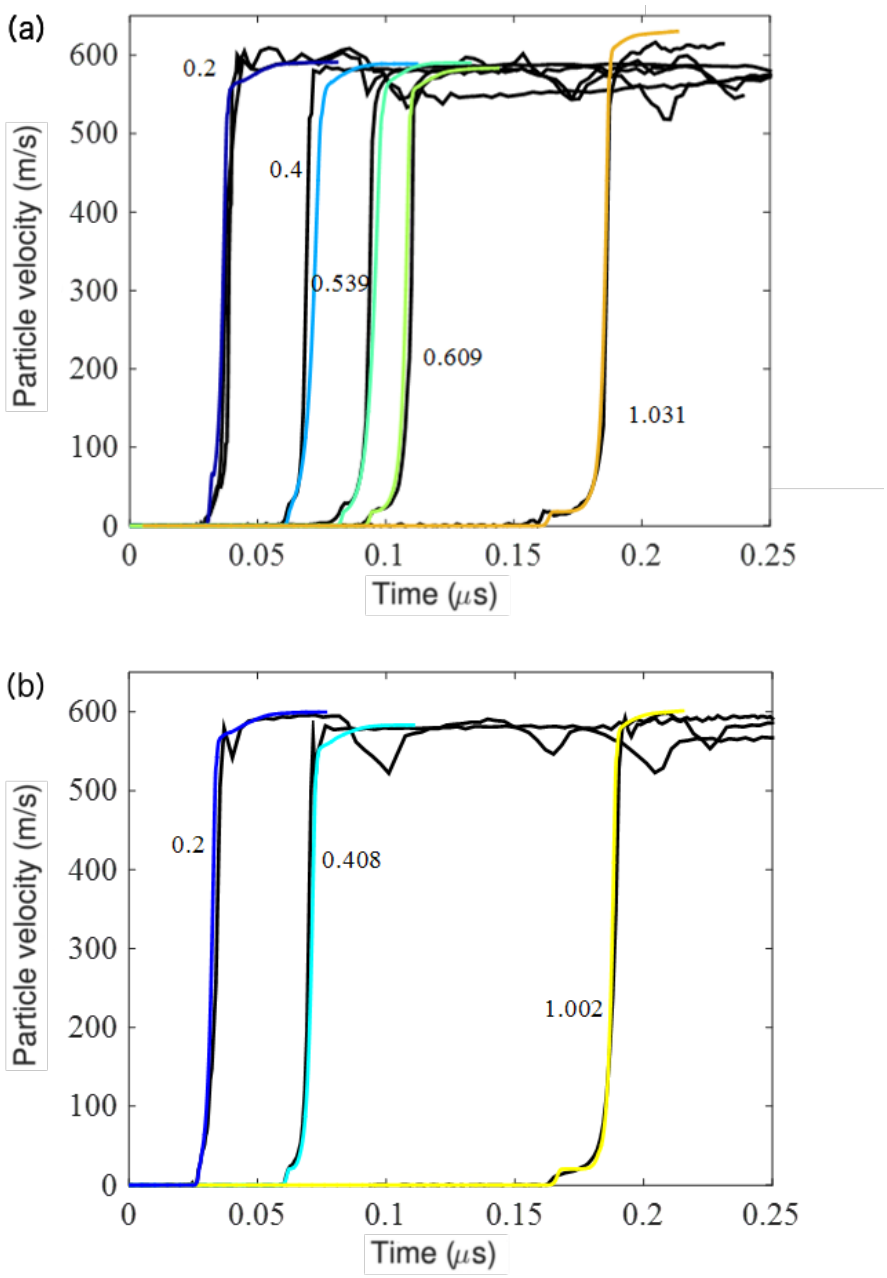



**Figure 5.24:** Free surface velocity histories obtained from simulations on a) 5N-Al S0, with $\rho_{m0} = 1 \times 10^{12}$ m$^{-2}$ and $\rho_{i0} = 1 \times 10^{14}$ m$^{-2}$, b) 5N-Al S3, with $\rho_{m0} = 2 \times 10^{12}$ m$^{-2}$ and $\rho_{i0} = 8.3 \times 10^{13}$ m$^{-2}$. Black curves show the corresponding experimental data for S0 and S3.

the immobile density set to $\rho_{i0} = 1 \times 10^{14}$ m$^{-2}$. Keeping all other parameters the same, the best fit for S3 was given by $\rho_{m0} = 2 \times 10^{12}$ m$^{-2}$ and $\rho_{i0} = 8.3 \times 10^{13}$ m$^{-2}$. This enabled both the pronounced decay of the elastic precursor wave as well as the decrease in peak stress with increasing swaging passes to be reproduced reasonably well. Unfortunately, the dislocation densities required for the fits

do not fully reflect experimental measurements. The total dislocation densities measured for 5N-Al S0 and S3 were $4 \times 10^{12}$ and $1.1 \times 10^{14}$ m$^{-2}$, respectively. While this does not distinguish between mobile or immobile dislocations, it can be assumed that most dislocations left after annealing in the S0 state could be considered immobile. The initial mobile dislocation density in the simulation for S0 therefore compares well with the TEM data, however the immobile density was two orders of magnitude too high. For the S3 simulation, the total dislocation density used in the model was close to the TEM data, but the immobile dislocation density had to be decreased with respect to the S0 simulation.

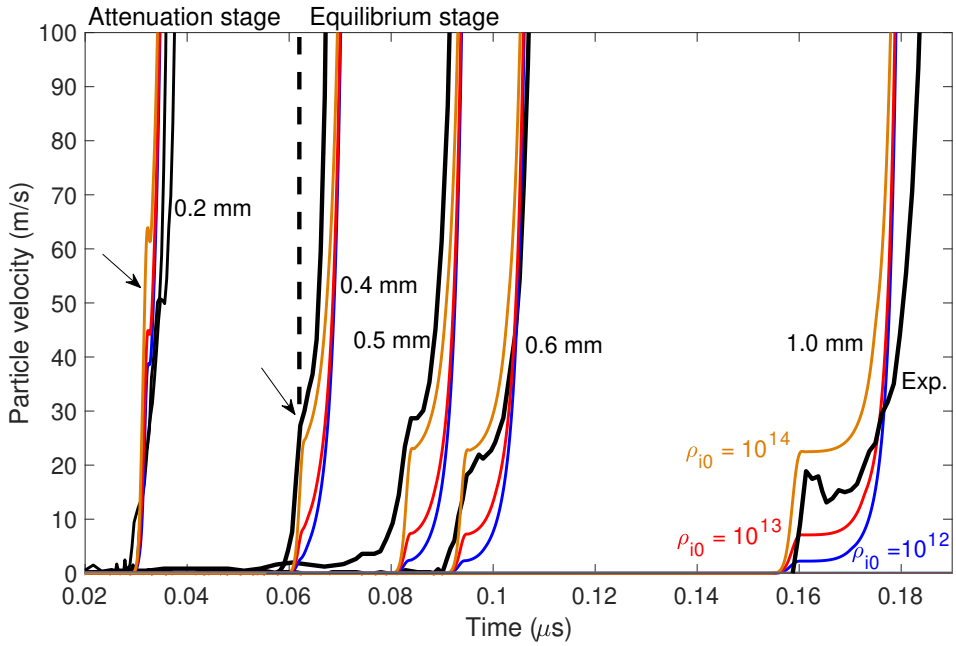



**Figure 5.25:** Simulations on 5N-Al in which $\rho_{m0} = 10^{12}$ m$^{-2}$ and $\rho_{i0}$ is varied as shown. The best fit, also shown in Figure 5.24a, is produced for $\rho_{i0} = 10^{14}$ m$^{-2}$. Black curves show the experimental data from plate impact experiments on 5N-Al S0. Arrows point to the low thickness experimental yield points. The precursor wave transitions from the attenuation phase to the equilibrium phase at around 0.4 mm thickness, at which point the majority of precursor decay has occurred.

These inconsistencies regarding the immobile dislocation densities in the simulations are currently unresolved. The reasons for the mismatch in the model is demonstrated in more detail in Figure 5.25, showing the 5N-Al S0 simulation results for different $\rho_{i0}$. Reducing the immobile dislocation density significantly

lowers the peak stress across all thicknesses. Constraining the immobile density to the measured value in S0 of around $10^{12}$ m$^{-2}$ would cause a significant under-prediction of the precursor stress. The same reason explains why $\rho_{i0}$ had to be decreased in the S3 simulation (compared to S0), which was done in order to produce a lower precursor stress than S0 (in the thicker samples in particular). The rest of this section is dedicated to discussing the reason for these simulation results, and the effects of varying the other model parameters.

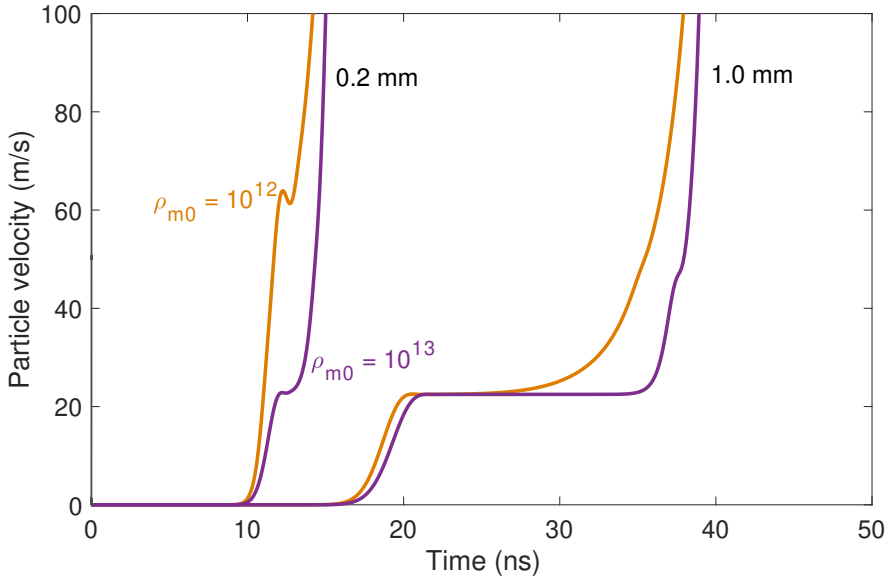



**Figure 5.26:** Effect of varying the initial mobile dislocation density in the dynamic strength model for 0.2 and 1.0 mm thick samples. Velocity histories are obtained from a simulation of pure aluminium in which $\rho_{i0} = 10^{14}$ m$^{-2}$ and $\rho_{m0} = 10^{12}$ or $10^{13}$ m$^{-2}$. Sample thicknesses are shown in the plot, and time has been shifted for clarity. It is found that increasing the initial mobile dislocation density reduces the yield point in the thin sample, however it causes no significant difference in the precursor amplitude in the thicker sample, as it is already fully decayed by this point.

Precursor decay in aluminium is here split into two different stages. The "attenuation" stage, as shown in Figure 5.25, is found at propagation distances below 0.4 mm (corresponding to initial plastic strain rates above $\sim 10^6$ s$^{-1}$), where yield points are significantly higher than the equilibrium value and fast attenuation takes place. In the "equilibrium" stage, above 0.4 mm, most of the decay has already occurred and the precursor amplitude is very close to its equilibrium value.

It is found that the immobile dislocation density affects the dynamic strength in both regions (see Figure 5.25), meaning it can be viewed as determining the baseline strength of the material. This is consistent with how precipitation hardening also causes an increased strength due to higher dislocation pinning, which is discussed in Section 5.5.2 in reference to the dynamic strengths of aluminium alloys with varying processing history. The mobile dislocation density however only affects the precursor amplitudes in the attenuation stage. As shown in Figure 5.26, increasing the mobile dislocation density results in a faster decay rate or lower peak stress at 0.2 mm distance. At 1.0 mm however the precursor has already reached equilibrium, and the only effect is on the strain rate in the plastic region of the wave, not the stress amplitude.

This behaviour, and the transition point from the attenuation to the equilibrium stages, is linked to the mobility of dislocations in the material. The mobility law, taken from MD simulation data [58, 255], determines the velocity of mobile dislocations as a function of the applied stress. In aluminium, dislocation movement is easily induced and reaches high values at relatively low shear. The result is that deviatoric stresses in the precursor wave can be relaxed quickly, and the peak stress is rapidly decreased (even with relatively low dislocation numbers). The base mobility curve fitted to the MD data is presented in Figure 5.27, and is used for the simulations shown in Figures 5.24-5.26. The same figure also demonstrates the effect of decreasing dislocation velocities by reducing the stress dependence of the mobility curve. The consequence is an extended attenuation region in which the decay rate is much slower and elastic stresses are higher.

This behaviour was observed in Mg AZ31, as discussed in detail in Section 4.4, in which the ED specimens displayed significant precursor attenuation up to 2.3 mm propagation, while the TD orientation had already reached close to its equilibrium value by 1 mm. It was shown that the latter deforms primarily through basal slip, which has by far the highest mobility [172], meaning the attenuation rate is very fast and equilibrium is reached quickly. ED samples on

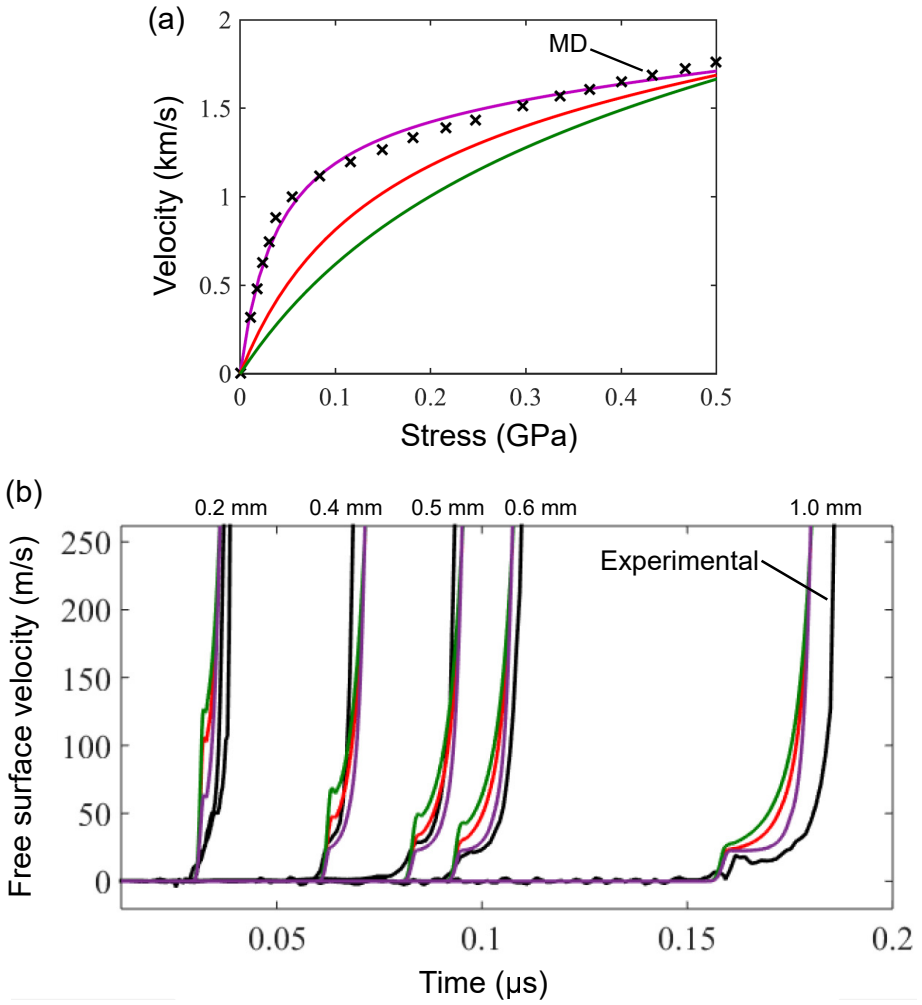



**Figure 5.27:** Effect of varying the mobility law in the dynamic strength model. a) Three different mobility curves, as well as data from MD simulations shown as crosses [58]. The mobility curve fitted to the MD data is used for the simulations shown in Figures 5.24-5.26. b) Colour coded velocity profiles corresponding to the three mobility curves shown in a), plotted along with experimental data from 5N-Al S0. Decreasing the stress dependence in the mobility relation slows the decay rate and raises elastic stresses.

the other hand were associated with a much higher proportion of prismatic slip which, with its lower mobility, resulted in a slower decay rate.

In the current model, reducing the mobility effectively shifts the equilibrium point of the precursor wave to higher propagation distances, extending the attenuation stage of the wave. This means that the thickness range within which the initial mobile dislocation density influences the precursor stress (by either alleviating or aggravating the lack of mobility) is also extended. Frequent

observations in tantalum of a cold work induced decrease in the dynamic strength were mentioned in Section 5.5.2 [57, 71, 93]. As Ta is a material with an already low mobility, i.e. with a long attenuation stage, the model is able to accurately explain these results as being caused by an increase in the mobile dislocation density. This was successfully applied to Ta and Va in a previous study [19]. In aluminium however, the high mobility means the initial mobile dislocation density only affects the precursor amplitudes below 0.4 mm propagation distance. While this could potentially be addressed by decreasing the mobility, that would instead introduce a discrepancy with the MD-derived mobility curve. The data used from these simulations was that of the screw dislocation mobility, which is already lower than the edge dislocations.

Keeping this in mind, the effects of the multiplication and nucleation parameters are now investigated. The multiplication rate in the model is proportional to the mobile dislocation density, the dislocation velocity, and a fitting parameter, $A_{mult}$. The effect of varying the multiplication rate by changing $A_{mult}$ is shown in Figure 5.28. It is found that multiplication primarily affects the strain rate after the yield point, where rapid dislocation generation causes the plastic strain rate to increase. The effects on the yield point itself however are again only significant in the very low propagation region, in this case below 0.2 mm.

The dislocation nucleation rate is examined in Figure 5.29. Nucleation is modelled using the Arrhenius equation (Equation 2.41), meaning it is dependent on the resolved shear stress. It is found that decreasing the nucleation rate leads to a sharp stress spike in the 0.2 mm target. This spike is a result of the higher shear stresses necessary in order to nucleate the amount of dislocations needed to accommodate the high strain rates right after impact. Once the dislocations have been generated the stress is quickly relaxed. At higher propagation distances, strain rates are lower and mobility alone can supply the required stress relaxation, meaning lessening the nucleation rate has only a minor effect.

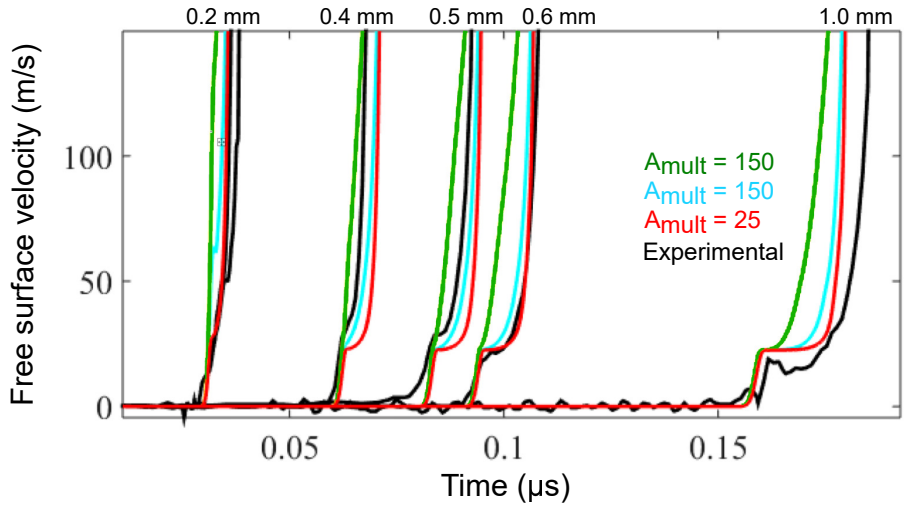



**Figure 5.28:** Effect of varying the multiplication parameter, $A_{mult}$, in the dynamic strength model. The velocity profiles from plate impact experiments on 5N-Al S0 at increasing thickness are plotted together with modelled velocity profiles using $A_{mult}$ set to between 25 and 150. It is found that a high multiplication rate raises the strain rate in the plastic rise of the shock.

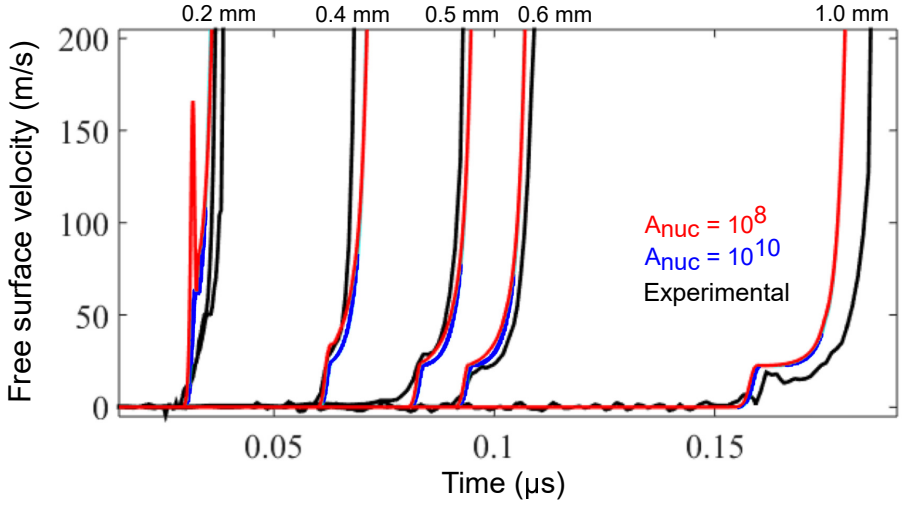



**Figure 5.29:** Effect of varying the nucleation parameter, $A_{nuc}$, in the dynamic strength model. The velocity profiles from plate impact experiments on 5N-Al S0 at increasing thickness are plotted together with modelled velocity profiles using $A_{nuc}$ set to $10^8$ and $10^{10}$ m$^{-2}$. A low nucleation produces a sharp stress spike in the low thickness (or high strain rate) targets. This is caused by higher shear stresses being reached before enough nucleation can be supplied to relax the imposed stress. In higher propagation distances, there is enough time for mobility alone to supply the stress relaxation, and lessening the nucleation rate has only a minor effect.

To summarise, the simulations propose that the higher dynamic strength in the annealed material can be explained by the fact that the low number of mobile

dislocations in the sample limits the plastic relaxation at very high strain rates. However, the range of influence of the initial mobile dislocation density is heavily dependent on the mobility of the material. In a high mobility metal such as aluminium, only the highest strain rates found at thicknesses below 0.4 mm have yield points significantly higher than the equilibrium limit. The model suggests that the mobile dislocation density has an effect only during this attenuation stage, where the precursor stress is still decaying and mobility alone is not sufficient for stress relaxation. The attenuation rate in this regime can therefore be adjusted by changing parameters such as the initial mobile dislocation density, nucleation or multiplication rates. These are summarised in the schematic diagram shown in Figure 5.30, which presents an illustration of a decaying precursor wave in an aluminium-like material. Mobility can be affected macroscopically by changing the temperature, as discussed in Section 2.3.2, or the slip plane, as was evident from the data on magnesium in Chapter 4. The initial dislocation density is changed through annealing or cold work, as was done in the present chapter. Exactly how to affect parameters such as the nucleation or multiplication rates from a macroscopic context is more complex. It is possible for example that increased nucleation rates can be achieved through increasing the grain boundary density (which may act as nucleation points).

At lower strain rates, i.e. in the equilibrium stage (above around 0.4 mm in this case), the mobility (or number) of mobile dislocations is no longer a limitation to achieving stress relaxation. Instead, the role of immobile dislocations and their contribution to hardening becomes the dominant factor in the simulations. After this transition, the effect of cold worked materials having a lower peak stress should therefore be concluded, as the increased mobile dislocation densities are now less important. The material should shift into low strain rate behaviour, in which cold working increases the strength and annealing decreases it. When examined as a function of propagation distance, this transition in the role of cold work in the simulations mimics the illustration in Figure 5.31.

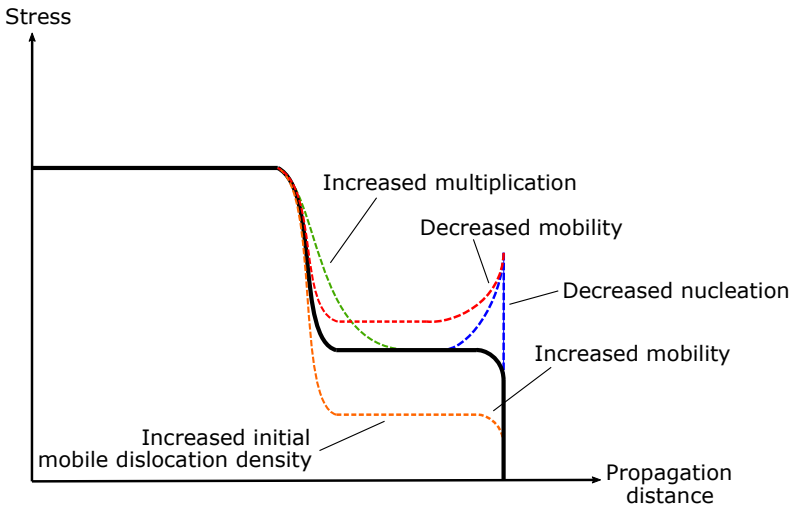



**Figure 5.30:** Illustration of precursor wave variations inside an aluminium-like material during the attenuation stage. Spikes originate from a lack of dislocation relaxation, which can be caused by a decrease in either mobility or nucleation (or the initial density in low mobility cases). Increasing the initial dislocation density or the mobility conversely results in faster stress relaxation and a lower precursor amplitude. Macroscopically, the mobility is affected by the temperature and the slip system (or orientation), while the initial dislocation density is changed through cold work or heat treatment.

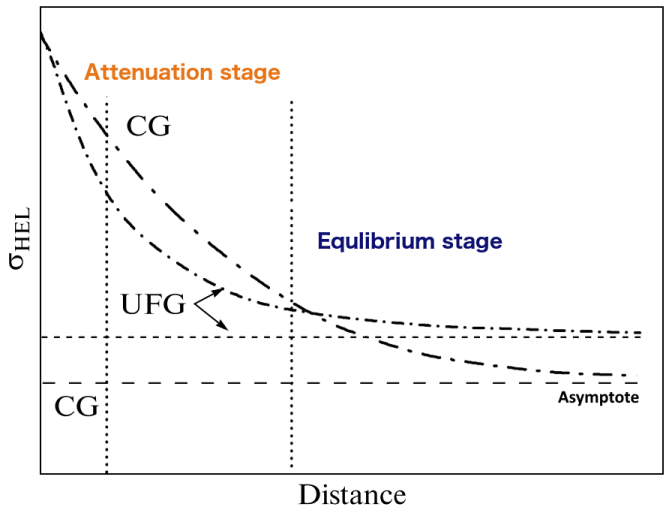



**Figure 5.31:** Illustration of the suggested reversal in strengths of an annealed (CG) and cold worked (UFG) metal as the shock wave propagates, adapted from [93]. In the attenuation stage, the role of mobile dislocations is critical, and a material with fewer initial mobile dislocations (e.g. annealed) will display slower precursor attenuation. In the equilibrium stage, rate effects are much less significant and the mobile dislocation density stops influencing the precursor amplitude. Cold working thus increases the strength of the material, similar to the behaviour at lower strain rates. The region between the two vertical lines indicates the thickness range of the current experimental data.

This theory currently causes a discrepancy between the model and the experimentally measured data in the thicker samples. As the simulations treat samples thicker than around 0.4 mm as being within the equilibrium stage, reproducing the velocity profiles of swaged specimens requires lowering their initial immobile dislocation densities compared to S0 (equivalent to simulating that swaging decreases the strength in low strain rate experiments as well). The issue can potentially be addressed by shifting the point at which the simulated precursor reaches its equilibrium amplitude, which is determined primarily by the mobility curve. Indeed, the peak precursor stresses measured experimentally in aluminium continue to decay up to 10 mm, albeit very slowly [20]. Decreasing the mobility results in a slower decay rate, which effectively extends the attenuation stage within which adjustments to the mobile dislocation density can be applied instead. The problem with this approach is that the model would then diverge from mobility data gathered from MD simulations. The issue may therefore need a deeper examination of exactly how immobile dislocations and the equilibrium yield point is determined. Although not shown here, the annihilation and trapping parameters both decrease the amount of available mobile dislocations in a fashion similar to a reduction in the multiplication parameter.

Whether or not the reversal in yield points could actually be observed in precursor decay experiments also needs confirmation. The closest example would be the studies on Ta discussed previously in Section 5.5.2. The depiction in Figure 5.31 was originally proposed in the study by Razorenov et al. [93], in which it was found that cold worked Ta displayed a lower elastic stress magnitude than the annealed version, but with the difference decreasing with propagation distance. It was theorised that the reversal in strengths should be observed at higher thicknesses. However, further investigation by Millett et al. of cold rolled versus as-received tantalum found no such transition, even up to 9 mm thickness (or a strain rate on the order of $10^4$ s$-1$, calculated using Equation 5.6) [57]. Note however that the as-received material displayed a precursor peak and pull-back, out of which the amplitude of the pullback did converge towards the yield point

of the cold rolled material. Another point of comparison is the current Al 6082 data, in which the precursor is clearly very close to the equilibrium limit but still displays lower yield point with increased dislocation density. While the reversal theory could therefore be considered inconsistent with the results on both Ta and Al 6082, it is possible that even higher thicknesses than expected are necessary in order to measure the switch in elastic stresses.

Another explanation could potentially be found in the theory suggested by Millett et al. in their Ta study [57]. In it, they propose that the increased mobile dislocation density created through cold work was not a result of increasing the overall dislocation density (which seemed relatively unchanged in TEM images); rather, it was achieved through unpinning dislocations originally trapped by interstitials (effectively turning immobile dislocations into mobile ones). Such a scenario would reduce the peak stress in both the attenuation and equilibrium stages of the simulations (due to a lower immobile dislocation density). However, the model would then be unable to capture the increased strength of the same cold worked Ta in SHPB or quasistatic experiments. Together this would indicate therefore that the distribution of what are defined as mobile versus immobile dislocations within a given sample may need adjustment depending on the applied strain rate. Perhaps, the unpinning stress of certain populations of dislocations are lowered enough by cold work to enable movement by the high shear stresses experienced during shock loading, but not during quasistatic loading. Whether or not this stands true for the Al 6082 is also a separate question. In the TEM observations in the S0 state, a significant amount of dislocations are observed as attached to or originating from precipitate particles, while the S1 specimen displayed a much higher fraction of mutually tangled dislocations. In the EBSD data, the S1 sample had by far the highest fraction of LABGs. Both of these measurements may point towards higher fractions of dislocations that are likely to become mobile at high strain rates, i.e. dislocations not pinned to either precipitates or HAGBs. If one speculates that S1 therefore exhibited a decrease in immobile dislocation density compared to S0, then the simulation results (and

the reversal theory as depicted in Figure 5.31) may hold true (although it still requires experimental measurement). This does not solve the overestimation of immobile dislocation densities in the S0 states however (in both 5N-Al and Al 6082), indicating that further consideration of mobility or model dislocation parameters is still needed.

## 5.8 Chapter summary

This chapter presents an investigation into the role of cold work and initial dislocation density on the dynamic strength of aluminium. Plate impact experiments were conducted on pure aluminium and aluminium alloy 6082-T6 with increasing passes of rotary swaging. Detailed material characterisation was performed in order to measure grain size, boundary misorientation, grain orientation, and dislocation density. Using both TEM and EBSD techniques, it is found that the dislocation density increases with increasing swaging passes in 5N-Al, with an increase of two orders of magnitude at a strain of 1.4. In Al 6082, the dislocation density increases after the first pass, but decreases slightly after the third pass at a strain of 2.8. Comparison of the peak precursor stress states to the measured dislocation densities reveal an inverse relationship, in which increased initial dislocation density results in a faster decay rate and lower peak stresses across all measured thicknesses.

In the high strain rate regime of shock experiments, the high non-equilibrium precursor states are a result of the failure of dislocation mobility alone to release the imposed deviatoric stresses. The result is a high dependence on dislocation generation, which requires time and high applied stress in order to initiate. Given the experimental results, it is theorised that cold work increases the availability of initial mobile dislocations, which are responsible for increased stress relaxation in the swaged samples and a lessened reliance on generation mechanisms. The findings imply that the increase in mobile dislocations dominates over the effects

of increased dislocation pinning when cold worked materials are loaded at high strain rates (above $10^5$ $s^{-1}$), with the opposite being the case in low strain rates (below $10^4$ $s^{-1}$). The inconsistent literature findings on the role of cold work are discussed, although a complete analysis was not possible given the lack of dislocation density measurements. Decreasing dynamic strength after cold work was observed in shocked Ta, Ti and some Al alloys, however the opposite was found in other Al alloys. It is proposed that the measured increases in dynamic strength in certain Al alloys was a result of the prior heat treatments conducted in these studies, which cause a significant decrease in the strength of the material before the cold work process is applied. The state of the alloy's progression along its precipitation sequence, and the amount of dislocations pinned to these precipitates, is likely dominant over any effects caused solely by variations the dislocation density. Cold working an annealed alloy likely causes a preferential increase in immobile rather than mobile dislocations.

Based on current experimental evidence, as well as analysis of previous experimental results and theoretical treatments, it is suggested that the effect of grain boundaries in high strain rate loading is either negligible in determining decay rates, or possibly contributes to an increased decay rate through enabling greater dislocation generation. Analytical modelling of the experimental data re-affirmed the importance of dislocation generation in determining the dynamic response. Using a model in which dislocation generation is ignored required initial dislocation densities at least 1 order of magnitude greater than measurements in order to fit experimental data. Application of a more recent analytical model, which incorporates the effects of dislocation generation and elastic nonlinearity, resulted in a reasonable fit of the experimental data in the annealed state. However, increasing the initial dislocation density in line with experimental measurement produced an over-estimation of the decay rate. It is indicated that the generation model needs to account for effects such as dislocation annihilation and recovery. The above conclusions were reinforced in the results from a collaboration on a numerical dynamic strength model in which the experimental velocity profiles

were simulated directly. The lower peak stresses in the cold worked samples are found to be a result of increased plastic relaxation at high strain rates due to the higher number of mobile dislocations in the sample. Good fits to the experimental velocity profiles were produced using reasonable values for the mobile dislocations, but required over-estimations of the immobile dislocation density. The influence of dislocation mobility, nucleation and multiplication are discussed.

Finally, a theoretical reversal in the effects of cold work as strain rate decreases (or propagation distance increases) in plate impact experiments is investigated. While the transition to a trend of cold work strengthening should occur before strain rates of around $10^3$ $s^{-1}$ (the domain of SHPB experiments), experimental measurement of this shift in Al is still outstanding. Measurement of the transition is of high importance to future work, as it can be used to quantify dislocation mobility, as well as the disparate behaviours of mobile and immobile dislocations.

# 6 Conclusions

This chapter presents a summary of the work and the conclusions of this thesis, split into two sections: first, the objectives of each experimental campaign are summarised individually, along with their principal results; second, the conclusions gathered from the results of all three campaigns are consolidated, from which a comprehensive overview is presented on the effects of each of the microstructural parameters which were concentrated on in this thesis.

## 6.1 Summary of work and results

The goal of the present work was to investigate the effects of microstructure on the yield point in materials under shock loading. This first involved the development of a high precision plate impact experimental platform, detailed in Chapter 3, with which dynamic yields points were measured up to time resolutions of around 1 ns. Three experimental campaigns were conducted, broadly focused on the effects of crystal orientation in Mg AZ31, grain size in Mg AZ91, and initial dislocation density in pure Al and Al 6082. To support these investigations, high emphasis was placed on conducting detailed characterisation of the initial microstructural state of the materials, including measurements of grain size, boundary misorientation, grain orientation, and dislocation density.

In the first study, described in Chapter 4, highly textured extruded Mg AZ31 was impacted parallel and perpendicular to the extrusion direction. This enabled

the study of different grain orientation distributions under states of constant grain boundary and dislocation density, as characterised in EBSD measurements. Significant differences were observed in the magnitude, shape and the decay rate of the elastic wave amplitude depending on the loading direction, proving that relative changes in slip system activity plays a key role in shock loaded polycrystals and not just single crystals. A novel orientation-based analysis framework was developed which enabled a good fit of the dynamic yield points of the alloy, built on a combination of the measured orientation distributions and the dynamic CRSS values of single crystal magnesium modified by a strengthening factor.

In the study on AZ91, the effect of grain boundary density was investigated by shock loading samples produced using the recently developed melt shearing technique, and comparing them to conventionally cast samples. The study was uniquely positioned to focus exclusively on changes in grain boundary density, as the melt-shearing method produces considerable grain refinement without significant changes in dislocation density or grain orientations, as is usually the case after the cold work or annealing implemented in previous studies. The measurements indicated that variations in grain size produced no significant differences in dynamic strength in AZ91 over the investigated regime.

Finally, Chapter 5 presented a long needed quantitative investigation on the role of initial dislocation density in pure aluminium and Al 6082. Both materials were subjected to increasing passes of rotary swaging, which was found in TEM measurements to result in order-of-magnitude variations in dislocation density. The linear intercept method was applied to quantify exact dislocation densities in each sample, supported by comparisons to GND density calculations from EBSD data. Plate impact experiments conclusively revealed a strong relationship in which increased initial dislocation densities lead to reductions in peak elastic stress as well as a faster decay rate across all propagation distances. While this relationship has long been theorised, quantitative experimental data has been necessary in order to further develop both models and theoretical understanding.

Analytical precursor decay models were indeed applied to the experimental data, producing an over-estimation of the decay rate in the high dislocation density samples. It was emphasised that careful development of dislocation generation terms in the models need to be considered to enable their wider applicability beyond annealed or single crystal material conditions. Finally, these conclusions were supported by results from a collaborative effort in reproducing the experimental wave profiles using a numerical dislocation-based dynamic strength model. The relationship between mobile and immobile dislocations was discussed, in which it was suggested that the mobile dislocation density affects the dynamic yield point only during it's attenuation stage, while immobile dislocations determine the overall strength of the material.

## 6.2 Synthesis and future work

While the aspects of microstructure examined in this work were separated into distinct experimental campaigns, a degree of overlap in these studies was inevitable. This was especially evident during the experiments on aluminium, in which the effects of cold work lead not only to variations in dislocation density, but also in grain boundary density and grain orientation, which in part motivated their separate study. This final section therefore serves as a synthesis of the conclusions gathered from the combined results in this thesis.

First, a baseline description of the process of precursor decay, built upon the current results and modelling analysis, is provided as follows: when subjecting a material to a rapid load, it will begin by responding purely as an elastic medium. Eventually, the resolved shear will build until it surpasses the CRSS of a given deformation mode. Dislocation motion and plastic flow is initiated, which in turn relaxes the shear stress. However, if the loading rate is high, then stress relaxation through mobility alone will be insufficient. The resolved shear will continue to build until it causes rapid dislocation generation, either through homogeneous or

heterogeneous nucleation. Similar to dislocation motion, once begun this will lead to fast relaxation of the imposed stress state. This process is repeated for every new volume element through which the shock wave passes. As the loading event progresses however, the relaxation waves from dislocations in previous volume elements will catch up to and attenuate the precursor wave amplitude. Eventually the stress relaxation will reach an equilibrium with the compression wave and the final stable HEL stress is reached. Our ability to quantitatively describe or model this transient process across a wide range of materials hinges upon our understanding of how the microstructural environment affects how dislocations operate. In the following sections, the effects of the four microstructural features which were the primary focus points for this work are summarised.

**Effects of grain size**

The grain boundary density is in theory capable of producing higher strength due to the additional obstacles presented to moving dislocations. Alternatively it could also result in lower stress states, as grain boundaries serve as points of facilitated dislocation nucleation. However, in the study on Mg AZ91 on varying grain size it was found that magnesium displays a grain size independent dynamic response, meaning neither effect influences dislocation behaviour to a detectable degree. It was noted that the swaging process in the study on aluminium also produced high grain refinement, but caused a reduction in the dynamic yield, meaning grain boundary strengthening was unlikely. Order of magnitude differences in grain size in literature studies also found no significant impact on dynamic strength. It is suggested that the underlying cause is the short rise times of the elastic precursor wave, often on the order of only a few nanoseconds. As this is comparable to the timescales necessary for dislocations to travel across a grain, it was concluded that there simply is not enough time for sufficient dislocation-grain boundary interactions to take place at these time-scales (nano-sized grains may be required to produce measurable differences).

Whether or not high grain boundary density leads to higher dislocation nucleation is a separate question, however again given the general trend of grain size insensitive response it seems that nucleation does not overly depend on the presence of grain boundaries to facilitate the process. Conclusive experimental proof would require measurement of the yield points in propagation distances where generation mechanisms dominate over mobility, i.e. below 200 $\mu$m in aluminium, and where grain boundary density is the only varied parameter. Such a study could for example consist of comparing shock loaded single crystals with annealed polycrystalline pure aluminium in this thickness range, however corrections would have to be made for the orientation distribution in the latter.

**Effects of secondary phase particles**

Contrary to grain boundary density, the addition of secondary phase particles is arguably the most dominant microstructural adjustment which can be made to the dynamic yield point, a fact that can be readily observed from even a brief survey of the literature. The peak elastic stress in Al 6082 was found to be between 2 to 5 times higher than pure aluminium, depending on the target thickness. Similarly, the orientation analysis conducted in Mg AZ31 found that a strengthening factor of 2.4 had to be applied in order to account for the increased strength compared to the predicted pure magnesium yield points. The primary effect of the precipitate particles are to act as obstacles to dislocation motion. Contrary to grain boundaries, secondary phases are spread all throughout the matrix, whether in the solid solution or in the precipitation hardened state. This raises the average critical shear stress needed to initiate plastic flow, which not only increases the magnitude of the elastic state, but was also observed to decrease the strain rate dependence in the Al 6082 measurements. The state of the alloy's progression along its precipitation sequence, and the amount of immobile dislocations pinned to these precipitates, is most likely dominant over variations in dislocation density on its own. Each stage of the precipitation sequence of the material increases the threshold stress for dislocation motion, effectively raising the transition point from the thermal activation to dislocation drag regimes. It was suggested that this could

potentially explain past observations on aluminium alloys, where the strength of annealed alloys was lower than the subsequently cold worked, and likely age-hardened, samples. The cold work processes likely produced a preferential increase in immobile over mobile dislocations, resulting in a higher strength.

**Effects of crystal orientation**

The crystal orientation is demonstrated to be of high importance for two reasons: 1) it changes the resolved shear stress acting on a slip system, and 2) in anisotropic materials it can result in the activation of entirely different deformation modes with very different CRSS and dynamic behaviour. Both of these effects were shown to influence the behaviour of textured AZ31 through application of an orientation-based analysis framework, in which the measured orientation distribution was combined with dynamic CRSS values in order to predict activation stresses on a per-grain basis. Compared to pure $a$-axis loading, impact on a distribution of grain orientations centered around the $a$-axis (i.e. ED targets) was predicted to cause some strengthening due to smaller fractions of resolved shear applied along the prismatic plane, but this was over-shadowed by the reduced strength in the high fraction of grains deforming through basal slip. Similarly, TD targets were shown to be slightly stronger than single crystals oriented optimally for basal slip, both because of the sub-optimal grain orientations, and the activation of higher threshold deformation systems. In the ED target, stress relaxation was hampered to the point that it activated fast dislocation multiplication at the precursor peak, resulting in a stress pull-back. This was not necessary for TD samples, where the decay rate was therefore significantly faster. The same orientation analysis was also utilised in the study on aluminium, where it was shown that crystal orientation should in theory also lead to significant differences in yield points (despite the more isotropic crystal structure), purely because of the associated changes in resolved shear stress. In the specific case of orientations in this study however, the predicted changes in the yield points were very small.

Further work is certainly needed to confirm these predictions. The most straight-forward approach would be to conduct a series of plate impact experiments on extruded pure magnesium and compare measurements to the predictions in this thesis. A full extension of the model to other HCP materials, such as Ti, or other crystal structures entirely, such as aluminium, is predicated upon access to single crystal data. A series of experiments on both single crystal as well as extruded pure aluminium in a wide thickness range would be an excellent starting point. Confirmation of the analysis framework would permit study of effects such as temperature or cold work in magnesium polycrystals, or examinations of grain boundary density in aluminium, where any grain re-orientations could be compensated for in the data analysis with relative simplicity.

**Effects of initial dislocation density**

In low strain rate loading, raising the dislocation density causes an increased presence of pinning points and longer-range strain fields, effectively increasing the threshold stress for dislocation movement. In the high strain rate regime however, the acting shear stresses are high enough that such obstacles are easily overcome. The high precursor states are instead caused by the failure of dislocation mobility alone to supply sufficient stress relaxation. This produces a high dependence on dislocation generation, which requires both time and high shear stress to initiate. Given the results on aluminium, it is suggested that cold work is responsible for increased stress relaxation due to the higher availability of initial mobile dislocations, effectively reducing the dependence on both generation and mobility. Modelling of the experimental data indicated that the dislocation generation terms need to account for differences in dislocation annihilation and recovery, in order to capture the lessened need for generation in cases of high initial dislocation density.

Future work should here focus on investigating the theoretical reversal in the effects of cold work as strain rate decreases (or propagation distance increases). A transition to cold work causing increased rather than reduced strength should occur between strain rates of around $10^3$-$10^4$ $s^{-1}$, however direct experimental

measurement of this reversal is still required. Measurement of the transition is of high importance to future work, as it can be used to quantify the point at which dislocation mobility starts to become a limitation in stress relaxation. Focus should also be placed on further investigating the role of mobile versus immobile dislocations. As a result, quantitative determination of dislocation densities in materials such as tantalum is needed, where cold work produced a decreased peak elastic stress despite qualitatively similar initial dislocation densities. Emphasis should also be placed on conducting similar studies in other materials of high purity, where complications due to secondary phase particles are eliminated.

# References


[1] E. L. Thomas. *Opportunities in Protection Materials Science and Technology for Future Army Applications*. Hoboken, NJ, USA.: John Wiley & Sons, Inc, 2012.

[2] R. J. Clifton. "High Strain Rate Behavior of Metals". In: *Applied Mechanics Reviews* 43.5S (1990), S9.

[3] M. A. Meyers et al. "Constitutive description of dynamic deformation: Physically-based mechanisms". In: *Materials Science and Engineering A* 322.1-2 (2002), pp. 194–216.

[4] G. R. Fowles. "Shock wave compression of hardened and annealed 2024 aluminum". In: *Journal of Applied Physics* 32.8 (1961), pp. 1475–1487.

[5] J. W. Taylor and M. H. Rice. "Elastic-Plastic Properties of Iron". In: *Journal of Applied Physics* 34.2 (1963), pp. 364–371.

[6] J. R. Asay. "Effects of Point Defects on Elastic Precursor Decay in LiF". In: (1971), pp. 2132–2145.

[7] R. J. Clifton and X. Markenscoff. "Elastic precursor decay and radiation from nonuniformly moving dislocations". In: *Journal of the Mechanics and Physics of Solids* 29.3 (1981), pp. 227–251.

[8] B. Gurrutxaga-Lerma et al. "The mechanisms governing the activation of dislocation sources in aluminum at different strain rates". In: *Journal of the Mechanics and Physics of Solids* 84 (2015), pp. 273–292.

[9] J. D. Clayton and J. T. Lloyd. "Analysis of nonlinear elastic aspects of precursor attenuation in shock-compressed metallic crystals". In: (2018).

[10] J. W. Taylor. "Dislocation dynamics and dynamic yielding". In: *Journal of Applied Physics* 36.10 (1965), pp. 3146–3150.

[11] J. N. Johnson, O. E. Jones, and T. E. Michaels. "Dislocation dynamics and single-crystal constitutive relations: Shock-wave propagation and precursor decay". In: *Journal of Applied Physics* 41.6 (1970), pp. 2330–2339.

[12] J. R. Asay et al. "Effects of point defects on elastic precursor decay in LiF". In: *Journal of Applied Physics* 43.5 (1972), pp. 2132–2145.

[13] Y. M. Gupta. "Effect of crystal orientation on dynamic strength of LiF". In: *Journal of Applied Physics* 48.12 (1977), pp. 5067–5073.

[14] M. A. Meyers et al. *Dislocations in Solids 15*. Vol. 15. Elsevier, 2009, pp. 91–197.

[15] M. A. Meyers. *Dynamic Behavior of Materials*. John Wiley  Sons, Ltd, 1994.

[16] P. P. Gillis, K. G. Hoge, and R. J. Wasley. "Elastic precursor decay in tantalum". In: *Journal of Applied Physics* 42.5 (1971), pp. 2145–2146.

[17] J. L. Ding, J. R. Asay, and T. Ao. "Modeling of the elastic precursor behavior and dynamic inelasticity of tantalum under ramp wave loading to 17 GPa". In: *Journal of Applied Physics* 107.8 (2010), pp. 1–12.

[18] R. A. Austin. "Elastic precursor wave decay in shock-compressed aluminum over a wide range of temperature". In: *Journal of Applied Physics* 123.3 (2018).

[19] R. Kositski and D. Mordehai. "On the origin of the stress spike decay in the elastic precursor in shocked metals". In: *Journal of Applied Physics* 085901.Accepted (2019).

[20] T. E. Arvidsson, Y. M. Gupta, and G. E. Duvall. "Precursor decay in 1060 aluminum". In: *Journal of Applied Physics* 46.10 (1975), pp. 4474–4478.

[21] Y. M. Gupta et al. “Large elastic wave amplitude and attenuation in shocked pure aluminum”. In: *Journal of Applied Physics* 105.3 (2009), pp. 2009–2011.

[22] J. M. Winey et al. “Elastic wave amplitudes in shock-compressed thin polycrystalline aluminum samples”. In: *Journal of Applied Physics* 106.7 (2009), pp. 3–7.

[23] R. F. Smith et al. “High strain-rate plastic flow in Al and Fe”. In: *Journal of Applied Physics* 110.12 (2011).

[24] V. H. Whitley et al. “The elastic-plastic response of aluminum films to ultrafast laser-generated shocks”. In: *Journal of Applied Physics* 109.1 (2011), pp. 4–7.

[25] E. B. Zaretsky and G. I. Kanel. “Effect of temperature, strain, and strain rate on the flow stress of aluminum under shock-wave compression”. In: *Journal of Applied Physics* 112.7 (2012).

[26] T. de Resseguier and M. Hallouin. *Stress relaxation and precursor decay in laser shock-loaded iron*. 1992.

[27] E. B. Zaretsky. “Shock response of iron between 143 and 1275 K”. In: *Journal of Applied Physics* 106.2 (2009).

[28] K. S. Tunison and Y. M. Gupta. “Effect of surface preparation on elastic precursor decay in shocked pure lithium fluoride”. In: *Applied Physics Letters* 48.20 (1986), pp. 1351–1353.

[29] E. B. Zaretsky and G. I. Kanel. “Response of copper to shock-wave loading at temperatures up to the melting point”. In: *Journal of Applied Physics* 114.8 (2013).

[30] J. C. Millett et al. “The Effects of Prior Cold Work on the Shock Response of Copper”. In: *Journal of Dynamic Behavior of Materials* 4.2 (2018), pp. 211–221.

[31] G. I. Kanel et al. “Shock response of magnesium single crystals at normal and elevated temperatures”. In: *Journal of Applied Physics* 116.14 (2014).

[32] J. M. Winey, P. Renganathan, and Y. M. Gupta. “Shock wave compression and release of hexagonal-close-packed metal single crystals: Inelastic deformation of c -axis magnesium”. In: *Journal of Applied Physics* 117.10 (2015).

[33] P. Renganathan, J. M. Winey, and Y. M. Gupta. “Shock compression and release of a-axis magnesium single crystals: Anisotropy and time dependent inelastic response”. In: *Journal of Applied Physics* 121.3 (2017).

[34] P. Renganathan and Y. M. Gupta. “Shock compression / release of magnesium single crystals along a low-symmetry orientation : Role of basal slip”. In: 115902.June (2019).

[35] X. Yu et al. “Influence of initial texture on the shock property and spall behavior of magnesium alloy AZ31B”. In: *Materials Science and Engineering A* 700.May (2017), pp. 259–268.

[36] G. I. Kanel, V. E. Fortov, and S. V. Razorenov. *Shock-Wave Phenomena and the Properties of Condensed Matter*. 2004.

[37] R. G. McQueen. “Shock waves in condensed media: Their properties and the equations of state of materials derived from them”. In: (1989).

[38] M. H. Rice, R. G. McQueen, and J. M. Walsh. “Compression of Solids by Strong Shock Waves”. In: *Solid State Physics - Advances in Research and Applications* 6.C (1958), pp. 1–63.

[39] D. Hull and D. J. Bacon. *Introduction to Dislocations*. 2011.

[40] Y. Kamimura, K. Edagawa, and S. Takeuchi. “Experimental evaluation of the Peierls stresses in a variety of crystals and their relation to the crystal structure”. In: *Acta Materialia* 61.1 (2013), pp. 294–309.

[41] M. Liu et al. “Twin-induced one-dimensional homojunctions yield high quantum efficiency for solar hydrogen generation”. In: *Nature Communications* 4 (2013).

[42] M. R. Barnett. “Twinning and the ductility of magnesium alloys. Part I: "Tension" twins”. In: *Materials Science and Engineering A* 464.1-2 (2007), pp. 1–7.

[43] S. A. Habib et al. “Anisotropy, tension-compression asymmetry and texture evolution of a rare-earth-containing magnesium alloy sheet, ZEK100, at different strain rates and temperatures: Experiments and modeling”. In: *International Journal of Plasticity* 95 (2017), pp. 163–190.

[44] J. N. Florando et al. “Effect of strain rate and dislocation density on the twinning behavior in tantalum”. In: *AIP Advances* 6.4 (2016).

[45] M. A. Meyers et al. “Deformation substructures and their transitions in laser shock-compressed copper-aluminum alloys”. In: *Metallurgical and Materials Transactions A: Physical Metallurgy and Materials Science* 39.2 (2008), pp. 304–321.

[46] B. Li et al. “A nucleation mechanism of deformation twins in pure aluminum”. In: *Acta Materialia* 57.15 (2009), pp. 4500–4507.

[47] G. Johnson and W. Cook. “A Constitutive Model and Data for Metals Subjected to Large Strains, High Strain Rates, and High Temperatures”. In: *Proceedings 7th International Symposium on Ballistics* (1983), pp. 541–547.

[48] B. Gurrutxaga-Lerma et al. “The effect of temperature on the elastic precursor decay in shock loaded FCC aluminium and BCC iron”. In: *International Journal of Plasticity* 96 (2017), pp. 135–155.

[49] C. G. Panait et al. “Evolution of dislocation density, size of subgrains and MX-type precipitates in a P91 steel during creep and during thermal ageing at 600°C for more than 100,000h”. In: *Materials Science and Engineering A* 527.16-17 (2010), pp. 4062–4069.

[50] M. A. Meyers. “A mechanism for dislocation generation in shock-wave deformation”. In: *Scripta Metallurgica* 12.1 (1978), pp. 21–26.

[51] W. G. Johnston and J. J. Gilman. “Dislocation velocities, dislocation densities, and plastic flow in lithium fluoride crystals”. In: *Journal of Applied Physics* 30.2 (1959), pp. 129–144.

[52] F. J. Zerilli. “Dislocation mechanics-based constitutive equations”. In: *Met. Mater. Trans. A* 35.9 (2004), pp. 2547–2555.

[53] B. A. Remington et al. “Material dynamics under extreme conditions of pressure and strain rate”. In: *Materials Science and Technology* 22.4 (2006), pp. 474–488.

[54] R. W. Armstrong and S. M. Walley. “High strain rate properties of metals and alloys”. In: *International Materials Reviews* 53.3 (2008), pp. 105–128.

[55] A. D. Brailsford. “Anharmonicity contributions to dislocation drag”. In: *Journal of Applied Physics* 43.4 (1972), pp. 1380–1393.

[56] B. Gurrutxaga–Lerma et al. “The mechanics and physics of high-speed dislocations: a critical review”. In: *International Materials Reviews* 66.4 (2021), pp. 215–255.

[57] J. C. F. Millett et al. “The role of cold work on the shock response of tantalum”. In: *Journal of Applied Physics* 113.23 (2013).

[58] K. Dang et al. “Mobility of dislocations in Aluminum: Faceting and asymmetry during nanoscale dislocation shear loop expansion”. In: *Acta Materialia* 168 (2019), pp. 426–435.

[59] G. D. Owen et al. “Spall behaviour of single crystal aluminium at three principal orientations”. In: *Journal of Applied Physics* 122.15 (2017), p. 155102.

[60] D. E. Grady. “Shock-wave strength properties of boron carbide and silicon carbide.” In: *Le Journal de Physique IV* 04.C8 (1994), pp. C8–385–C8–391.

[61] R. W. Goranson et al. “Dynamic determination of the compressibility of metals”. In: *Journal of Applied Physics* 26.12 (1955), pp. 1472–1479.

[62] J. M. Walsh and R. H. Christian. “Equation of state of metals from shock wave measurements”. In: *Physical Review* 97.6 (1955), pp. 1544–1556.

[63] J. M. Walsh et al. “Shock-wave compressions of twenty-seven metals. equations of state of metals”. In: *Physical Review* 108.2 (1957), pp. 196–216.

[64] O. E. Jones, F. W. Neilson, and W. B. Benedick. “Dynamic yield behavior of explosively loaded metals determined by a quartz transducer technique”. In: *Journal of Applied Physics* 33.11 (1962), pp. 3224–3232.

[65] J. R. Holland. “Strain ageing effects and stress relaxation in iron during shock loading”. In: 15.May (1967).

[66] O. E. Jones and J. R. Holland. “Effects of grain size on dynamic yielding in explosively loaded mild steel”. In: 16.August (1968).

[67] R. W. Rohde. “Dynamic yield behavior of shock-loaded iron from 76 to 573°k”. In: *Acta Metallurgica* 17.3 (1969), pp. 353–363.

[68] O. E. Jones and J. D. Mote. “Shock-induced dynamic yielding in copper single crystals”. In: *Journal of Applied Physics* 40.12 (1969), pp. 4920–4928.

[69] W. J. Murri and G. D. Anderson. “Hugoniot elastic limit of single-crystal sodium chloride”. In: *Journal of Applied Physics* 41.8 (1970), pp. 3521–3525.

[70] Y. G. Wang, H. L. He, and L. L. Wang. “Experimental investigation of precursor decay in shock-compressed mild steel by the VISAR interferometry technique”. In: *Strain* 46.3 (2010), pp. 298–301.

[71] J. R. Asay et al. “Yield strength of tantalum for shockless compression to 18 GPa”. In: *Journal of Applied Physics* 106.7 (2009).

[72] E. B. Zaretsky and G. I. Kanel. “Dynamic response of Sn over the temperature range 115-503 K”. In: 2009 (2009), pp. 27–33.

[73] G. I. Kanel et al. “Stress relaxation in vanadium under shock and shockless dynamic compression”. In: *Journal of Applied Physics* 118.4 (2015).

[74] L. M. Barker and R. E. Hollenbach. “Interferometer technique for measuring the dynamic mechanical properties of materials”. In: *Review of Scientific Instruments* 36.11 (1965), pp. 1617–1620.

[75] J. N. Johnson and L. M. Barker. “Dislocation dynamics and steady plastic wave profiles in 6061-T6 aluminum”. In: *Journal of Applied Physics* 40.11 (1969), pp. 4321–4334.

[76] J. Lipkin and J. R. Asay. “Reshock and release of shock-compressed 6061-T6 aluminum”. In: *Journal of Applied Physics* 48.1 (1977), pp. 182–189.

[77] B. M. Butcher, D. L. Hicks, and D. B. Holdridge. “Elastic Precrsor Decay and Steady Wave Evolution in Porous Aluminium and Porous Polyurethane”. In: September (1972).

[78] G. I. Kanel et al. “Dynamic yield and tensile strength of aluminum single crystals at temperatures up to the melting point”. In: *Journal of Applied Physics* 90.1 (2001), pp. 136–143.

[79] J. P. Davis. “Experimental measurement of the principal isentrope for aluminum 6061-T6 to 240 GPa”. In: *Journal of Applied Physics* 99.10 (2006).

[80] R. F. Smith et al. “Stiff response of aluminum under ultrafast shockless compression to 110 GPA”. In: *Physical Review Letters* 98.6 (2007), pp. 9–12.

[81] P. B. Trivedi et al. “Influence of grain size on the tensile response of aluminum under plate-impact loading”. In: *Journal of Applied Physics* 102.8 (2007).

[82] E. B. Zaretsky, N. Frage, and S. Kalabukhov. “Shock wave determination of the strengthening of commercial aluminum alloy 6061 by point defects”. In: *Materials Science and Engineering A* 761.April (2019), p. 138066.

[83] R. W. Armstrong, W. Arnold, and F. J. Zerilli. “Dislocation mechanics of copper and iron in high rate deformation tests”. In: *Journal of Applied Physics* 105.2 (2009), pp. 1–8.

[84] E. B. Zaretsky and G. I. Kanel. “Plastic flow in shock-loaded silver at strain rates from 10 4s-1 to 107s-1 and temperatures from 296 K to 1233 K”. In: *Journal of Applied Physics* 110.7 (2011).

[85] G. I. Kanel et al. “Thermal “softening” and “hardening” of titanium and its alloy at high strain rates of shock-wave deforming”. In: *Physics of the Solid State* 45.4 (2003), pp. 656–661.

[86] E. B. Zaretsky. “Impact response of cobalt over the 300-1400 K temperature range”. In: *Journal of Applied Physics* 108.8 (2010).

[87] E. B. Zaretsky and G. I. Kanel. “Tantalum and vanadium response to shock-wave loading at normal and elevated temperatures. Non-monotonous decay of the elastic wave in vanadium”. In: *Journal of Applied Physics* 115.24 (2014).

[88] G. V. Garkushin et al. “Submicrosecond strength of ultrafine-grained materials”. In: *Mechanics of Solids* 45.4 (2010), pp. 624–632.

[89] S. V. Razorenov. “Influence of structural factors on the strength properties of aluminum alloys under shock wave loading”. In: *Matter and Radiation at Extremes* 3.4 (2018), pp. 145–158.

[90] I. G. Brodova et al. “Resistance of submicrocrystalline aluminum alloys to high-rate deformation and fracture after dynamic channel angular pressing”. In: *Physics of Metals and Metallography* 116.5 (2015), pp. 519–526.

[91] K. V. Ivanov, S. V. Razorenov, and G. V. Garkushin. “Quasi-static and shock-wave loading of ultrafine-grained aluminum: effect of microstructural characteristics”. In: *Journal of Materials Science* 53.20 (2018), pp. 14681–14693.

[92] R. L. Whelchel et al. “Spall properties of Al 5083 plate fabricated using equi-channel angular pressing (ECAP) and rolling”. In: *Journal of Physics: Conference Series* 500.PART 11 (2014).

[93] S. V. Razorenov et al. “Resistance to dynamic deformation and fracture of tantalum with different grain and defect structures”. In: *Physics of the Solid State* 54.4 (2012), pp. 790–797.

[94] S. V. Razorenov et al. “Effect of preliminary strain hardening on the flow stress of titanium and a titanium alloy during shock compression”. In: *Physics of the Solid State* 47.4 (2005), pp. 663–669.

[95] G. I. Kanel et al. “Spall fracture properties of aluminum and magnesium at high temperatures”. In: *Journal of Applied Physics* 79.11 (1996), pp. 8310–8317.

[96] L. Farbaniec et al. “Microstructural effects on the spall properties of ECAE-processed AZ31B magnesium alloy”. In: *International Journal of Impact Engineering* 98 (2016), pp. 34–41.

[97] L. Farbaniec et al. “Spall response and failure mechanisms associated with a hot-extruded AMX602 Mg alloy”. In: *Materials Science and Engineering A* 707.September (2017), pp. 725–731.

[98] J. C. Millett et al. “On the behaviour of the magnesium alloy, AZ61 to one-dimensional shock loading”. In: *Acta Materialia* 58.17 (2010), pp. 5675–5682.

[99] N. Dixit, L. Farbaniec, and K. T. Ramesh. “Twinning in single crystal Mg under microsecond impact along the (a) axis”. In: *Materials Science and Engineering A* 693.January (2017), pp. 22–25.

[100] G. V. Garkushin, G. I. Kanel’, and S. V. Razorenov. “High strain rate deformation and fracture of the magnesium alloy Ma2-1 under shock wave loading”. In: *Physics of the Solid State* 54.5 (2012), pp. 1079–1085.

[101] P. J. Hazell et al. “The influence of microstructure on the shock and spall behaviour of the magnesium alloy, Elektron 675”. In: *Acta Materialia* 60.17 (2012), pp. 6042–6050.

[102] J. T. Lloyd, C. L. Williams, and J. D. Clayton. “Dynamic Strength of AZ31B-4E and AMX602 Magnesium Alloys Under Shock Loading”. In: *Journal of Dynamic Behavior of Materials* 0123456789 (2020).

[103] P. J. Hazell et al. “The shock and spall response of three industrially important hexagonal close-packed metals: Magnesium, titanium and zirconium”. In: *Philosophical Transactions of the Royal Society A: Mathematical, Physical and Engineering Sciences* 372.2023 (2014).

[104] M. R. Barnett. “A Taylor model based description of the proof stress of magnesium AZ31 during hot working”. In: *Metallurgical and Materials Transactions A: Physical Metallurgy and Materials Science* 34 A.9 (2003), pp. 1799–1806.

[105] S. R. Agnew, M. H. Yoo, and C. N. Tomé. “Application of texture simulation to understanding mechanical behavior of Mg and solid solution alloys containing Li or Y”. In: *Acta Materialia* 49.20 (2001), pp. 4277–4289.

[106] H. Yoshinaga and R. Horiuchi. “Deformation Mechanisms in Magnesium Single Crystals Compressed in the Direction Parallel to Hexagonal Axis”. In: *Transactions of the Japan Institute of Metals* 4.1 (1963), pp. 1–8.

[107] P. J. F. Stohr and J. P. Poirier. “Etude en Microscopie Electronique du Glissement Pyramidal (1122) (1123) dans le Magnesium”. In: *Philosophical Magazine* 25.6 (1972), pp. 1313–1329.

[108] A. Chapuis and J. H. Driver. “Temperature dependency of slip and twinning in plane strain compressed magnesium single crystals”. In: *Acta Materialia* 59.5 (2011), pp. 1986–1994.

[109] T. Obara, H. Yoshinga, and S. Morozumi. “{1122}1123 Slip system in magnesium”. In: *Acta Metallurgica* 21.7 (1973), pp. 845–853.

[110] H. Tonda and S. Ando. “Effect of temperature and shear direction on yield stress by {1122}1123 slip in HCP metals”. In: *Metallurgical and Materials Transactions A: Physical Metallurgy and Materials Science* 33.3 (2002), pp. 831–836.

[111] J. T. Lloyd and R. Becker. “Stress-based crystal analysis of yielding in rolled Mg AZ31B”. In: *Philosophical Magazine* 96.4 (2016), pp. 370–386.

[112] J. Koike et al. “The activity of non-basal slip systems and dynamic recovery at room temperature in fine-grained AZ31B magnesium alloys”. In: *Acta Materialia* 51.7 (2003), pp. 2055–2065.

[113] K. K. Alaneme and E. A. Okotete. “Enhancing plastic deformability of Mg and its alloys—A review of traditional and nascent developments”. In: *Journal of Magnesium and Alloys* 5.4 (2017), pp. 460–475.

[114] I. Ulacia et al. “Mechanical behavior and microstructural evolution of a Mg AZ31 sheet at dynamic strain rates”. In: *Acta Materialia* 58.8 (2010), pp. 2988–2998.

[115] J. D. Robson. “Critical Assessment 9: Wrought magnesium alloys”. In: *Materials Science and Technology* 31.3 (2015), pp. 257–264.

[116] T. Wang, B. Zuanetti, and V. Prakash. “Shock Response of Commercial Purity Polycrystalline Magnesium Under Uniaxial Strain at Elevated Temperatures”. In: *Journal of Dynamic Behavior of Materials* 3.4 (2017), pp. 497–509.

[117] T. Wang and V. Prakash. “Inelastic Deformation Mechanisms in Shock Compressed Polycrystalline Pure Magnesium at Temperatures Approaching Melt”. In: *Journal of Dynamic Behavior of Materials* 0123456789 (2021).

[118] J. C. Millett et al. “The role of anisotropy in the response of the titanium alloy Ti-6Al-4V to shock loading”. In: *Journal of Applied Physics* 104.7 (2008).

[119] G. T. Gray. “Influence of crystallographic anisotropy on the Hopkinson fracture “spallation” of zirconium”. In: 509.February (2003), pp. 509–512.

[120] Y. M. Gupta et al. “Experimental developments to obtain real-time x-ray diffraction measurements in plate impact experiments”. In: *Review of Scientific Instruments* 70.10 (1999), p. 4008.

[121] Y. M. Gupta et al. “Real-time, high-resolution x-ray diffraction measurements on shocked crystals at a synchrotron facility”. In: *Review of Scientific Instruments* 83.12 (2012).

[122] S. M. Sharma et al. “Real-Time Observation of Stacking Faults in Gold Shock Compressed to 150 GPa REAL-TIME OBSERVATION of STACKING FAULTS in GOLD ... SHARMA SURINDER M. et al.” In: *Physical Review X* 10.1 (2020), p. 11010.

[123] D. E. Eakins and D. J. Chapman. “X-ray imaging of subsurface dynamics in high-Z materials at the Diamond Light Source”. In: *Review of Scientific Instruments* 85.12 (2014).

[124] O. T. Strand et al. “Compact system for high-speed velocimetry using heterodyne techniques”. In: *Review of Scientific Instruments* 77.8 (2006).

[125] N. Barnes and N. K. Bourne. “The shock hugoniot of an epoxy resin”. In: (2002), pp. 5–8.

[126] B. Zuanetti et al. “Measurement of elastic precursor decay in pre-heated aluminum films under ultra-fast laser generated shocks”. In: *Journal of Applied Physics* 123.19 (2018).

[127] L. M. Barker and R. E. Hollenbach. “Shock-wave studies of PMMA, fused silica, and sapphire”. In: *Journal of Applied Physics* 41.10 (1970), pp. 4208–4226.

[128] D. H. Dolan. “Accuracy and precision in photonic doppler velocimetry”. In: *Review of Scientific Instruments* 81.5 (2010).

[129] D. H. Dolan. “Extreme measurements with Photonic Doppler Velocimetry (PDV)”. In: *The Review of scientific instruments* 91.5 (2020), p. 051501.

[130] P. E. Fischione et al. “A Small Spot, Inert Gas, Ion Milling Process as a Complementary Technique to Focused Ion Beam Specimen Preparation”. In: *Microscopy and Microanalysis* 23.4 (2017), pp. 782–793.

[131] N. Kamikawa et al. “Quantification of annealed microstructures in ARB processed aluminum”. In: *Acta Materialia* 54.11 (2006), pp. 3055–3066.

[132] C. L. Williams et al. “On the shock stress, substructure evolution, and spall response of commercially pure 1100-O aluminum”. In: *Materials Science and Engineering A* 618 (2014), pp. 596–604.

[133] R. Hu et al. “Dispersoid formation and recrystallization behavior in an Al-Mg-Si-Mn alloy”. In: *Journal of Materials Science and Technology* 26.3 (2010), pp. 237–243.

[134] C. Zhang et al. “Influence of extrusion parameters on microstructure, texture, and second-phase particles in an Al-Mg-Si alloy”. In: *Journal of Materials Processing Technology* 270.July (2019), pp. 323–334.

[135] D. B. Williams and C. B. Carter. *Transmission Electron Microscopy A Textbook for Material Science*. New York: Springer, 1996.

[136] R. K. Ham. “The determination of dislocation densities in thin films”. In: *Philosophical Magazine* 6.69 (1961), pp. 1193–1194.

[137] Y. Miyajima et al. “Quantification of internal dislocation density using scanning transmission electron microscopy in ultrafine grained pure aluminium fabricated by severe plastic deformation”. In: *Materials Science and Engineering A* 528.2 (2010), pp. 776–779.

[138] R. K. Ham and N. G. Sharpe. “A systematic error in the determination of dislocation densities in thin films”. In: *Philosophical Magazine* 6.69 (1961), pp. 1193–1194.

[139] F. Dalla Torre et al. “Microstructures and properties of copper processed by equal channel angular extrusion for 1-16 passes”. In: *Acta Materialia* 52.16 (2004), pp. 4819–4832.

[140] X. Huang, N. Kamikawa, and N. Hansen. “Strengthening mechanisms in nanostructured aluminum”. In: *Materials Science and Engineering A* 483-484.1-2 C (2008), pp. 102–104.

[141] H. Asgharzadeh, A. Simchi, and H. S. Kim. “Microstructural features, texture and strengthening mechanisms of nanostructured AA6063 alloy processed by powder metallurgy”. In: *Materials Science and Engineering A* 528.12 (2011), pp. 3981–3989.

[142] S. C. Wang, Z. Zhu, and M. J. Starink. “Estimation of dislocation densities in cold rolled Al-Mg-Cu-Mn alloys by combination of yield strength data, EBSD and strength models”. In: *Journal of Microscopy* 217.2 (2005), pp. 174–178.

[143] K. Iakoubovskii et al. “Thickness measurements with electron energy loss spectroscopy”. In: *Microscopy Research and Technique* 71.8 (2008), pp. 626–631.

[144] J. Gubicza et al. “Microstructure of ultrafine-grained fcc metals produced by severe plastic deformation”. In: *Current Applied Physics* 6.2 (2006), pp. 194–199.

[145] A. P. Zhilyaev, A. A. Gimazov, and T. G. Langdon. “Recent developments in modelling of microhardness saturation during SPD processing of metals and alloys”. In: *Journal of Materials Science* 48.13 (2013), pp. 4461–4466.

[146] S. D. Yadav et al. “Evolution of the substructure of a novel 12% Cr steel under creep conditions”. In: *Materials Characterization* 115 (2016), pp. 23–31.

[147] A. A. Ameri et al. “General methodology to estimate the dislocation density from microhardness measurements”. In: *Materials Characterization* 131.January (2017), pp. 324–330.

[148] A. Muiruri, M. Maringa, and W. du Preez. “Evaluation of dislocation densities in various microstructures of additively manufactured ti6al4v (Eli) by the method of x-ray diffraction”. In: *Materials* 13.23 (2020), pp. 1–23.

[149] I. Groma and F. Székely. “Analysis of the asymptotic properties of X-ray line broadening caused by dislocations”. In: *Journal of Applied Crystallography* 33.6 (2000), pp. 1329–1334.

[150] W. Pantleon. “Resolving the geometrically necessary dislocation content by conventional electron backscattering diffraction”. In: *Scripta Materialia* 58.11 (2008), pp. 994–997.

[151] A. J. Wilkinson and D. Randman. “Determination of elastic strain fields and geometrically necessary dislocation distributions near nanoindents using electron back scatter diffraction”. In: *Philosophical Magazine* 90.9 (2010), pp. 1159–1177.

[152] R. Hielscher, F. Bartel, and T. B. Britton. “Gazing at crystal balls: Electron backscatter diffraction pattern analysis and cross correlation on the sphere”. In: *Ultramicroscopy* 207.September (2019), p. 112836.

[153] J. F. Nye. “Some geometrical relations in dislocated crystals”. In: *Acta Metallurgica* 1.2 (1953), pp. 153–162.

[154] O. Muránsky et al. “On the measurement of dislocations and dislocation substructures using EBSD and HRSD techniques”. In: *Acta Materialia* 175 (2019), pp. 297–313.

[155] D. A. Hughes, N. Hansen, and D. J. Bammann. “Geometrically necessary boundaries, incidental dislocation boundaries and geometrically necessary dislocations”. In: *Scripta Materialia* 48.2 (2003), pp. 147–153.

[156] F. Castro and Y. Jiang. “Fatigue life and early cracking predictions of extruded AZ31B magnesium alloy using critical plane approaches”. In: *International Journal of Fatigue* 88 (2016), pp. 236–246.

[157] S. H. Park et al. “Effect of anisotropy on the low-cycle fatigue behavior of rolled AZ31 magnesium alloy”. In: *Materials Science and Engineering A* 527.3 (2010), pp. 417–423.

[158] X. Y. Lou et al. “Hardening evolution of AZ31B Mg sheet”. In: *International Journal of Plasticity* 23.1 (2007), pp. 44–86.

[159] H. Watanabe and K. Ishikawa. “Effect of texture on high temperature deformation behavior at high strain rates in a Mg-3Al-1Zn alloy”. In: *Materials Science and Engineering A* 523.1-2 (2009), pp. 304–311.

[160] J. T. Lloyd et al. “Simulation of shock wave propagation in single crystal and polycrystalline aluminum”. In: *International Journal of Plasticity* 60 (2014), pp. 118–144.

[161] L. Lu et al. “Anisotropic deformation of extruded magnesium alloy AZ31 under uniaxial compression: A study with simultaneous in situ synchrotron x-ray imaging and diffraction”. In: *Acta Materialia* 120 (2016), pp. 86–94.

[162] L. Wu et al. “The effects of texture and extension twinning on the low-cycle fatigue behavior of a rolled magnesium alloy, AZ31B”. In: *Materials Science and Engineering A* 527.26 (2010), pp. 7057–7067.

[163] H. Somekawa and T. Mukai. “Effect of texture on fracture toughness in extruded AZ31 magnesium alloy”. In: *Scripta Materialia* 53.5 (2005), pp. 541–545.

[164] S. Kleiner and P. J. Uggowitzer. “Mechanical anisotropy of extruded Mg-6% Al-1% Zn alloy”. In: *Materials Science and Engineering A* 379.1-2 (2004), pp. 258–263.

[165] D. H. Dolan, T. Ao, and O. Hernandez. “Note: Frequency-conversion photonic Doppler velocimetry with an inverted circulator”. In: *Review of Scientific Instruments* 83.2 (2012).

[166] R. E. Winter, P. T. Keightley, and E. J. Harris. “Derivation of the constitutive model of high elastic limit window materials”. In: *AIP Conference Proceedings* 1195 (2009), pp. 537–540.

[167] H. Huang and J. R. Asay. “Reshock response of shock deformed aluminum”. In: *Journal of Applied Physics* 100.4 (2006).

[168] D. Sarker, J. Friedman, and D. L. Chen. “Influence of pre-strain on de-twinning activity in an extruded AM30 magnesium alloy”. In: *Materials Science and Engineering A* 605 (2014), pp. 73–79.

[169] K. Ishikawa, H. Watanabe, and T. Mukai. “High temperature compressive properties over a wide range of strain rates in an AZ31 magnesium alloy”. In: *Journal of Materials Science* 40.7 (2005), pp. 1577–1582.

[170] C. Y. Gao and L. C. Zhang. “Constitutive modelling of plasticity of fcc metals under extremely high strain rates”. In: *International Journal of Plasticity* 32-33 (2012), pp. 121–133.

[171] C. Y. Gao et al. “Dynamic plasticity of AZ31 magnesium alloy: Experimental investigation and constitutive modeling”. In: *Materials Science and Engineering A* 613 (2014), pp. 379–389.

[172] S. Groh et al. “Dislocation motion in magnesium: A study by molecular statics and molecular dynamics”. In: *Modelling and Simulation in Materials Science and Engineering* 17.7 (2009).

[173] J. N. Johnson. “Shock propagation produced by planar impact in linearly elastic anisotropic media”. In: *Journal of Applied Physics* 42.13 (1971), pp. 5522–5530.

[174] J. N. Johnson. “Calculation of plane-wave propagation in anisotropic elastic-plastic solids”. In: *Journal of Applied Physics* 43.5 (1972), pp. 2074–2082.

[175] J. N. Johnson. “An analysis of thermally-induced plane waves in elastic-plastic single crystals”. In: *Journal of the Mechanics and Physics of Solids* 20.6 (1972), pp. 367–380.

[176] L. Pope and J. Johnson. “Shockwave compression of singlecrystal beryllium”. In: *Journal of Applied Physics* 720.46 (1975).

[177] L. J. Slutsky and C. W. Garland. “Elastic constants of magnesium from 4.2°K to 300°K”. In: *Physical Review* 107.4 (1957), pp. 972–976.

[178] X. L. Nan et al. “Calculation of Schmid factors in magnesium: Analysis of deformation behaviors”. In: *Scripta Materialia* 67.5 (2012), pp. 443–446.

[179] G. I. Kanel. “Unusual behaviour of usual materials in shock waves Unusual behaviour of usual materials in shock waves”. In: (2014).

[180] J. Wang, J. M. Molina-Aldareguía, and J. LLorca. “Effect of Al content on the critical resolved shear stress for twin nucleation and growth in Mg alloys”. In: *Acta Materialia* 188 (2020), pp. 215–227.

[181] S. H. Kim et al. “Anisotropic in-plane fatigue behavior of rolled magnesium alloy with {1012} twins”. In: *Materials Science and Engineering A* 700.June (2017), pp. 191–197.

[182] J. H. Park et al. “Role of tension twins on warm deformation behavior of AZ31 Mg alloy”. In: *Metals and Materials International* 19.3 (2013), pp. 389–398.

[183] M. R. Barnett, Z. Keshavarz, and X. Ma. “A semianalytical Sachs model for the flow stress of a magnesium alloy”. In: *Metallurgical and Materials Transactions A: Physical Metallurgy and Materials Science* 37.7 (2006), pp. 2283–2293.

[184] L. Zhou et al. “Microstructural evolution of Mg–6Zn–0.6Zr alloy during high strain rate compression deformation”. In: *Materials Science and Technology (United Kingdom)* (2021), pp. 0–11.

[185] W. B. Hutchinson and M. R. Barnett. “Effective values of critical resolved shear stress for slip in polycrystalline magnesium and other hcp metals”. In: *Scripta Materialia* 63.7 (2010), pp. 737–740.

[186] S. R. Agnew, D. W. Brown, and C. N. Tomé. “Validating a polycrystal model for the elastoplastic response of magnesium alloy AZ31 using in situ neutron diffraction”. In: *Acta Materialia* 54.18 (2006), pp. 4841–4852.

[187] J. Koike and R. Ohyama. “Geometrical criterion for the activation of prismatic slip in AZ61 Mg alloy sheets deformed at room temperature”. In: *Acta Materialia* 53.7 (2005), pp. 1963–1972.

[188] A. Jain and S. R. Agnew. “Modeling the temperature dependent effect of twinning on the behavior of magnesium alloy AZ31B sheet”. In: *Materials Science and Engineering A* 462.1-2 (2007), pp. 29–36.

[189] M. Ardeljan et al. “Strain rate and temperature sensitive multi-level crystal plasticity model for large plastic deformation behavior: Application to AZ31 magnesium alloy”. In: *International Journal of Plasticity* 83 (2016), pp. 90–109.

[190] V. Herrera-Solaz et al. “An inverse optimization strategy to determine single crystal mechanical behavior from polycrystal tests: Application to AZ31 Mg alloy”. In: *International Journal of Plasticity* 57 (2014), pp. 1–15.

[191] Z. Fan et al. “Melt conditioning by advanced shear technology (MCAST) for refining solidification microstructures”. In: *International Journal of Cast Metals Research* 22.1-4 (2009), pp. 103–107.

[192] Z. Fan, G. Liu, and Y. Wang. “Microstructure and mechanical properties of rheo-diecast AZ91D magnesium alloy”. In: *Journal of Materials Science* 41.12 (2006), pp. 3631–3644.

[193] Z. Y. Fan, Y. B. Zuo, and B. Jiang. “A New Technology for Treating Liquid Metals with Intensive Melt Shearing”. In: *Materials Science Forum* 690 (2011), pp. 141–144.

[194] S. Kumar et al. “Influence of intensive melt shearing on the microstructure and mechanical properties of an Al-Mg alloy with high added impurity content”. In: *Metallurgical and Materials Transactions A: Physical Metallurgy and Materials Science* 42.10 (2011), pp. 3141–3149.

[195] H. Men, B. Jiang, and Z. Fan. “Mechanisms of grain refinement by intensive shearing of AZ91 alloy melt”. In: *Acta Materialia* 58.19 (2010), pp. 6526–6534.

[196] Y. Wang, G. Liu, and Z. Fan. “Microstructural evolution of rheo-diecast AZ91D magnesium alloy during heat treatment”. In: *Acta Materialia* 54.3 (2006), pp. 689–699.

[197] D. J. Luscher et al. “A dislocation density-based continuum model of the anisotropic shock response of single crystal $\alpha$-cyclotrimethylene trinitramine”. In: *Journal of the Mechanics and Physics of Solids* 98 (2017), pp. 63–86.

[198] X. Markenscoff and R. J. Clifton. “The nonuniformly moving edge dislocation”. In: *Journal of the Mechanics and Physics of Solids* 29.3 (1981), pp. 253–262.

[199] B. Gurrutxaga-Lerma et al. “A dynamic discrete dislocation plasticity method for the simulation of plastic relaxation under shock loading”. In: *Proceedings of the Royal Society A: Mathematical, Physical and Engineering Sciences* 469.2156 (2013), pp. 20130141–20130141.

[200] R. A. Austin and D. L. McDowell. “Parameterization of a rate-dependent model of shock-induced plasticity for copper, nickel, and aluminum”. In: *International Journal of Plasticity* 32-33 (2012), pp. 134–154.

[201] G. I. Taylor. “Plastic strain in metals”. In: *Journal of the Institute of Metals* 62 (1938), pp. 307–324.

[202] M. A. Abdulstaar et al. “Severe plastic deformation of commercial purity aluminum by rotary swaging: Microstructure evolution and mechanical properties”. In: *Materials Science and Engineering A* 565 (2013), pp. 351–358.

[203] Y. Yang et al. “Improving the combination of electrical conductivity and tensile strength of Al 1070 by rotary swaging deformation”. In: *Results in Physics* 13.March (2019), p. 102236.

[204] H. Huang and J. R. Asay. “Compressive strength measurements in aluminum for shock compression over the stress range of 4-22 GPa”. In: *Journal of Applied Physics* 98.3 (2005).

[205] N. Kamikawa et al. “Strengthening mechanisms in nanostructured high-purity aluminium deformed to high strain and annealed”. In: *Acta Materialia* 57.14 (2009), pp. 4198–4208.

[206] N. Q. Chinh et al. “Experimental evidence for grain-boundary sliding in ultrafine-grained aluminum processed by severe plastic deformation”. In: *Advanced Materials* 18.1 (2006), pp. 34–39.

[207] Y. Ito and Z. Horita. “Microstructural evolution in pure aluminum processed by high-pressure torsion”. In: *Materials Science and Engineering A* 503.1-2 (2009), pp. 32–36.

[208] M. Lipinska et al. “Ultrafine-Grained Plates of Al-Mg-Si Alloy Obtained by Incremental Equal Channel Angular Pressing: Microstructure and Mechanical Properties”. In: *Metallurgical and Materials Transactions A: Physical Metallurgy and Materials Science* 48.10 (2017), pp. 4871–4882.

[209] J. May et al. “Mechanical properties, dislocation density and grain structure of ultrafine-grained aluminum and aluminum-magnesium alloys”. In: *Metallurgical and Materials Transactions A: Physical Metallurgy and Materials Science* 38 A.9 (2007), pp. 1941–1945.

[210] W. M. Gan et al. “Microstructures and mechanical properties of pure Mg processed by rotary swaging”. In: *Materials and Design* 63 (2014), pp. 83–88.

[211] S. J. Lim, H. J. Choi, and C. H. Lee. “Forming characteristics of tubular product through the rotary swaging process”. In: *Journal of Materials Processing Technology* 209.1 (2009), pp. 283–288.

[212] M. Abdulstaar et al. “Corrosion behaviour of Al 1050 severely deformed by rotary swaging”. In: *Materials and Design* 57 (2014), pp. 325–329.

[213] L. Malecek et al. “Preface: International Conference on Recent Trends in Physics (ICRTP 2016)”. In: *Journal of Physics: Conference Series* 755.1 (2016).

[214] Z. Yan et al. “Ratcheting strain and microstructure evolution of AZ31B magnesium alloy under a tensile-tensile cyclic loading”. In: *Materials* 11.4 (2018).

[215] J. Nacházel et al. “Effects of rotary swaging parameters and artificial ageing on mechanical properties and microstructure of 2024 precipitation-hardenable aluminium alloy”. In: *Materials* 13.1 (2020).

[216] D. Yadav and R. Bauri. “Effect of friction stir processing on microstructure and mechanical properties of aluminium”. In: *Materials Science and Engineering A* 539.December 2017 (2012), pp. 85–92.

[217] T. Sakai et al. “Dynamic and post-dynamic recrystallization under hot, cold and severe plastic deformation conditions”. In: *Progress in Materials Science* 60.1 (2014), pp. 130–207.

[218] Y. El-Madhoun, A. Mohamed, and M. N. Bassim. “Cyclic stress-strain response and dislocation structures in polycrystalline aluminum”. In: *Materials Science and Engineering A* 359.1-2 (2003), pp. 220–227.

[219] N. Kumar et al. “The influence of metallurgical factors on low cycle fatigue behavior of ultra-fine grained 6082 Al alloy”. In: *International Journal of Fatigue* 110.December 2017 (2018), pp. 130–143.

[220] M. Cabibbo, E. Evangelista, and M. Vedani. “Influence of severe plastic deformations on secondary phase precipitation in a 6082 Al-Mg-Si alloy”. In: *Metallurgical and Materials Transactions A: Physical Metallurgy and Materials Science* 36.5 (2005), pp. 1353–1364.

[221] M. Liu et al. “Deformation structures in 6082 aluminium alloy after severe plastic deformation by equal-channel angular pressing”. In: *Materials Science and Engineering A* 483-484.1-2 C (2008), pp. 59–63.

[222] X. C. Liu, H. W. Zhang, and K. Lu. “Strain-Induced Ultrahard and Ultrastable Nanolaminated Structure in Nickel”. In: *Science* 342.October (2013), pp. 337–340.

[223] V. Y. Gertsman and R. Birringer. “On the room-temperature grain growth in nanocrystalline copper”. In: *Scripta Metallurgica et Materiala* 30.5 (1994), pp. 577–581.

[224] Y. Miyajima et al. “Dislocation density of FCC metals processed by ARB”. In: *IOP Conference Series: Materials Science and Engineering* 63.1 (2014).

[225] N. Kumar et al. “Effect of cryorolling and annealing on recovery, recrystallisation, grain growth and their influence on mechanical and corrosion behaviour of 6082 Al alloy”. In: *Materials Chemistry and Physics* 165 (2015), pp. 177–187.

[226] M. Muzyk, Z. Pakiela, and K. J. Kurzydlowski. “Ab initio calculations of the generalized stacking fault energy in aluminium alloys”. In: *Scripta Materialia* 64.9 (2011), pp. 916–918.

[227] J. C. F. Millett et al. “The role of aging on the mechanical and microstructural response of aluminum 6061 to one-dimensional shock loading”. In: *Journal of Applied Physics* 108.7 (2010), pp. 1–9.

[228] J. C. Millett, G. Whiteman, and N. K. Bourne. “Lateral stress and shear strength behind the shock front in three face centered cubic metals”. In: *Journal of Applied Physics* 105.3 (2009).

[229] J. Jiang, T. B. Britton, and A. J. Wilkinson. “Measurement of geometrically necessary dislocation density with high resolution electron backscatter diffraction: Effects of detector binning and step size”. In: *Ultramicroscopy* 125 (2013), pp. 1–9.

[230] C. Zhu et al. “Dislocation-type evolution in quasi-statically compressed polycrystalline nickel”. In: *Acta Materialia* 155.May (2018), pp. 104–116.

[231] M. F. Ashby. “The deformation of plastically non-homogeneous materials”. In: *Philosophical Magazine* 21.170 (1970), pp. 399–424.

[232] K. Sakino. “Transition in rate controlling mechanism of FCC metals at very high strain rates and high temperatures”. In: *Journal de Physique* 10 (2000).

[233] J. R. Asay et al. “Effect of initial properties on the flow strength of aluminum during quasi-isentropic compression”. In: *Journal of Applied Physics* 103.8 (2008).

[234] G. E. Dieter. “In Strengthening Mechanisms in Solids”. In: *ASM* (1962), p. 279.

[235] W. C. Leslie. *Metallurgical Effects at High Strain Rates*. Ed. by R. W. Rohde et al. New York: Plenum Press, 1973, p. 571.

[236] L. E. Murr and D. Kuhlmann-Wilsdorf. “Experimental and theoretical observations on the relationship between dislocation cell size, dislocation density, residual hardness, peak pressure and pulse duration in shock-loaded nickel”. In: *Acta Metallurgica* 26.5 (1978), pp. 847–857.

[237] D. H. Liu, H. P. Yu, and C. F. Li. “Comparative study of the microstructure of 5052 aluminum alloy sheets under quasi-static and high-velocity tension”. In: *Materials Science and Engineering A* 551 (2012), pp. 280–287.

[238] Q. Liu et al. “The response of dislocations , low angle grain boundaries and high angle grain boundaries at high strain rates”. In: *Materials Science & Engineering A* 822.June (2021), p. 141704.

[239] N. Zhou and L. Zhou. “Structure and nucleation mechanisms of misfit dislocations in epitaxial FCC thin films with positive and negative mismatches”. In: *Materials Chemistry and Physics* 100.1 (Nov. 2006), pp. 168–173.

[240] D. Hull and D. Bacon. “Dislocation Arrays and Crystal Boundaries”. In: *Introduction to Dislocations* (2011), pp. 171–204.

[241] A. G. Perez-Bergquist et al. “The role of the structure of grain boundary interfaces during shock loading”. In: *AIP Conference Proceedings* 1426.March (2012), pp. 1359–1362.

[242] E. K. Cerreta et al. “Early stage dynamic damage and the role of grain boundary type”. In: *Scripta Materialia* 66.9 (2012), pp. 638–641.

[243] E. Zaretsky. “Dislocation multiplication behind the shock front”. In: *Journal of Applied Physics* 78.6 (1995), pp. 3740–3747.

[244] B. Gurrutxaga-Lerma et al. “The Role of Homogeneous Nucleation in Planar Dynamic Discrete Dislocation Plasticity”. In: *Journal of Applied Mechanics* 82.7 (2015), pp. 71008–71012.

[245] R. F. Smith et al. “Orientation and rate dependence in high strain-rate compression of single-crystal silicon”. In: *Physical Review B* 86 (24 Dec. 2012), p. 245204.

[246] L. W. Meyer et al. “Compressive behaviour of ultrafine-grained AA6063T6 over a wide range of strains and strain rates”. In: *Zeitschrift fuer Metallkunde/Materials Research and Advanced Techniques* 98.3 (2007), pp. 191–199.

[247] I. Brodova et al. “The influence of the structure of ultrafine-grained aluminium alloys on their mechanical properties under dynamic compression and shock-wave loading The influence of the structure of ultrafine-grained aluminium alloys on their mechanical properties under”. In: (2017).

[248] R. L. Whelchel et al. “Spall behavior of rolled aluminum 5083-H116 plate”. In: *Journal of Applied Physics* 113.23 (2013).

[249] A. P. Mouritz. *Introduction to aerospace materials*. Reston, VA : American Institute of Aeronautics and Astronautics, 2012.

[250] J. C. F. Millett et al. “On the behaviour of body-centred cubic metals to one-dimensional shock loading”. In: *Journal of Materials Science* 46.11 (2011), pp. 3899–3906.

[251] C. H. Karnes and E. A. Ripperger. *STRAIN RATE EFFECTS IN COLD WORKED HIGH-PURITY ALUMINIUM*". Tech. rep. 1966, pp. 75–88.

[252] J. T. Lloyd et al. “Plane wave simulation of elastic-viscoplastic single crystals”. In: *Journal of the Mechanics and Physics of Solids* 69 (2014), pp. 14–32.

[253] U. F. Kocks and H. Mecking. “Physics and phenomenology of strain hardening: the FCC case U.F.” In: *Progress in Materials Science* 48 (2003), pp. 171–273.

[254] R. Kositski and D. Mordehai. “A dislocation-based dynamic strength model for tantalum across a large range of strain rates A dislocation-based dynamic strength model for tantalum across a large range of strain rates”. In: 165108.April (2021).

[255] K. Dang et al. “Mobility of dislocations in aluminum: The role of non-Schmid stress state”. In: *Acta Materialia* 185 (2020), pp. 420–432.